Distribution Agreement

In presenting this thesis or dissertation as a partial fulfillment of the requirements for an advanced degree from Emory University, I hereby grant to Emory University and its agents the non-exclusive license to archive, make accessible, and display my thesis or dissertation in whole or in part in all forms of media, now or hereafter known, including display on the world wide web. I understand that I may select some access restrictions as part of the online submission of this thesis or dissertation. I retain all ownership rights to the copyright of the thesis or dissertation. I also retain the right to use in future works (such as articles or books) all or part of this thesis or dissertation.

Signature:

_____ _____

Zihao Xu Date

Ultrafast Charge and Energy Transfer Dynamics in Photoelectrochemical and QD-based Photon Upconversion Systems

By

Zihao Xu
Doctor of Philosophy

Chemistry

_____

Dr. Tianquan Lian
Advisor

_____

Dr. Craig L. Hill
Committee Member

_____

Dr. Brian Dyer
Committee Member

Accepted:

_____

Lisa A. Tedesco, Ph.D.
Dean of the James T. Laney School of Graduate Studies

_____

Date

Ultrafast Charge and Energy Transfer Dynamics in Photoelectrochemical and QD-based Photon Upconversion Systems

By

Zihao Xu

B.S., Nanjing University, China, 2013

Advisor: Tianquan Lian, Ph.D.

An abstract of

A dissertation submitted to the Faculty of the

James T. Laney School of Graduate Studies of Emory University

in partial fulfillment of the requirements for the degree of

Doctor of Philosophy

in Chemistry

2019

Abstract

Ultrafast Charge and Energy Transfer Dynamics in Photoelectrochemical and QD-based Photon Upconversion Systems

By Zihao Xu

Photocatalysis at the semiconductor-liquid interface is a complex process, which includes the separation, transport, surface recombination, and ultimately interfacial transfer of photoexcited carriers. The rates and efficiencies of these processes are influenced by the electrostatic fields within the semiconductor at the solid/liquid interface. However, direct *in situ* time-resolved probe of the interfacial field and their influence on the aforementioned elementary steps have been difficult so far, and as a result, mechanistic understandings of key efficiency limiting factors remains poorly developed. Here in the first section, we use *in situ* transient reflectance spectroscopy to directly both the dynamics and efficiency of charge separation across the p-GaP/TiO_2 interface through the Franz-Keldysh effect. We demonstrate that with more negative applied electrochemical potentials, both rate and efficiency of interfacial carrier separation increases. The efficiency of this initial charge separation event (occurring on the < 200 ps time scale) correlates well with the incident photon to current efficiency (IPCE) of these photoelectrodes over a wide range of potentials and excitation power densities, which provides direct evidence that the steady state IPCE is determined by the transiently separated charge carriers on the ultrafast time scale. This study establishes a powerful and general method for *in situ* time-resolved probe of carrier dynamics in other semiconductor photoelectrode. Photogenerated carrier eventually migrates to the semiconductor/liquid interface for charge transfer to the redox species in electrolyte. Observation of this step and understanding the reaction mechanism could reveal mechanistic insights on the effect of catalysts and other surface modifications. We have also developed a time resolved electrical field induced second harmonic generation (EFISH) technique probe the extent of band bending and carrier dynamics in the semiconductor, which is general method that is applicable to all semiconductors.

Quantum dot sensitized triplet-triplet annihilation photon upconversion is a promising method to utilize sub band gap photons for photoelectrochemical applications that requires high energy photon. It is a constant challenge to develop efficient up conversion system. In the last section we utilized transient absorption spectroscopy to study the key efficiency limiting factors in quantum dot sensitized triplet energy transfer.

Ultrafast Charge and Energy Transfer Dynamics in Photoelectrochemical and QD-based Photon Upconversion Systems

By

Zihao Xu

B.S., Nanjing University, China, 2013

Advisor: Tianquan Lian, Ph.D.

A dissertation submitted to the Faculty of the

James T. Laney School of Graduate Studies of Emory University

in partial fulfillment of the requirements for the degree of

Doctor of Philosophy

in Chemistry

2019

ACKNOWLEDGEMENT

First, I would like to express my deepest gratitude to my advisor, Dr. Tianquan Lian, for his patient guidance and strong support throughout my graduate study. It is my great honor to have the opportunity in the last six years to learn from him how scientific research is done. His broad knowledge and expertise in both physical chemistry and other fields, his critical thinking, and desire to always pursue deeper understanding of a problem have shaped me as a scientist. He collaborates widely with many scientists from various fields and generates wonderful topics and results from the collaboration. Dr. Lian will always be my model in my future research career. Here I'd also like to express my sincere gratitude to my committee members, Dr. Craig L. Hill and Dr. Brian Dyer, for valuable feedbacks on my research progress and for stimulating discussions and research collaborations.

I'd like to thank Dr. Jinquan Chen for his patient training on the transient spectroscopy and femtosecond laser, which most of my work is based on. Dr. Kaifeng Wu, Dr. Aimin Ge and my roommate Dr. Qiuyang Li, for our time spent together both in- and out- side the labs. You have taught me a lot and I enjoyed the time very much. To my labmates, Dr. Qiongyi Shang, Jia Song, Yawei Liu, Qiliang Liu, Tao Jin, Sara Gebre, Fengyi Zhao, Jinhui Meng, Dr. Wenxing Yang and Dr. Laura Kiefer, thank you for making the lab a comfortable place where I can call home. I'd also like to thank my collaborators from whom I learned a lot, Dr. Ming Lee Tang, Dr. Steve Cronin, Dr. Wenshan Cai, Dr. Eilaf Egap, Dr. Francesco Evangelista, Dr. Jamal Musaev, Dr. Alexey Kaledin, Dr. Yiming Huang, Dr. Zhiyuan Huang and Mohammad Taghinejad.

Finally, I'd like to express my love to my family, my father, my mother and, especially, my wife, Yurui Mu. They supported me with unconditional love. I treasure every moment I spent with them.

Table of Contents

List of Figures

List of Tables

1. Chapter 1. Introduction

1.1 Solar water splitting with semiconductor electrode

Photoelectrochemical (PEC) system can capture the energy of sunlight photons and store them in the form of chemicals, which can be used in fuel cells to generate electricity on demand. The fuel, such as hydrogen or alcohol, is an easily stored energy form compared to electricity generated from photovoltaic devices, whose work performance also depends greatly on the weather conditions.[1] Photons absorbed by sensitizers generate charge carriers that transport potential energy to the surface reactive sites for photoreaction.[2] The key factor in determining the performance of a photoelectrochemical cell is the semiconductor electrode material. The semiconductor's first key function is to absorb the incident photon and convert it to separated charge carriers, which the minority carriers (holes for n-type semiconductor and electrons for p-type) are responsible for the chemical reactions, that is holes for n type semiconductors and electrons for p type semiconductors.[3] There are several efficiency limiting factors associated with the band gap of the semiconductor materials. First, the band gap between the valence band and the conduction band within the bulk semiconductor determines the upper limit of the energy conversion efficiency, because only photons with greater energy than the band gap can be absorbed.

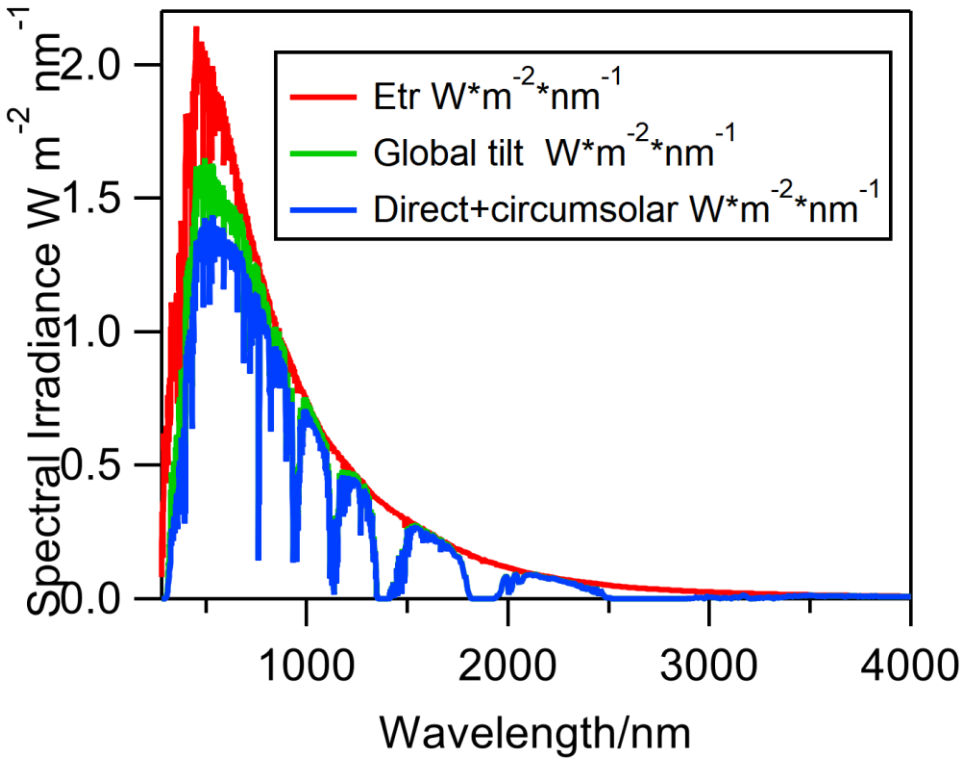

Figure 1.1 ASTM G173-03 Reference spectra reproduced from NREL.[4] Here the Etr represents the extraterrestrial radiation at the mean sun-earth distance, the global tilt represents the AM 1.5G solar flux. The direct represents the direct normal irradiance and circumsolar is the spectral irradiance within +/- 2.5 degrees field of view.

Considering the AM 1.5G solar spectrum, which stands for the spectral radiation from solar disk plus sky diffuse and diffuse reflected from ground on south facing surface tilted 37 degree from horizonal (Figure 1.1 green curve), the vast majority of the solar irradiation is between 1 and 3 eV with its peak at ~2.5 eV. This aspect indicates that a semiconductor material with a small band gap around 1 eV is favored. And to compete with the direct photovoltaics cell, energy conversion efficiency above 10% is necessary, which means the band gap must be smaller than 2.2eV.[5-6] However, in an ideal design of a photoelectrochemical cell, which results in total water splitting by a single semiconductor ($2H_2O+h\upsilon \rightarrow 2H_2+O_2$), the oxidation side of the reaction

requires the valence band of the semiconductor to be lower than the redox potential of O_2/H_2O (1.23 V vs RHE) to complete the oxidation process while the conduction band higher than the redox potential of H_2O/H_2 (0 V vs RHE). Thus, the band gap between the valence band and conduction band needs to be larger than the redox potential gap between O_2/H_2O and H_2O/H_2 which is 1.23 eV. Thus, this criterion requires the band gap to be larger. These two contradicting requirements represent a fundamental challenge in developing suitable semiconductor materials for solar water splitting. So far, there are a number of developed materials such as TiO_2, Fe_2O_3, WO_3 and $BiVO_4$ n type semiconductors for water oxidation and III-V p type semiconductors for water reduction.[7-13] These materials only focus on the half reaction, namely water oxidation or water reduction reaction, and avoid the band gap issue discussed here.

However, due to the rapid development in silicon single crystal fabrication, III-V single crystal semiconductors that could be produced with similar techniques with 1.6-1.8 eV bandgap as light absorbers are also studied in depth, showing promising solar water splitting performance in PEC systems.[14-19] For solar water splitting systems, chemical stability is crucial to many aspects, such as overall performance, semiconductor/liquid junction reaction and system lifetime. However as stated in previous context, the stable metal oxide system due to the wide bandgap has low efficiency while the III-V semiconductors with higher theoretical efficiency are unstable. To counter the instability of these semiconductors in PEC conditions, such as photo-degradation and photo-corrosion, several studies suggested TiO_2 as a promising protection layer with advantages in photostability over a wide pH and potential range.[2 20] TiO_2 as a naturally n-type semiconductor, can form a p-n junction with p-type light absorbing semiconductors with appropriate band alignment as discussed above, which promotes charge separation across the p-n junction. Various

OER/HER successful III-V semiconductor materials after TiO_2 protection were proven to have greatly enhanced stability under PEC conditions.[13, 21-25]

TiO_2 as an intrinsic n-type semiconductor, will form a p-n junction with p-type light absorbing semiconductors, which promote charge separation and stability. III-V semiconductors are not good candidates due to their instability under water reduction conditions resulting in the reduction of group III elements to their metal form.[26] However, many studies as listed below have successfully addressed this instability via TiO2 protection, and achieved good performance using III-V semiconductors. In 2012 Lee et al. studied nanotextured p-type InP coated with 2-5nm atomic layer deposition (ALD) deposited TiO_2 and determined it could achieve a 35 mA/cm^2 photocurrent in pH=0 conditions and stability over 4 h, while the onset potential of photocurrent is over 600mV vs RHE.[21] In 2015, Lin et al. improved the onset potential of p-InP to over 800mV vs RHE.[22] The Cronin group, in 2015, reported CO_2 reduction to methanol by TiO_2 passivated InP nanopillars, in which TiO_2 not only acts as a protection layer, but also provides reaction sites via O group vacancies in TiO_2.[23] The Cronin group also reported other TiO_2 passivated III-V semiconductors in the past two years. For p-GaP, they reported n-TiO_2 could form a p-n junction which increased the onset potential of CO_2 reduction by 500 mV while the electrode could work stably over 8h.[27] Later, they deposited Au nanoparticles on a TiO_2 surface, which allows the plasmons to enhance the charge carrier transportation from the GaP to the surface. An increase of onset potential for both water reduction and photocurrent was reported, as well as system stability for over 12h.[24] In 2015, Qiu et al. reported ALD TiO_2 protected GaAs electrode could achieve high quantum efficiency of photo-driven water reduction and CO_2 reduction. It showed an increase of onset potential and photocurrent and also reported that Ti^{3+} defects (O vacancy) provide reaction active sites and thinner, amorphous TiO_2 perform better compared to thicker, crystalline film due

to the conductivity.[25] Recently, the Turner group reported a new p-$InGaP_2$ semiconductor combined with ALD TiO_2 and a low cost cobalt molecular catalyst, which performs as well as bare semiconductor with expensive Pt catalyst, but with 20 hour stability.[13] In the studies summarized here, there are in-depth research for methods to improve the performance of TiO_2 protected III-V semiconductors for water splitting system.

For photoanodes, as early as 1977, Tomkiewic et al. used CVD and sputtering to put TiO_2 on n-Si, n-GaAs, n-GaP, n-InP, n-CdS and n-GaAlAs as a protection layer.[28] However, in this study, the efficiency is limited by the charge carrier diffusion length due to the poor performance of hole conduction in TiO_2. TiO_2 as a protection layer acts like a barrier for photogenerated holes due to the much lower valence band of TiO_2 compared to other non-oxide semiconductors, despite the improved stability for light absorbing semiconductors.[28] In 2011, Chen et al. addressed this problem by depositing 2 nm thick TiO_2 layer on n-Si, followed by 3 nm Ir overlayer, which achieved 15 mA/cm^2 photocurrent and 24 h stability in 1 M NaOH as a photoanode.[29] The hole conduction problem was addressed by a mechanism of trap-assisted tunneling, thus the thickness is strictly controlled at 2 nm. More recent studies conducted by Nate Lewis' group and the McIntyre group suggested that amorphous TiO_2 could stabilize semiconductor, as well as maintain the hole conductivity.[30-31] The amorphous TiO_2 layer grown by ALD from the precursor of tetrakisdimethylamido titanium (TDMAT) could stabilize Si, GaAs, GaP and CdTe for over 100 h in pH=14 condition, with the presence of NiO_x as a catalyst. Si nanowire was found to operate over 2200 h under the same conditions.[31] In conclusion, a TiO_2 protection layer, so far, provides both stability and performance enhancement, proven to be suitable for most III-V semiconductors and is becoming one of the general methods to address the photostability of semiconductor electrodes.

1.2 Charge transfer in solar water splitting system

1.2.1 Semiconductor depletion layer at equilibrium in dark

Most photoelectrochemical (PEC) systems using semiconductors as light absorbing materials show strong bias dependence on photocurrent density.[13, 19, 21-27, 32-35] This section is a brief overview of the charge carrier dynamics under applied potential and under illumination.

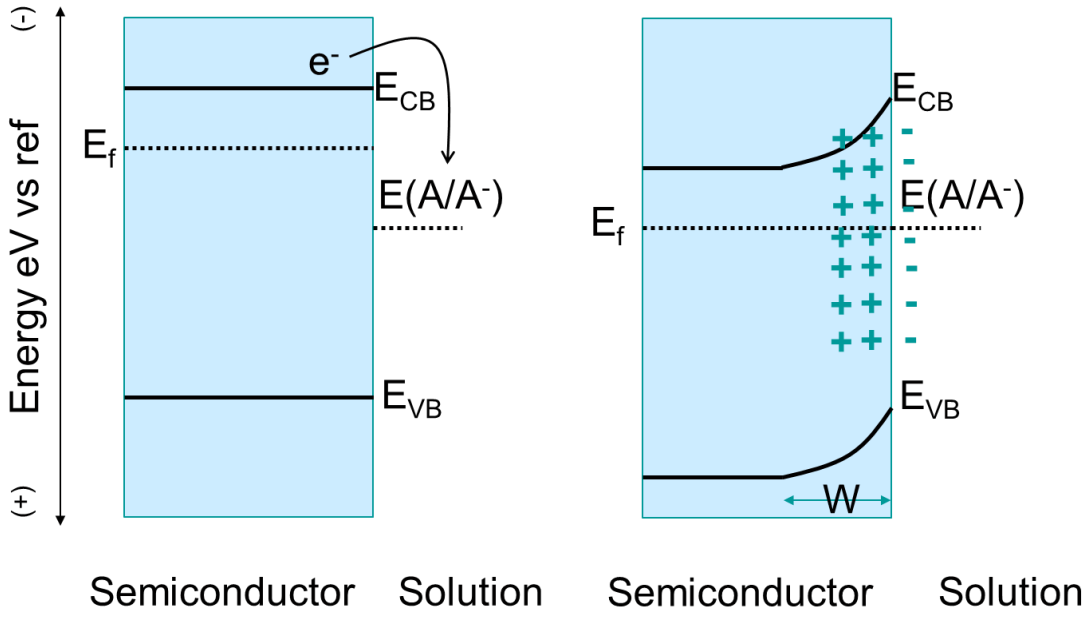

Figure 1.2 The diagram of energy level at semiconductor/liquid interface in dark condition. Left: before equilibrium and right: after equilibrium, reproduced with permission from Tan, M. X., Laibinis, P. E., Nguyen, S. T., Kesselman, J. M., Stanton, C. E., & Lewis, N. S. (1994). *Progress in inorganic chemistry*, 21-144.

The more fundamental property of a water splitting semiconductor is the band bending that happens at the semiconductor-electrolyte junction when immersed in the liquid solution. The Fermi level, which indicates the redox potential of the electron in the semiconductor, is different than the redox potential of the electrolytes in solution. The Fermi level of semiconductor is essentially a similar representation of the electron affinity in a semiconductor that could be compared to the electrolyte redox potential. At the same time, the Fermi level could also be considered the 50% density of states (DOS) for electrons. This Fermi level can be controlled by external applied potential as explained in the later text. Here, in Figure 1.2, we use an n-type semiconductor as an example, before the charge equilibration happens at the semiconductor/liquid junction, the energy level of the valence band and conduction band are "flat" along the x direction, which is the direction perpendicular to the semiconductor/liquid junction surface. This is the "flat band" condition. But since the Fermi level of the semiconductor is more reducing than the liquid redox potential, electrons will flow from the semiconductor to the liquid, causing the net charge to be positive inside the semiconductor, establishing an electrical field with a direction from the semiconductor to the liquid. This causes the energy level to bend closer to the interface. Eventually the Fermi level of the semiconductor is equal to the redox potential in solution after the equilibrium is established, and band bending is established also. As shown in Figure 1.2, under ideal conditions without Fermi level pinning, the band bending, which is called the built-in potential, is equal to the difference between the Fermi level and the redox potential. The extension of the band bending along the *x* direction is called the depletion layer, or space charge layer, as the majority charges are depleted from the semiconductor in this region; the thickness is denoted as *W* here.

The Fermi level before equilibrium can be expressed as:

$$E_f = E_{CB} - kT \ln(n / N_C) \qquad \text{Eq. 1.1}$$

where n is the dopant level and N_C is the DOS in the conduction band. The built-in potential is equal to:

$$V_{bi} = \frac{E_f - E(A/A^-)}{q} \qquad \text{Eq. 1.2}$$

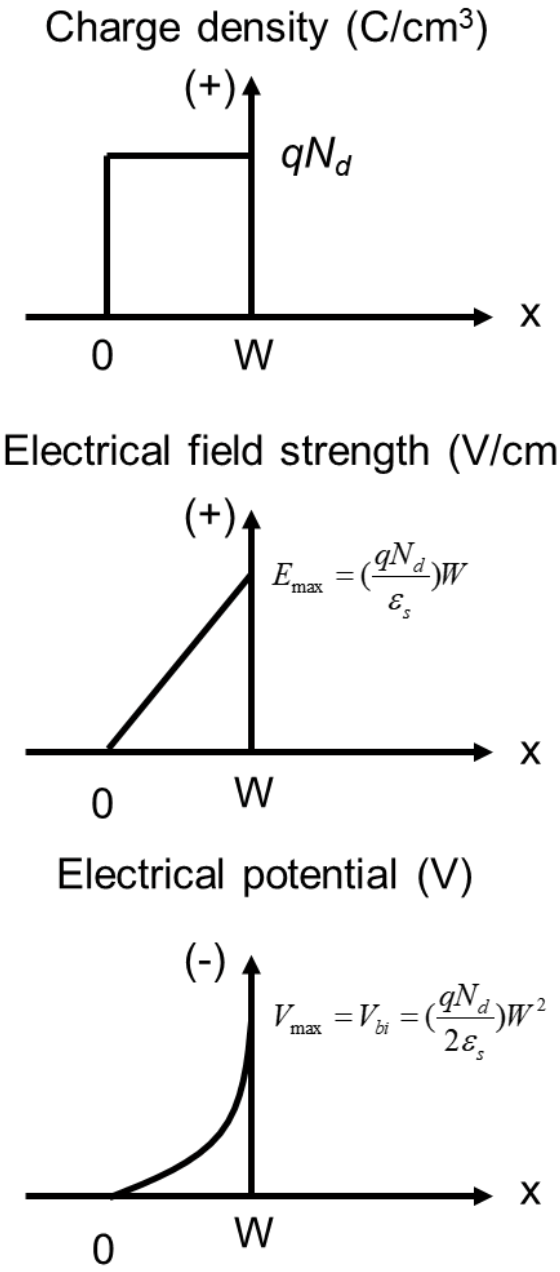

Figure 1.3 Quantitative description of semiconductor depletion layer's charge density, electrical field strength and electrical potential. Reproduced with permission from Tan, M. X., Laibinis, P. E., Nguyen, S. T., Kesselman, J. M., Stanton, C. E., & Lewis, N. S. (1994). *Progress in inorganic chemistry*, 21-144.

A quantitative description of at the equilibrium is obtained after applying electrostatic analysis.[36] Under the assumption that the charge carrier density is the same across the depletion layer and that the free carriers are depleted, the positive charge density is simply equal to the dopant density in the depletion region times the elemental charge, qN_d. Here, the zero on the *x*-axis is defined as the starting point of the depletion region and the semiconductor phase terminates at $x = W$, and the solution phase is when $x > W$. Then the electrical field strength at position *x* along the *x*-axis is

$$E(x) = (\frac{qN_d}{\varepsilon_s})x, 0 \le x \le W \qquad \text{Eq. 1.3}$$

As shown by Eq 1.3, the electrical field strength reaches maximum at the interface when *x* is equal to *W*. Here, the ε_s is the dielectric constant of the semiconductor. Integrating the linear electrical field in Eq 1.3 yields the electrical potential in semiconductor,

$$V(x) = -(\frac{qN_d}{2\varepsilon_s})x^2, 0 \le x \le W \quad . \qquad \text{Eq. 1.4}$$

Note that the electrical potential is more negative at the interface. This means that the electron will be swept toward the bulk, or it would take external energy to drive electron from the bulk to the surface. The depletion width, *W*, can be determined by the dopant density and the built-in voltage as shown in Eq 1.5.

$$V_{bi} = (\frac{qN_d}{2\varepsilon_s})W^2, \text{ or } W = \sqrt{\frac{2\varepsilon_s V_{bi}}{qN_d}} \qquad \text{Eq 1.5}$$

From the electrical potential in a semiconductor, one could obtain the carrier concentration at a given position as:

$$n(x) = n_b \exp[\frac{qV(x)}{kT}] \qquad \text{Eq 1.6}$$

Here, n_b represents the bulk carrier concentration. The carrier concentration reaches minimum at the interface when $V(x)$ is equal to V_{bi}. This concentration is called the surface carrier concentration:

$$n_s = n_b \exp[-\frac{qV_{bi}}{kT}] \qquad \text{Eq 1.7}$$

where n_s is the surface charge carrier density (when in equilibrium in dark the n_s is denoted as n_{so}).

1.2.2 Semiconductor potential-current under applied potential

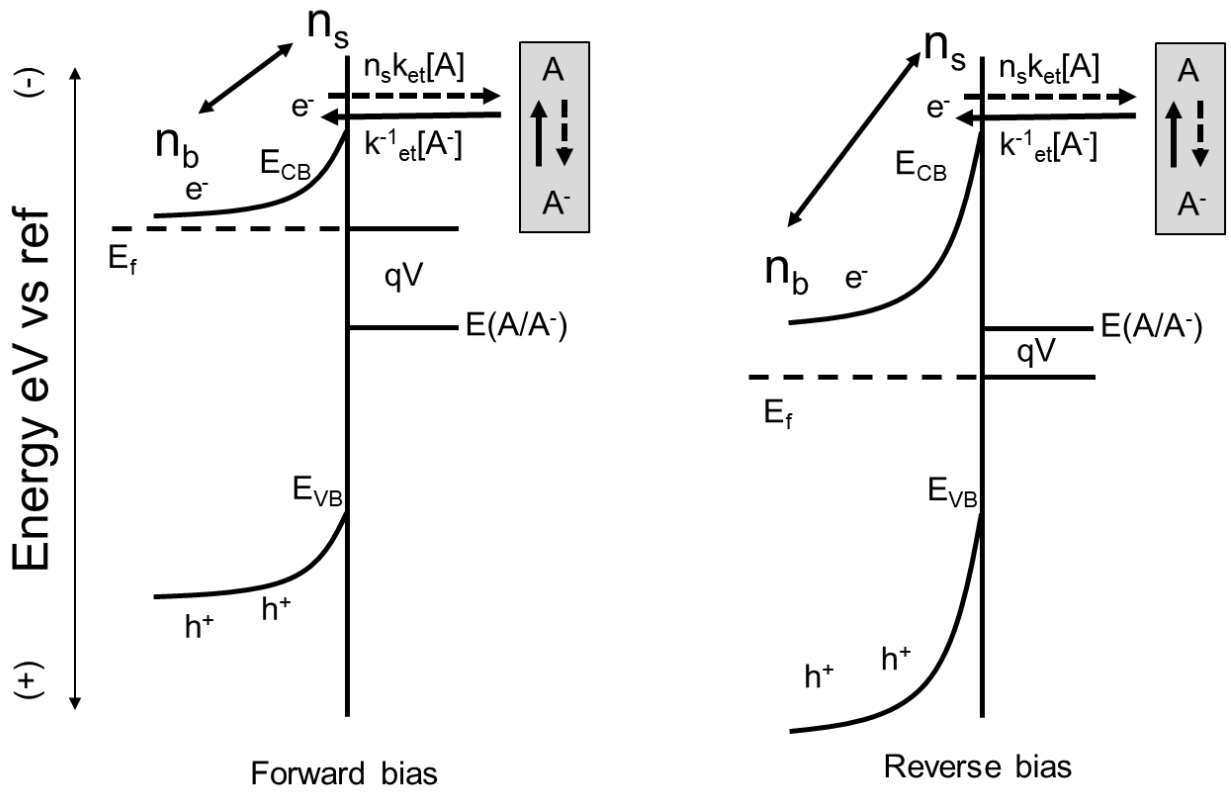

Figure 1.4 Interfacial electron transfer rate in dark under (Left) forward bias and (right) reverse bias. Reproduced with permission from Kumar, Amit, Patrick G. Santangelo, and Nathan S. Lewis. *The Journal of Physical Chemistry* 96.2 (1992): 834-842. Copyright 1992 American Chemical Society.

Under the equilibrium condition described above, the forward electron injection from semiconductor into solution is

$$k_{et} n_s [A]_s$$

and the back electron transfer is

$$k_{et}^{-1} [A^-]_s .$$

Therefore, the net electron transfer is

$$\frac{dn}{dt} = k_{et}^{-1} [A^{-1}]_s - k_{et} n_s [A]_s = -k_{et} [A]_s (n_s - n_{so}) \ . \qquad \text{Eq 1.8}$$

Thus, the current can be expressed by the net charge flow rate times an elemental charge q and surface area B:

$$I = -qB(-\frac{dn}{dt}) = -qBk_{et} [A]_s (n_s - n_{so}) \qquad \text{Eq 1.9}$$

When the Fermi level is shifted away from the equilibrium condition by applying potential, the surface electron density is shifted based on Eq 1.7

$$n_s = n_b \exp[-\frac{q(V_{bi} + V)}{kT}]$$

which generates a simple relationship between the equilibrium surface density and non-equilibrium one:

$$\frac{n_s}{n_{so}} = \exp(-\frac{qV}{kT})$$

Therefore, under applied potential and in dark the current is expressed as:

$$I = -qBk_{et} [A]_s n_{so} [\exp(-\frac{qV}{kT}) - 1] = I_0 [\exp(-\frac{qV}{kT}) - 1] \qquad \text{Eq 1.10}$$

As shown in Figure 1.4, when the applied potential is more negative than equilibrium, a net reduction current will flow, denoted as forward bias. When the potential is more positive, i.e.

reverse bias, the net current will be oxidation. To summarize, the reverse reaction, which is the electron injection into the semiconductor, will always remain constant, while the forward reaction changes due to the equilibrium surface electron density.

1.2.3 Semiconductor potential-current under illumination

Under relatively low illumination, the photogenerated carriers are minimal compared to the majority carrier, while the photogenerated minority carrier dominates the overall minority carrier concentration. Therefore, the total current is expressed as:

$$I = I_{Ph} - I_0[\exp(-\frac{qV}{kT}) - 1] = \Phi\Gamma_0 - I_0[\exp(-\frac{qV}{kT}) - 1] \qquad \text{Eq 1.11}$$

Here, the photocurrent is simply the product of photon flux Γ_0 and the collection efficiency Φ. Due to possible back electron transfer, the collection efficiency is also applied potential dependent. Therefore, the photocurrent is also applied potential dependent. However, photogenerated carriers change the population of both majority and minority carriers, so that the built-in voltage is decreased; this is the band flattening effect as reported before. [37-43]

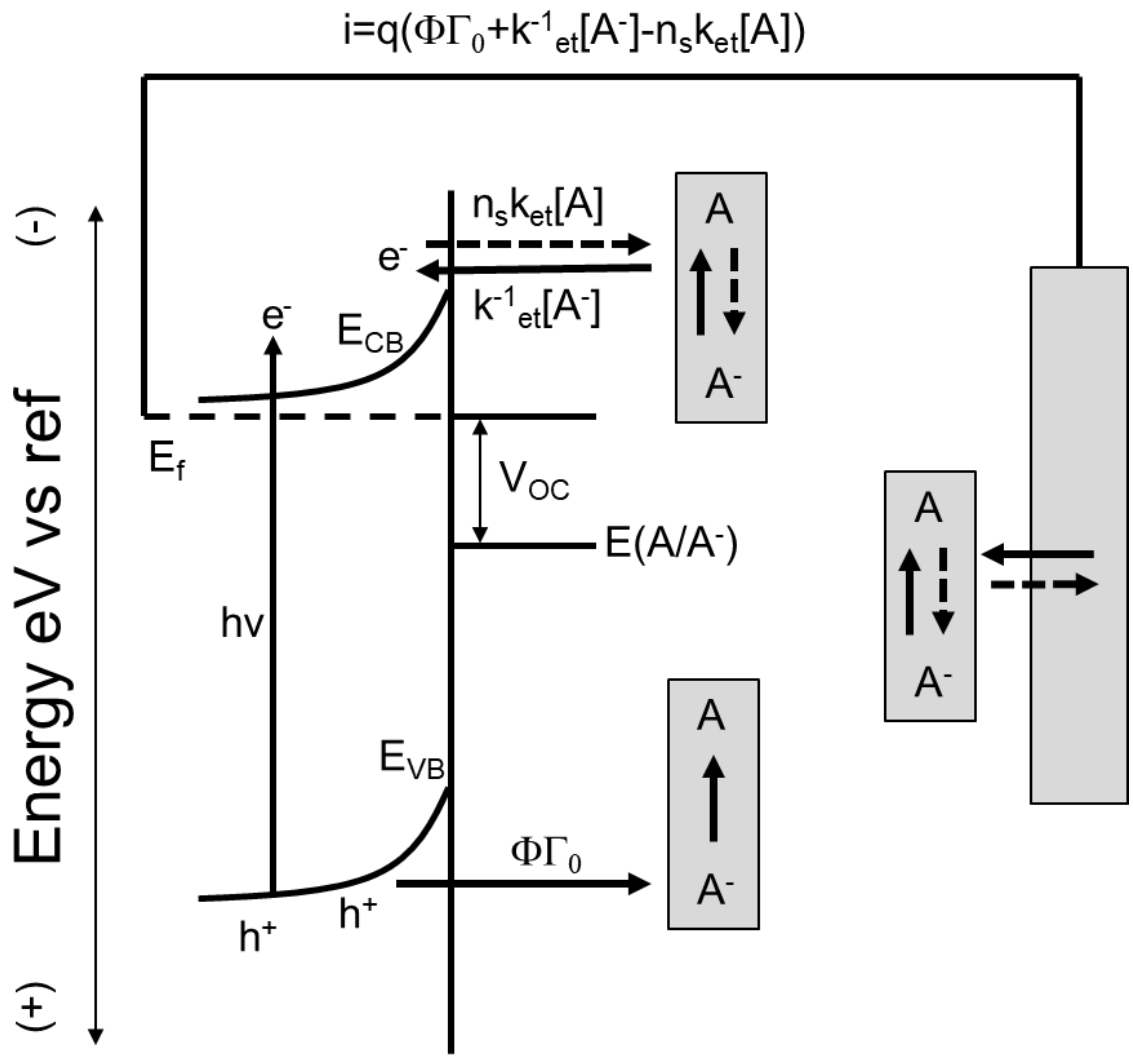

Figure 1.5 n-type semiconductor under photoelectrochemical condition. Reproduced with permission from Kumar, Amit, Patrick G. Santangelo, and Nathan S. Lewis. *The Journal of Physical Chemistry* 96.2 (1992): 834-842. Copyright 1992 American Chemical Society.

One could define an open circuit potential considering an n-type semiconductor under illumination, as shown in Figure 1.5. The open circuit potential is determined when the external net current *i* is equal to zero:

$$i = q(\Phi\Gamma_0 + k^{-1}{}_{et}[A^-] - n_s k_{et}[A]) = 0$$

and the open circuit potential is equal to

$$V_{OC} = (kT / q)\ln\{\Phi\Gamma_0 / n_{so}k_{et}[A]\}. \qquad \text{Eq 1.12}$$

Here, under applied potential, the band flattening quantity will be equal to Eq 1.12. As the equation shows, the extent of the band flattening has a logarithmic dependence on the illumination intensity under a certain bias. The band flattening extent under continuous wave (CW) illumination is generally small, as we explore the band bending extent in Chapter 3. However, this situation is no longer true under transient spectroscopy experimental conditions. We explored in detail how this impairs the charge carrier dynamics measured and demonstrated two effective methods, both in ultrafast time resolution and slower chemical reaction time scales, to obtain meaningful charge carrier dynamics in Chapters 2 and 3.

1.3 Challenges in studying charge carrier dynamics in semiconductor water splitting systems

Although macroscopic efficiency of charge carrier related processes can be characterized by J-V curves under dark and illumination conditions, time resolved, microscopic dynamics of charge carriers can provide important mechanistic insight on the efficiency of each individual steps such as charge separation, charge transport and interfacial charge transfer. However, time resolved observation of charge carrier dynamics proved to be very hard and largely remain unclear. In such systems, charge carriers undergo multiple processes including charge separation, charge migration, charge recombination, charge accumulation on the surface, interfacial charge transfer, etc. Understanding these processes requires a high time resolution, sensitive technique that could give insight on limitations and give guidance on designing a more efficient system. Compared to the vast amount of developed solar water splitting semiconductor materials, research focused on the charge carrier dynamics to reveal the mechanistic insights are limited. There is a fundamental

challenge between generating enough charge carriers transiently for detection and generating too many charge carriers that disturb the band structure.

Solar water splitting measurements are typically conducted under standard illumination conditions (i.e., AM 1.5G), which correspond to a power density of 100 mW/cm^2. On the contrary, in femtosecond transient absorption spectroscopy (TAS) experiments, the peak power density is in the order of 10^{10} mW/cm^2 (estimated from 1 nJ pulse energy, 150 fs FWHM duration, 1×10^{-3} cm^2 beam size) or larger. This drastic eight order of magnitude difference in the excitation power disrupts the typical band bending conditions that drive the charge carrier separation in semiconductor electrodes under the AM 1.5G conditions.[37-43] Under low photon flux conditions, e.g., AM 1.5G, the photogenerated charge carriers are separated and driven to the semiconductor-electrolyte interface (SEI) or external circuit by band bending. This band bending can be mostly removed once the transiently excited charge carrier concentration (10^{17}-10^{22} cm^{-3}) is comparable to the dopant concentration (10^{17}-10^{20} cm^{-3}). This phenomenon is called the 'band flattening' effect and has been previously studied by several methods in various systems.[37-41] From a time-resolved perspective, the flattened band will not recover before the photoexcited charge carriers are depleted, meanwhile the major depletion pathway for these charge carriers is diffusion and recombination.[37-41] This would result in two expected observations: first, an electrode with a good incident photon to current efficiency (IPCE) under AM 1.5G conditions would perform at a significantly lower IPCE under femtosecond laser pulse illumination as shown in Figure 1.6, and second, any TAS measured kinetics would show minimal potential dependence if there is not efficient charge separation as shown in Figure 1.7. For TAS, excitation power densities on the order of 10^{10} mW/cm^2 or larger are required in order to produce detectable signal amplitudes (~0.1 mOD). We

believe that addressing this inherent contradiction provides the key to allow any meaningful study on charge carrier kinetics on such systems with femtosecond time resolution.

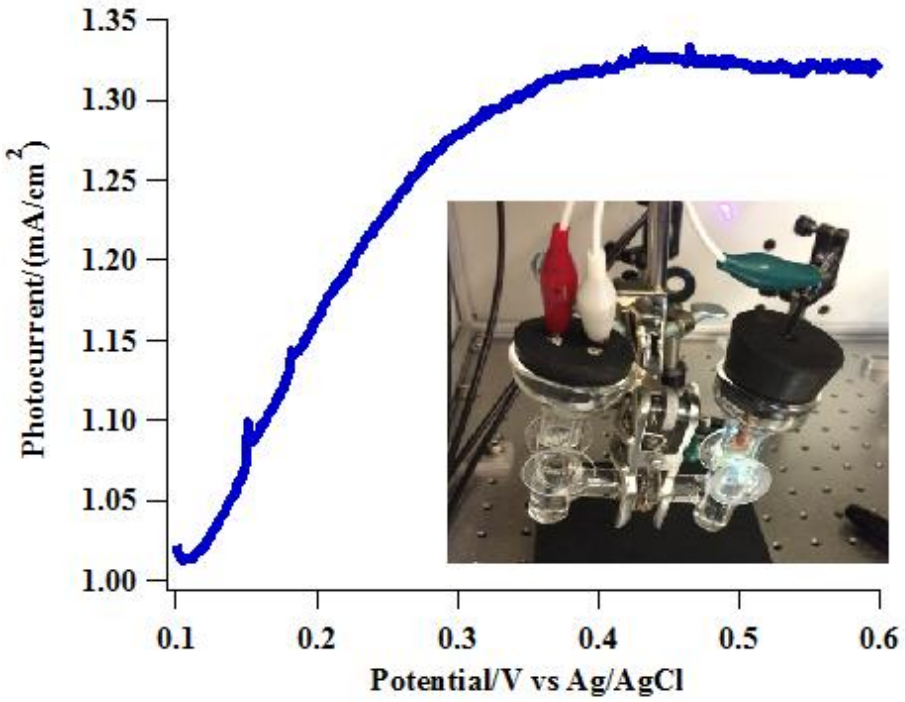

Figure 1.6 $BiVO_4$ photocurrent under 400 nm femtosecond pulsed illumination under 3-electrode setup in a pH 7 buffer solution.

We saw as low as 0.1% IPCE at optimal bias (>0.4 V vs Ag/AgCl) in $BiVO_4$ as shown in Figure 1.6 and 0.03% IPCE in α-Fe_2O_3 water oxidation system under TAS condition, where as in AM 1.5G condition shows well above 40% IPCE.[7, 12] On the other hand, excitation power density in the order of 10^8 W/cm^2 or larger is required in TAS for detectable signal amplitude (~0.1mOD). Apparently, addressing this intrinsic contradiction would be the key to allow any meaningful study on charge carrier kinetics on such systems with femtosecond time resolution.

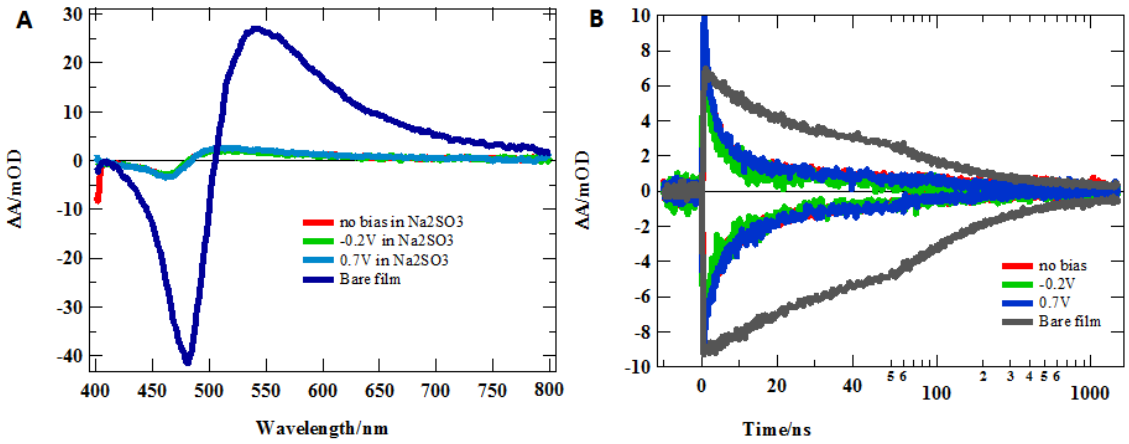

Figure 1.7 (A) $BiVO_4$ between different applied bias' of film in electrolyte and the dry film. (B) showed the kinetics comparison, for bare film the kinetics is taken at 480 nm and 540 nm while for the sample in the electrolyte it is taken at 460 nm and 510 nm.

In previous studies of time-resolved charge carrier kinetics in Oxygen evolution reaction/Hydrogen evolution reaction (OER/HER) systems,[44-55] several methods were employed to address this contradiction. Apart from using a longer duration excitation pulse to lower the transiently generated carrier concentration, high redox species concentrations were also employed.[56] The former method provides a direct solution to transiently generating too large charge carrier concentrations, whereas the latter enables fast charge carrier transfer from the semiconductor to the electrolyte to compete with recombination of charge carriers. In these studies, efficient charge separation is achieved by artificial tuning of experimental conditions rather than the device itself. Recent studies showed that the direct engineering of a layer of *n*-type TiO_2 on a *p*-type semiconductor efficiently prevented charge recombination and enhanced the carrier separation even at high carrier concentrations.[13, 22, 25, 27, 31, 57-59] However, a detailed time-resolved charge carrier dynamics study on such a system under electrochemical working conditions has not yet been carried out to the best of our knowledge. In the work presented in Chapter 3, we utilized

the efficient charge separation that occurs in the *p-n* junction at the surface of a TiO_2/GaP semiconductor electrode, and we conducted *in situ* TR spectroscopy and photoelectrochemical measurements. The high sensitivity of the TR technique to probe the band structure and charge separation efficiency of the semiconductor electrode, even using femtosecond pulse excitation, enables us to observe the correlation between transiently separated charge carriers and IPCE. This study revealed the charge separation mechanism under applied potential on a femtosecond time scale.

The photogenerated carriers, after separation and migration, reach the surface reactive sites. However, these carrier dynamics are limited by slow kinetics. It remains a challenge for time resolved spectroscopy to directly probe these carriers under such a time window, but observation of these dynamics renders great importance for studies on the mechanisms of interfacial charge transfer and catalyst effects. In Chapter 4, we demonstrated a time resolved second harmonic generation as a tool to directly probe charge carriers at this time scale without relying on the optical transitions used in transient spectroscopy.

1.4 Photon upconversion sensitized by quantum dots

In the second part of this dissertation, we focused on how to utilize low band gap photons in order to improve photovoltaic and photoelectrochemical systems to go beyond the Shockley-Queisser limit. We first studied a molecular system consisted of a modified BODIPY molecule

with radical attached, focusing on the factors that govern the triplet yield and triplet lifetime in Chapter 5. Next, we discovered a new family of triplet energy transfer mediators that exhibit good air stability and we demonstrated a direct triplet energy transfer sensitized by quantum dots in Chapter 6. Last, we studied the efficiency limiting factors in an established quantum dot sensitized triplet-triplet annihilation based upconversion system in Chapters 7 and 8.

1.4.1 Intersystem Crossing in molecule

Triplet excitons in molecules enhance the excited state lifetime longevity, allowing long distance triplet exciton transfer to occur. Understanding and controlling spin dynamics and kinetics is of a significant interest in applications ranging from photocatalysis,[60] photodynamic therapy,[61-64] photovoltaics[65] and triplet-triplet annihilation upconversion.[66-71] Triplet excitons with low-lying energy levels[72] and long lifetimes[73] are of great interest in a variety of energy and/or charge transfer schemes,[74-77] and would enable the above-mentioned applications. The most common approach to triplet formation include intermolecular Dexter-type triplet energy transfer from a photosensitizer,[78-79] substitution with heavy atoms to promote strong spin-orbit coupling,[80-84] singlet fission,[85] and enhanced intersystem crossing (EISC) caused by persistent radicals.[68, 86-92] Incorporation of a pendant radical to π-conjugated fluorophore allows for additional excited-state decay pathways and has been a useful tool to study and modify excited-state photophysical properties.[93-94]

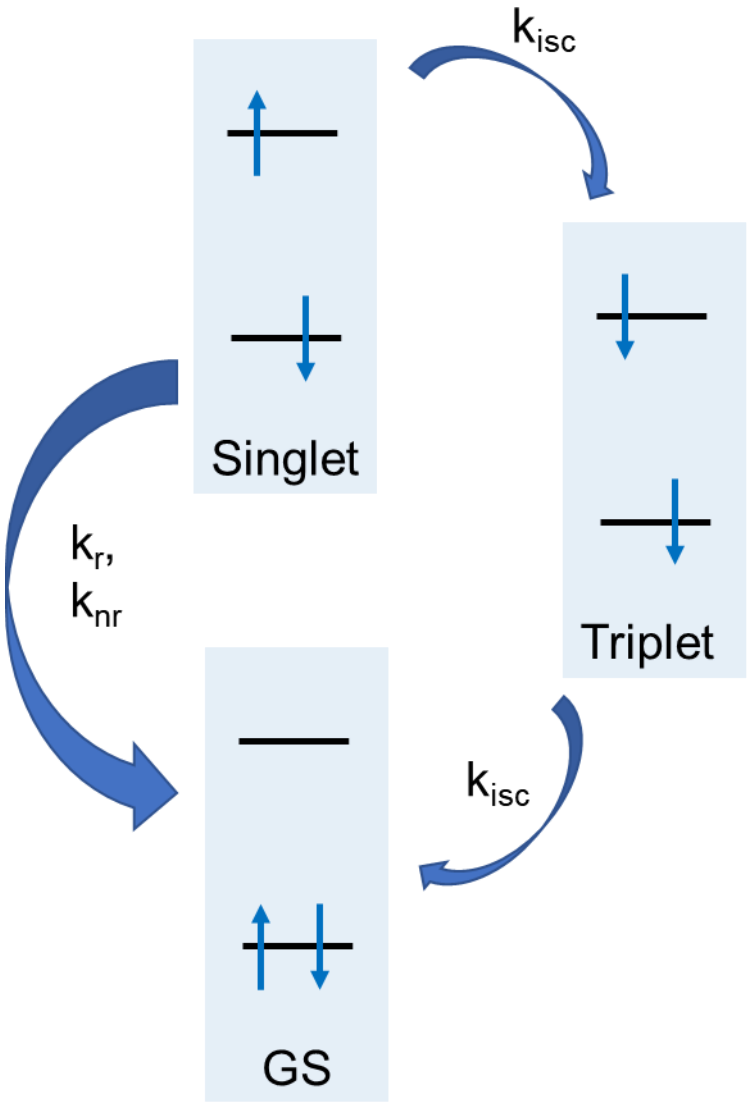

Figure 1.8 Transition between singlet, triplet excited state and ground state.

The long lifetime of a triplet exciton is due to the lack of efficient recombination pathways. In a molecular system, as shown in Figure 1.8, the singlet could decay back to ground state via either radiative recombination, which leads to fluorescence, and nonradiative decay. Although spin forbidden, a certain percentage of singlet could undergo intersystem crossing, which refers to a spin flip of one electron to generate a triplet state. Many factors determine this percentage, known as triplet yield in the molecular system. This triplet excited state is generally much longer lived

than singlet state, because the decay pathway back to ground state requires a similar electron spin flip, deeming such transition's oscillator strength very small.

It is natural to assume the same spin forbidden transition governs both the intersystem crossing from the singlet to triplet, and from triplet to ground state. That is to say, when the triplet yield is enhanced, the triplet lifetime at the same time would be shortened. This fundamental contradiction seems to void the effect of modifying molecular structures for a higher triplet yield. In Chapter 5, we studied a modified dye molecule with a radical attached to it and showed that it is possible to both enhance the triplet yield while maintaining a relatively long triplet lifetime.

1.4.2 Quantum dot sensitized triplet energy transfer

In recent years, quantum dot (QD) sensitized upconversion systems [95-98] have attracted intense interest as a versatile and promising approach because of their large absorption coefficient,[99] small singlet-to-triplet energy gap and fast intersystem crossing (ISC) rate,[100] and tunable band gap and band alignment.[101]

In a typical photon-upconversion system, triplet excitons are generated through a sensitizer that undergoes intersystem crossing from an excited singlet state to a triplet state. This process is followed by a sequential triplet energy transfer first to the transmitter then to the emitter. The latter can undergo triplet-triplet-annihilation (TTA) and emit a higher energy photon. [95, 97, 102-107] Thus, the efficiency of a typical sensitizer-emitter-based upconversion system can be represented by the following equation:[102]

$$\Phi_{UC} = \Phi_{ISC}\Phi_{TET}\Phi_{TTA}\Phi_{FL}\,. \qquad \text{Eq. 1.13}$$

The overall upconversion efficiency (Φ_{UC}) is the product of efficiencies in each step involved, namely the ISC of the sensitizer (Φ_{ISC}), the triplet energy transfer (TET)[108] from the

sensitizer to transmitter to emitter (Φ_{TET}), TTA of the emitter (Φ_{TTA}), and the emitter's fluorescence (Φ_{FL}). For a specific sensitizer and emitter, $\Phi_{ISC,}$ Φ_{TTA} and Φ_{FL} are determined by the material's properties. A promising area for performance improvement is the design of QD/transmitter complexes to enable efficient TET.[109] The advantage of using quantum dots as a photosensitizer is that the small singlet-triplet energy gap makes its singlet state essentially a degenerated state of singlet and triplet. [110-111] In most reported QD sensitized upconversion systems, the transmitter/emitter molecules are solely limited to acenes and their derivatives, which have limited structural and energetic tunability and poor stability. [95, 97, 103-107, 112] Oligothiophenes have wide range of tunability in energetics and molecular structure,[113] making them a very desirable class of triplet acceptors/transmitters in QD-organic hybrid TTA upconversion systems. In Chapter 6, we demonstrated a direct energy transfer from CdSe QD to oligothiophene molecule to show that besides acenes, oligothiophene is also a potential triplet energy acceptor.

1.4.3 Competition of charge and energy transfer in quantum dot sensitized triplet energy transfer

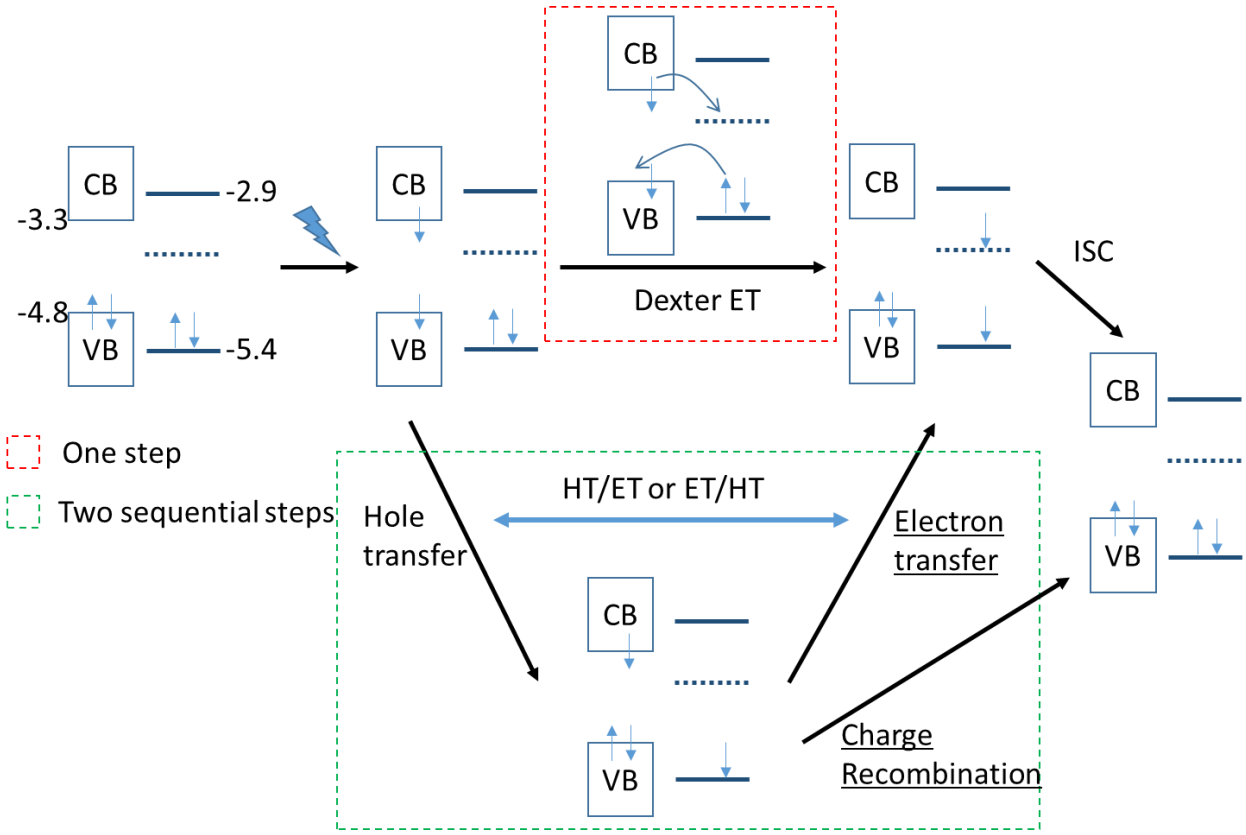

Figure 1.9 Dexter type direct triplet energy transfer, denoted Dexter ET, here as one step and sequential charge transfer to form a triplet excited state, denoted as two sequential steps shown in a PbS-Tetracene QD-Molecule complex band energy diagram.

Despite the advantages of quantum dots as sensitizers, efforts to achieve efficient triplet sensitization in the infrared have been hampered, in part, by competition with other exciton decay pathways (such as electron or hole transfer and nonradiative recombination within the QD). As shown in Figure 1.9, apart from a direct energy transfer discussed above, there exists a secondary pathway that could either enhance the triplet transfer efficiency or impair it. The total efficiency is

determined based on how the charge separation state decays. If it undergoes charge recombination to the ground state, then this will be a loss pathway, otherwise triplet yield is enhanced. Previous studies have shown that core/shell structures, with type I or type II band alignments between the core and shell materials, can be used to control the spatial distribution of the electron and hole.[114-115] This offers additional control of the rate of electron and hole transfer. In principle, such core/shell heterostructures can also be used to selectively suppress charge transfer and enhance TET. In Chapter 7, we demonstrated that with an addition of a sub monolayer CdS shell, the charge separation state is supressed and the triplet lifetime is enhanced.

1.4.4 Surface chemistry of quantum dot affects the molecular triplet lifetime

Colloidal semiconductor nanocrystals (NCs) have quantum confined states that make them interesting for many optoelectronic applications.[116-119] However, these quantized states are subject to the vagaries of the surface, i.e. differences at the atomic scale that are difficult to quantify, especially when compounded with the intrinsic disorder both at the nanoscale and in the ensemble. Thus, nominally identical nanomaterials may give rise to dramatically different rates and yields of energy and charge transfer. A case and point are two recent reports that are in direct conflict with each other, regarding singlet fission (or lack thereof) from the same tetracene molecule covalently bound to PbS NCs. One found no evidence of singlet fission from TIPS-tetracene bound to three different sizes of PbS NCs[120] while the other reported quantitative yields of singlet fission and subsequent energy transfer on nominally the same material combination.[121] Both used the same carboxylic acid functionalized TIPS-tetracene with oleic acid capped PbS NCs. In this case, the dissimilar ligand exchange protocol and solvent during photoexcitation may explain the discrepancy between the electronic communication in surface bound tetracene in both reports.

This extreme sensitivity to quenching mechanisms on the surface is not surprising for short-range Dexter-type processes describing charge and energy transfer. In comparison, long-range Förster type transfers are relatively forgiving.[122-125] In Chapter 8, we explored the differences between two different PbS QD sensitized triplet energy transfers and found that the surface chemistry dictates the mediator's triplet lifetime, which is now believed to be the most important factor in heavy atom containing quantum dot sensitized photon up conversion system. However, more controlled studies need to be done to both confirm the surface chemistry as a key factor in determining the triplet energy transfer efficiency and optimize such system to a higher overall efficiency.

1.5 References

1. Lewis, N. S.; Nocera, D. G., *Proceedings of the National Academy of Sciences* **2006,** *103* (43), 15729-15735.
2. Hu, S.; Lewis, N. S.; Ager, J. W.; Yang, J.; McKone, J. R.; Strandwitz, N. C., *The Journal of Physical Chemistry C* **2015,** *119* (43), 24201-24228.
3. Ding, C. M.; Qin, W.; Wang, N.; Liu, G. J.; Wang, Z. L.; Yan, P. L., . . . Li, C., *Phys Chem Chem Phys* **2014,** *16* (29), 15608-15614.
4. Gueymard, C. A.; Myers, D.; Emery, K., *Solar Energy* **2002,** *73* (6), 443-467.
5. Lewis, N. S., *MRS bulletin* **2007,** *32* (10), 808-820.
6. Walter, M. G.; Warren, E. L.; McKone, J. R.; Boettcher, S. W.; Mi, Q.; Santori, E. A.; Lewis, N. S., *Chemical reviews* **2010,** *110* (11), 6446-6473.
7. Lin, Y.; Yuan, G.; Sheehan, S.; Zhou, S.; Wang, D., *Energy & Environmental Science* **2011,** *4* (12), 4862-4869.
8. Cristino, V.; Caramori, S.; Argazzi, R.; Meda, L.; Marra, G. L.; Bignozzi, C. A., *Langmuir* **2011,** *27* (11), 7276-7284.
9. Su, J.; Guo, L.; Bao, N.; Grimes, C. A., *Nano Letters* **2011,** *11* (5), 1928-1933.
10. Sivula, K.; Formal, F. L.; Grätzel, M., *Chemistry of Materials* **2009,** *21* (13), 2862-2867.
11. de Respinis, M.; Joya, K. S.; De Groot, H. J. M.; D'Souza, F.; Smith, W. A.; van de Krol, R.; Dam, B., *J. Phys. Chem. C* **2015,** *119* (13), 7275-7281.
12. Kim, T. W.; Choi, K.-S., *Science* **2014,** *343* (6174), 990-994.

13. Gu, J.; Yan, Y.; Young, J. L.; Steirer, K. X.; Neale, N. R.; Turner, J. A., *Nat Mater* **2015,** *advance online publication*.
14. Weber, M. F.; Dignam, M. J., *Journal of The Electrochemical Society* **1984,** *131* (6), 1258-1265.
15. Bolton, J. R.; Strickler, S. J.; Connolly, J. S., *Nature* **1985,** *316*, 495.
16. Hu, S.; Xiang, C.; Haussener, S.; Berger, A. D.; Lewis, N. S., *Energy & Environmental Science* **2013,** *6* (10), 2984-2993.
17. Döscher, H.; Geisz, J.; Deutsch, T.; Turner, J., *Energy & Environmental Science* **2014,** *7* (9), 2951-2956.
18. Seitz, L. C.; Chen, Z.; Forman, A. J.; Pinaud, B. A.; Benck, J. D.; Jaramillo, T. F., *ChemSusChem* **2014,** *7* (5), 1372-1385.
19. Coridan, R. H.; Nielander, A. C.; Francis, S. A.; McDowell, M. T.; Dix, V.; Chatman, S. M.; Lewis, N. S., *Energy & Environmental Science* **2015,** *8* (10), 2886-2901.
20. Acevedo-Peña, P.; Vazquez-Arenas, J.; Cabrera-Sierra, R.; Lartundo-Rojas, L.; González, I., *Journal of The Electrochemical Society* **2013,** *160* (6), C277-C284.
21. Lee, M. H.; Takei, K.; Zhang, J.; Kapadia, R.; Zheng, M.; Chen, Y. Z., . . . Ager, J. W., *Angewandte Chemie International Edition* **2012,** *51* (43), 10760-10764.
22. Lin, Y.; Kapadia, R.; Yang, J.; Zheng, M.; Chen, K.; Hettick, M., . . . Ager, J. W., *The Journal of Physical Chemistry C* **2015,** *119* (5), 2308-2313.
23. Qiu, J.; Zeng, G.; Ha, M.-A.; Ge, M.; Lin, Y.; Hettick, M., . . . Cronin, S. B., *Nano Letters* **2015,** *15* (9), 6177-6181.
24. Qiu, J.; Zeng, G.; Pavaskar, P.; Li, Z.; Cronin, S. B., *Phys Chem Chem Phys* **2014,** *16* (7), 3115-3121.
25. Qiu, J.; Zeng, G.; Ha, M.-A.; Hou, B.; Mecklenburg, M.; Shi, H., . . . Cronin, S. B., *Chemistry of Materials* **2015,** *27* (23), 7977-7981.
26. Kaiser, B.; Fertig, D.; Ziegler, J.; Klett, J.; Hoch, S.; Jaegermann, W., *ChemPhysChem* **2012,** *13* (12), 3053-3060.
27. Zeng, G.; Qiu, J.; Li, Z.; Pavaskar, P.; Cronin, S. B., *ACS Catalysis* **2014,** *4* (10), 3512-3516.
28. Tomkiewicz, M.; Woodall, J. M., *Journal of The Electrochemical Society* **1977,** *124* (9), 1436-1440.
29. Chen, Y. W.; Prange, J. D.; Dühnen, S.; Park, Y.; Gunji, M.; Chidsey, C. E.; McIntyre, P. C., *Nature materials* **2011,** *10* (7), 539-544.
30. Lichterman, M. F.; Shaner, M. R.; Handler, S. G.; Brunschwig, B. S.; Gray, H. B.; Lewis, N. S.; Spurgeon, J. M., *The Journal of Physical Chemistry Letters* **2013,** *4* (23), 4188-4191.
31. Hu, S.; Shaner, M. R.; Beardslee, J. A.; Lichterman, M.; Brunschwig, B. S.; Lewis, N. S., *Science* **2014,** *344* (6187), 1005-1009.
32. Wu, X.; Park, H.; Zhu, X.-Y., *The Journal of Physical Chemistry C* **2014,** *118* (20), 10670-10676.
33. Shaner, M. R.; Hu, S.; Sun, K.; Lewis, N. S., *Energy & Environmental Science* **2015,** *8* (1), 203-207.
34. Shaner, M. R.; McKone, J. R.; Gray, H. B.; Lewis, N. S., *Energy & Environmental Science* **2015,** *8* (10), 2977-2984.
35. Zhou, X.; Liu, R.; Sun, K.; Friedrich, D.; McDowell, M. T.; Yang, F., . . . Lewis, N. S., *Energy & Environmental Science* **2015,** *8* (9), 2644-2649.
36. pp 21-144.

37. Fiore, J. L.; Fomenko, V. V.; Bodlaki, D.; Borguet, E., *Applied Physics Letters* **2011,** *98* (4), 041905.
38. Campen, R. K.; Pymer, A. K.; Nihonyanagi, S.; Borguet, E., *The Journal of Physical Chemistry C* **2010,** *114* (43), 18465-18473.
39. McClelland, A.; Fomenko, V.; Borguet, E., *The Journal of Physical Chemistry B* **2004,** *108* (12), 3789-3793.
40. Fomenko, V.; Borguet, E., *Physical Review B* **2003,** *68* (8), 081301.
41. Fomenko, V.; Lami, J.-F.; Borguet, E., *Physical Review B* **2001,** *63* (12), 121316.
42. Lantz, J. M.; Corn, R. M., *The Journal of Physical Chemistry* **1994,** *98* (18), 4899-4905.
43. Lantz, J. M.; Corn, R. M., *The Journal of Physical Chemistry* **1994,** *98* (38), 9387-9390.
44. Moss, B.; Hegner, F. S.; Corby, S.; Selim, S.; Francàs, L.; López, N., . . . Durrant, J. R., *ACS Energy Letters* **2019,** *4* (1), 337-342.
45. Selim, S.; Francàs, L.; García-Tecedor, M.; Corby, S.; Blackman, C.; Gimenez, S., . . . Kafizas, A., *Chemical Science* **2019,** *10* (9), 2643-2652.
46. Kafizas, A.; Ma, Y.; Pastor, E.; Pendlebury, S. R.; Mesa, C.; Francàs, L., . . . Durrant, J. R., *ACS Catalysis* **2017,** *7* (7), 4896-4903.
47. Farnum, B.; Wee, K.-R.; J. Meyer, T., *Nature Chemistry* **2016,** *8*.
48. Kafizas, A.; Wang, X.; Pendlebury, S. R.; Barnes, P.; Ling, M.; Sotelo-Vazquez, C., . . . Durrant, J. R., *The Journal of Physical Chemistry A* **2016,** *120* (5), 715-723.
49. Ma, Y.; Mesa, C. A.; Pastor, E.; Kafizas, A.; Francàs, L.; Le Formal, F., . . . Durrant, J. R., *ACS Energy Letters* **2016,** *1* (3), 618-623.
50. Ma, Y.; Le Formal, F.; Kafizas, A.; Pendlebury, S. R.; Durrant, J. R., *J. Mater. Chem. A* **2015,** *3* (41), 20649-20657.
51. Le Formal, F.; Pastor, E.; Tilley, S. D.; Mesa, C. A.; Pendlebury, S. R.; Grätzel, M.; Durrant, J. R., *Journal of the American Chemical Society* **2015,** *137* (20), 6629-6637.
52. Ma, Y.; Pendlebury, S. R.; Reynal, A.; Le Formal, F.; Durrant, J. R., *Chemical Science* **2014,** *5* (8), 2964-2973.
53. Le Formal, F.; Pendlebury, S. R.; Cornuz, M.; Tilley, S. D.; Grätzel, M.; Durrant, J. R., *Journal of the American Chemical Society* **2014,** *136* (6), 2564-2574.
54. Pendlebury, S. R.; Wang, X.; Le Formal, F.; Cornuz, M.; Kafizas, A.; Tilley, S. D., . . . Durrant, J. R., *Journal of the American Chemical Society* **2014,** *136* (28), 9854-9857.
55. Le Formal, F.; Pendlebury, S. R.; Cornuz, M.; Tilley, S. D.; Grätzel, M.; Durrant, J. R., *Journal of the American Chemical Society* **2014,** *136* (6), 2564-2574.
56. Chen, X.; Choing, S. N.; Aschaffenburg, D. J.; Pemmaraju, C. D.; Prendergast, D.; Cuk, T., *Journal of the American Chemical Society* **2017,** *139* (5), 1830-1841.
57. Yang, Y.; Gu, J.; Young, J. L.; Miller, E. M.; Turner, J. A.; Neale, N. R.; Beard, M. C., *Science* **2015,** *350* (6264), 1061-1065.
58. V Sheridan, M.; Hill, D.; D Sherman, B.; Wang, D.; L Marquard, S.; Wee, K.-R., . . . J Meyer, T., *Journal of the American Chemical Society* **2017,** *17*.
59. McDowell, M. T.; Lichterman, M. F.; Carim, A. I.; Liu, R.; Hu, S.; Brunschwig, B. S.; Lewis, N. S., *ACS Applied Materials & Interfaces* **2015,** *7* (28), 15189-15199.
60. Prier, C. K.; Rankic, D. A.; MacMillan, D. W. C., *Chem. Rev.* **2013,** *113* (7), 5322--5363.
61. Cakmak, Y.; Kolemen, S.; Duman, S.; Dede, Y.; Dolen, Y.; Kilic, B., . . . Akkaya, E. U., *Angew. Chem. Int. Ed.* **2011,** *50* (50), 11937--11941.
62. Kamkaew, A.; Lim, S. H.; Lee, H. B.; Kiew, L. V.; Chung, L. Y.; Burgess, K., *Chem. Soc. Rev.* **2013,** *42* (1), 77--88.

63. Lim, S. H.; Thivierge, C.; Nowak-Sliwinska, P.; Han, J.; van den Bergh, H.; Wagnières, G., . . . Lee, H. B., *J. Med. Chem.* **2010,** *53* (7), 2865--2874.
64. Zhao, J.; Xu, K.; Yang, W.; Wang, Z.; Zhong, F., *Chem. Soc. Rev.* **2015,** *44* (24), 8904--8939.
65. Rao, A.; Chow, P. C. Y.; Glinas, S.; Schlenker, C. W.; Li, C.-Z.; Yip, H.-L., . . . Friend, R. H., *Nature* **2013,** *500* (7463), 435--9.
66. Wu, W.; Guo, H.; Wu, W.; Ji, S.; Zhao, J., *J. Org. Chem.* **2011,** *76* (17), 7056--64.
67. Zhao, J.; Ji, S.; Guo, H., *RSC Adv.* **2011,** *1* (6), 937--950.
68. Wang, Z.; Zhao, J.; Barbon, A.; Toffoletti, A.; Liu, Y.; An, Y., . . . Hayvali, M., *J. Am. Chem. Soc.* **2017,** *139* (23), 7831--7842.
69. Wen, X.; Xu, W.; Zhao, W.; Khurgin, J. B.; Xiong, Q., *Nano letters* **2018,** *18* (3), 1686-1692.
70. Singh-Rachford, T. N.; Castellano, F. N., *Coord. Chem. Rev.* **2010,** *254* (21-22), 2560--2573.
71. Zhou, J.; Liu, Q.; Feng, W.; Sun, Y.; Li, F., *Chem. Rev.* **2015,** *115* (1), 395--465.
72. Yersin, H.; Rausch, A. F.; Czerwieniec, R.; Hofbeck, T.; Fischer, T., *Coord. Chem. Rev.* **2011,** *255* (21-22), 2622--2652.
73. Romero, N. A.; Nicewicz, D. A., *Chem. Rev.* **2016,** *116* (17), 10075--10166.
74. Bardeen, C. J., *Annu. Rev. Phys. Chem.* **2014,** *65* (1), 127--148.
75. Schmidt, T. W.; Castellano, F. N., *J. Phys. Chem. Lett.* **2014,** *5* (22), 4062--4072.
76. Shockley, W.; Queisser, H. J., *J. Appl. Phys.* **1961,** *32* (3), 510--519.
77. de Wild, J.; Meijerink, A.; Rath, J. K.; van Sark, W. G. J. H. M.; Schropp, R. E. I.; Nelles, G., . . . Wu, Y., *Energy Environ. Sci.* **2011,** *4* (12), 4835--4848.
78. Singh-Rachford, T. N.; Haefele, A.; Ziessel, R.; Castellano, F. N., *J. Am. Chem. Soc.* **2008,** *130* (48), 16164--16165.
79. Zhao, J.; Wu, W.; Sun, J.; Guo, S., *Chem. Soc. Rev.* **2013,** *42* (12), 5323--5351.
80. Turro, N. J.; Kavarnos, G. J.; Cole, T.; Scribe, P.; Dalton, J. C., *J. Am. Chem. Soc.* **1971,** *93* (4), 1032--1034.
81. Koziar, J. C.; Cowan, D. O., *Acc. Chem. Res.* **1978,** *11* (9), 334--341.
82. Carrera, E. I.; Seferos, D. S., *Macromolecules* **2015,** *48* (2), 297--308.
83. Gutierrez, G. D.; Sazama, G. T.; Wu, T.; Baldo, M. A.; Swager, T. M., *J. Org. Chem.* **2016,** *81* (11), 4789--4796.
84. Rey, Y. P.; Abradelo, D. G.; Santschi, N.; Strassert, C. A.; Gilmour, R., *Eur. J. Org. Chem.* **2017,** *2017* (15), 2170--2178.
85. Smith, M. B.; Michl, J., *Chem. Rev.* **2010,** *110* (11), 6891--6936.
86. Franco, L.; Mazzoni, M.; Corvaja, C.; Gubskaya, V. P.; Berezhnaya, L. S.; Nuretdinov, I. A., *Chem. Commun.* **2005,** *33* (16), 2128--2130.
87. Ishii, K.; Hirose, Y.; Kobayashi, N., *J. Am. Chem. Soc.* **1998,** *120* (40), 10551--10552.
88. Ishii, K.; Fujisawa, J.-i.; Adachi, A.; Yamauchi, S.; Kobayashi, N., *J. Am. Chem. Soc.* **1998,** *120* (13), 3152--3158.
89. Takeuchi, S.; Ishii, K.; Kobayashi, N., *J. Phys. Chem. A* **2004,** *108* (16), 3276--3280.
90. Giacobbe, E. M.; Mi, Q.; Colvin, M. T.; Cohen, B.; Ramanan, C.; Scott, A. M., . . . Wasielewski, M. R., *J. Am. Chem. Soc.* **2009,** *131* (10), 3700--3712.
91. Colvin, M. T.; Giacobbe, E. M.; Cohen, B.; Miura, T.; Scott, A. M.; Wasielewski, M. R., *J. Phys. Chem. A* **2010,** *114* (4), 1741--1748.

92. Ito, A.; Shimizu, A.; Kishida, N.; Kawanaka, Y.; Kosumi, D.; Hashimoto, H.; Teki, Y., *Angew. Chem. Int. Ed.* **2014,** *53* (26), 6715--6719.
93. Likhtenstein, G. I.; Ishii, K.; Nakatsuji, S. i., *Photochem. Photobiol.* **2007,** *83* (4), 871--881.
94. Huang, Y.; Egap, E., *Polym. J.* **2018,** *50*, 603--614.
95. Huang, Z.; Li, X.; Mahboub, M.; Hanson, K. M.; Nichols, V. M.; Le, H., . . . Bardeen, C. J., *Nano Letters* **2015,** *15* (8), 5552-5557.
96. Mongin, C.; Garakyaraghi, S.; Razgoniaeva, N.; Zamkov, M.; Castellano, F. N., *Science* **2016,** *351* (6271), 369-372.
97. Wu, M.; Congreve, D. N.; Wilson, M. W. B.; Jean, J.; Geva, N.; Welborn, M., . . . Baldo, M. A., *Nat Photon* **2016,** *10* (1), 31-34.
98. Okumura, K.; Mase, K.; Yanai, N.; Kimizuka, N., *Chem-Eur J* **2016,** *22* (23), 7721-7726.
99. Yu, W. W.; Qu, L.; Guo, W.; Peng, X., *Chemistry of Materials* **2003,** *15* (14), 2854-2860.
100. Scholes, G. D.; Rumbles, G., *Nat Mater* **2006,** *5* (9), 683-696.
101. Jasieniak, J.; Califano, M.; Watkins, S. E., *ACS Nano* **2011,** *5* (7), 5888-5902.
102. Singh-Rachford, T. N.; Castellano, F. N., *Coordination Chemistry Reviews* **2010,** *254*, 2560-2573.
103. Huang, Z.; Li, X.; Yip, B. D.; Rubalcava, J. M.; Bardeen, C. J.; Tang, M. L., *Chemistry of Materials* **2015,** *27* (21), 7503-7507.
104. Mahboub, M.; Huang, Z.; Tang, M. L., *Nano Letters* **2016,** *16* (11), 7169-7175.
105. Gray, V.; Xia, P.; Huang, Z.; Moses, E.; Fast, A.; Fishman, D. A., . . . Lee Tang, M., *Chem Sci* **2017,** *8* (8), 5488-5496.
106. Mahboub, M.; Maghsoudiganjeh, H.; Pham, A. M.; Huang, Z.; Tang, M. L., *Advanced Functional Materials* **2016,** *26* (33), 6091-6097.
107. Huang, Z.; Simpson, D. E.; Mahboub, M.; Li, X.; Tang, M. L., *Chemical Science* **2016,** *7* (7), 4101-4104.
108. L. J. Dexter, D., 1953; Vol. 21, p 836-850.
109. Huang, Z.; Tang, M. L., *Journal of the American Chemical Society* **2017,** *139* (28), 9412-9418.
110. Nirmal, M.; Norris, D. J.; Kuno, M.; Bawendi, M. G.; Efros, A. L.; Rosen, M., *Phys Rev Lett* **1995,** *75* (20), 3728-3731.
111. Efros, A. L.; Rosen, M.; Kuno, M.; Nirmal, M.; Norris, D. J.; Bawendi, M., *Physical Review B* **1996,** *54* (7), 4843.
112. Reddy, A. R.; Bendikov, M., *Chemical Communications* **2006,** (11), 1179-1181.
113. Becker, R. S.; deMelo, J. S.; Macanita, A. L.; Elisei, F., *J Phys Chem-Us* **1996,** *100* (48), 18683-18695.
114. Zhu, H. M.; Lian, T. Q., *Energy & Environmental Science* **2012,** *5* (11), 9406-9418.
115. Ding, T. N. X.; Olshansky, J. H.; Leone, S. R.; Alivisatos, A. P., *Journal of the American Chemical Society* **2015,** *137* (5), 2021-2029.
116. Alivisatos, A. P., *Science* **1996,** *271* (5251), 933-937.
117. Colvin, V. L.; Schlamp, M. C.; Alivisatos, A. P., *Nature* **1994,** *370* (6488), 354-357.
118. Pietryga, J. M.; Park, Y.-S.; Lim, J.; Fidler, A. F.; Bae, W. K.; Brovelli, S.; Klimov, V. I., *Chemical Reviews* **2016,** *116* (18), 10513-10622.
119. Carey, G. H.; Abdelhady, A. L.; Ning, Z.; Thon, S. M.; Bakr, O. M.; Sargent, E. H., *Chemical Reviews* **2015,** *115* (23), 12732-12763.

120. Kroupa, D. M.; Arias, D. H.; Blackburn, J. L.; Carroll, G. M.; Granger, D. B.; Anthony, J. E., . . . Johnson, J. C., *Nano Letters* **2018,** *18* (2), 865-873.
121. Davis, N. J. L. K.; Allardice, J. R.; Xiao, J.; Petty, A. J.; Greenham, N. C.; Anthony, J. E.; Rao, A., *The Journal of Physical Chemistry Letters* **2018,** *9* (6), 1454-1460.
122. Főrster, T., *Discussions of the Faraday Society* **1959,** *27* (0), 7-17.
123. Dexter, D. L., *The Journal of Chemical Physics* **1953,** *21* (5), 836-850.
124. Wenger, O. S., *Chemical Society Reviews* **2011,** *40* (7), 3538-3550.
125. Adams, D. M.; Brus, L.; Chidsey, C. E. D.; Creager, S.; Creutz, C.; Kagan, C. R., . . . Zhu, X., *The Journal of Physical Chemistry B* **2003,** *107* (28), 6668-6697.

2. Chapter 2. Experimental Methods

2.1 Transient absorption and reflectance spectroscopy

Femtosecond transient spectroscopy setup is based on a kilohertz Coherent Legend system which provides a 2.3 mJ 150 fs 800 nm fundamental pulse. For 800 nm or 400 nm excitation wavelengths, a type I BBO crystal is used to double 0.2 mJ 800 nm into 400 nm (photon energy 3.1 eV) to be used as the pump pulse (circular beam, area $\approx 1\times10^{-3}$ cm^2). For other visible wavelengths, 2 mJ of the 800 nm fundamental pulse is delivered to an Optical Parametric Amplifier (TOPAS-C, Spectra-Physics, or OperA Solo, Coherent) to generate a signal and idler that are in the ranges of 1200~1600 nm and 1600~2400 nm, respectively. This NIR pulse is then aligned with the previous 800 nm, both spatially and temporally. The type I BBO now generates signal sum frequency generation (SFG) for 480~530 nm, idler SFG for 540~590 nm. Or the type I BBO can double the signal to generate the doubled wavelengths that cover 600~800 nm. By this, we could obtain tunable excitation wavelength at 400 nm and continuously from 480 to 800 nm. The pump pulse was chopped at a frequency of 500 Hz to provide pumped and un-pumped contrast. A fraction of 800 nm (~0.1 mJ) is focused onto a CaF_2 crystal which rotates to prevent photo etching, generating a probe light which ranges from 1.5 eV to 3.1 eV. The crystal is changed to sapphire when more stable probe above 600 nm region is needed. The generated white light continuum (WLC) is passed through 800 nm filter to remove excess 800 nm, and then a beam splitter (70:30 T/R, or 90:10 depending on the sample OD) to provide a signal which interacts with the sample and a reference which is used to compensate noise and fluctuation. The WLC is then focused by a broadband parabolic mirror (15 cm focal length, Thorlabs) to reduce group velocity dispersion onto the sample and then collimated by a second parabolic mirror (10 cm focal length,

Thorlabs) and finally focused into the optical fiber. The delay time between pump and probe pulse is achieved by delaying the pump pulse using a delay stage. The polarization of the pump is controlled by a broad band half wave plate (400~800 nm, Thorlabs) to obtain the magic angle between the pump and probe pulses. A second broadband half wave plate is added to the probe light when individual control of polarization of pump and probe is needed. The angle of incidence (AOI) for pump pulse is 15 degrees while probe light is at 0 degrees. The probe light was then guided into grating and CMOS detector (Ultrafast System, Helios) via the optical fiber mentioned above to collect the time resolved signal.

The nanosecond transient absorption measurements are done with a commercially available system (Ultrafast System, EOS). The pump pulse is the same as described above. The probe is generated directly by a supercontinuum light source (Leukos) at 2 kHz repetition rate. The delay between pump and probe pulses is controlled electronically. Data analysis was carried out by Surface Xplorer (Ultrafast Systems) and Igor Pro (Wavemetrics).

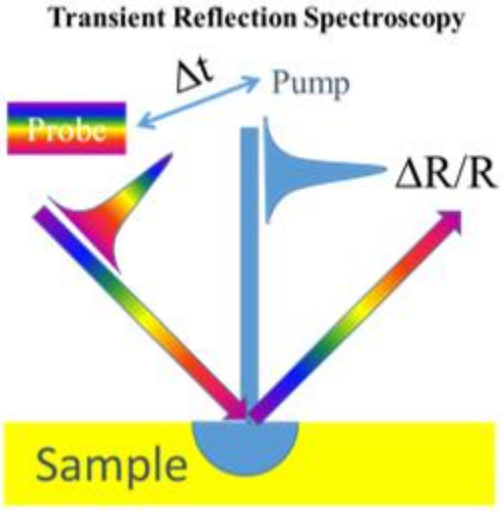

Figure 2.1 Transient Reflectance Spectroscopy Scheme.

In addition to the broadly used transmission mode of ultrafast spectroscopy, we also utilized the reflectance mode for different systems that we studied. As shown in Figure 2.1, the

geometry of pump and probe relative to the sample surface is changed, while all other experimental parameters remained the same. The angle of incidence (AOI) for the pump pulse is 35 degrees while the probe light was at 45 degrees. The reflectance scheme not only allows us to study optically opaque or reflective samples, but also provides unique surface sensitivity that the transmission mode lacks. The advantages of reflectance mode will be further discussed in detail in Chapter 3.

2.2 Time resolved microscopy platform

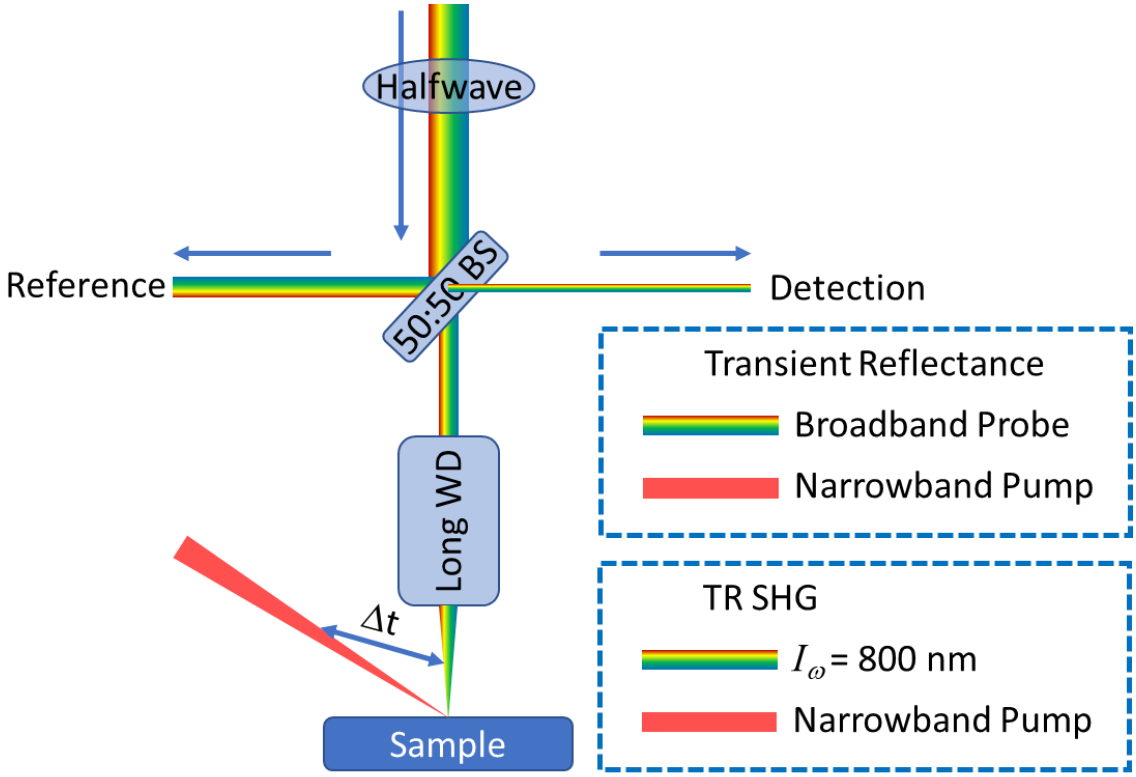

Figure 2.2 Schematics of the transient reflectance microscopy and time resolved SHG.

In addition to the transient reflectance spectroscopy, we developed a transient microscopy platform, shown in Figure 2.2. This setup allows us to study microscopic solid-state structures and specifically isolate points of interest for spectroscopic study on a large-scale sample. With the

same light source, the white light continuum (WLC) passed through a broadband half wave plate (Thorlabs) to adjust the polarization during measurements, followed by a 50:50 beam splitter allowing a normal angle of incidence configuration. The reflected 50% of WLC is collected and used as a reference to compensate for the fluctuation of the WLC. The transmitted WLC is then focused onto the desired sample location by a long working distance, large NA objective (Mitutoyo 50X objective, 0.55 NA, 13 mm WD). This objective is chosen based on the balance between a large enough NA and a long enough WD to suit both transient reflectance microscopy (TR) and time resolved second harmonic generation (TR-SHG) measurements. The excitation pulse (control light) generated from the OPA is focused onto the sample. The delay between the excitation and probe is controlled by a delay stage (Thorlabs). The reflected WLC by the sample travels back to the 50:50 beam splitter and is collected (denoted signal in the scheme). The collected WLC for both the reference and signal are coupled into a fiber and transmitted to a spectrometer then a 1024 element CMOS detector and recorded by the software (Helios, Ultrafast systems). For TR-SHG, the optical path is unchanged, except for removing the sapphire crystal to change the probe from WLC to the fundamental 800 nm. The SHG signal (400 nm) is then collected by a large core optical fiber and coupled into a liquid nitrogen cooled CCD detector (1340x100 pixels, PyLoN, Princeton Instruments) after passing through a 400 nm bandpass filter (Thorlabs). The delay is controlled by the same software as in TR.

2.3 Time resolved second harmonic generation spectroscopy

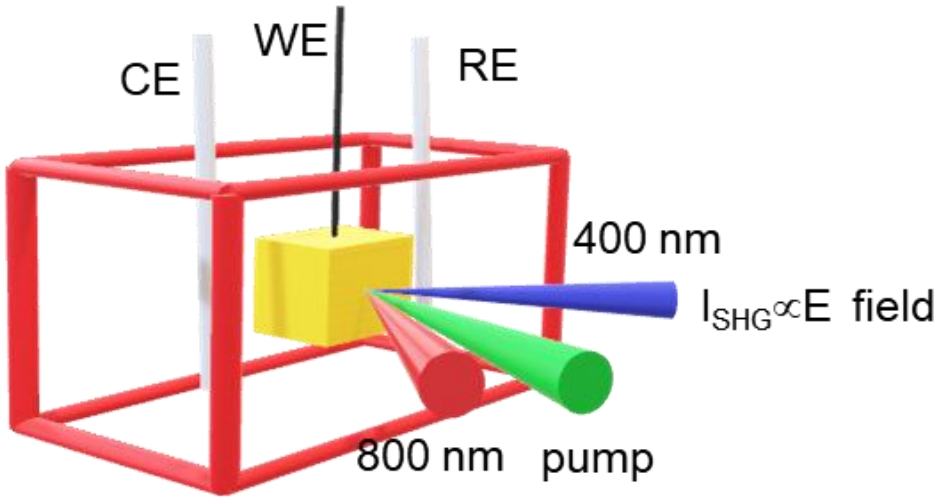

Figure 2.3 Time resolved SHG on photoelectrochemical system with three electrodes setup.

2.3.1 Femtosecond time resolution second harmonic generation

Similar to the transient spectroscopy setup, the femtosecond time resolved SHG is done by simply changing the WLC to the 800 nm and detection of the doubled 400 nm is detected by the liquid nitrogen cooled CCD detector (PyLoN, Princeton Instruments) as shown in Figure 2.3. The delay is controlled by a delay stage between pump and 800 nm pulse. The time window by this setup is limited to 2 ns.

2.3.2 Microsecond time resolution SHG

A longer time window is achieved by coupling the detector with a digital acquisition card (DAQ) from National Instruments. The probe is provided by a tunable oscillator from 770~1000 nm (Tsunami, Spectra Physics) at an 80 MHz repetition rate, and is focused onto the sample by a focal lens and the resulting SHG signal is collected by a second focal lens and guided into a PMT (Thorlabs) after passing through two 400 nm band pass filters. The illumination light source is a fiber couple LED driven by a power supply that could be modulated externally. The AOI for the

pump and probe is 0 degree and 45 degrees, respectively. The time resolution of this setup is determined by the sampling rate of the DAQ, which is 4 microseconds in this setup.

2.4 Photoelectrochemistry setup

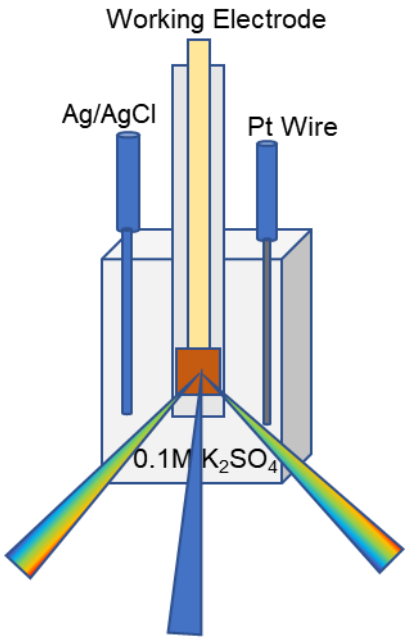

Figure 2.4 Three electrode setup for *in situ* photoelectrochemical study.

The electrochemistry experiments conducted here are done using a three electrodes electrochemical workstation (CHI660E, CH Instruments). A three electrodes setup is selected to provide accurate control of the potential applied on the working electrode. The counter electrode is a platinum wire, the reference electrode is an Ag/AgCl in 1M KCl solution. The electrochemical compartment is a quartz cell with a self-made top holder that allows for three electrodes to be situated snugly and a cell holder with two plates that allow it to be mounted in commercially available IR cell mounts, which is then, in turn, mounted to a 3-axis translational stage for adjustments. The electrolyte solution generally consisted of a buffer solution, supporting electrolyte and redox species. The buffer solution concentration and supporting electrolyte

concentration is calculated to have enough buffer strength and same ionic strength between different conditions.

2.5 Time resolved photoluminescence spectroscopy

The time resolved photoluminescence spectroscopy is based on a time correlated single photon counting (TCSPC) technique. The excitation light source is the same oscillator described above with an 80 MHz repetition rate. The fundamental pulse is picked by a pulse picker to generate enough temporal spacing between two pulses and the pulse picker provides an external trigger to the TCSPC system. The sample is placed at the focal point of the doubled fundamental light for excitation and the fluorescence is collected by a focal length and then filtered by band pass filter to remove the excitation pulse. The fluorescence is then coupled into a monochromator for wavelength detection and the data is collected by the TCSPC system of Becker&Hickel SPC 600.

2.6 Sample preparation

The electrode is generally prepared by a secure ohmic contact of the single crystal back and a copper conductive tape, both supported by a glass substrate. The surrounding of the single crystal and copper tape are then sealed with chemically stable epoxy (stable over applied potential as well).

The solution phase sample for transient studies were usually loaded into a 1 mm cuvette (Starna Cells), in a glovebox with an air-tight cap and parafilm wrapped, if needed.

3. Chapter 3. Ultrafast Dynamics of Photoinduced Charge Carriers and Electrical Fields at Semiconductor/Liquid Interface

3.1 Introduction

Photoelectrochemical (PEC) systems are able to capture the energy from sunlight and store it in the form of chemical bonds that can later be used to generate electricity on demand.[1] The fuel, such as hydrogen or alcohol, is an easily storable form of energy compared to electricity generated from photovoltaic devices, where the power output depends strongly on the weather conditions and the night/day intermittency of sunlight.[2] In a typical PEC system, photon excitation of a semiconductor absorber generates energetic charge carriers that then transport to the surface reactive sites for photoreaction.[3] III-V semiconductors with band gaps in the range 1.6-1.8eV band gap have been studied in depth and shown promising solar water splitting performances in PEC systems.[4-9] To counter the instability of these semiconductors under PEC conditions, several studies suggested TiO_2 as a promising protection layer with advantages in photostability over a wide pH and potential range.[3, 10] TiO_2 is a naturally *n*-type semiconductor due to oxygen vacancies, and it forms a *p*-*n* junction with *p*-type light absorbing semiconductors with appropriate band alignment, which promotes charge separation across the *p*-*n* junction.[11-13] Various III-V semiconductor materials with TiO_2 protection have demonstrated greatly enhanced stability under PEC conditions for OER and HER reactions.[14-19] However, excessive TiO_2 thickness insulates charge carrier migration across protection layer due to the low mobility of TiO_2.

For *p*-type GaP single crystal electrode, Jing et al. reported that an *n*-TiO_2 coating layer forms a *p*-*n* junction, which increases the onset potential of the HER by 500mV while remaining stable under PEC conditions for over 8h.[17] Many studies have focused on improving the performance of TiO_2 protected III-V semiconductors for the water splitting system. Although the optimal device parameters such as TiO_2 thickness could be optimized based on the applied potential-current (J-V) measurement, the detailed enhancement mechanism by the p-n junction is not clear. There has been limited research on the charge carrier dynamics in III-V semiconductors and TiO_2 passivated photoelectrodes. Most PEC systems using semiconductors as light absorbing materials show a strong potential dependence on photocurrent density.[14-26] While the macroscopic

efficiency of charge carriers can be characterized by J-V curves under dark and illumination conditions, the time resolved dynamics of charge carriers has proved to be very hard to observe and remains largely unclear. In these systems, charge carriers undergo multiple processes including charge separation, charge migration, charge recombination, charge accumulation at the surface and interfacial charge transfer. Understanding these processes requires high time resolution and sensitive detection to provide insight on the key limiting factors and guidance on designing more efficient PEC systems.

Transient spectroscopy as a powerful tool to study the microscopic charge carrier kinetics, generally requires a much higher excitation power density compared to the AM 1.5G. This high flux requirement originates from the necessity of large quantity of excited charge carriers to induce a large enough optical transition change to be detectable. However, under this condition particularly in semiconductor electrode the excess amount of charge carriers disturb the band bending condition. This phenomenon is called the 'band flattening' effect and has been previously studied by several methods in various systems.[27-31] This results in different conditions between continuous wave (CW) and transient illuminations although the averaged power density is comparable. In previous studies of time-resolved charge carrier kinetics in OER/HER systems,[12, 32-42] several methods were employed to address this contradiction. Apart from using longer duration excitation pulse to lower the transiently generated carrier concentration, high redox species concentration were also employed.[43] The former method provides a direct solution to transiently high charge carrier concentrations, whereas the latter enables fast charge carrier transfer from the semiconductor to the electrolyte to compete with recombination of charge carriers. However, in these studies, efficient charge separation is achieved by artificial tuning of experimental conditions rather than the device itself. Recent studies showed that the direct engineering of a layer of *n*-type TiO_2 on a *p*-type semiconductor efficiently prevented charge recombination and enhanced the carrier separation even at high carrier concentrations.[11, 15, 18-19, 21-23, 44] However, a detailed time-resolved charge carrier dynamics study on such a system under electrochemical working conditions has not yet been carried out to the best of our knowledge. In the work presented here, we utilized the efficient charge separation that occurs in the *p-n* junction at the surface of TiO_2/GaP semiconductor electrode, and we conducted *in situ* TR spectroscopy and photoelectrochemical measurements. The high sensitivity of the TR technique to probe the band structure and charge separation efficiency of the semiconductor electrode even at

femtosecond pulse excitation enables us to observe the correlation between transiently separated charge carriers and IPCE. This study revealed the charge separation mechanism under applied potential at a femtosecond time scale.

3.2 Materials and Methods

3.2.1 Materials preparation

The Zn doped 100 oriented GaP has a dopant concentration of ~1.2×10^{17} cm^{-3} (determined by impedance spectroscopy, see below for detail) . The electrode was prepared according to a previous study.[17, 22] In brief, the TiO_2 layer was deposited by atomic layer deposition (ALD) at 250°C with $TiCl_4$ as titanium source and water vapor as oxygen source. The ALD TiO_2 was verified to be anatase phase with Raman spectroscopy. A Ga-In alloy was painted to the back of the GaP for ohmic contact which is later connected to the copper conductive tape and sealed with epoxy to form an electrode for study.

The ALD TiO_2 protected GaP demonstrated excellent stability under CO_2 reduction condition (>8h measured) while enhancing onset potential and photocurrent.[17, 22] In this study the 5nm TiO_2 was chosen to study comparing to the bare GaP for its good stability and photocurrent for reduction reaction while very minimal (<4%) scatter and absorbance of the pump and probe pulse in TR measurement. TiO_2-GaP electrode with >10 nm thickness of TiO_2 showed drastically decreased photocurrent mainly due to the insulating nature of TiO_2.

3.2.2 Photoelectrochemical Setup

All electrochemical experiments were carried out by a CHI660E workstation (CH Instrument) with three electrode-setup. A Pt wire acts as counter electrode and Ag/AgCl (in 1M KCl) acts as reference electrode (CH Instrument) in buffered aqueous solution. The electrolyte is a buffered aqueous solution at pH=7 with ionic strength of 0.2 M, which is prepared by dissolving

96 mg disodium phosphate, 156 mg monosodium phosphate and 270 mg sodium sulfate into 100 mL water under room temperature. All chemicals used is purchased from Sigma-Aldrich without further preparation. All potential is relatively to Ag/AgCl unless state otherwise. The CW illumination experiment used a 405 nm LED (Ocean Optics) coupled with a focal lens and a ND filter to adjust the beam size and intensity. The photocurrent is measured by the difference in current when the illumination is modulated on and off as shown below in Figure 3.1.

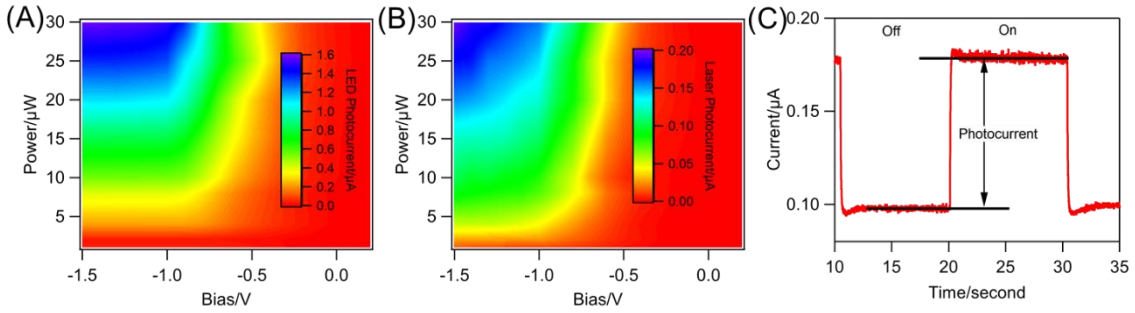

Figure 3.1 The photocurrent under various potential and illumination power of (A) laser excitation and (B) LED excitation. The left axis showed the total illumination power instead of power density in order to directly compare the photocurrent. (C) panel shows the photocurrent measurement method that avoids the non faradaic (charging and discharging current) current by modulating excitation light on/off under -1 V and 10 mW/cm^2.

3.2.3 Transient reflectance spectroscopy

Femtosecond transient reflectance (TR) spectroscopy setup consists of a Coherent Legend system which produces 150 fs 800 nm pulses at kilohertz with a pulse energy of 2.3 mJ. Pump pulses at 400 nm(photon energy 3.1 eV) are generated by converting a portion of 800nm pulses by second harmonic generation in a type I BBO crystal. The pump pulse is chopped at 500 Hz to provide pumped and un-pumped contrast and pump beam size at the sample as a circular area of ~1×10^{-3} cm^2. A fraction of 800 nm is focused onto a constantly rotating CaF_2 crystal to generates

a white light probe pulse from 1.5 eV to 3.1 eV. The delay time between pump and probe pulses is achieved by delaying the pump pulse through a delay stage. The probe light was divided by a beam splitter to provide a signal which interacts with the sample and a reference which is used to compensate noise and fluctuation. The angle of incidence (AOI) for pump pulse is 35 degrees while probe light at 45 degrees. The probe and references beams were collected by fibers and guided into grating and CMOS detector (Ultrafast System, Helios).

The nanosecond TR measurement is done with a commercially available system (Ultrafast System, EOS). The pump pulse is the same as above. The probe is generated by a supercontinuum light source (Leukos) at 2 kHz repetition rate. The delay between pump and probe pulses is controlled electronically. Data analysis is carried out by Surface Xplorer (Ultrafast Systems) and Igor Pro (Wavemetrics).

Ellipsometry data from previous study for bare GaP (100) single crystals are used to estimate the penetration depth of the pump and probe beams.[45] The pump penetration depths is estimated to be 138 nm at 3.1 eV by $d=1/\alpha=\lambda/4\pi\kappa$, and probe detection depth is 8~21 nm for 3.1~1.5 eV by $d=1/\alpha=\lambda/4\pi n$.

3.3 Results and Discussion

3.3.1 Characterization of 5 nm TiO_2 GaP electrode

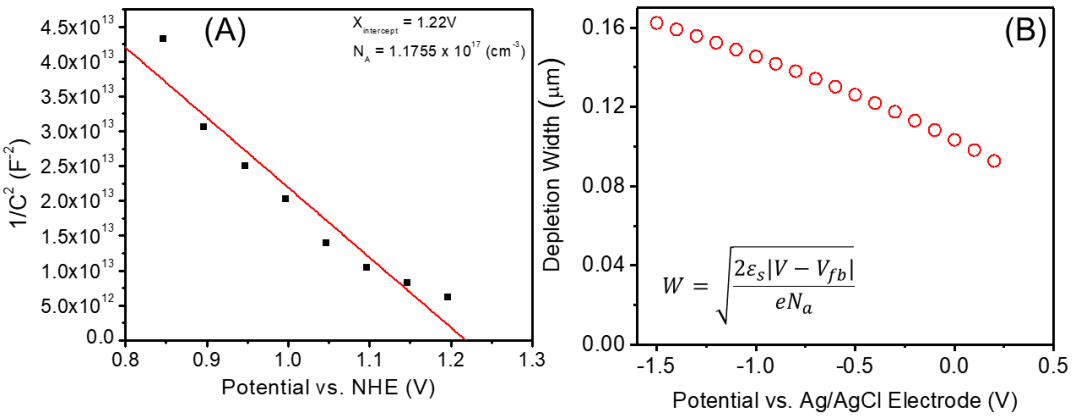

Figure 3.2 Mott-Schottky analysis of GaP/5nm-TiO_2 electrode (A) Flat band potential and dopant concentration measured by impedance spectroscopy. (B) Calculated depletion width based on the value from panel (A).

The dopant concentration is determined by Mott-Schottky equation

$$C^{-2} = \frac{2}{qA^2\varepsilon N_D}(V - V_{fb} - \frac{k_B T}{q})$$

Here, C is the capacitance, q is the elementary charge, ε is the permittivity of GaP, V is applied potential, V_{fb} is the flat band potential, k_B is Boltzmann constant and N_D is the dopant concentration. By fitting the data in Figure 3.2, the slope gives the dopant concentration to be 1.18E17 cm^{-3}. The intercept of the curve to the x axis indicate the flat band potential as:

$$V_{fb} = V - \frac{k_B T}{q} = 1.2\ V$$

The depletion width in GaP could be calculated by

$$x_p = \sqrt{\frac{2\varepsilon}{q}\frac{1}{N_d}|V - V_{fb}|}$$

3.3.2 Potential and excitation power dependent IPCE

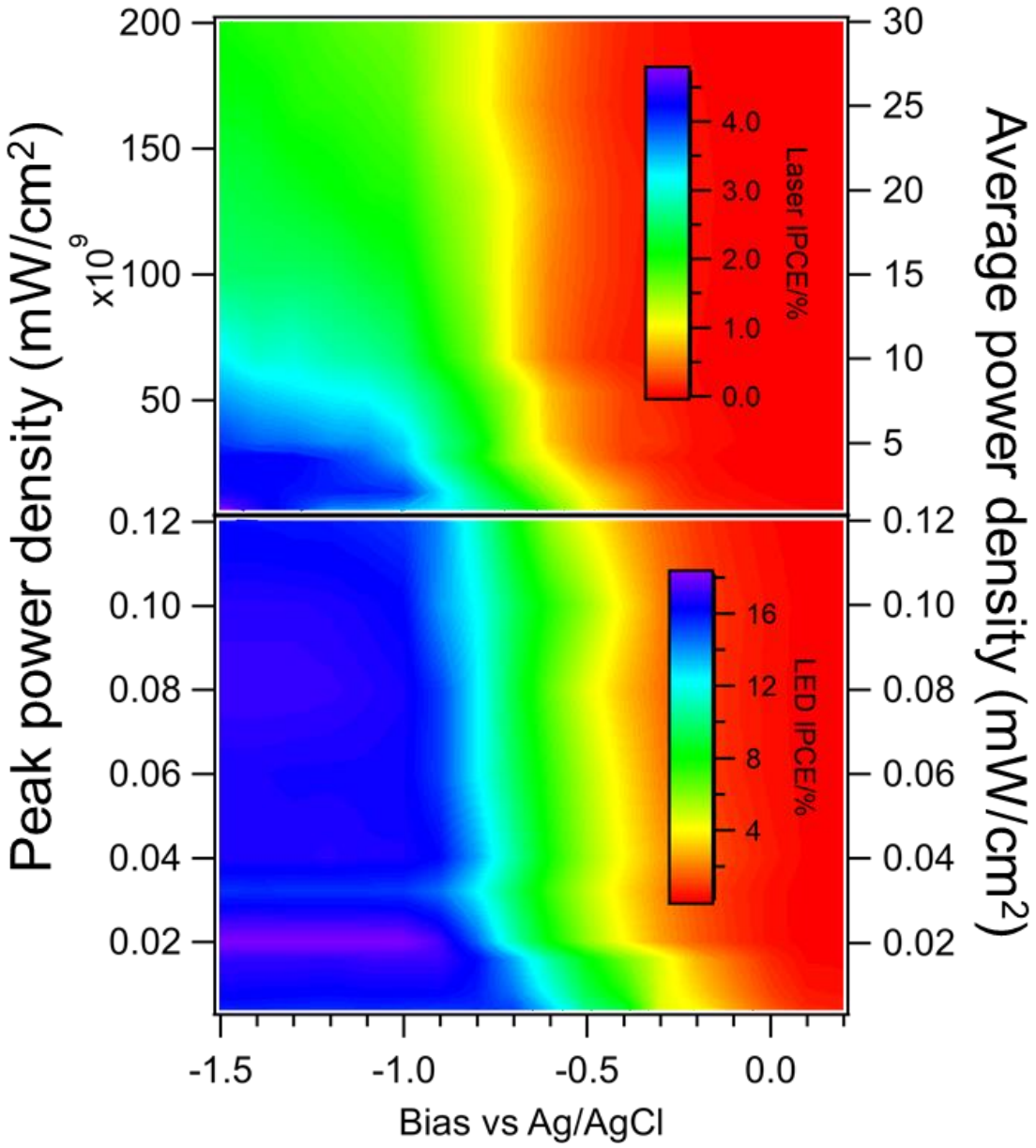

Figure 3.3 IPCE of the 5 nm-thick TiO_2-coated GaP photoelectrode measured with 405 nm continuous LED illumination (bottom panel) and in situ IPCE under the Transient Reflectance Spectroscopy (TRS) condition with ~150 fs 400 nm laser pulse (500 Hz repetition rate) excitation (top panel). The right axis indicates the averaged power density for these two excitation sources,

while the left axis shows the peak power density. Note: the color scale bar represents different range in the top and bottom panels.

Solar water splitting measurements are typically conducted under solar illumination conditions, such as AM 1.5G, which correspond to a power density of 100 mW/cm^2. On the contrary, in femtosecond transient absorption spectroscopy (TAS) experiments, the peak power density is in the order of 10^{10} mW/cm^2 (estimated from 1 nJ pulse energy, 150 fs FWHM duration, 0.001 cm^2 beam size) or larger. This drastic eight order of magnitude difference in the excitation power disrupts the typical band bending conditions that drive the charge carrier separation in semiconductor electrodes under the AM 1.5G conditions.[27-31, 46-47] Under low photon flux conditions, e.g., AM 1.5G, the photogenerated charge carriers are separated and driven to the semiconductor-electrolyte interface (SEI) or external circuit by band bending. This band bending can be mostly removed once the transiently excited charge carrier concentration is comparable to the dopant concentration (10^{17}-10^{20} cm^{-3}). This phenomenon is called the 'band flattening' effect and has been previously studied by several methods in various systems.[27-31] From a time-resolved perspective, the flattened band will not recover until the photoexcited charge carriers are depleted, by diffusion and/or recombination. [27-31] This would result in two expected observations: first, an electrode with a good incident photon to current efficiency (IPCE) under AM 1.5G condition would perform at a significantly lower IPCE under femtosecond laser pulse illumination as shown in Figure 1, and second, any TAS measured kinetics would show minimal potential dependence if there is not efficient charge separation. For TAS, excitation power densities on the order of 10^{10} mW/cm^2 or larger are required in order to produce detectable signal amplitudes (~0.1 mOD) in most materials. We believe that addressing this inherent contradiction provides the key to allow any meaningful study on charge carrier kinetics on such systems with femtosecond time resolution.

A common measurement to characterize the efficiency of charge separation is the incident photon to current efficiency (IPCE). We measured the photocurrent for hydrogen evolution reaction (HER)[17] of the 5 nm TiO_2 GaP system in situ (Figure 3.1) and calculated the IPCE at various excitation powers and applied potentials under LED continuous illumination and pulsed femtosecond illumination as shown in Figure 3.1. The IPCE is calculated as

$$IPCE\% = \frac{N\ of\ extracted\ electron}{N\ of\ incident\ photon} = \frac{I_p/e}{P/hv} \times 100\% \qquad \text{Eq. 3.1}$$

where I_p is photocurrent, e is electron charge, P is incident illumination power, and hv is photon energy. Here for the 1 mm thick GaP, the 400 nm or 405 nm illumination light is fully absorbed.

For continuous excitation with a 405 nm LED, the IPCE at -1.5V is around 18% when excitation power ranges from 120 μw/cm^2 to 4 μw/cm^2 and a generally higher IPCE than femtosecond pulsed excitation, as shown in Figure 3.3. For example, at -1.5 V the maximum IPCE is 4.6% and 18% for laser and LED illumination, respectively, at the lowest excitation power. The power independent IPCE observed under continuous LED illumination is expected since the low photon flux does not perturb the band bending and, therefore, the charge separation efficiency at a given potential is constant regardless of the excitation power. Under femtosecond pulsed excitation, the IPCE is substantially lower and decreases with increasing higher power density. Under femtosecond laser excitation, the transiently generated carrier concentration is large enough to flatten the band bending and prevents a portion of photoexcited charge carrier separation from occurring. Apparently, this loss pathway is excitation power dependent. However, for typical single junction photoelectrodes where the band bending is mainly created by the semiconductor-electrolyte, this power dependent IPCE is hard to observe because, even at the lowest excitation power that yields an observable signal in femtosecond excitation, the bands are completely flattened. The uniqueness of the *p-n* junction electrode, such as the TiO_2/GaP studied here,

provides a large built-in electrical field with a larger potential for charge separation, even under femtosecond excitation. Additionally, these large built-in fields induce a larger and easier to observe modulation signal (ΔR/R), as indicated in Eq. 3.2, and effectively lower the excitation power required to observe the separation of photoexcited charge carriers.

3.3.3 Charge Separation enhancement by p-n junction

The GaP single crystal (100) studied here is a *p*-type (Zn doped) and the TiO_2 is *n*-doped intrinsically due to oxygen vacancies. The Fermi level difference between TiO_2 and GaP drives electron flow from TiO_2 to GaP upon contact, resulting in a downward sloping band bending near the *p*-*n* interface for GaP until the Fermi levels are in equilibrium, as shown in Figure 3.4A. In the work presented here, we studied this TiO_2/GaP material system with transient reflectance (TR) spectroscopy in order to directly probe the charge separation efficiency and kinetics.

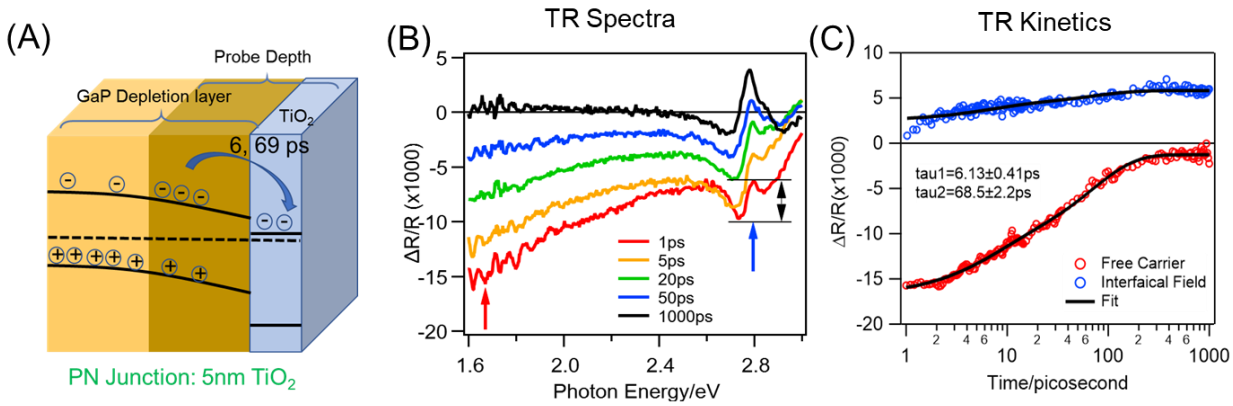

Figure 3.4 (A) Schematic diagram of the charge separation process in a 5 nm-coated TiO_2-GaP photoelectrode. (B) Time resolved TR spectra observed at various delay times under 400 nm pump excitation of 5 nm TiO_2 GaP in air. (C) ΔR/R kinetics of the free carrier signal (indicated in panel B by the red arrow) and Franz Keldysh Oscillation (FKO) signal amplitude (blue) and corresponding fits. The pump excitation power density was 0.6 W/cm^2.

In TR spectroscopy, the change in the reflected intensity of the probe beam is measured, which allows the study of optically opaque samples and provides surface sensitivity. As calculated in the previous section, the pump penetration depth is only ~150 nm, comparable to the depletion layer width as shown in Figure 3.2, ensuring the photogenerated carriers are mostly localized within the depletion region. The probe penetration depth is < 20 nm in the 1.5eV-3.1eV spectral range, making TR spectroscopy detection an interface sensitive approach. This ensures that the photogenerated carriers are mostly localized within the depletion region, and the detection is interface sensitive. Figure 3.4B shows the TR spectra of 5 nm-thick TiO_2-coated GaP electrodes at various delay times from 1 ps to 1 ns after 400 nm excitation. For delay times up to ~100 ps, the TR spectra have two main features: (1) a broad negative ΔR/R signal from 1.6 to 3 eV, and (2) an oscillation signal centered at 2.78 eV, at the direct band gap of GaP. We assigned the former feature to free carrier absorption in the GaP when photoexcited at relatively high power densities. The reason for this assignment is that, after Kramers-Kronig conversion,[11, 48] this broad signal's origin corresponds to the blocked transition at the indirect band gap (2.26eV) , as shown in Figure 3.5.[45]

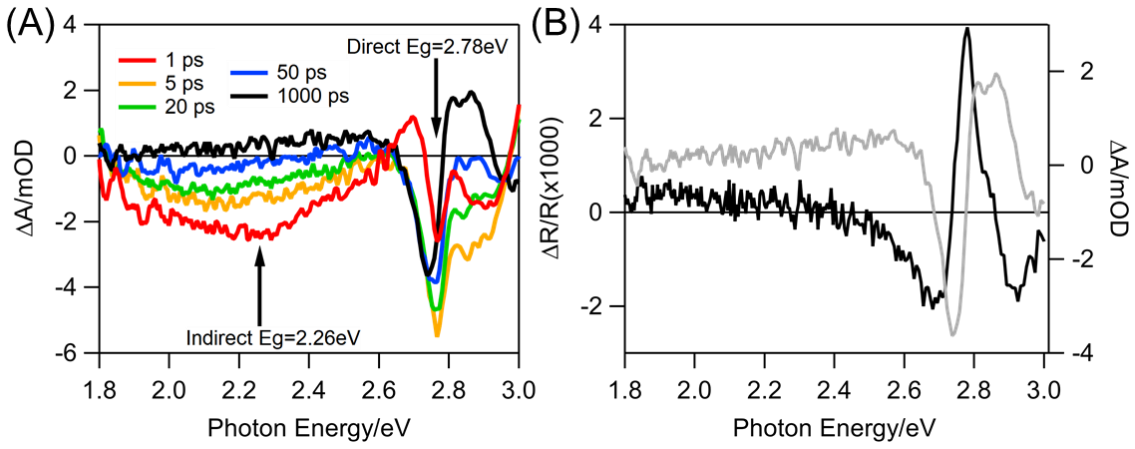

Figure 3.5 Kramers-Kronig conversion of the 5 nm TiO_2 GaP bare film transient reflectance spectrum in panel A. A direct comparison of the transient reflectance spectrum and the transient absorption spectrum at 1 ns delay time is shown in panel B.

Here, the ΔR/R and ΔA could be related the imaginary and real part of the complex refractive index via Kramers-Kronig relationship[48-49]:

$$n(\omega) - 1 = \frac{c}{\pi}\mathcal{P}\int_0^{\infty} \frac{\alpha(\Omega)d\Omega}{\Omega^2 - \omega^2}$$

whereas P is the Cauchy principle integral, c is the light speed, ω is the light frequency and α is the absorption coefficient.

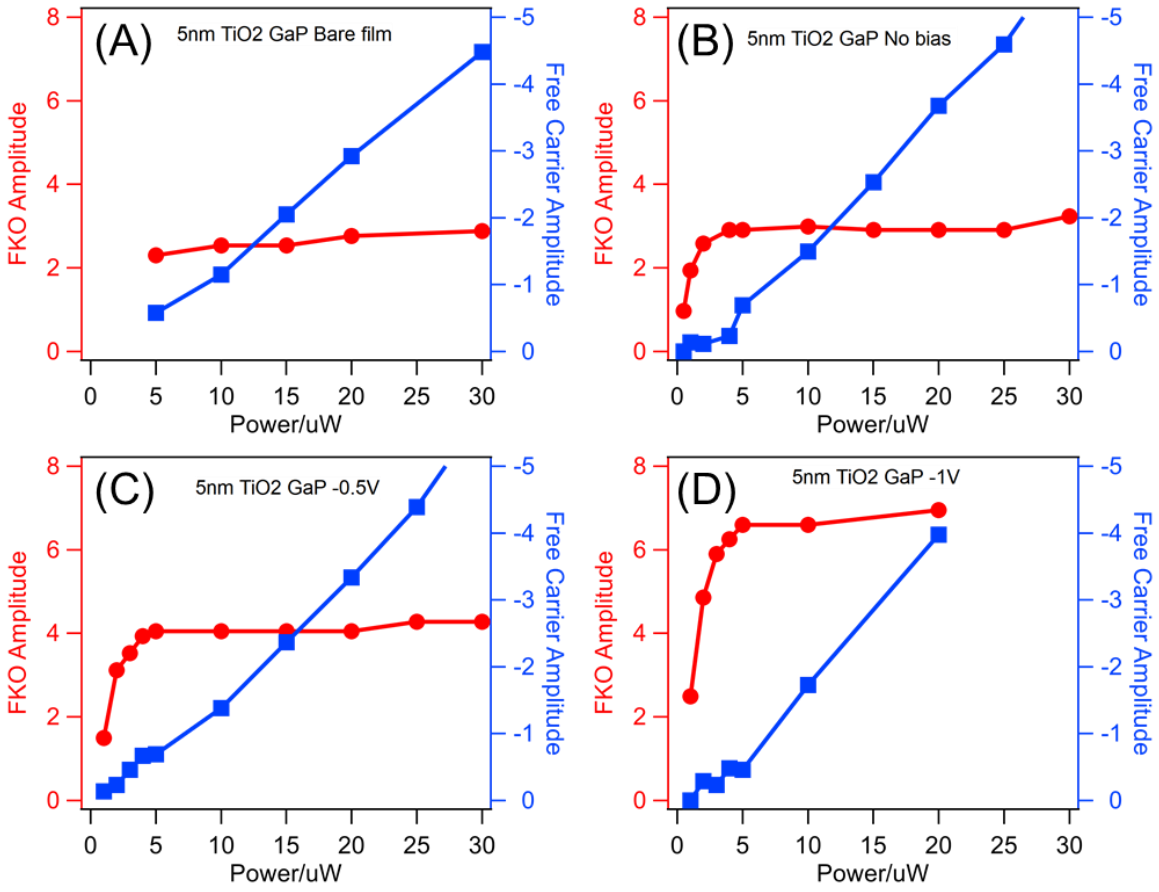

Figure 3.6 Franz Keldysh Oscillation signal amplitude (red circle, monitored at 2.78 eV) and free carrier signal amplitude (blue square, monitored at 1.5 eV) excitation power dependence at various bias: (A) bare film (B) No bias, in solution under open circuit condition (C) – 0.5 V (D) -1.0 V

Additionally, this signal amplitude increases linearly with excitation power, as shown in Figure 3.6A. The latter oscillation feature is more pronounced at longer delay times (~1 ns) and is

assigned to the separated electron across the *p-n* junction. Upon photoexcitation of this TiO_2-GaP sample, the generated electrons and holes inside the GaP have different energetics at the interface, as discussed previously. The electrons favor injection into the TiO_2 conduction band with a ~1 eV driving force. Meanwhile, the holes have a ~2 eV barrier preventing their injection into the TiO_2 valence band. This results in a large driving force for electron injection into the TiO_2 while the holes are blocked inside the GaP. This explains the earlier onset potential and higher photocurrent for electrode performance measurement reported previously.[17] The oscillatory TR feature is assigned to the change in the Franz-Keldysh Oscillation (FKO) signal caused by the separated carriers across the GaP-TiO_2 *p-n* junction. [50-51] The built-in electric field in the depletion region drives the photogenerated CB electrons to TiO_2 and the valence band holes to the bulk of GaP (Figure 2A). These separated charge carriers form a perturbing electric field (E_{ac}) in the opposite direction of the built-in field (E_{dc}), resulting in a modulated refractive index change known as Franz-Keldysh Oscillation.[50-51] When E_{ac} is smaller than E_{dc} the built-in field, the transient reflectance spectra can be expressed as:

$$\Delta R/R\ (\hbar\omega) \propto E_{ac} \cdot A(E_{dc}) \qquad \text{Eq. 3.2}$$

Here, $A(E_{dc})$ is a convoluted function of E_{dc} including an Airy function that determines the oscillatory line shape. However, due to the unobservable oscillation above 3.1 eV, it is difficult to extract the DC built-in field strength and the separated charge carrier-induced field. However, Eq. 3.2 showed that the TR signal amplitude under a certain built-in field is directly proportional to the separated charge carrier-induced field strength, which is proportional to the separated carrier density. Upon photoexcitation carriers are generated, part of which then migrate across the junction under the built-in field E_{dc} and form the modulation signal. Here, Figure 3.4C shows that the separated carrier growth kinetics follows the free carrier decay kinetics. To determine the charge

separation rate, we fit both kinetics with bi-exponential fittings and the rate constants are determined to be 6.1±0.4 ps and 68.5±2.2 ps. The two different time constants are considered an averaged measurement of carriers generated close to the GaP-TiO_2 interface and ones that are further away as they experience different field strengths, and therefore undergo different injection rate.

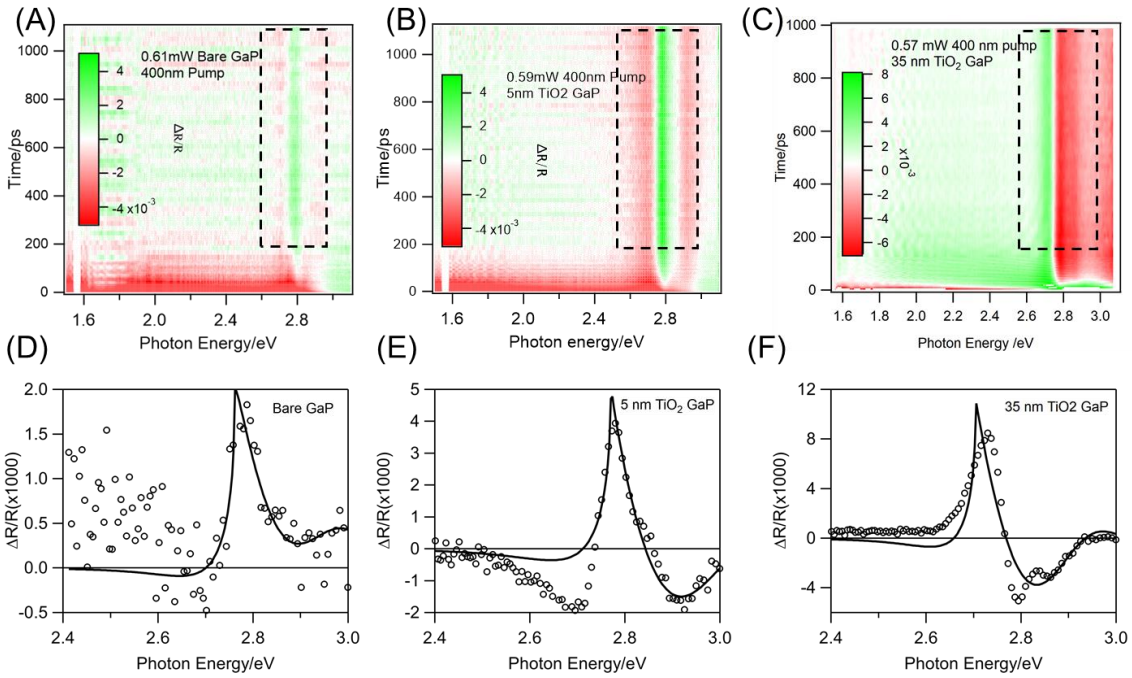

Figure 3.7 Transient reflectance spectroscopy with increasing TiO_2 layer thickness on GaP single crystal electrode in air excited by ~0.6 W/cm^2 400 nm. (A) 0 nm, (B) 5 nm, (C) 35 nm. (D)-(E) showed TR spectra at 1000 ps delay time and corresponding fit.

In Figure 3.7A-F, comparing the bare GaP, 5 nm TiO_2 coated GaP and 35 nm TiO_2- GaP TR spectra at 1000 ps delay, the TR spectra showed larger signal when excited at 400 nm under same excitation power density with thicker TiO_2 layer. From the refractive index of TiO_2, only 4% of 400 nm excitation light is lost at most when penetrating the TiO_2 layer, so the signal difference is not due to different excitation intensity at the GaP surface. In the bare GaP there is no band

bending or built-in field, the transient reflectance response is mainly the surface states induced weak electrical field.[50-51]

The Franz-Keldysh oscillation (FKO) has been established in previous studies.[51] The variation to the dielectric function $\delta\epsilon_{PR}$ (photoreflectance) under a built in DC and transiently photogenerated AC electrical field could be expressed as

$$\delta\epsilon_{PR}(hv, E_{DC}, E_{AC}) = \epsilon(hv, E_{DC}) - \epsilon(hv, E_{DC} - E_{AC}) = \Delta\epsilon(hv, E_{DC}) - \Delta\epsilon(hv, E_{DC} - E_{AC})$$

Here, the AC field direction is opposite to the built in DC field, therefore the field strength after excitation is E_{DC}-E_{AC}.

$$\Delta\epsilon(hv, E) = \frac{B}{(hv)^2}(\hbar\theta)^{\frac{1}{2}}[G(\eta) + iF(\eta)]$$

Where

$$\hbar\theta = \sqrt[3]{e^2\hbar^2E^2/2\mu}$$

$$\eta = (E_0 - hv)/\hbar\theta$$

Here, μ is the reduced effective mass, E_0 is the semiconductor band gap and B is a quantity number related to matrix element effects.

The G and F function are the electro-optic functions:

$$G(\eta) = \pi[Ai'(\eta)Bi'(\eta) - \eta Ai(\eta)Bi(\eta)] + \eta^{\frac{1}{2}}H(-\eta)$$

$$F(\eta) = \pi[Ai'(\eta)Ai'(\eta) - \eta Ai(\eta)Ai(\eta)] - (-\eta)^{\frac{1}{2}}H(-\eta)$$

Ai, Bi and Ai' and Bi' are Airy function and derivatives. H function is the unit step function.

As discussed above, the efficient charge separation here is due to the built-in field. Thus, as the excitation power increased, the transient electric field (E_{ac}) generated by the separated charge carriers will saturate this built-in field, and eventually the not-yet-separated carriers will be

screened from the built-in field and recombine. Therefore, the modulation signal amplitude would reach a maximum as the excitation power increased. This phenomenon can be observed by excitation power-dependence measurements, as shown in Figure 3.6A. Different thicknesses of atomic layer deposited (ALD) TiO_2 showed different levels of enhancement in the onset potential and photocurrent density. These enhancements indicated better charge separation efficiencies with increasing TiO_2 layer thickness up to 10 nm as reported previously.[17] Here, we studied the transient reflectance response with 0, 5 and 35 nm TiO_2 GaP single crystal in order to observe the effect of increased TiO_2 thickness. TR spectra suggested that with an increased TiO_2 thickness, the built-in field strength increases, resulting in a higher ability to separate charge carriers and a faster charge separation rate. These results are shown and analyzed in Figure S5 and S6. However, due to the poor conductivity of the 35 nm TiO_2 layer and the poor photochemical stability of pristine GaP single crystal, the following photoelectrochemical measurements were focused on the 5 nm-thick TiO_2-coated GaP electrode.

3.3.4 Potential and excitation power dependent charge separation efficiency

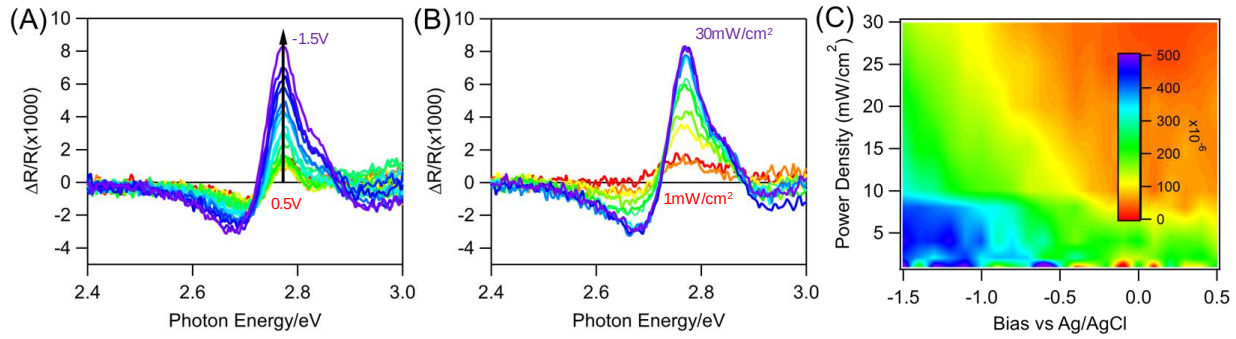

Figure 3.8 (A) Electrochemical potential dependence of TR spectra at 50 ps delay time on 5 nm-thick TiO_2-passivated GaP under 30 mW/cm^2, 400 nm excitation from 0.5 V (red) to -1.5 V (purple) in 0.1 V increments. (B) Pump pulse power dependence of TR spectra at 50 ps delay time under -1.5 V applied potential from to purple represents 1, 2, 4, 5, 8, 10, 15, 20, 25, 30 mW/cm^2,

respectively. (C) The normalized modulation amplitude (ΔR/R divided by excitation power density) mapped at different excitation power densities and applied potential in arbitrary units. The spikes under low excitation power is mainly due to small TR signal amplitude and bad signal to noise ratio.

Following the charge separation model discussed in the previous section, the amount of separated charge carriers at saturation will be different under different applied potentials. With increased applied potential, more charge carriers are separated.[1] To map the charge separation efficiency under various potential and power conditions, a series of excitation power and potential dependent TR spectra were measured in a three-electrode setup. As shown in Figure 3.8A, the TR spectrum at 50 ps showed a clear potential dependence with the ΔR/R signal increasing with more negative potential. This result fits our model's prediction as more charge carriers are separated under more negative potentials. However, under femtosecond laser excitation, the enhancement of charge carrier separation by a higher potential is not the same with broadband whitelight. Under 400 nm excitation, the penetration depth is merely ~140 nm, whereas the calculated depletion width in GaP is at comparable level (Figure 3.2). Here, the increased depletion width is not the only determining factor for the increased charge separation efficiency. Instead, the increased electrical field strength at the *p*-*n* junction interface provides more efficient charge carrier separation, which plays a more important role. Moreover, under a certain potential condition, the signal amplitude saturates as the excitation power is increased, as shown in Figure 3.2 and Figure 3.6, because the photogenerated carriers have saturated the built-in field's ability to separate charge carriers. From Eq. 3.2, the signal amplitude provides a direct measure of the AC field, which is proportional to the separated charge carrier density. We could then estimate the charge separation

efficiency, which is a similar method to the IPCE (incident photon to current efficiency, defined in Eq. 3.1), and is defined as the *normalized amplitude*, equal to the measured ΔR/R divided by the excitation power.

The normalized amplitude results under various excitation powers and applied potentials are plotted in Figure 3.8C. Here, we find that the charge carrier separation is most efficient in the lower left corner, where the applied potential is most negative and the excitation power is at minimum. Interestingly, the charge separation efficiency decreases with increasing excitation power. This is generally not observable under continuous illumination, such as AM 1.5G, since the excitation power is too low to disturb the band bending within the semiconductor. Under femtosecond excitation, however, this phenomenon is possible to observe due to the excess charge carriers initially generated, which flatten the bands and screen the free carriers from the electrical field throughout depletion region. To the best of our knowledge, this is the first time that the charge separation efficiency dependence on excitation power has been observed in a semiconductor HER system. This is mainly because, in previous studies using femtosecond laser excitation, the excitation power was far beyond this region to the extent that charge separation efficiency is actually very low and showed no dependence on the applied potential. In this study, an observable FKO requires a much smaller excitation power density (1~ 30 mW/cm^2) and the *p*-*n* junction offers a superior charge separation ability under relatively high carrier concentrations, both factors contribute our observing the power dependence of carrier separation efficiency.

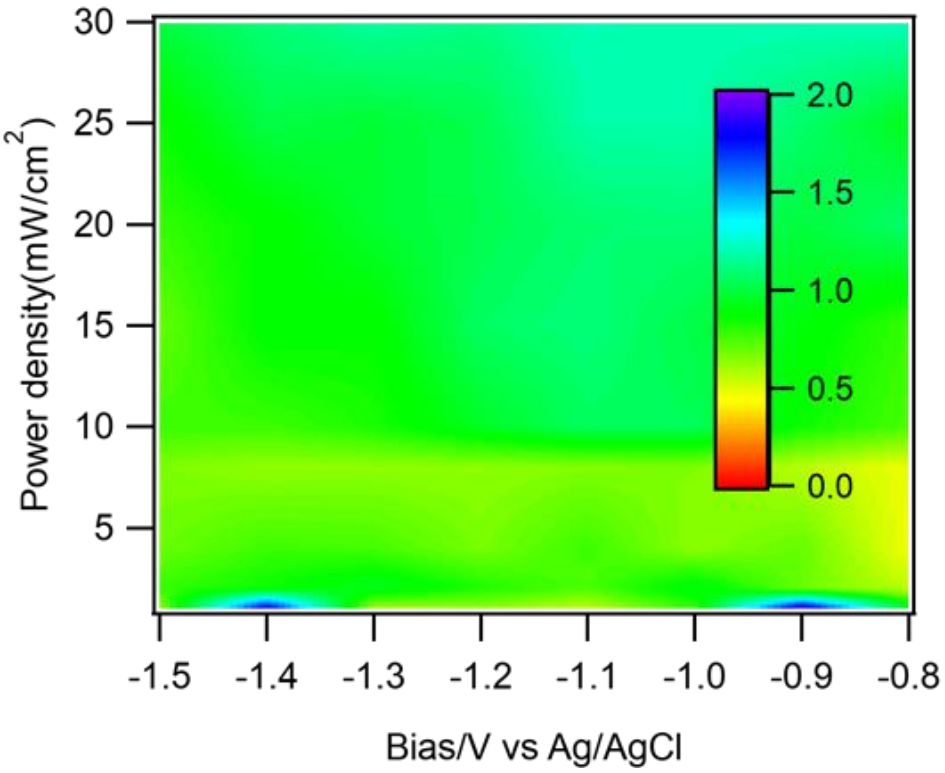

Figure 3.9 Correlation between IPCE and normalized FKO amplitude.

Upon further inspection, a strong resemblance can be seen between Figure 3.3 top panel and Figure 3.8C, suggesting that they indeed are both measuring the charge separation efficiency. To further verify our observed correlation, we generated a correlation matrix between IPCE and the normalized TR amplitude, as shown in Figure 3C. The matrix element is calculated as:

$$c_{m,n} = A * \frac{IPCE_{m,n}}{(\frac{\Delta R}{R})_{m,n}/p(n)}$$

Here, *m*, *n* are the matrix element indices for potential and power, respectively. ΔR/R is the FKO amplitude. A is a global normalization factor that is same for every matrix element. Figure 3.9 shows a plot of this correlation matrix plotted as a function of power density and electrochemical potential. Here, a strong correlation can be seen, in which most of the matrix elements lie within 0.8~1.2. This reveals that the normalized FKO amplitude fundamentally provides a measurement

of the charge separation efficiency at picosecond time scales, whereas the IPCE is a measurement of same property at the photoelectrochemical reaction time scale on the order of seconds. This correlation strongly suggests that the final chemical reaction is largely determined by how efficient the initially separation of charge carriers is. This correlation also suggests that the intermediate steps between the initial charge separation and final chemical reaction are mostly potential independent.

3.3.5 Potential and excitation power dependent charge separation kinetics

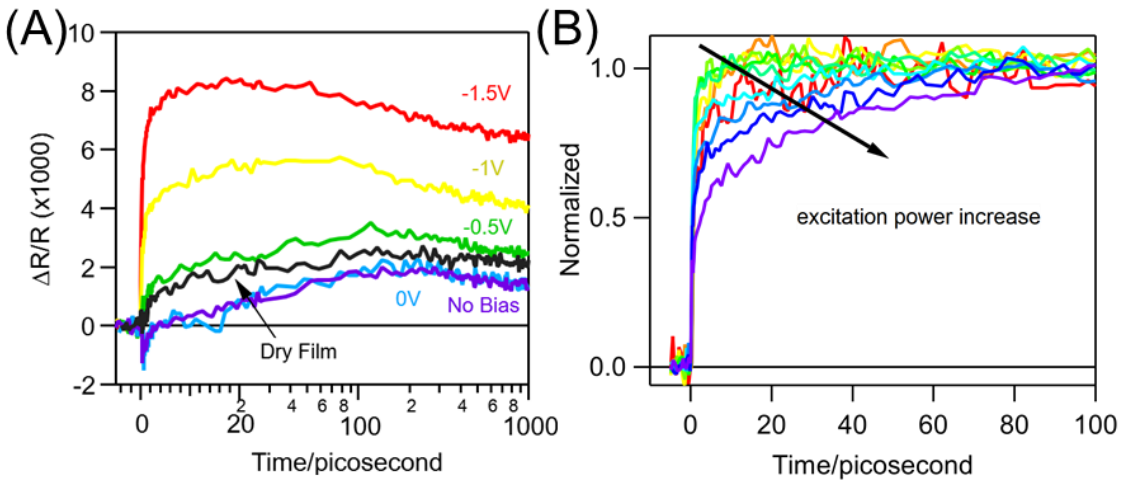

Figure 3.10 FKO and free carrier kinetics of 5 nm TiO2 GaP under different applied potential and excitation power. (A) Kinetics of the FKO ΔR/R signal at various applied potentials as indicated, under 30 mW/cm^2 excitation power. (B) Normalized FKO kinetics under -0.5 V applied potential with increasing 400 nm excitation power density at 1, 2, 3, 4, 5, 10, 15, 20, 25, 30 mW/cm^2. Slower charge separation is observed.

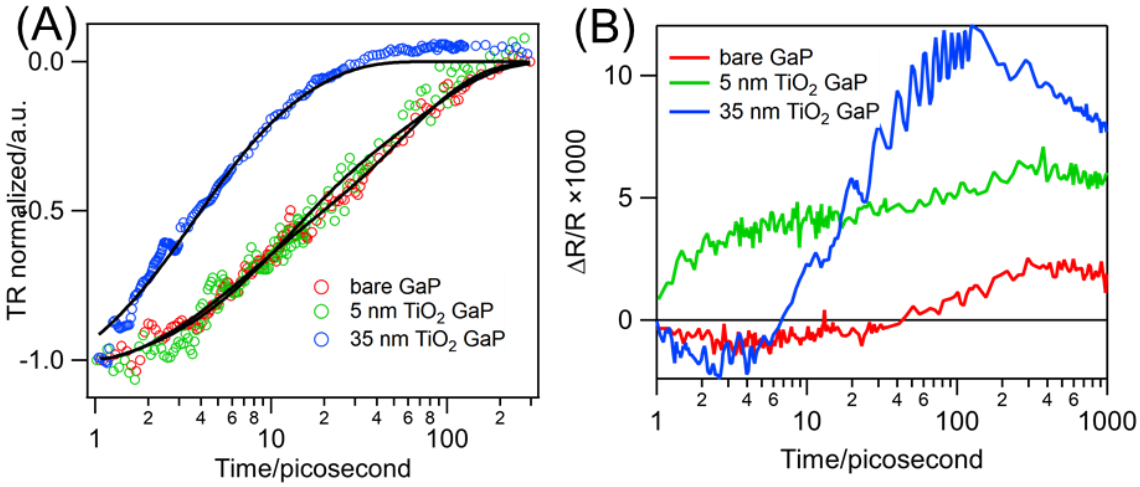

Figure 3.11 (A) Normalized free carrier kinetics monitored at 1.5 eV for bare, 5 nm TiO_2 and 35 nm TiO_2 coated GaP in air. (B) FKO amplitude kinetics, obtained by comparing the difference of the peak and valley of FKO signal as shown in Figure 3.7. Same condition as in Figure 3.7.

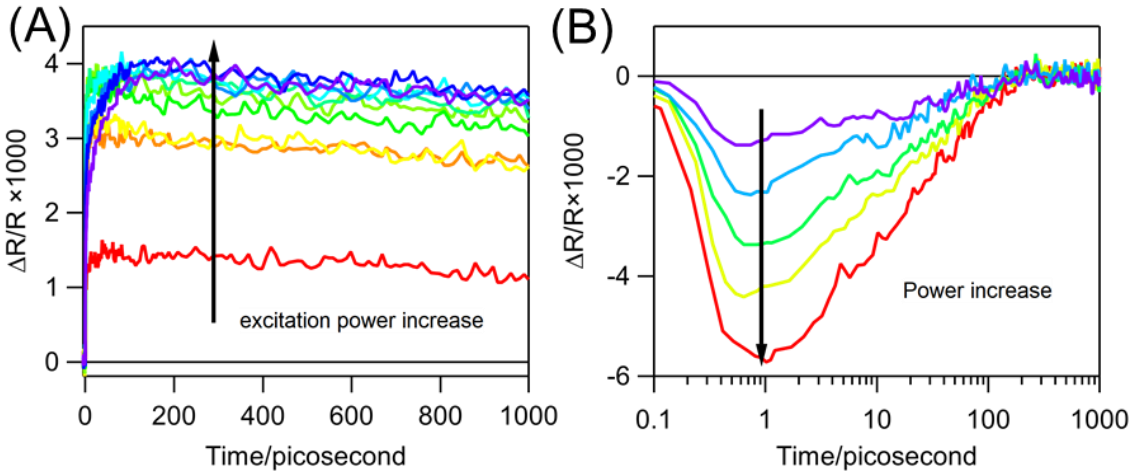

Figure 3.12 5 nm TiO_2 GaP kinetics under -0.5 V potential and various excitation power. (A) FKO kinetics excited by 400 nm at excitation power density of 1, 2, 3, 4, 5, 10, 15, 20, 25, 30 mW/cm^2. (B) Free carrier kinetics under -0.5 V applied potential with 400 nm excitation power density at 10, 15, 20, 25, 30 mW/cm^2.

The charge separation rate increases under a more negative potential, since the electrical field is the driving force of the separation. This can be seen in Figure 3.10A, where the growth of the FKO signal becomes faster with increasing potential, indicating that electron's injection rate into the TiO_2 becomes faster. Interestingly the FKO signal growth kinetics is also excitation power dependent, as shown in Figure 3.10B the saturation time for FKO signal is increasing as the excitation power increased from 1 to 30 mW/cm^2. The normalized kinetics in Figure 3.10B shows that the time for FKO signal to reach maximum amplitude increases from ~10 ps to ~100 ps from low to high excitation power. This result could be understood by that the overwhelming free carriers density at relatively high excitation power has a stronger band flattening effect, resulting in a smaller effective field that slows charge separation. The raw data before normalization (Figure 3.12) have shown that from 10 to 30 mW/cm^2 the maximum amplitude for FKO is similar, further confirming the saturation of separated charge carriers under a certain potential.

The free carrier (Figure 3.12A) and FKO (Figure 3.12B) signal that represents the separated charge carriers in 35 nm TiO_2 exhibits faster kinetics when compared to 5 nm TiO_2 and bare GaP. The fitting of the free carrier depletion in Figure S6A yields the rate constant for 35 nm TiO_2 GaP to be 5.58±0.3 ps (100%), significantly faster than the similar 5 nm TiO_2 and bare GaP rate at 3.0±0.8 ps (32.0%), 40.0±3.8 ps (68.0%) and 4.4±1.3 ps (32.0%), 52.7±5.8 ps (68.0%), respectively. This fitting results show that the 35 nm TiO_2 GaP lacks the slower component for the free carrier decay, suggesting the slower component in 5 nm TiO_2 GaP is due to charge carriers that are far from the TiO_2/GaP interface, which experiences a smaller electrical field strength. The same trend is also observed in the FKO kinetics as shown in Figure S6B, where the 35 nm TiO_2 GaP FKO signal saturates fastest, and 5 nm TiO_2 GaP and pristine GaP is comparably slower. Furthermore, these results also suggest the 5 nm TiO_2 GaP has a relatively small built in field.

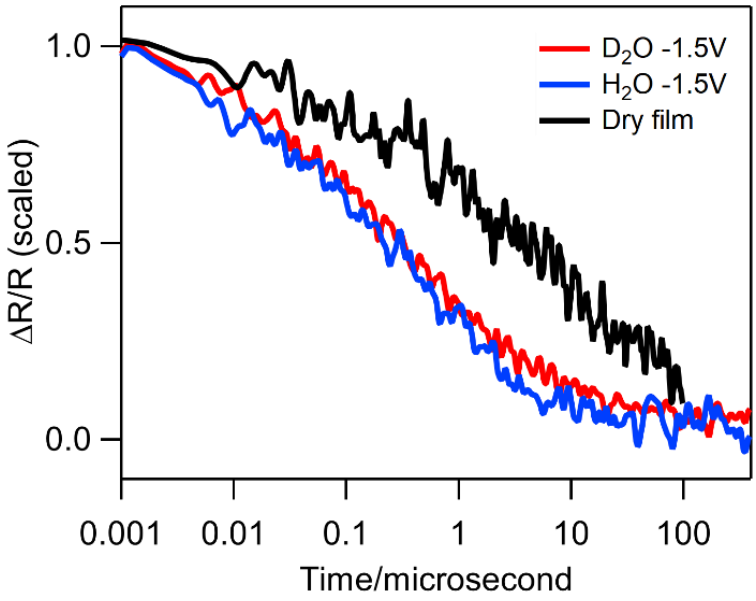

Figure 3.13 Nanosecond kinetics of 5nm TiO_2 GaP electrode under 400 nm excitation under dry film condition (black), -1.5V in H_2O solution (blue) and -1.5V in D_2O solution (red). The kinetics are normalized at 1 ns delay time.

The correlation between transiently separated charge carriers and IPCE in Figure 4 proves their correlation. To understand the pathway from the transiently generated carriers to the reaction in solid-electrolyte interface, a series of long delay time transient reflectance measurements were conducted, and the results are shown in Figure 3.13. Comparing between the dry electrode and under potential in solution, a faster decay indicates the faster depletion of the photogenerated carriers comparing to recombination process. However, the absence of the kinetic isotope effect (KIE) when reducing protons or deuterium cations indicates that this faster depletion pathway is not the first or second electron transfer to the redox species in the solution. The same kinetics between H_2O and D_2O under -1.5V suggests that this observed decay is a process that occurs before the actual redox reaction, which could be the electron migration across TiO_2, electron trapping on

the TiO_2 surface sites, etc. However, due to the limitation of instruments, the origin of this decay is not yet determined and is still under investigation.

3.4 Conclusion

In this work, we demonstrated an *in situ* measurement of transient reflectance modulation signal and IPCE simultaneously. Through modelling and fitting, we have demonstrated that both measurements are fundamentally based on the charge separation efficiency. Under high intensity pulsed laser excitation, the power dependent charge separation efficiency is attributed to the effect of band flattening. We have also revealed that the *p-n* junction photoelectrode has a stronger built-in field that enhances charge separation even at very high photon flux and is, thus, superior to single junction photoelectrodes. This unique property has enabled us to measure meaningful IPCEs even under femtosecond laser excitation. We have also established a strong correlation between the initial charge carrier separation efficiency obtained by TR spectroscopy and the IPCE in this TiO_2/GaP system. This discovery provides an insight that the overall photoelectrochemical current is largely determined by the initial charge carrier separation efficiency. This method also provides a powerful tool to study similar PEC systems to evaluate the charge separation efficiency.

3.5 References

1. Walter, M. G.; Warren, E. L.; McKone, J. R.; Boettcher, S. W.; Mi, Q.; Santori, E. A.; Lewis, N. S., *Chemical Reviews* **2010,** *110* (11), 6446-6473.
2. Lewis, N. S.; Nocera, D. G., *Proceedings of the National Academy of Sciences* **2006,** *103* (43), 15729-15735.
3. Hu, S.; Lewis, N. S.; Ager, J. W.; Yang, J.; McKone, J. R.; Strandwitz, N. C., *The Journal of Physical Chemistry C* **2015,** *119* (43), 24201-24228.
4. Weber, M. F.; Dignam, M. J., *Journal of The Electrochemical Society* **1984,** *131* (6), 1258-1265.
5. Bolton, J. R.; Strickler, S. J.; Connolly, J. S., *Nature* **1985,** *316*, 495.

6. Hu, S.; Xiang, C.; Haussener, S.; Berger, A. D.; Lewis, N. S., *Energy & Environmental Science* **2013,** *6* (10), 2984-2993.
7. Döscher, H.; Geisz, J.; Deutsch, T.; Turner, J., *Energy & Environmental Science* **2014,** *7* (9), 2951-2956.
8. Seitz, L. C.; Chen, Z.; Forman, A. J.; Pinaud, B. A.; Benck, J. D.; Jaramillo, T. F., *ChemSusChem* **2014,** *7* (5), 1372-1385.
9. Coridan, R. H.; Nielander, A. C.; Francis, S. A.; McDowell, M. T.; Dix, V.; Chatman, S. M.; Lewis, N. S., *Energy & Environmental Science* **2015,** *8* (10), 2886-2901.
10. Acevedo-Peña, P.; Vazquez-Arenas, J.; Cabrera-Sierra, R.; Lartundo-Rojas, L.; González, I., *Journal of The Electrochemical Society* **2013,** *160* (6), C277-C284.
11. Yang, Y.; Gu, J.; Young, J. L.; Miller, E. M.; Turner, J. A.; Neale, N. R.; Beard, M. C., *Science* **2015,** *350* (6264), 1061-1065.
12. Selim, S.; Francàs, L.; García-Tecedor, M.; Corby, S.; Blackman, C.; Gimenez, S., . . . Kafizas, A., *Chemical Science* **2019,** *10* (9), 2643-2652.
13. Shockley, W.; Queisser, H. J., *J. Appl. Phys.* **1961,** *32* (3), 510--519.
14. Lee, M. H.; Takei, K.; Zhang, J.; Kapadia, R.; Zheng, M.; Chen, Y. Z., . . . Ager, J. W., *Angewandte Chemie International Edition* **2012,** *51* (43), 10760-10764.
15. Lin, Y.; Kapadia, R.; Yang, J.; Zheng, M.; Chen, K.; Hettick, M., . . . Ager, J. W., *The Journal of Physical Chemistry C* **2015,** *119* (5), 2308-2313.
16. Qiu, J.; Zeng, G.; Ha, M.-A.; Ge, M.; Lin, Y.; Hettick, M., . . . Cronin, S. B., *Nano Letters* **2015,** *15* (9), 6177-6181.
17. Qiu, J.; Zeng, G.; Pavaskar, P.; Li, Z.; Cronin, S. B., *Phys Chem Chem Phys* **2014,** *16* (7), 3115-3121.
18. Qiu, J.; Zeng, G.; Ha, M.-A.; Hou, B.; Mecklenburg, M.; Shi, H., . . . Cronin, S. B., *Chemistry of Materials* **2015,** *27* (23), 7977-7981.
19. Gu, J.; Yan, Y.; Young, J. L.; Steirer, K. X.; Neale, N. R.; Turner, J. A., *Nat Mater* **2015,** *advance online publication*.
20. Kaiser, B.; Fertig, D.; Ziegler, J.; Klett, J.; Hoch, S.; Jaegermann, W., *ChemPhysChem* **2012,** *13* (12), 3053-3060.
21. Hu, S.; Shaner, M. R.; Beardslee, J. A.; Lichterman, M.; Brunschwig, B. S.; Lewis, N. S., *Science* **2014,** *344* (6187), 1005-1009.
22. Zeng, G.; Qiu, J.; Li, Z.; Pavaskar, P.; Cronin, S. B., *ACS Catalysis* **2014,** *4* (10), 3512-3516.
23. McDowell, M. T.; Lichterman, M. F.; Carim, A. I.; Liu, R.; Hu, S.; Brunschwig, B. S.; Lewis, N. S., *ACS Applied Materials & Interfaces* **2015,** *7* (28), 15189-15199.
24. Shaner, M. R.; Hu, S.; Sun, K.; Lewis, N. S., *Energy & Environmental Science* **2015,** *8* (1), 203-207.
25. Shaner, M. R.; McKone, J. R.; Gray, H. B.; Lewis, N. S., *Energy & Environmental Science* **2015,** *8* (10), 2977-2984.
26. Zhou, X.; Liu, R.; Sun, K.; Friedrich, D.; McDowell, M. T.; Yang, F., . . . Lewis, N. S., *Energy & Environmental Science* **2015,** *8* (9), 2644-2649.
27. Fiore, J. L.; Fomenko, V. V.; Bodlaki, D.; Borguet, E., *Applied Physics Letters* **2011,** *98* (4), 041905.
28. Campen, R. K.; Pymer, A. K.; Nihonyanagi, S.; Borguet, E., *The Journal of Physical Chemistry C* **2010,** *114* (43), 18465-18473.

29. McClelland, A.; Fomenko, V.; Borguet, E., *The Journal of Physical Chemistry B* **2004,** *108* (12), 3789-3793.
30. Fomenko, V.; Borguet, E., *Physical Review B* **2003,** *68* (8), 081301.
31. Fomenko, V.; Lami, J.-F.; Borguet, E., *Physical Review B* **2001,** *63* (12), 121316.
32. Moss, B.; Hegner, F. S.; Corby, S.; Selim, S.; Francàs, L.; López, N., . . . Durrant, J. R., *ACS Energy Letters* **2019,** *4* (1), 337-342.
33. Kafizas, A.; Ma, Y.; Pastor, E.; Pendlebury, S. R.; Mesa, C.; Francàs, L., . . . Durrant, J. R., *ACS Catalysis* **2017,** *7* (7), 4896-4903.
34. Ma, Y.; Kafizas, A.; Pendlebury, S. R.; Le Formal, F.; Durrant, J. R., *Advanced Functional Materials* **2016,** *26* (27), 4951-4960.
35. Kafizas, A.; Wang, X.; Pendlebury, S. R.; Barnes, P.; Ling, M.; Sotelo-Vazquez, C., . . . Durrant, J. R., *The Journal of Physical Chemistry A* **2016,** *120* (5), 715-723.
36. Ma, Y.; Mesa, C. A.; Pastor, E.; Kafizas, A.; Francàs, L.; Le Formal, F., . . . Durrant, J. R., *ACS Energy Letters* **2016,** *1* (3), 618-623.
37. Ma, Y.; Le Formal, F.; Kafizas, A.; Pendlebury, S. R.; Durrant, J. R., *J. Mater. Chem. A* **2015,** *3* (41), 20649-20657.
38. Le Formal, F.; Pastor, E.; Tilley, S. D.; Mesa, C. A.; Pendlebury, S. R.; Grätzel, M.; Durrant, J. R., *Journal of the American Chemical Society* **2015,** *137* (20), 6629-6637.
39. Ma, Y.; Pendlebury, S. R.; Reynal, A.; Le Formal, F.; Durrant, J. R., *Chemical Science* **2014,** *5* (8), 2964-2973.
40. Le Formal, F.; Pendlebury, S. R.; Cornuz, M.; Tilley, S. D.; Grätzel, M.; Durrant, J. R., *Journal of the American Chemical Society* **2014,** *136* (6), 2564-2574.
41. Pendlebury, S. R.; Wang, X.; Le Formal, F.; Cornuz, M.; Kafizas, A.; Tilley, S. D., . . . Durrant, J. R., *Journal of the American Chemical Society* **2014,** *136* (28), 9854-9857.
42. Le Formal, F.; Pendlebury, S. R.; Cornuz, M.; Tilley, S. D.; Grätzel, M.; Durrant, J. R., *Journal of the American Chemical Society* **2014,** *136* (6), 2564-2574.
43. Chen, X.; Choing, S. N.; Aschaffenburg, D. J.; Pemmaraju, C. D.; Prendergast, D.; Cuk, T., *Journal of the American Chemical Society* **2017,** *139* (5), 1830-1841.
44. V Sheridan, M.; Hill, D.; D Sherman, B.; Wang, D.; L Marquard, S.; Wee, K.-R., . . . J Meyer, T., *Journal of the American Chemical Society* **2017,** *17*.
45. Jellison, G. E., *Optical Materials* **1992,** *1* (3), 151-160.
46. Lantz, J. M.; Corn, R. M., *The Journal of Physical Chemistry* **1994,** *98* (18), 4899-4905.
47. Lantz, J. M.; Corn, R. M., *The Journal of Physical Chemistry* **1994,** *98* (38), 9387-9390.
48. de L. Kronig, R., *J. Opt. Soc. Am.* **1926,** *12* (6), 547-557.
49. Hutchings, D. C.; Sheik-Bahae, M.; Hagan, D. J.; Van Stryland, E. W., *Optical and Quantum Electronics* **1992,** *24* (1), 1-30.
50. Shen, H.; Dutta, M., *Journal of Applied Physics* **1995,** *78* (4), 2151-2176.
51. Shen, H.; Pollak, F. H., *Physical Review B* **1990,** *42* (11), 7097.

4. Chapter 4. Time resolved Second Harmonic Generation for Probing Band Structure at Semiconductor/Liquid Interface

4.1 Introduction

Efficient water oxidation requires photoanode materials with suitable light absorption, charge separation, charge transport and catalytic properties. In recent years, coating photoactive photoelectrodes with a layer of water oxidation catalysts has received broader attention as a flexible, modular approach for fabricating efficient water oxidation photoanodes. This hybrid modular approach offers multiple advantages that greatly expand material and catalyst choices: 1) It allows independent tuning and optimization of both the light absorbing semiconductor and the catalytic components; 2) It can utilize both molecular and heterogeneous catalysts, including catalysts that are not photoactive; and 3) It can be applied to many semiconductor electrodes, including dye sensitized oxides, [1-10] catalytically active oxide materials (such as TiO_2, Fe_2O_3, WO_3, $BiVO_4$),[11-17] as well as oxide protected narrow band gap semiconductors (Si, GaP, GaAs, etc.).[5, 18-26]There have been many reports of enhanced photocurrent and reduced onset potential upon the application of catalytic layers to semiconductor electrodes, suggesting that indeed this is a promising and powerful approach for constructing water oxidation photoanodes. However, the mechanism of photocurrent enhancement remains poorly understood. This is especially true for catalytic active photoelectrodes, such as Fe_2O_3 and $BiVO_4$, that are coated with a layer of catalysts. These electrodes are particularly interesting because it offers the possibility to further enhance the activity of reasonably efficient and stable oxide electrodes.

The performances of photoelectrodes is often evaluated by photocurrent-applied bias curves, in which the effect of the catalyst layer is often characterized by the enhancement of

photocurrent amplitude and lowering of photocurrent onset potential.[1-10, 18-30] Recent studies have demonstrated that further mechanistic insight can be obtained by direct time resolved spectroscopic, especially transient absorption (TA), measurements of the photo-generated carriers and catalytic reactions.[6-7, 10, 31-49] For example, the effect of cobalt phosphate (CoPi), an efficient water oxidation catalyst,[50] on n-type semiconductors, such as α-Fe_2O_3[31, 51] and $BiVO_4$,[41, 52-53] has been examined in recent years. Hamann and co-workers reported that the enhanced performance of CoPi coated hematite primarily results from hole transfer from hematite to CoPi. [51] Collection and storage of photogenerated holes in CoPi suppresses charge recombination and increases the photocurrent. These findings were also supported by the impedance spectrum of CoPi modified $BiVO_4$, which shows increased interfacial capacitance and reduced charge transfer resistance upon the addition of CoPi. Moreover, Gamelin and coworkers[52] reported that CoPi modified W:$BiVO_4$ can eliminate surface electron hole recombination and attributed this enhancement to the efficient transfer of holes from $BiVO_4$ to CoPi. These results imply that CoPi functions as catalysts to enhance water oxidation current. However, in a combined spectroelectrochemical and transient photocurrent measurement study of CoPi modified $BiVO_4$ photoanodes, Durrant and co-workers[41, 54] argued that $BiVO_4$ surface remains the predominant water oxidation site while the enhancement of photoanode performance is mainly caused by the decrease of surface state induced Fermi level pinning and the resulting retardation of back electron-hole recombination. Thus, until today, it remains unclear whether CoPi functions mainly as a water oxidation catalyst to speed up the reaction or enhances the oxide photoanode performance by retarding of electron-hole recombination.

The above examples illustrate both the power and technical challenges of mechanistic investigation of hybrid semiconductor/catalyst dyadic photoanodes by combined transient

absorption and electrochemical characterizations. The technical challenges are associated with sensitivity and selectivity limitations of TA spectroscopy, which, currently, is one of the most widely used techniques for time-resolved studies of photocatalytic processes. This technique probes the total and average sample response within pump/probe overlap region, covering both the bulk electrode and surface/catalyst responses. Although surface/catalyst responses are the key to understanding the catalytic reaction mechanism, they are often much smaller than the bulk signal, hindering their reliable detection. This issue can be resolved using high surface area electrodes, such as catalyst functionalized dye-sensitized nanoporous TiO_2, but it remains an unresolved challenge for many other electrodes. Furthermore, the catalytically active photogenerated holes at the surface (for the n-semiconductor/liquid junction) often have broad and weak absorption features,[41, 54] which makes their unambiguous assignment challenging. Their small extinction coefficient also hinders their detection by conventional time-resolved spectroscopy. For example, the extinction coefficient of holes in $BiVO_4$ has been estimated to be 420 $M^{-1}cm^{-1}$.[41, 54] Assuming the holes are accumulated in ~100 nm space charge layer region, it requires a hole concentration of $1.4x10^{19}$ cm^{-3} to generate an absorbance of 0.1 mOD. At this hole density, which is close to the dopant density in these materials, a significant band flattening has occurred to speed up electron-hole recombination and the observation of such small signal requires a very sensitive transient absorption spectrometer.

In this section, we propose to address the above-mentioned limitations of TA spectroscopy by developing and applying new and complementary *in situ* spectroscopy tools to probe the catalytic photoanodes. Namely, we developed transient second harmonic generation spectroscopic methods to directly probe the catalyst/electrode interface. The latter has much improved sensitivity compared to transient absorption and is general to all materials, making it a very powerful new

tool. Finally, the structural heterogeneity and complexity of many heterogeneous catalysts, such as CoPi, presents a difficult challenge for identifying and assigning spectral features to catalytic intermediates.

Understanding the mechanism of water splitting catalyst remains an intriguing problem. Over the years many studies have been trying to monitor the charge carrier dynamics with time resolved spectroscopy to answer this question.[3, 36, 38, 55-57] However, our recent study in Chapter 3 on water reduction electrode p-type gallium phosphide and water oxidation electrode n-type bismuth vanadate, along with other studies, revealed that the typical transient absorption techniques disturbed the band bending to the extent of nearly generating a flat-band due to the excess amount of carrier transiently generated.[36, 38] Under such conditions, the carrier dynamics are dominated by recombination, which deemed this measurement's results far from the continuous illumination condition. Moreover, the typical transient spectroscopy also encounters a signal-to-noise issue at a millisecond-second time scale and above when the catalytic reaction occurs, due to the small extinction coefficients that most charge carriers have.[38, 58] Therefore, this type technique that relies on very short pulsed excitation is hardly applicable to single junction water splitting semiconductors and catalysts.

The ideal technique for catalyst and semiconductor carrier dynamics studies is one that does not perturb the band bending and could be combined with *in situ* photoelectrochemical measurements. Second harmonic generation (SHG) proves to be exactly the such a method that directly probes interfacial electrical field at the semiconductor-catalyst-electrolyte interface without perturbing the band structure.[59-70] This electrical field carries detailed information on the band bending at the interface, which then provides in depth understanding of the photogenerated

carriers. Here we propose that time resolved SHG is suitable and powerful for studying the photophysics of water oxidation semiconductors and catalyst systems.

4.2 Results and Discussion

4.2.1 In situ EFISH

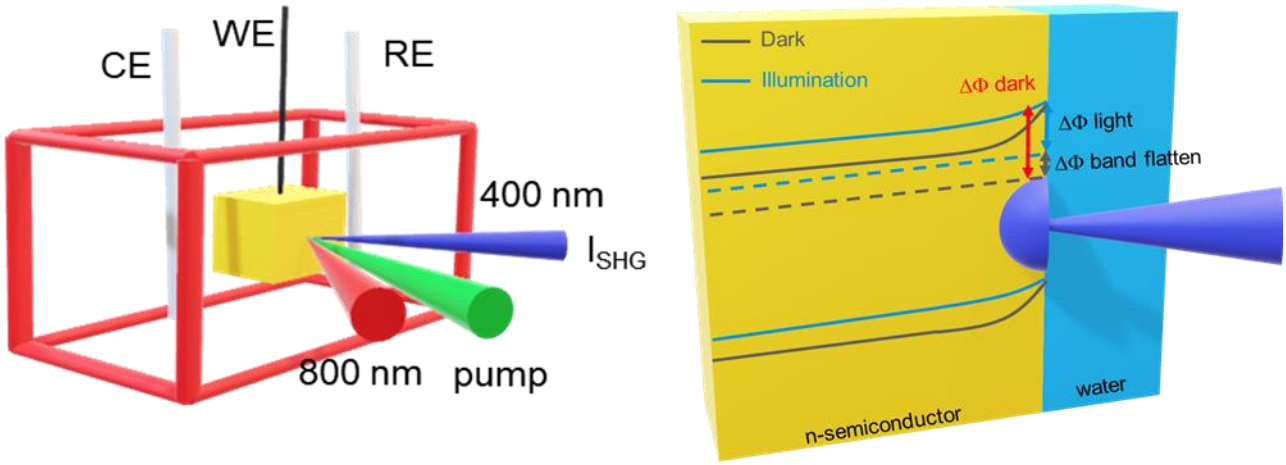

Figure 4.1 Cartoon of SHG measurement on a semiconductor electrode *in situ* revealing the interfacial electrical field at the semiconductor-catalyst-electrolyte interface

Although the transient reflection spectroscopy technique described above provides a way to measure charge transfer across a p-n junction through the Franz-Keldysh Oscillation (FKO) effect, this effect is most pronounced for direct gap transitions (Figure 3.5). Therefore, it is desirable to develop an alternative *in situ* technique that is applicable to all materials. Electrical field induced second harmonic response (EFISH) from the semiconductor electrolyte interface (SEI) has been shown to be directly proportional to the electric field strength at the space charge layer region (Figure 3.9).[59-70] In brief, at the n-semiconductor/electrolyte junction, the Fermi level equilibration between the n-semiconductor and redox species in electrolyte is achieved by electron moving across the SEI. This results in excess positive charge at the semiconductor space charge layer and net negative charge on the electrolyte, which induces an electrical field and the bending

of the semiconductor valence and conduction bands, as shown in Figure 4.1. The total SHG at the semiconductor/liquid junction is given by[71-72]

$$I(2\omega) \propto \left|\chi_{\text{eff}}^{(2)}\right|^2 I(\omega)^2 = \left|\chi_{\text{sur}}^{(2)} + \chi_{\text{solid}}^{(3)}\text{F}_{sc} + \chi_{\text{liquid}}^{(2)}\right|^2 I(\omega)^2. \quad \text{Eq. 4.1}$$

Here $I(\omega)$and $I(2\omega)$ are the intensities of the fundamental and second harmonic signals, respectively. The second harmonic response contains three contributions: the second order response of the solid surface ($\chi_{\text{sur}}^{(2)}$) and interfacial liquid ($\chi_{\text{liquid}}^{(2)}$), and the bulk solid response at the semiconductor space charge layer region($\chi_{\text{solid}}^{(3)}\text{F}_{sc}$) induced by the presence of a DC field (F_{sc}). The latter is the electric field induced second harmonic response (EFISH). It should be noted the liquid contribution may also contain electric field induced response in the double layer, but it is often much weaker and does not change with the applied bias. We have also assumed that bulk solid has negligible second order response in the absence of the band bending. This equation shows that when the EFISH term dominates the overall response, the second harmonic signal should be quadratic with respect to the band bending ($\text{F}_{sc} \propto \Delta\Phi = \text{E}_f - \text{E}_{fb}$), with a minimum at the flat-band potential ($\text{E}_f = \text{E}_{fb}$). The simplified equation based on this discussion is:

$$I(2\omega) \propto \left|\chi_{\text{eff}}^2 e^{i\theta} + \chi_{\text{eff}}^3 \Delta\Phi\right|^2 \propto \left|\chi_{\text{eff}}^2 e^{i\theta} + \chi_{\text{eff}}^3(\text{E} - E_{fb})\right|^2. \quad \text{Eq 4.2}$$

In this simplified equation describing SHG intensity, χ^2 is the effective second order susceptibility, χ^3 is the third order susceptibility and θ is the phase difference between them. The $\Delta\Phi$ term describes the potential drop across the SHG probed region, which is determined by the penetration depth of detection wavelength. $\Delta\Phi$ is proportional to the amount of band bending, which is equal to difference between the applied bias and the flat band potential. Here, although

different semiconductor materials have a different χ^2 intrinsic response, the dependence of the SHG response on band bending is universal. This greatly enhances the capability of studying materials with different morphology and optical properties, makes SHG more advantageous for the water oxidation semiconductor study.

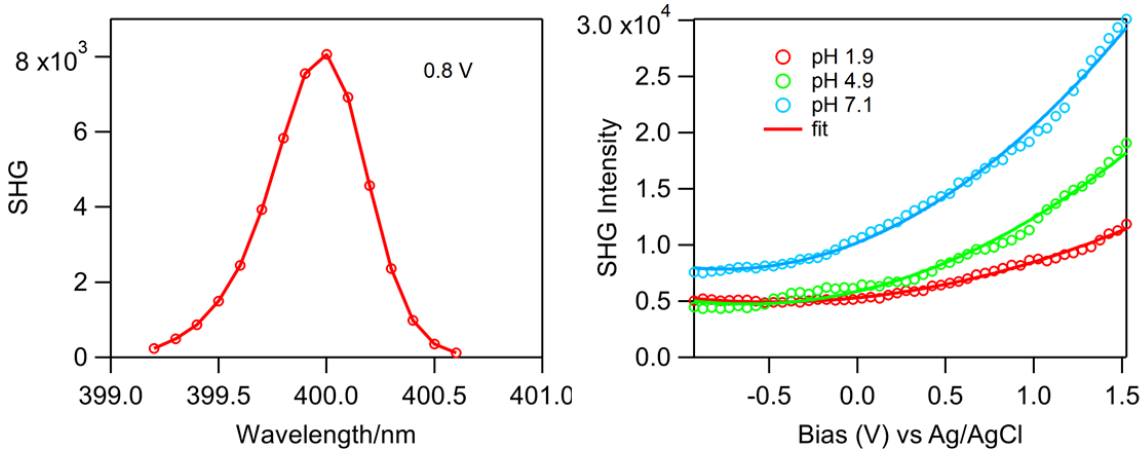

Figure 4.2 Left: SHG response from a Nb doped n-TiO_2. Right: SHG response from -1 to 1.5 V potential at various pH, the solid lines are fitted according to eq 4.2

Figure 4.2 shows is the SHG response at the n-doped TiO_2/water interface as a function of applied bias at three different pHs. These potential dependences can be well fit by the quadratic relationship shown in eq. 4.1, indicating the dominance of the EFISH response at this interface. The fit also reveals that the flat band potential (minimum point) changes with pH, occurring at more negative values at higher pH, consistent with the expected pH dependent shift of flat band potential that was observed in previous SHG measurements of similar TiO_2 crystals.[59-60, 62]

The quadratic dependence on the applied potential on TiO_2 semiconductors can be easily explained by Eq 4.1 and Eq 4.2 and our observation supports this theory. However, one must consider the fundamental and doubled SHG light wavelength, as this will change the probe depth and in return, change the quadratic dependence. In this study, both the fundamental light at 800 nm and the doubled SHG response at 400 nm are both below the band gap of the TiO_2

semiconductor. Therefore, when detecting the SHG response, the whole depletion layer is probed as the 400 nm is able to penetrate the whole semiconductor. However, when the SHG response wavelength is above the band gap, due to the high optical density at that wavelength, the SHG response will have a very shallow penetration depth as discussed in Chapter 3. In extreme conditions, this penetration depth will result in only probing the interface of the semiconductor/liquid. Here, the band bending at the interface becomes:

$$q_{SC} = \left(2\varepsilon\varepsilon_0 e N_d\right)^{1/2} \Delta V_{SC}^{1/2} \qquad \text{Eq. 4.3}$$

where q_{sc} is the charge carrier in the space charge layer, N_d is the dopant concentration, ΔVsc is the band bending, which is the difference between the applied potential minus the flat band potential, and ε is the dielectric constant of the sample perpendicular to the sample surface. The electrical field strength at that interface is directly proportional to the accumulated charge based on Gauss's law. Therefore,

$$I(2\omega) \propto (E|_{x=0})^2 \propto q_{SC}^2 \propto \Delta V_{SC}\,.$$

Like the quadratic relationship, the lowest SHG response is achieved at the flat band potential. However, this yields a linear relationship between SHG response and the applied potential as reported. [59-60, 62] The above section shows that quadratic or linear SHG intensity dependence on the applied potential is based on the penetration depth of the SHG response. Different penetration depth determines the probing of the whole depletion layer's electrical field strength or the surface electrical field strength.

4.2.2 Photoinduced EFISH spectroscopy

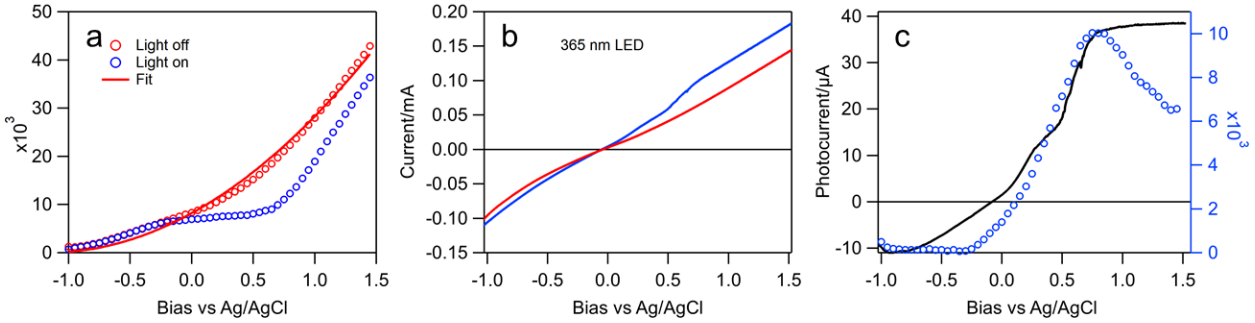

Figure 4.3 Nb-TiO_2 electrode SHG response under illumination. (a) SHG response from -1 to 1.5 V with and without 14 mW (power density=1 mW/cm^2) 365 nm CW LED illumination. (b) Current measured in situ simultaneously with panel (a). (c) Comparison of photocurrent and ΔSHG.

Typically, the fundamental light used in SHG measurements is below the bandgap of studied material to avoid photo-generating charge carriers that disrupt the band bending. Here, for TiO_2, neither the fundamental 800 nm nor the 400 nm is above the band gap, thus making the SHG a reliable *in situ* measurement of band bending under CW illumination. A CW illumination source of 365 nm was added to photoexcite the TiO_2. The photogenerated electron and hole, will move across the SEI at opposite directions due to the band bending. However, for n-type semiconductors the electron sweeping to an external circuit is much faster than that of hole, the electron are swept on a microsecond time scale determined by the RC constant of the equivalent circuit. Holes are accumulated at the SEI because of the slower rate constant of water oxidation at seconds time scale.[3, 38] The accumulated hole's concentration eventually reaches an equilibrium where the generation and depletion is at the same rate. This concentration of holes will inevitably flatten the band bending due to more carriers accumulated, and this so-called band flattening effect could be precisely detected by the SHG response as shown in Figure 4.3. The SHG intensity decreased when the CW light is on indicating the flattening of the band bending. The *in situ* photocurrent

was measured and shown in Figure 4.3b. The comparison of photocurrent and ΔSHG (Figure 4.3c) deepened our understanding of the equilibrium state under illumination. In panel (c), the photocurrent showed positive dependence over applied bias and reached a plateau at ~0.8V. This is well understood due to the charge separation efficiency reaching a maximum at this band bending.[73] However, it is essential to understand what the photocurrent is measuring. Effectively, the photocurrent measures the number of electrons that migrate to the external circuit per unit time. On the other side, SHG measures the accumulated hole concentration. Therefore, combining both the photocurrent and SHG measurements provides information on both photogenerated electrons and holes. We can see that in Figure 4.3c the photocurrent and ΔSHG trace each other from around -1 to 0.8 V. This can be understood as, under illumination with the increased bias, the separation efficiency increased. In this bias range, the electron and hole concentration increased similarly, yielding overlapping photocurrent and ΔSHG. However, the photocurrent starts to plateau above 0.8V, indicating maximum separation efficiency has been reached, while ΔSHG is starting to decrease. This indicates the hole concentration at this specific equilibrium is decreasing. Given that the hole generation is already at maximum and the only depletion pathway is water oxidation reaction, we speculate that the band edge is no longer pinned under this bias region and the band edge is more oxidizing,[74] resulting in a faster water oxidation rate.

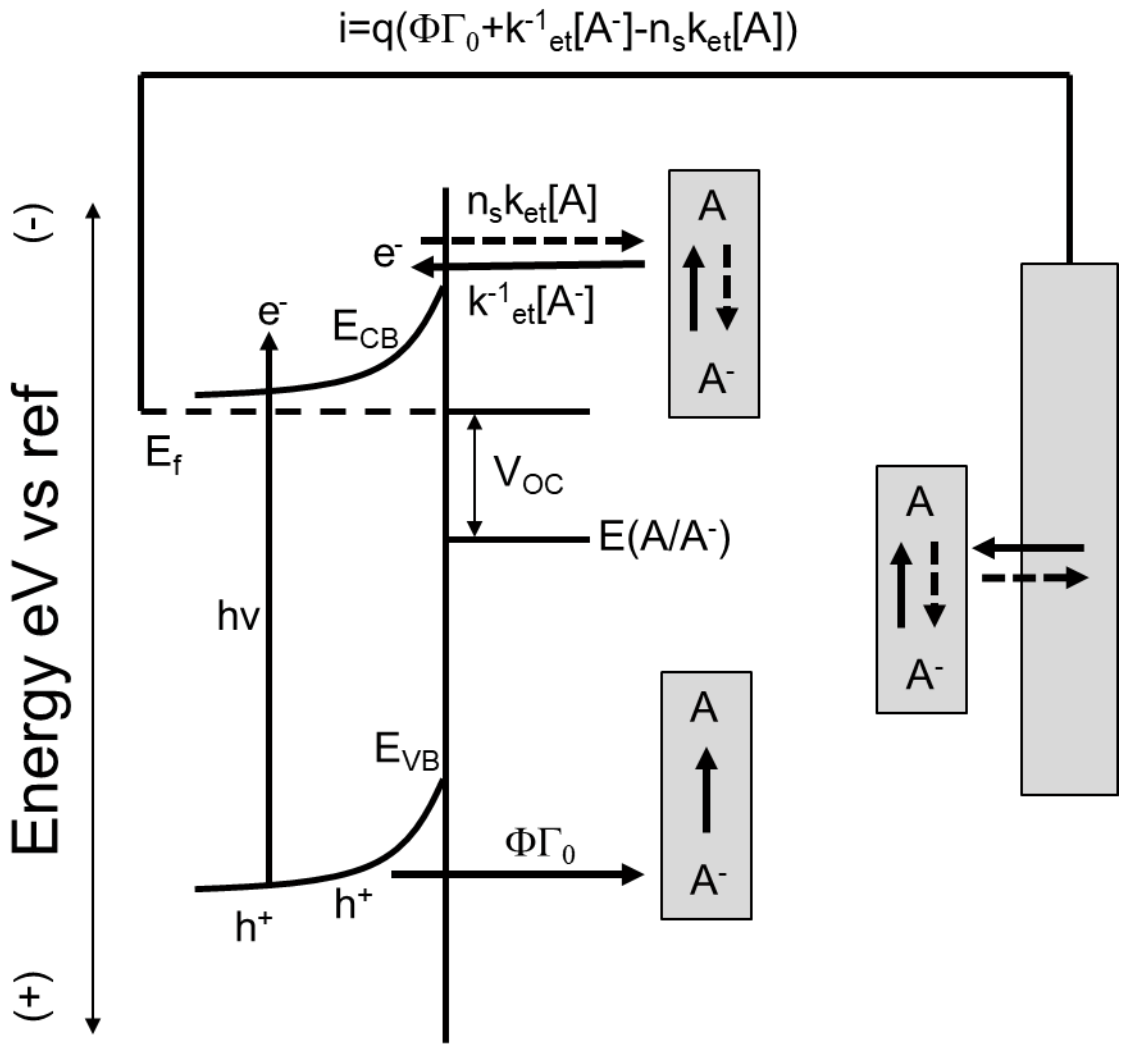

Figure 4.4 n-type semiconductor under photoelectrochemical condition. Reproduced with permission from Kumar, Amit, Patrick G. Santangelo, and Nathan S. Lewis. *The Journal of Physical Chemistry* 96.2 (1992): 834-842. Copyright 1992 American Chemical Society.

Before moving on to the discussion of how SHG effectively probes the band structure, it is important to quantitively describe a photoelectrochemical semiconductor band structure under illumination. As introduced in Chapter 1, the band structure and current at the semiconductor conduction and valence bands is shown in Figure 4.4. Here, we only review the related parameters for band structure under illumination.

In Figure 4.4, the $\Phi\Gamma_0$ represents the hole flux with Φ represents photon flux and Γ_0 represents the hole extraction quantum yield. Under open circuit potential, the total current is 0.

$$i = q\left(\Phi\Gamma_0 + k_{et}^{-1}\left[A^-\right] - n_s k_{et}[A]\right) = 0 \text{ , that is}$$

$$\Phi\Gamma_0 = k_{et}[A]\left(n_s - n_{so}\right)$$

Both the n_s and n_{so} can be related to the semiconductor dopant level and built in voltage:

$$n_{so} = n_b \exp\{-q(V_{bi})/kT\} \quad \text{and}$$

$$n_{so} = n_b \exp\{-q(V_{bi} - V_{OC})/kT\}.$$

Therefore, the open circuit voltage is calculated to be

$$V_{OC} = (kT/q)\ln\{\Phi\Gamma_0 / n_{so}k_{et}[A]\}.$$

It is clear that the open circuit voltage has a logarithmic dependence on the illumination intensity. At the same time, in a quasi-steady state under a certain applied bias, the current is non-zero. Although the open circuit condition is no longer satisfied, the current is still a constant. Therefore, the band bending's ("unbending" in this context) logarithmic dependence on the illumination light intensity still holds.

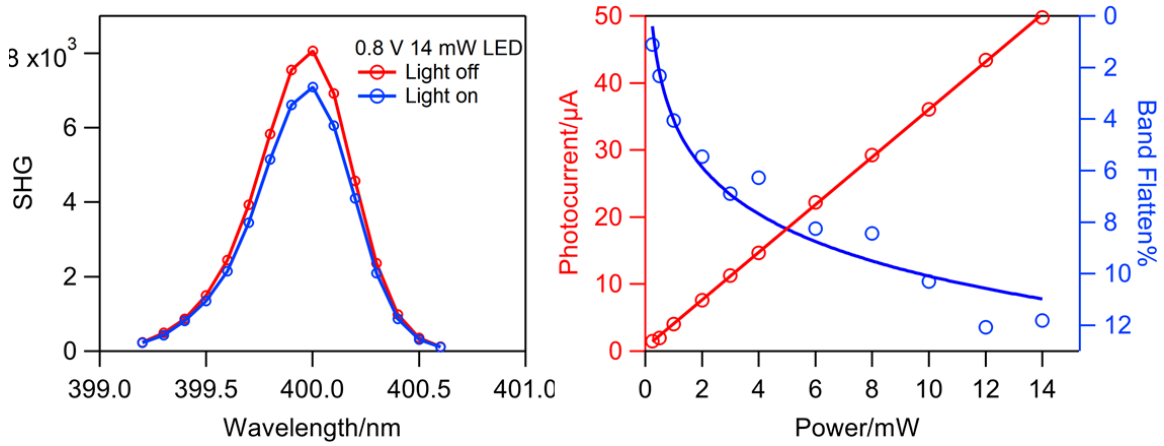

Figure 4.5 Left: SHG light on/off comparison under 14 mW illumination. Right: Photocurrent and band flattening effect as a function of illumination power.

We also evaluate the band flattening effect by varying the illumination power. As shown in Figure 4.5, the band flattening effect can be quantified by comparing the ratio between light on and light off.[59, 61] Under a certain bias the separation efficiency is generally considered a constant, which can be proved by the photocurrent's linear dependence on illumination power. Therefore, the band flattening ratio showed a logarithmic dependence on illumination power.[75]

4.2.3 Time resolved EFISH probing carrier dynamics

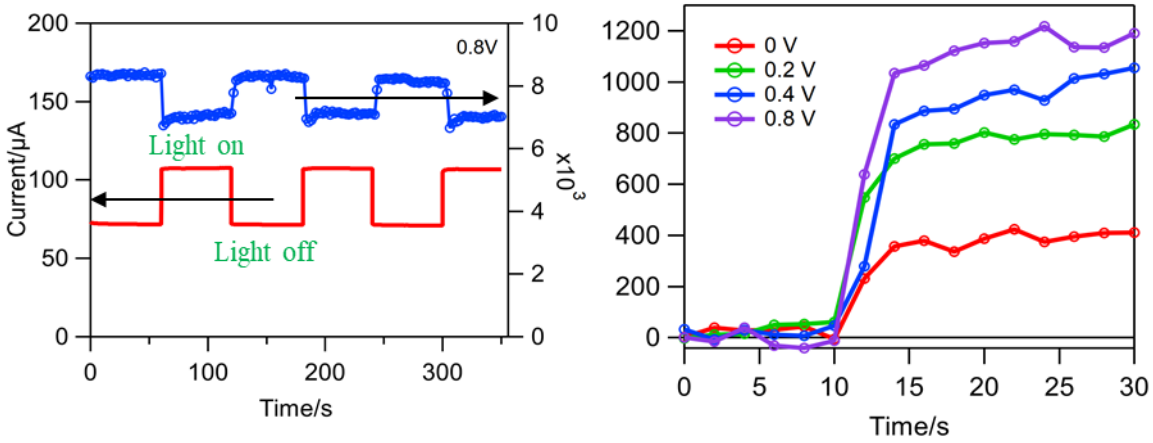

Figure 4.6 Left: SHG signal (blue) and current (red) when illumination is modulated. Right: The recovery of SHG after subtracting the baseline response at various applied biases.

It should be noted that although band bending and flat band position can be measured by electrochemical techniques, EFISH is inherently a time resolved technique (because of the use of short laser pulses) and can be used to measure the time evolution of the response of the semiconductor/liquid junction from optical illumination on the sub-picosecond and longer timescale with the introduction of a pulsed excitation, similar to transient absorption (or pump/probe) spectroscopy. To verify our speculation, we introduced a modulation to the illumination source. One can measure the chemical reaction rate by observing the SHG signal recovery kinetics. When the illumination was turned off, the SHG signal recovered to a higher level, which is due to the depletion of photo generated carrier and thus, the restoring of band bending. In n-type semiconductors the accumulated holes are depleted mainly due to the water oxidation reaction, as the electrons needed for recombination are swept away earlier.[56] Therefore, the recovery kinetics are a direct measurement on the water oxidation kinetics. As shown in Figure 4.6, the SHG and photocurrent showed matching modulations and the ΔSHG kinetics showed increasing recovering rate with increased applied bias.

4.2.4 Effect of catalyst on water oxidation

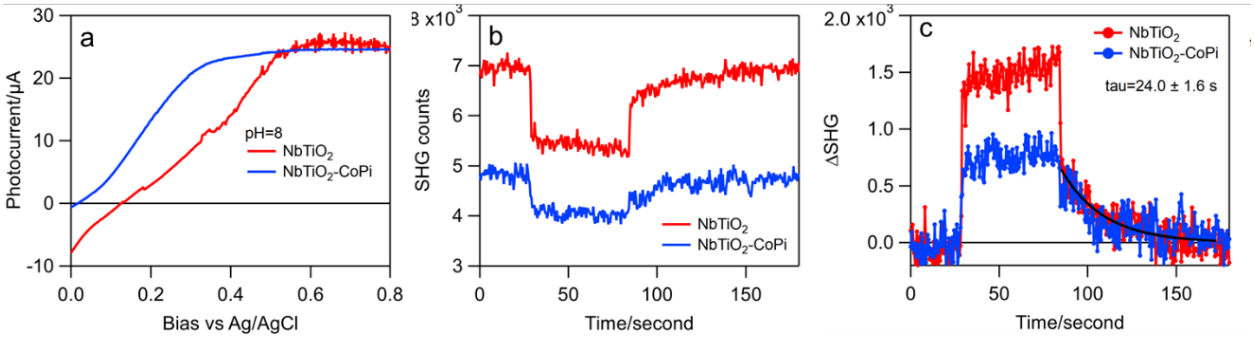

Figure 4.7 (a) Photocurrent with and without CoPi, (b) SHG response with illumination power off-on-off modulation at 0.7 V bias, (c) SHG recovery kinetics on second time scale after subtraction of panel (b).

We have demonstrated the capability of time resolved SHG on a Nb doped TiO_2 single crystals. We then grafted a well known water oxidation catalyst, cobalt phosphate (CoPi), to show that the SHG is suitable and capable of studying the catalytic activity enhancement.[3] Our preliminary results, shown in Figure 4.7a, indicate the CoPi catalyst decreased the onset potential by ~0.17V and enhanced the water oxidation photocurrent from 0 to 0.5 V. In the meantime, the SHG recovery kinetics showed significant difference. The pure TiO_2 showed a fast recovery around 0.5 seconds time constant, then a slower recovery as shown in Figure 4.7c, whereas the CoPi coated TiO_2 only showed the slower time constant. This indicates the accumulated holes in pure TiO_2 decays first by the bulk recombination, whereas the holes in CoPi-TiO_2 are effectively separated and protected against bulk recombination. The slower kinetics with the time constant of ~20 s indicates the water oxidation process. Here, we could hypothesize the mechanism of the CoPi enhancement is to prevent the hole recombination while the water oxidation reaction rate was not enhanced. This fits well with the photocurrent measurement, where the onset is decreased, and the maximum photocurrent does not increase.

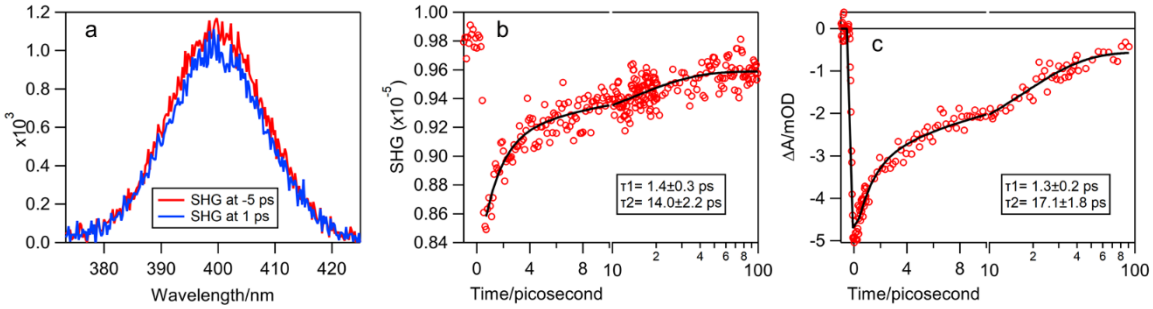

Figure 4.8 (a) time resolved SHG on monolayer MoS_2 with 150 fs 800 nm fundamental and 600 nm excitation light at -5 ps and 1 ps, (b) time resolved SHG and (c) transient absorption kinetics showed similar rate constant.

The time resolved SHG measurement could also be used to directly look at charge separation kinetics, as well as at very early delay times.[76-79] This technique depends little on the interpretation between the transient spectrum signal and the charge separation state, which usually poses complication in transient spectroscopy techniques. Figure 4.8 we show a 150-femtosecond time resolved SHG response from a 2D monolayer MoS_2 on SiO_2, which yields an almost identical time constant as the transient absorption measurement. However, the transient kinetics in panel (c) relied on an excitonic peak, whereas the SHG response is almost universal.

4.3 Conclusion

In conclusion, time resolved SHG in a typical pump-probe setup provides direct observation over charge separation kinetics where interpretation is greatly simplified. We propose to further develop this technique for application on water oxidation systems where we could extract the charge separation rate constant. This completes the charge carrier dynamics from generation to chemical reaction. Such studies are highly valuable in understanding the mechanism and yet no other technique offers similar feasibility in application to multiple systems. Therefore, we consider this technique to be promising as a solution to answering many intriguing questions.

4.4 Reference

1. Alibabaei, L.; D Sherman, B.; Norris, M.; Brennaman, M.; J Meyer, T., *Proceedings of the National Academy of Sciences of the United States of America* **2015,** *112*.
2. D. Sherman, B.; V. Sheridan, M.; Wee, K.-R.; L. Marquard, S.; Wang, D.; Alibabaei, L., . . . J. Meyer, T., *Journal of the American Chemical Society* **2016,** *138*.
3. Farnum, B.; Wee, K.-R.; J. Meyer, T., *Nature Chemistry* **2016,** *8*.
4. D Brady, M.; Neiva Sampaio, R.; Wang, D.; J. Meyer, T.; J. Meyer, G., *Journal of the American Chemical Society* **2017,** *139*.

5. V Sheridan, M.; Hill, D.; D Sherman, B.; Wang, D.; L Marquard, S.; Wee, K.-R., . . . J Meyer, T., *Journal of the American Chemical Society* **2017,** *17*.
6. Eberhart, M.; M. Rader Bowers, L.; Shan, B.; Troian-Gautier, L.; Brennaman, M.; M. Papanikolas, J.; J. Meyer, T., *Journal of the American Chemical Society* **2018,** *140*.
7. Vincent Sheridan, M.; Wang, Y.; Wang, D.; Troian-Gautier, L.; J Dares, C.; D Sherman, B.; J Meyer, T., *Angewandte Chemie International Edition* **2018,** *57*.
8. Eberhart, M.; Wang, D.; Neiva Sampaio, R.; L. Marquard, S.; Shan, B.; Brennaman, M., . . . J. Meyer, T., *Journal of the American Chemical Society* **2017,** *139*.
9. Wang, D.; L Marquard, S.; Troian-Gautier, L.; V. Sheridan, M.; D. Sherman, B.; Wang, Y., . . . J. Meyer, T., *Journal of the American Chemical Society* **2017,** *140*.
10. Wang, D.; Eberhart, M.; V. Sheridan, M.; Hu, K.; D. Sherman, B.; Nayak, A., . . . J. Meyer, T., *Proceedings of the National Academy of Sciences* **2018,** *115*, 201802903.
11. Lin, Y.; Yuan, G.; Sheehan, S.; Zhou, S.; Wang, D., *Energy & Environmental Science* **2011,** *4* (12), 4862-4869.
12. Kim, T. W.; Choi, K.-S., *Science* **2014,** *343* (6174), 990-994.
13. Wang, G.; Wang, H.; Ling, Y.; Tang, Y.; Yang, X.; Fitzmorris, R. C., . . . Li, Y., *Nano Letters* **2011,** *11* (7), 3026-3033.
14. Park, J. H.; Kim, S.; Bard, A. J., *Nano Letters* **2006,** *6* (1), 24-28.
15. Cristino, V.; Caramori, S.; Argazzi, R.; Meda, L.; Marra, G. L.; Bignozzi, C. A., *Langmuir* **2011,** *27* (11), 7276-7284.
16. Su, J.; Guo, L.; Bao, N.; Grimes, C. A., *Nano Letters* **2011,** *11* (5), 1928-1933.
17. Sivula, K.; Formal, F. L.; Grätzel, M., *Chemistry of Materials* **2009,** *21* (13), 2862-2867.
18. Gu, J.; Yan, Y.; Young, J. L.; Steirer, K. X.; Neale, N. R.; Turner, J. A., *Nat Mater* **2015,** *advance online publication*.
19. Lin, Y.; Kapadia, R.; Yang, J.; Zheng, M.; Chen, K.; Hettick, M., . . . Ager, J. W., *The Journal of Physical Chemistry C* **2015,** *119* (5), 2308-2313.
20. McDowell, M. T.; Lichterman, M. F.; Carim, A. I.; Liu, R.; Hu, S.; Brunschwig, B. S.; Lewis, N. S., *ACS Applied Materials & Interfaces* **2015,** *7* (28), 15189-15199.
21. Qiu, J.; Zeng, G.; Ha, M.-A.; Ge, M.; Lin, Y.; Hettick, M., . . . Cronin, S. B., *Nano Letters* **2015,** *15* (9), 6177-6181.
22. Qiu, J.; Zeng, G.; Ha, M.-A.; Hou, B.; Mecklenburg, M.; Shi, H., . . . Cronin, S. B., *Chemistry of Materials* **2015,** *27* (23), 7977-7981.
23. Shaner, M. R.; Hu, S.; Sun, K.; Lewis, N. S., *Energy & Environmental Science* **2015,** *8* (1), 203-207.
24. Hu, S.; Shaner, M. R.; Beardslee, J. A.; Lichterman, M.; Brunschwig, B. S.; Lewis, N. S., *Science* **2014,** *344* (6187), 1005-1009.
25. Qiu, J.; Zeng, G.; Pavaskar, P.; Li, Z.; Cronin, S. B., *Phys Chem Chem Phys* **2014,** *16* (7), 3115-3121.
26. Zeng, G.; Qiu, J.; Li, Z.; Pavaskar, P.; Cronin, S. B., *ACS Catalysis* **2014,** *4* (10), 3512-3516.
27. Kaiser, B.; Fertig, D.; Ziegler, J.; Klett, J.; Hoch, S.; Jaegermann, W., *ChemPhysChem* **2012,** *13* (12), 3053-3060.
28. Lee, M. H.; Takei, K.; Zhang, J.; Kapadia, R.; Zheng, M.; Chen, Y. Z., . . . Ager, J. W., *Angewandte Chemie International Edition* **2012,** *51* (43), 10760-10764.
29. Shaner, M. R.; McKone, J. R.; Gray, H. B.; Lewis, N. S., *Energy & Environmental Science* **2015,** *8* (10), 2977-2984.

30. Zhou, X.; Liu, R.; Sun, K.; Friedrich, D.; McDowell, M. T.; Yang, F., . . . Lewis, N. S., *Energy & Environmental Science* **2015,** *8* (9), 2644-2649.
31. Barroso, M.; Cowan, A. J.; Pendlebury, S. R.; Grätzel, M.; Klug, D. R.; Durrant, J. R., *Journal of the American Chemical Society* **2011,** *133* (38), 14868-14871.
32. Pendlebury, S. R.; Barroso, M.; Cowan, A. J.; Sivula, K.; Tang, J.; Grätzel, M., . . . Durrant, J., *Chem. Commun.* **2011,** *47* (2), 716-718.
33. Barroso, M.; Mesa, C. A.; Pendlebury, S. R.; Cowan, A. J.; Hisatomi, T.; Sivula, K., . . . Durrant, J. R., *Proceedings of the National Academy of Sciences* **2012,** *109* (39), 15640-15645.
34. Huang, Z.; Lin, Y.; Xiang, X.; Rodríguez-Córdoba, W.; McDonald, K. J.; Hagen, K. S., . . . Lian, T., *Energy & Environmental Science* **2012,** *5* (10), 8923-8926.
35. Pendlebury, S. R.; Cowan, A. J.; Barroso, M.; Sivula, K.; Ye, J.; Grätzel, M., . . . Durrant, J. R., *Energy & Environmental Science* **2012,** *5* (4), 6304-6312.
36. Le Formal, F.; Pendlebury, S. R.; Cornuz, M.; Tilley, S. D.; Grätzel, M.; Durrant, J. R., *Journal of the American Chemical Society* **2014,** *136* (6), 2564-2574.
37. Feckl, J. M.; Dunn, H. K.; Zehetmaier, P. M.; Müller, A.; Pendlebury, S. R.; Zeller, P., . . . Bein, T., *Advanced Materials Interfaces* **2015,** *2* (18), 1500358.
38. Le Formal, F.; Pastor, E.; Tilley, S. D.; Mesa, C. A.; Pendlebury, S. R.; Grätzel, M.; Durrant, J. R., *Journal of the American Chemical Society* **2015,** *137* (20), 6629-6637.
39. Wu, X.; Park, H.; Zhu, X.-Y., *The Journal of Physical Chemistry C* **2014,** *118* (20), 10670-10676.
40. Ravensbergen, J.; Abdi, F. F.; van Santen, J. H.; Frese, R. N.; Dam, B.; van de Krol, R.; Kennis, J. T. M., *J. Phys. Chem. C* **2014,** *118* (48), 27793-27800.
41. Ma, Y.; Le Formal, F.; Kafizas, A.; Pendlebury, S. R.; Durrant, J. R., *J. Mater. Chem. A* **2015,** *3* (41), 20649-20657.
42. Ma, Y.; Mesa, C. A.; Pastor, E.; Kafizas, A.; Francàs, L.; Le Formal, F., . . . Durrant, J. R., *ACS Energy Letters* **2016,** *1* (3), 618-623.
43. Hess, L. H.; Cooper, J. K.; Loiudice, A.; Jiang, C.-M.; Buonsanti, R.; Sharp, I. D., *Nano Energy* **2017,** *34*, 375-384.
44. Cooper, J. K.; Reyes-Lillo, S. E.; Hess, L. H.; Jiang, C.-M.; Neaton, J. B.; Sharp, I. D., *J. Phys. Chem. C* **2018,** *122* (36), 20642-20652.
45. Moss, B.; Hegner, F. S.; Corby, S.; Selim, S.; Francàs, L.; López, N., . . . Durrant, J. R., *ACS Energy Letters* **2019,** *4* (1), 337-342.
46. Selim, S.; Francàs, L.; García-Tecedor, M.; Corby, S.; Blackman, C.; Gimenez, S., . . . Kafizas, A., *Chemical Science* **2019,** *10* (9), 2643-2652.
47. Pesci, F. M.; Cowan, A. J.; Alexander, B. D.; Durrant, J. R.; Klug, D. R., *The Journal of Physical Chemistry Letters* **2011,** *2* (15), 1900-1903.
48. Herlihy, D. M.; Waegele, M. M.; Chen, X. H.; Pemmaraju, C. D.; Prendergast, D.; Cuk, T., *Nature Chemistry* **2016,** *8* (6), 556-556.
49. Herlihy, D. M.; Waegele, M. M.; Chen, X. H.; Pemmaraju, C. D.; Prendergast, D.; Cuk, T., *Nature Chemistry* **2016,** *8* (6), 549-555.
50. Kanan, M. W.; Nocera, D. G., *Science* **2008,** *321* (5892), 1072-1075.
51. Klahr, B.; Gimenez, S.; Fabregat-Santiago, F.; Bisquert, J.; Hamann, T. W., *J. Am. Chem. Soc.* **2012,** *134* (40), 16693-16700.
52. Zhong, D. K.; Choi, S.; Gamelin, D. R., *J. Am. Chem. Soc.* **2011,** *133* (45), 18370-18377.
53. Huang, Z. Y.; Simpson, D. E.; Mahboub, M.; Li, X.; Tang, M. L., *Chemical Science* **2016,** *7* (7), 4101-4104.

54. Ma, Y.; Kafizas, A.; Pendlebury, S. R.; Le Formal, F.; Durrant, J. R., *Adv. Funct. Mater.* **2016,** *26* (27), 4951-4960.
55. Ma, Y.; Pendlebury, S. R.; Reynal, A.; Le Formal, F.; Durrant, J. R., *Chemical Science* **2014,** *5* (8), 2964-2973.
56. Pendlebury, S. R.; Wang, X.; Le Formal, F.; Cornuz, M.; Kafizas, A.; Tilley, S. D., . . . Durrant, J. R., *Journal of the American Chemical Society* **2014,** *136* (28), 9854-9857.
57. Barroso, M.; Pendlebury, S. R.; Cowan, A. J.; Durrant, J. R., *Chemical Science* **2013,** *4* (7), 2724-2734.
58. Klahr, B.; Gimenez, S.; Fabregat-Santiago, F.; Bisquert, J.; Hamann, T. W., *Journal of the American Chemical Society* **2012,** *134* (40), 16693-16700.
59. Lantz, J. M.; Corn, R. M., *The Journal of Physical Chemistry* **1994,** *98* (18), 4899-4905.
60. Lantz, J. M.; Corn, R. M., *The Journal of Physical Chemistry* **1994,** *98* (38), 9387-9390.
61. Corn, R. M.; Higgins, D. A., *Chemical reviews* **1994,** *94* (1), 107-125.
62. Lantz, J. M.; Baba, R.; Corn, R. M., *The Journal of Physical Chemistry* **1993,** *97* (29), 7392-7395.
63. Corn, R. M.; Romagnoli, M.; Levenson, M. D.; Philpott, M. R., *Chemical physics letters* **1984,** *106* (1-2), 30-35.
64. Fiore, J. L.; Fomenko, V. V.; Bodlaki, D.; Borguet, E., *Applied Physics Letters* **2011,** *98* (4), 041905.
65. Campen, R. K.; Pymer, A. K.; Nihonyanagi, S.; Borguet, E., *The Journal of Physical Chemistry C* **2010,** *114* (43), 18465-18473.
66. McClelland, A.; Fomenko, V.; Borguet, E., *The Journal of Physical Chemistry B* **2004,** *108* (12), 3789-3793.
67. Fomenko, V.; Borguet, E., *Physical Review B* **2003,** *68* (8), 081301.
68. Fomenko, V.; Lami, J.-F.; Borguet, E., *Physical Review B* **2001,** *63* (12), 121316.
69. Wang, H.; Borguet, E.; Eisenthal, K., *J. Phys. Chem. A* **1997,** *101* (4), 713-718.
70. Shi, X.; Borguet, E.; Tarnovsky, A. N.; Eisenthal, K. B., *Chem. Phys.* **1996,** *205* (1-2), 167-178.
71. Guyot-Sionnest, P.; Tadjeddine, A.; Liebsch, A., *Phys. Rev. Lett.* **1990,** *64* (14), 1678.
72. Guyot-Sionnest, P.; Tadjeddine, A., *J. Chem. Phys.* **1990,** *92* (1), 734-738.
73. Walter, M. G.; Warren, E. L.; McKone, J. R.; Boettcher, S. W.; Mi, Q.; Santori, E. A.; Lewis, N. S., *Chemical Reviews* **2010,** *110* (11), 6446-6473.
74. Waegele, M. M.; Chen, X.; Herlihy, D. M.; Cuk, T., *Journal of the American Chemical Society* **2014,** *136* (30), 10632-10639.
75. Kumar, A.; Santangelo, P. G.; Lewis, N. S., *The Journal of Physical Chemistry* **1992,** *96* (2), 834-842.
76. Wen, X.; Xu, W.; Zhao, W.; Khurgin, J. B.; Xiong, Q., *Nano letters* **2018,** *18* (3), 1686-1692.
77. Wang, Z.; Dong, Z.; Zhu, H.; Jin, L.; Chiu, M.-H.; Li, L.-J., . . . Wee, A. T., *ACS nano* **2018,** *12* (2), 1859-1867.
78. Tyson, A. L.; Woods, D. A.; Verlet, J. R., *The Journal of Chemical Physics* **2018,** *149* (20), 204201.
79. Goodman, A. J.; Dahod, N. S.; Tisdale, W. A., *The journal of physical chemistry letters* **2018,** *9* (15), 4227-4232.

5. Chapter 5. Enhanced Intersystem Crossing from Singlet to Triplet by Radical in BODIPY Molecule

5.1 Introduction

Understanding and controlling spin dynamics and kinetics is of a significant interest in applications ranging from photocatalysis,[1] photodynamic therapy[2-5] to photovoltaics[6] and triplet-triplet annihilation upconversion.[7-12] Triplet excitons with low-lying energy levels[13] and long lifetime[14] are of great interest in a variety of energy and/or charge transfer schemes,[15-18] and would enable the above-mentioned applications. The most common approaches to the triplet formation include intermolecular Dexter-type triplet energy transfer from a photosensitizer,[19-20] substitution with heavy atoms to promote strong spin-orbit coupling,[21-25] singlet fission,[26] and enhanced intersystem crossing (EISC) caused by persistent radicals.[9, 27-33] Incorporation of a pendant radical to π-conjugated fluorophore allows for additional excited-state decay pathways and has been a useful tool to study and modify excited-state photophysical properties.[34-35]

Boron dipyrromethene (BODIPY) derivatives are highly fluorescent dyes that allow versatile structural modifications to tune optical and electronic properties,[36-38] and they have been exploited in fluorescence probes and bioimaging.[39-41] On the other hand, access to triplet excited state in BODIPY core structure by intersystem crossing (ISC) is comparatively difficult due to the spin selection rules.[15] While fluorescence quenching of radical-labeled fluorophores has been extensively used for detection of reactive oxygen species (ROS),[42-46] the photophysical processes that result in quenching have not been elucidated nor the excited-state dynamics. In most cases, the fluorescence can be quenched by the radical due to one of the following photophysical processes: energy transfer, electron transfer, enhanced internal conversion (EIC), and enhanced

intersystem crossing (EISC).[31, 47-48] EISC provides a pathway for efficent triplet generation, which is an essential step in triplet-triplet annihilation based photon-upconversion schemes. However, its dependence on structural factors such distance and topology of the radical with respect to the chromophores, as well as the resulting electronic coupling between them are not well understood and are yet to be determined.[9, 31, 49-52] While some reports have suggested that short distance increases triplet quantum yields,[9, 31, 47, 49-53] how distance affects other excited state properties (such as triplet lifetime, the rate of ISC and IC) has not been elucidated.

Here, we report the synthesis of BODIPY derivatives with TEMPO radical covalently linked either from 2-position or the *meso*-position to elucidate structural factors such as distance and topology on the efficiency of EISC and apply the new BODIPY-TEMPO dyads in TTA upconversion. We sought to systematically investigate the roles of the distance and topology on triplet yields, triplet lifetimes, and ISC and IC rate constants. Thus, we targeted three BODIPY-TEMPO dyads, **BDP-2AR**, **BDP-2TR**, and **BDP-mTR** along with **BDP**, a non-radical reference compound (Figure 5.1). In **BDP-2AR**, TEMPO is connected via an alkyl amine at the 2-position of BODIPY and has the shortest through-bond distance among all three radicals with 6-atoms separation from the edge of BODIPY core to TEMPO oxygen. In **BDP-2TR**, the BODIPY and TEMPO were separated with a longer and flexible triazole-containing linker at the 2-position of BODIPY with 10-atoms separation from the BODIPY core to the TEMPO oxygen. On the other hand, to examine the role of the topology, **BDP-mTR** was synthesized using the same linker and through-bond distance as the **BDP-2TR**, but the TEMPO is linked to the *meso*-position of BODIPY. During the progress of this work, a TEMPO-labeled BODIPY similar to **BDP-2AR** was reported.[10] Photophysical properties of all BODIPY-TEMPO dyads were probed using steady-state absorption and photoluminescence, and ultrafast transient absorption spectroscopy (TAS).

Fluorescence of BODIPY was significantly quenched in the dyads by about 70-80%. We find that the rate constants (singlet decay to ground state rate k_S, triplet formation rate $k_{ISC,}$ and triplet decay to ground state rate k_T) of all three dyads are influenced by both distance and topology, while the triplet quantum yields were mainly influenced by the topology of the radical rather than the distance. The **BDP-2AR** exhibits favorable property including longer triplet lifetime and higher intersystem crossing rate simultaneously.

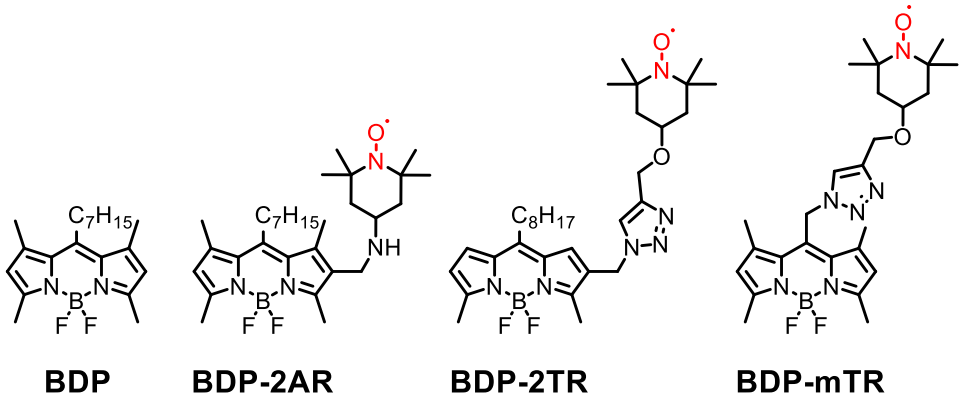

Figure 5.1 Structures of BODIPY-TEMPO radicals and the reference compound **BDP**.

5.2 Results and Discussion

5.2.1 Design and Synthesis of BODIPY-TEMPO Dyads

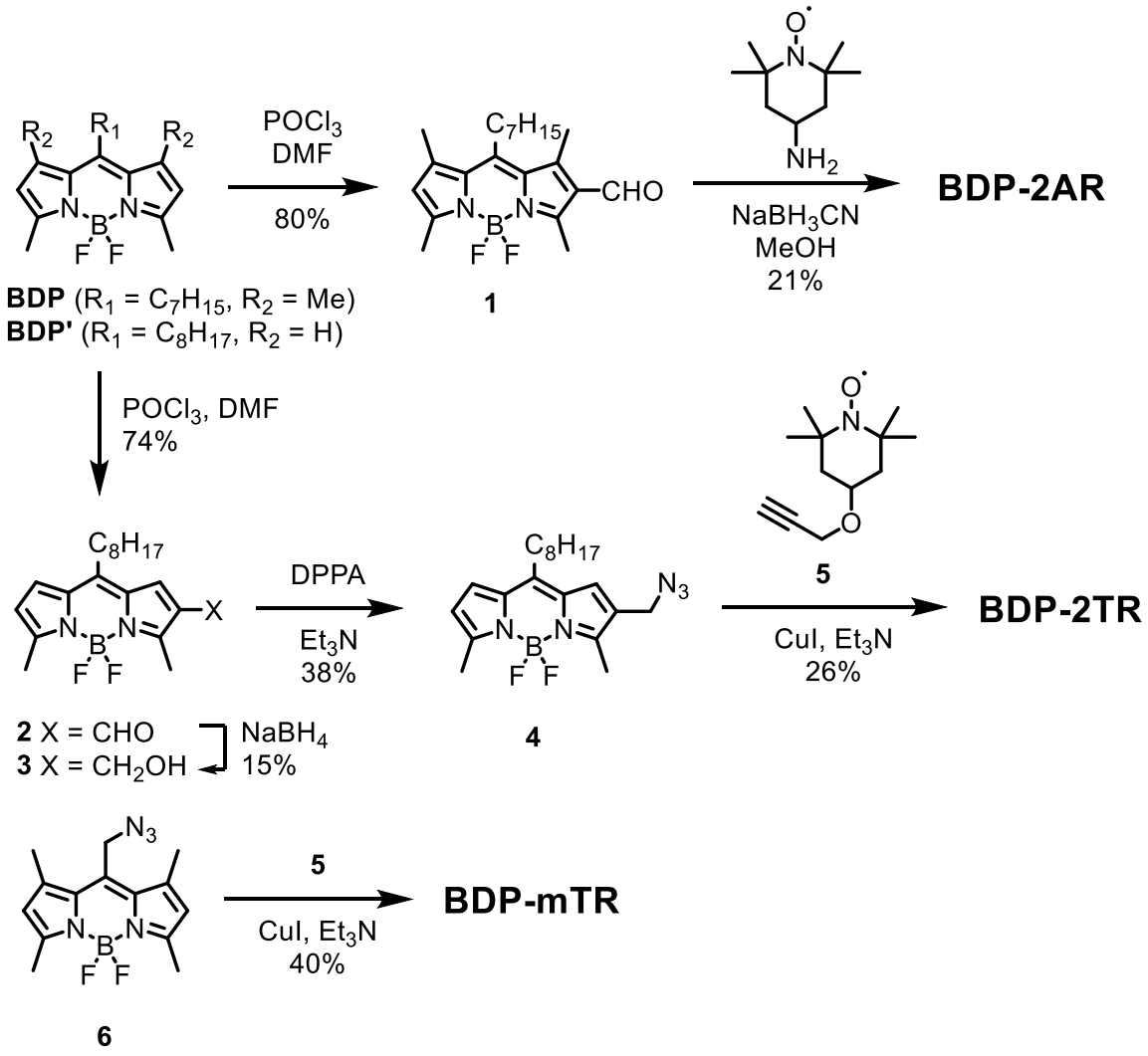

Figure 5.2 Synthesis of BODIPY-TEMPO dyads

Synthesis of the three BODIPY-TEMPO radicals are summarized in Figure 5.2. The synthesis of **BDP-2AR** started from the conversion of **BDP** to BDP-aldehyde **1** following a reported procedure[54] by Vilsmeier-Haack reaction. Subsequent reductive amination of **1** with 4-amino-TEMPO afforded **BDP-2AR** in 21% yield. Separately, following the same procedure for preparation of **1**, BODIPY-aldehyde **2** was obtained from the **BDP'**. The aldehyde in compound **2**

was reduced to the alcohol by $NaBH_4$ to give **3** in 15% yield before converted to azide **4** by diphenyl phosphoryl azide (DPPA) and Et_3N in 38% yield. Click reaction of azide **4** and previously reported 4-propargyloxy-TEMPO[9] (compound **5**) completed the synthesis of **BDP-2TR**. **BDP-mTR** was synthesized from click reaction of *meso*-substituted BODIPY-azide **6** and compound **5** according to procedures reported by Wang et al.[9] All BODIPY-TEMPO radical products were purified by silica-packed flash column chromatography and obtained as red solids, but were unable to yield a crystal structure due to the high flexibility of these structures. The NMR spectra are shown in Figure 5.3 and Figure 5.4 below.

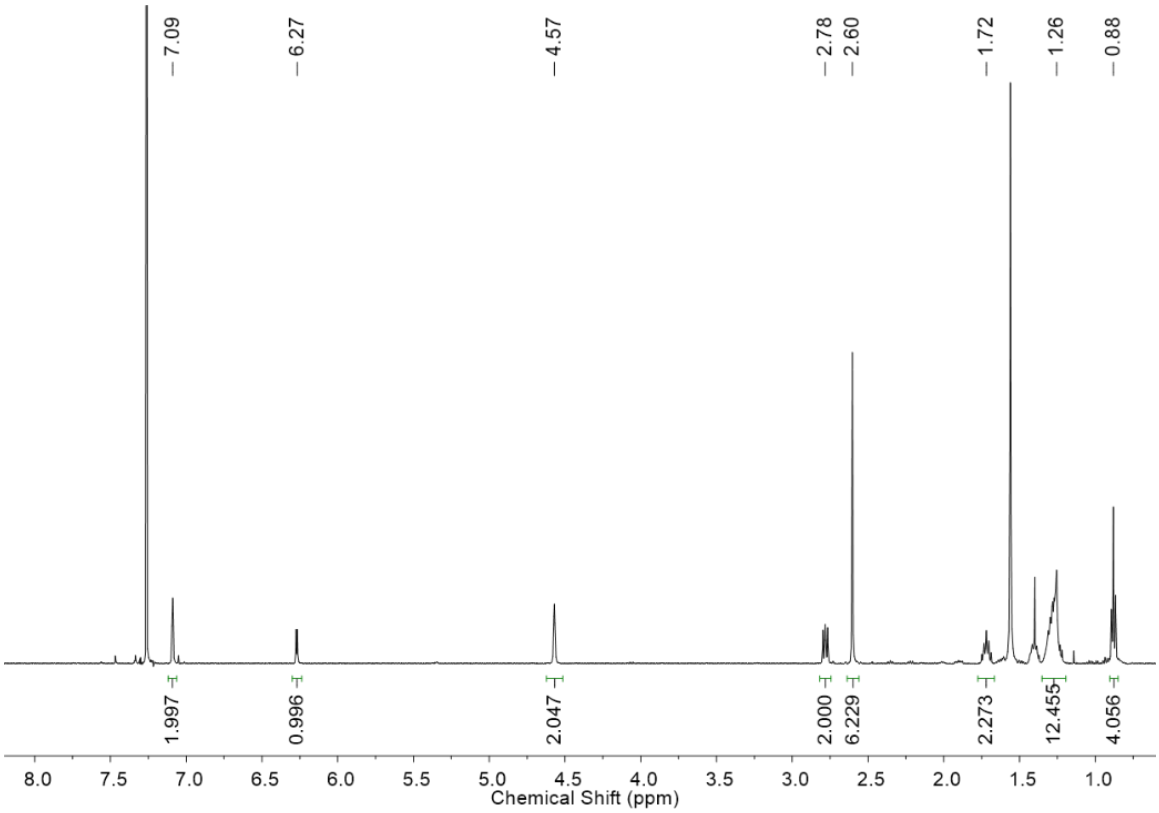

Figure 5.3 ^1H NMR spectra of BODIPY **3**

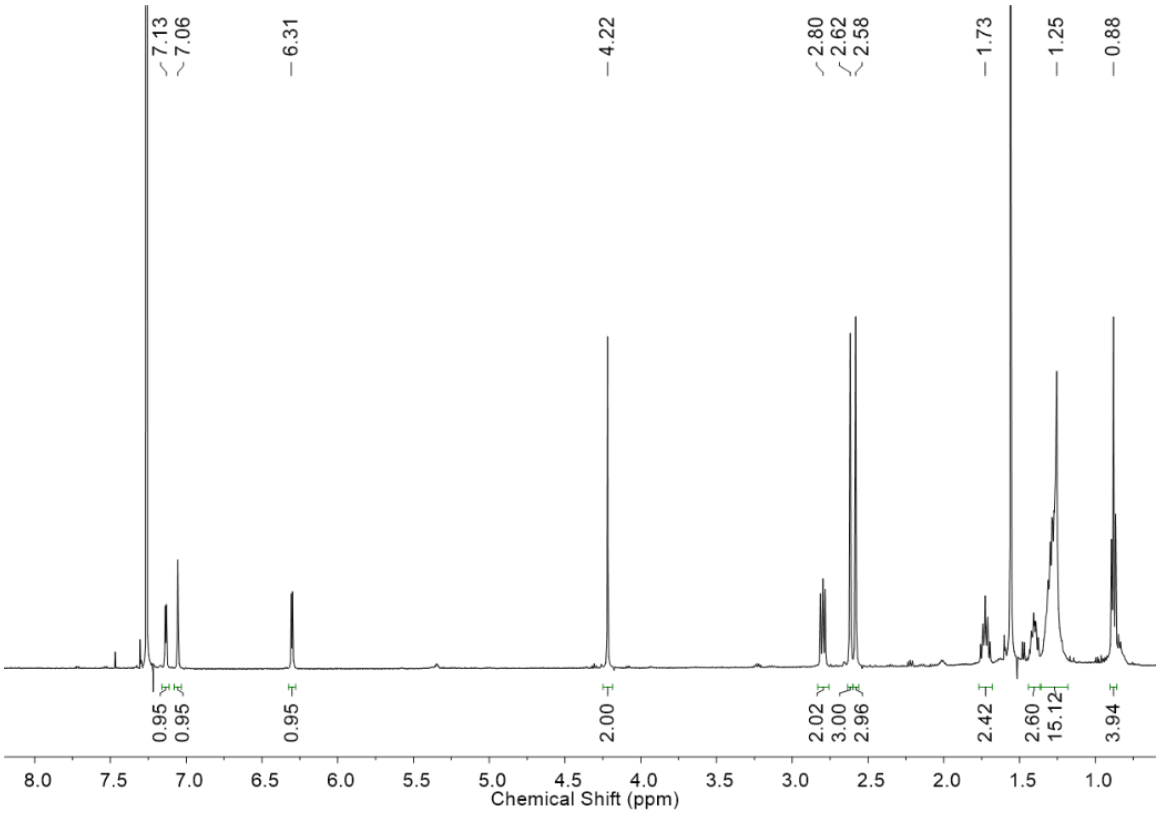

Figure 5.4 ^{1}H NMR spectra of BODIPY **4**

BDP-2AR. A mixture of compound **1** (20 mg, 0.053 mmol), 4-amino-TEMPO (20 mg, 0.12 mmol), and 60 mg neutral alumina was stirred for 48 h before the alumina was filtered off. To the remaining filtrate was added a solution of 5 mg $NaBH_3CN$ in 1 mL MeOH. The new mixture was stirred for another 3 h, washed with saturated aqueous NaCl, extracted with DCM, and concentrated under vacuum. The crude material was purified by column chromatography (SiO_2, EtOAc) to give the product as a red solid (6 mg, 21%). ESI-MS 527.3835 [M+H], calculated for [M+H] 527.3889.

Compound **3**. At −78°C, $NaBH_4$ (9 mg, 0.24 mmol) was added to a solution of compound **2** (78 mg, 0.22 mmol) in 25 mL THF, and the mixture was stirred until the starting material was fully consumed by checking TLC (approx. 4 h). The reaction mixture was washed with 1 M HCl, extracted with DCM, and concentrated under vacuum. The crude material was purified by column

chromatography (SiO_2, hexanes / EtOAc, gradient) to give the product as a red solid (12 mg, 15%). ^{1}H NMR (500 MHz, $CDCl_3$) δ 7.09 (s, 2H), 6.27 (d, *J* = 4 Hz, 1H), 4.57 (s, 2H), 2.78 (m, 2H), 2.60 (s, 6H), 1.72 (m, 2H), 1.26 (m, 12H), 0.88 (t, 3H).

Compound **4**. To a solution of compound **3** (12 mg, 0.033 mmol) in 1 mL THF at 0°C was added 50 μL diphenyl phosphoryl azide, and then 50 μL Et_3N. The mixture was stirred at room temperature overnight until the starting material was fully consumed by checking TLC. The reaction mixture was washed with saturated aqueous $NaHCO_3$, extracted with DCM, and concentrated under vacuum. The crude material was purified by column chromatography (SiO_2, hexanes / EtOAc, gradient) to give the product as a red solid (5 mg, 38%). ^{1}H NMR (500 MHz, $CDCl_3$) δ 7.13 (d, *J* = 4 Hz, 1H), 7.06 (s, 1H), 6.30 (d, *J* = 4 Hz, 1H), 4.22 (s, 2H), 2.80 (m, 2H), 2.62 (s, 3H), 2.58 (s, 3H), 1.73 (m, 2H), 1.25 (m, 12H), 0.88 (t, 3H).

BDP-2TR. A mixture of compound **4** (5 mg, 0.013 mmol), 4-propagyloxy-TEMPO (9 mg, 0.043 mmol), 0.5 mg CuI, 50 μL Et_3N in 1 mL THF was stirred at room temperature for 24 h. The reaction mixture was washed with saturated aqueous NaCl, extracted with DCM, and concentrated under vacuum. The crude material was purified by column chromatography (SiO_2, hexanes / EtOAc, gradient) to give the product as a red solid (2 mg, 26%). ESI-MS 598.4052 [M+H], calculated for [M+H] 598.5908.

5.2.2 Absorption and Emission Spectra

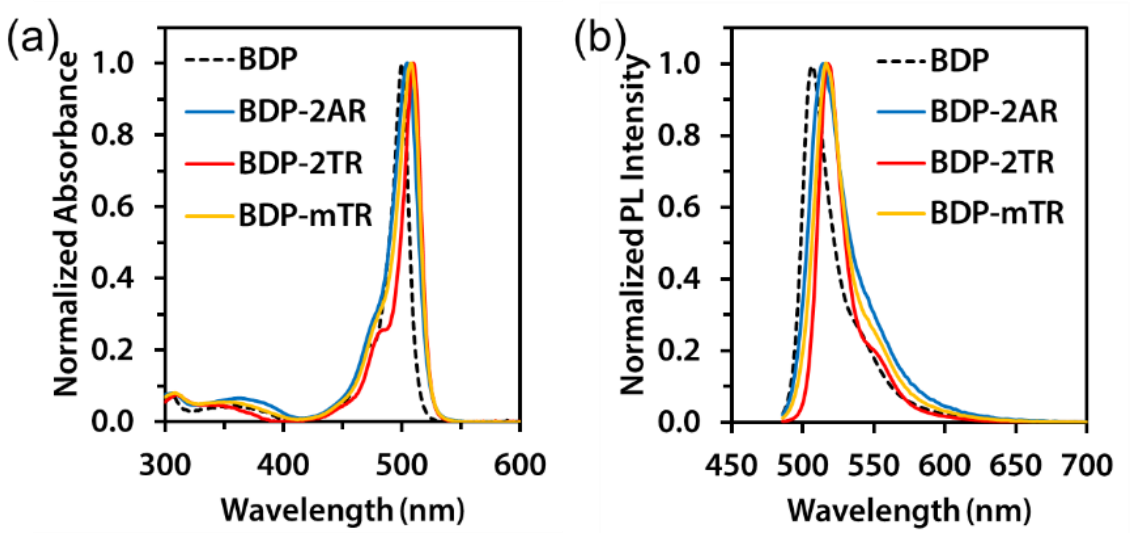

Figure 5.5 (a) Absorption and (b) photoluminescence (PL) spectra of non-radical **BDP** and BODIPY-TEMPO radicals in PhMe.

Table 5.1 Absorption and photoluminescence maximum, fluorescence quantum yield, and calculated charge separation free energy of BODIPY-TEMPO radicals in various solvents.

entry	solv.	λ_{max} (nm)	λ_{em} (nm)	ϕ_F	ΔG_{CS} (eV)
BDP-2AR	PhMe	508	518	0.146	+0.25
	DCM	505	514	0.100	−0.53
	MeCN	501	514	0.045	−0.75
BDP-2TR	PhMe	513	521	0.194	+0.56
	DCM	509	518	0.153	−0.44
	MeCN	505	514	0.119	−0.73
BDP-mTR	PhMe	510	518	0.145	+0.24
	DCM	506	516	0.117	−0.55
	MeCN	503	516	0.106	−0.78

λ_{max} and λ_{em} are wavelengths of absorption and emission maximum. Relative fluorescence quantum yield (ϕ_F) was calculated using **BDP** as the reference (ϕ_F = 0.99, PhMe).

The steady-state absorption and emission data of all BODIPY-TEMPO radicals in dilute toluene solution are shown in Figure 5.5 and summarized in Table 5.1. The absorption spectra of **BDP-2AR**, **BDP-2TR**, and **BDP-mTR** show a main absorption peak assigned to the π-π* transition with absorption maximum (λ_{max}) at 508, 513, and 510 nm, respectively (Figure 5.5a).[9] All BODIPY-TEMPO dyads show similar absorption spectra to that of the non-radical **BDP** (λ_{max} = 499 nm) with a slight red-shift of 9-14 nm, suggesting weak electronic coupling between TEMPO and the BODIPY core. No additional absorption feature was observed at wavelength longer than 550 nm. The photoluminescence (PL) spectra of the non-radical **BDP** has an emission peak (λ_{em}) at 506 nm (Figure 5.5b) with a fluorescence quantum yield (ϕ_F) of 0.99.[55] In contrast, all of the BODIPY-TEMPO dyads have a relatively weak emission peak with λ_{em} of 518-521 nm, red-shifted by 12-15 nm compared to **BDP**. At low concentration (10 μM), BODIPY-TEMPO dyads exhibited ϕ_F of 0.15-0.19, corresponding to the quenching of 81-85% of the BDP fluorescence by the appended TEMPO radical (Table 5.1). To further probe whether this quenching is due to intramolecular or intermolecular interactions, we measured the photoluminescence and ϕ_F of a mixture of **BDP** with an equimolar of 4-amino-TEMPO (10 μM) in PhMe, in which no fluorescence quenching was observed (Figure 5.6a). Even 100 equivalent excess of TEMPO did not generate the large decrease in PL intensity observed in our BODIPY-TEMPO dyads. This suggests that the covalent attachment of TEMPO to BODIPY in the BODIPY-TEMPO dyads results in intramolecular fluorescence quenching of BODIPY despite the long through-bond distance of 13 Å.

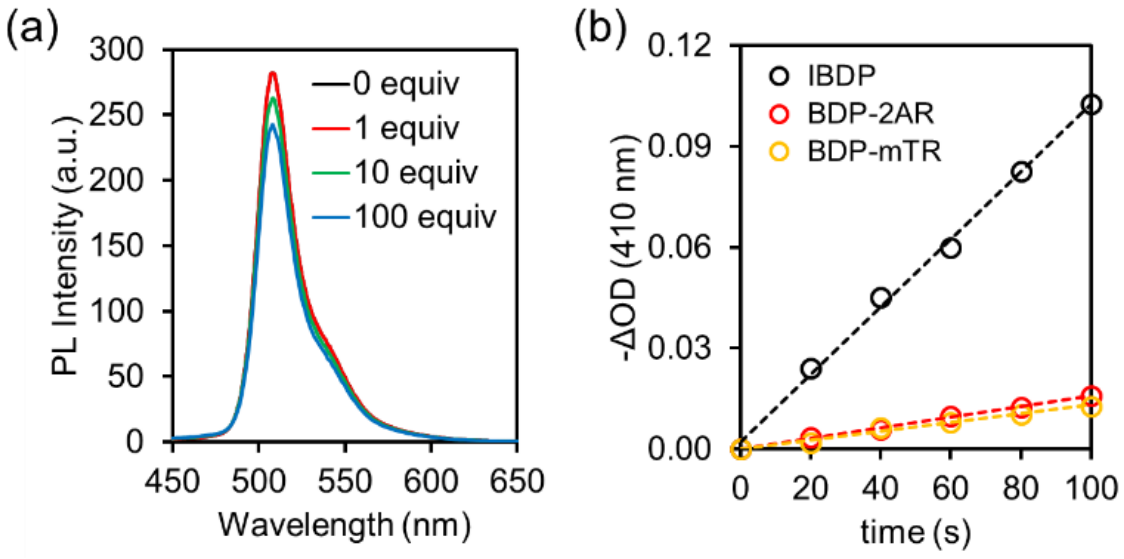

Figure 5.6 (a) Decrease of **BDP** photoluminescence intensity (10^{-5} mol/L in MeCN) upon mixing with various equivalents of 4-amino-TEMPO. (b) Decrease of 1,3-diphenylisobenzofuran (DPBF) absorption (-ΔOD at 410 nm) monitored at multiple time intervals upon photoexcitation of **BDP-2AR** and **BDP-mTR**, and comparison to an efficient triplet sensitizer **IBDP**.

To understand the fluorescence quenching mechanism, we examine all possible decay pathways of BODIPY-TEMPO radicals including energy transfer or charge transfer from BODIPY to TEMPO, internal conversion and intersystem crossing. Förster energy transfer from the singlet excited state (^{1}BODIPY*) of the energy donor to the acceptor (TEMPO) requires a considerable donor/acceptor spectral overlap and strong transition dipoles,[31, 47] but this cannot be realized because of (1) the mismatched TEMPO absorption (λ_{max} = 475 nm) and BODIPY emission (>500 nm), and (2) the low extinction coefficient of n-π* transition of TEMPO (~10^2).[32] The energy mismatch between the donor and acceptor excited state also precludes Dexter type of energy transfer from ^{1}BODIPY*. Regarding the charge transfer pathway, the presence of charge transfer interaction between the donor and acceptor is often experimentally examined by changing solvent

polarity,[56-57] so we compared the absorption and emission spectra of all BODIPY-TEMPO radicals in solvents with different dielectric constant (toluene, DCM, and acetonitrile). Increasing solvent dielectric led to a total of 7-8 nm blue-shift in both λ_{max} and λ_{em} peak wavelengths (Table 5.1, Figure 5.7) and a 3-fold decrease in the ϕ_F in more polar solvent, indicating considerable charge transfer between BODIPY and its pendant TEMPO. Thus, electron transfer and EISC are among possible decay pathways for the chromophore-radical complex, and the competition between these two can be altered by changing the solvent.[32]

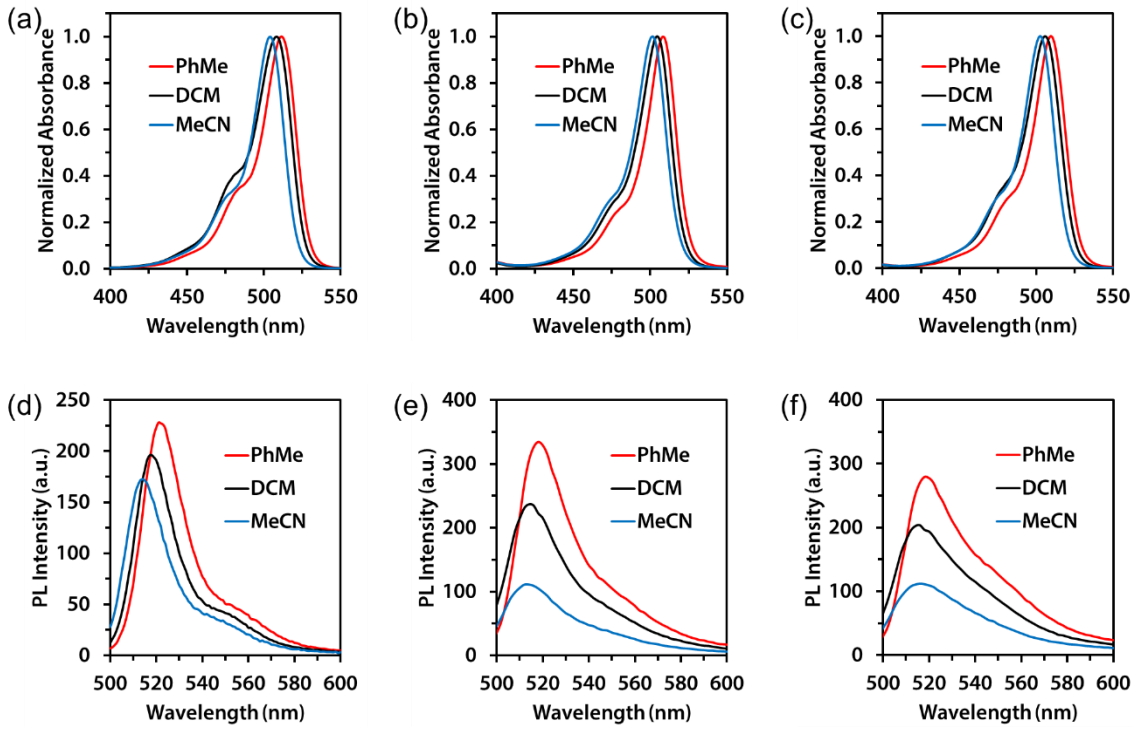

Figure 5.7 Absorption spectra of (a) **BDP-2AR**, (b) **BDP-2TR**, (c) **BDP-mTR**, and photoluminescence spectra of (d) **BDP-2AR**, (e) **BDP-2TR**, (f) **BDP-mTR** in different solvents.

5.2.3 Gibbs Free Energy Calculation

Although there is limited study to investigate the EISC efficiency's dependence on the solvent polarity, the Gibbs free energy change of possible charge separation (ΔG_{CS}) can be evaluated according to the Rehm-Weller equation.[58]

$$\Delta G_{CS} = -(E_{00} + E_A - E_D) - \frac{e^2}{4\pi\varepsilon_0\varepsilon_s r_{DA}} + \frac{e^2}{4\pi\varepsilon_0}\left(\frac{1}{2r_D} + \frac{1}{2r_A}\right)\left(\frac{1}{\varepsilon_s} - \frac{1}{\varepsilon_{sp}}\right)$$

E_{00} is the optical band gap of **BDP-2AR**, **BDP-2TR** and **BDP-mTR**, E_A and E_D are the reduction potential of BDP (−1.43 V) and oxidation potential of TEMPO (+0.32 V), respectively vs. SCE. ε_s is the solvent dielectric constants where electron transfer takes place, ε_{sp} is the dielectric constants of support solvent (37.5 for MeCN). r_D and r_A are the radii of TEMPO (2.5 Å) and BDP (3.8 Å). r_{DA} is the donor-acceptor distance, assuming $r_{DA} = r_D + r_A$ in **BDP-2AR**, and r_{DA} = 9.0 Å in **BDP-2TR** and **BDP-mTR**.[20] In our calculation (Table 5.2), ΔG_{CS} for all three BODIPY-TEMPO radicals were positive in toluene, but negative in DCM and more negative in MeCN, indicating possible occurrence of electron transfer in these two solvents. To focus on the radical-enhanced ISC pathway rather than the electron transfer, we chose to use non-polar solvents such as PhMe for all further time resolved photophysical studies.

Table 5.2 Calculation of ΔG_{CS} of BODIPY-TEMPO in multiple solvents.

entry	solvent	ε_s	E_{00} (eV)	r_{DA} (Å)	ΔG_{CS} (eV)
BDP-2AR	PhMe	2.38	2.42	6.3	+0.25
	DCM	8.93	2.43	6.3	−0.53
	MeCN	37.5	2.44	6.3	−0.75
BDP-2TR	PhMe	2.38	2.40	9.0	+0.56
	DCM	8.93	2.41	9.0	−0.44
	MeCN	37.5	2.43	9.0	−0.73
BDP-mTR	PhMe	2.38	2.43	9.0	+0.24
	DCM	8.93	2.45	9.0	−0.55
	MeCN	37.5	2.47	9.0	−0.78

5.2.4 Singlet Oxygen Quantum Yield (ϕ_Δ)

To further verify the intersystem crossing is the main singlet exciton quenching pathway in a non polar solvent, we examined the conversion from triplet oxygen ($^3O_2$) to singlet oxygen ($^1O_2$) with the BODIPY-TEMPO radical complexes. To reflect the efficiency of ISC in BODIPY-TEMPO, we measured the quantum yield of singlet oxygen generation (ϕ_Δ) by the sensitized photochemical reaction involving $^1O_2$ and 1,3-diphenylisobenzofuran (DPBF),[59] in which the Diels-Alder reaction between $^1O_2$ and DPBF leads to the bleaching of DPBF. A mixture of BODIPY-TEMPO and DPBF in aerated PhMe was irradiated at the BODIPY absorption near 500 nm, and the decrease in DPBF absorption (-ΔOD) at 410 nm was monitored at multiple time intervals. ϕ_Δ was calculated by plotting the -ΔOD against irradiation time using 2,6-diiodinated BODIPY (IBDP, ϕ_Δ = 0.85) as the standard (Figure 5.6b).[9] ϕ_Δ of the **BDP-2AR** and **BDP-mTR** were found to be 0.16 and 0.14, respectively, which cannot completely explain all the decrease of ϕ_F caused by the radical. While EISC will be further discussed in the following time resolved spectroscopy, the remainder of the fluorescence quenching is presumably attributed to EIC with the excitation energy dissipated as vibrational relaxation.[31, 56] Through the generation of the singlet oxygen we confirmed that the formation of triplet state in BDP-TEMPO complexes.

5.2.5 Transient Absorption Spectroscopy Study

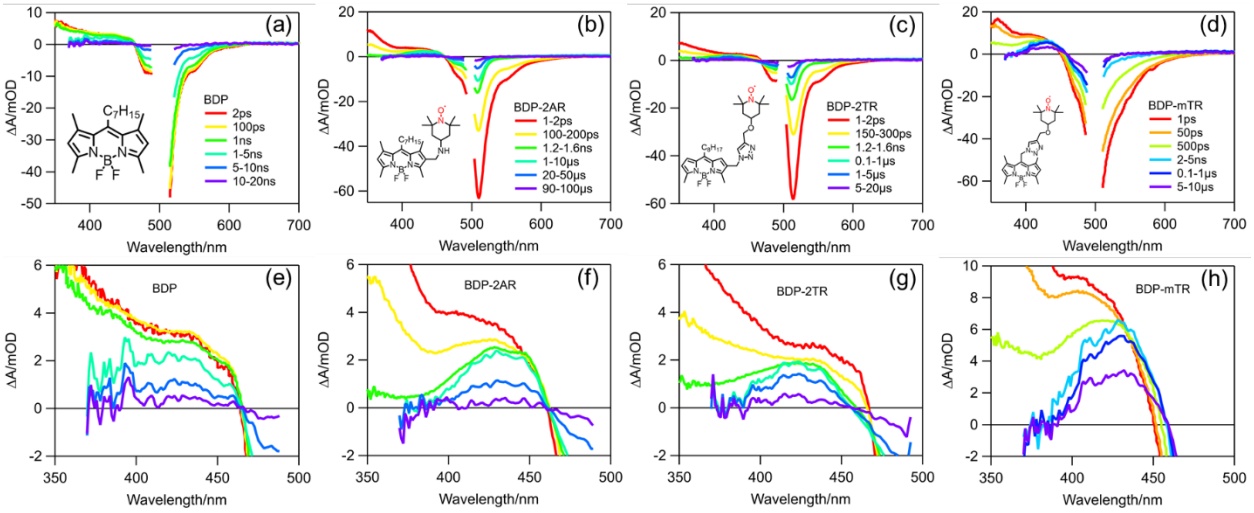

Figure 5.8 Transient absorption spectra (10 μM in PhMe) of (a)(e) **BDP**, (b)(f) **BDP-2AR**, (c)(g) **BDP-2TR**, and (d)(h) **BDP-mTR** at indicated delay times after 500 nm excitation. The bottom panels (e-h) show the expanded TA spectra at 350-500 nm at the same delay times as the corresponding top panels (with legends in the top panels). TA spectra above 2 ns shows low signal to noise with probe wavelength above 400 nm due to the insufficient intensity.

To investigate the detailed mechanism and related process of fluorescence quenching, the femtosecond and nanosecond transient absorption (TA) spectra of these BODIPY-TEMPO complexes and the non-radical **BDP** were recorded in PhMe at 10 μM concentration with 500 nm excitation. The TA spectra of **BDP** (Figure 5.8a, e) show a broad absorption band at 350-450 nm that can be attributed to BODIPY singlet excited-state (^{1}BODIPY*) absorption (ESA). This assignment is based on the reported near 100% singlet emission ϕ_F of BODIPY, which suggests that only the ^{1}BODIPY* can be observed.[9] The generation of ^{1}BODIPY* also leads to the ground state bleach (GSB) of BODIPY, a sharp negative peak at 509 nm, due to the decrease of ground state population, and a less intense negative signals at 520-600 nm (at the region of ^{1}BODIPY* fluorescence emission) that can be attributed to ^{1}BODIPY* stimulated emission. These features decay on the < 10 ns time scale, caused by the radiative decay of the singlet excited state.

Compared to **BDP** the TA spectra of **BDP-2AR** at 500 nm (Figure 5.8b, 3f) show similar spectral evolution at < 100 ps, suggesting the formation of ^{1}BODIPY* excited state in the **BDP** part of the complex. However, the decay of ^{1}BODIPY* become faster and leads to formation of a new product. After the first 1 ns (Figure 5.8b, f), the TA spectra consist mainly of a new absorption feature centered at 430 nm and the GSB at 509 nm and these features persist up to tens of microseconds. The 430 nm peak matches well the reported absorption spectrum of BODIPY triplet excited state (^{3}BODIPY*).[9] These results suggest the generation of long-lived ^{3}BODIPY* in **BDP-2AR** through the radical-induced EISC process. The TA spectra of **BDP-2TR** (Figure 5.8c, g) and **BDP-mTR** **(**Figure 5.8d, h) resemble those of **BDP-2AR**, showing the initial decay of ^{1}BODIPY* and formation of the long-lived ^{3}BODIPY*.

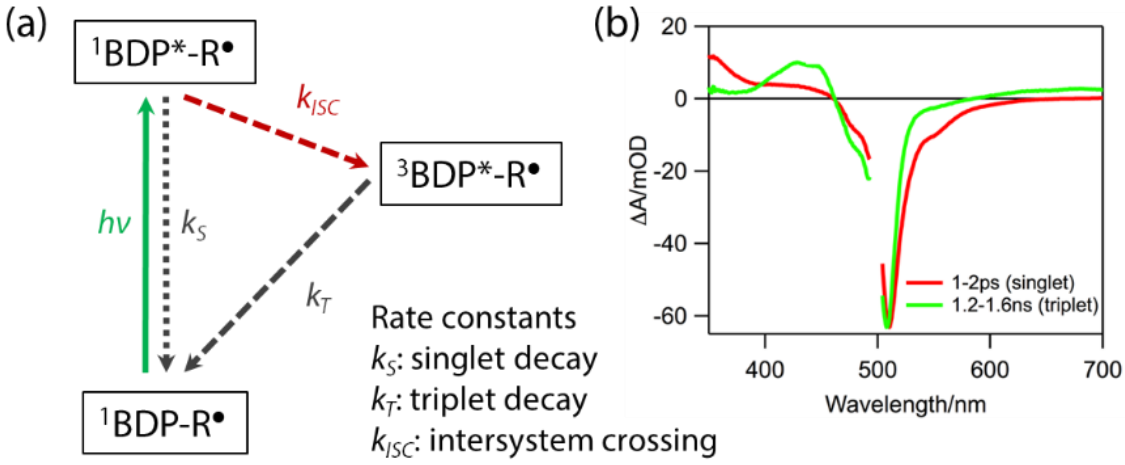

Figure 5.9 (a) Energy diagram of radical (R) labeled BDP and photophysical processes of interest. (b) Representative TA spectra of BODIPY singlet and triplet (scaled) in **BDP-2AR**.

The excited state photo-physical transformations of BODIPY-TEMPO complexes and their rate constants can be illustrated using a Jablonski diagram (Figure 5.9a). After the photoexcitation, ^{1}BODIPY*-R• can either return to the ground state via radiative or non-radiative internal conversion (with rate constant k_S) or undergo radical-enhanced ISC (k_{ISC}) to generate

^{3}BODIPY*-R$^\bullet$, which would eventually decay back to the ground state through triplet ISC process (k_T). In the absence of a radical, k_{ISC} and k_T are negligible due to inefficient ISC of **BDP**, while the k_S is dominated radiative decay.

The rate constants of these process can be obtained by fitting kinetics traces at selective wavelengths of in the TA spectra. For **BDP**, the decay of the ^{1}BODIPY* can be monitored by the decay of ESA (420 nm) and recovery of GSB (514 nm). A global single exponential fitting of the **BDP** kinetics at both the GSB and singlet ESA provided a ^{1}BODIPY* lifetime of τ_S = 5.03±0.00 ns comparable to previous work,[9] and a corresponding singlet decay rate constant of $k_S = 1.99\times10^8$ s^{-1}. In BODIPY-TEMPO complexes, the presence of the EISC pathway complicates the analysis because of the spectral overlap between the singlet and triplet states. As shown in Figure 5.9b, a comparison of the TA spectra of **BDP-2AR** at 1-2 ps (red) and 1.2-1.6 ns (green), representing ^{1}BODIPY* and ^{3}BODIPY*, respectively, indicates that the signal at 355 nm, the peak of ^{1}BODIPY*, contains only the contribution of the ^{1}BODIPY* species; while the peak of the triplet absorption at ~ 430 nm and GSB at ~ 510 nm contain overlapping contributions of the singlet and triplet states. A comparison of these kinetics for the BODIPY-TEMPO complexes is shown in Figure 5.10. The rate constants of the internal conversion, intersystem crossing and triplet decay process can be obtained by fitting these kinetic profiles to a model described below. The rate fitting parameters are listed in Table 5.3 and Table 5.4.

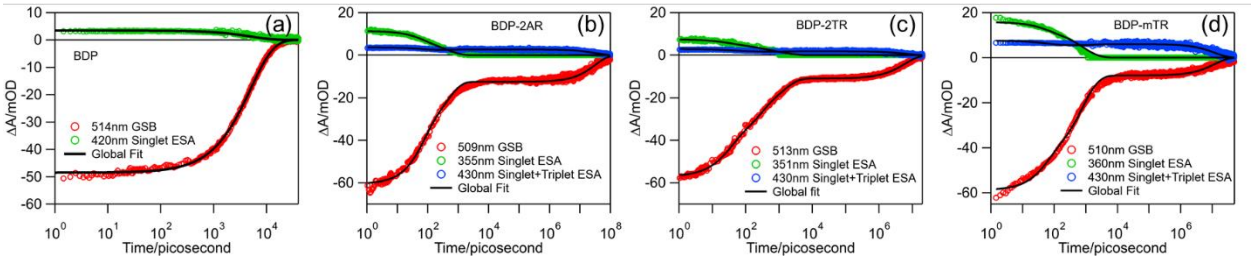

Figure 5.10 Kinetics of ground state bleach (GSB in red), singlet excited state absorption (ESA in green) and triplet ESA in blue of (a) **BDP**, (b) **BDP-2AR**, (c) **BDP-2TR**, and (d) **BDP-mTR**

obtained at indicated wavelengths and corresponding global fit (black lines) by equation described below:

The decay of ^{1}BODIPY* would follow the first-order kinetics of its population and can be fitted with an exponential decay:

$$[BDP]_S(t) = [BDP]_S(0)e^{-(k_S+k_{ISC})t} \qquad \text{Eq. 5.1}$$

Here, the $[BDP]_S(t)$ represents the population of ^{1}BODIPY* at delay time (t). For ^{3}BODIPY*, k_{ISC} and k_T are responsible for the generation and decay of its population, $[BDP]_T(t)$, which can be expressed as:

$$\frac{d[BDP]_T(t)}{dt} = k_{ISC}[BDP]_S(t) - k_T[BDP]_T(t) \qquad \text{Eq. 5.2}$$

Integrating and solving Eq 5.2 provides the ^{3}BODIPY* kinetics as:

$$[BDP]_T(t) = \frac{[BDP]_S(0)k_{ISC}}{k_S+k_{ISC}-k_T}[e^{-k_T t} - e^{-(k_S+k_{ISC})t}] \qquad \text{Eq. 5.3}$$

From the TA spectral data, the kinetic profiles at the three key wavelengths (510, 430, 355 nm) identified above (Figure 5.9b) were used for global fittings to extract the lifetime of ^{1}BODIPY* and ^{3}BODIPY* excited states. The 355 nm kinetics represents the ^{1}BODIPY* exclusively and can be fit by Eq. 5.4.

$$\Delta A_{355} = L\varepsilon_{S355}[BDP]_S(t) \qquad \text{Eq. 5.4}$$

ε_{S355} is the extinction coefficient of ^{1}BODIPY* absorption at 355 nm and L is the effective pathlength of the sample.

The ground state bleach (510 nm) contains the contributions of both ^{1}BODIPY* and ^{3}BODIPY* and can be fit to:

$$\Delta A_{510} = -L\varepsilon_{BDP510}([BDP]_S(t) + [BDP]_T(t)) \qquad \text{Eq. 5.5}$$

Here, ε_{BDP510} is the extinction coefficient of ground state at 510 nm (1.03×10^5 $M^{-1}cm^{-1}$) obtained from the steady-state absorption spectra.

The signal at 430 nm also contains the contributions of both ^{1}BODIPY* and ^{3}BODIPY* and can be fit to

$$\Delta A_{430} = L\varepsilon_{S430}[BDP]_S(t) + L\varepsilon_{T430}[BDP]_T(t) \qquad \text{Eq. 5.6}$$

Here ε_{S430} is the extinction coefficient of ^{1}BODIPY* absorption at 430 nm, determined by the ratio of ($\Delta A_{430}/\Delta A_{510}$) at 1-2 ps as shown in Figure 5.9b. Similarly, the extinction coefficient of ^{3}BODIPY* at 430 nm, ε_{T430}, is determined by the ratio of ($\Delta A_{430}/\Delta A_{510}$) at 1.2-1.6 ns.

Table 5.3 Photophysical parameters of BODIPY derivatives.

entry	Extinction coefficients (ε, 10^4 $M^{-1}cm^{-1}$)				Time constants			Triplet yield (ϕ_{ISC})
	GSB	^{1}BODIPY*		^{3}BODIPY*	τ_S (ps)	τ_{ISC} (ps)	τ_T (μs)	
BDP-2AR	10.3 (509 nm)	1.92 (355 nm)	0.63 (430 nm)	2.22 (430 nm)	434±26	1417±61	31.7±4.3	0.234
BDP-2TR	7.17 (513 nm)	0.93 (351 nm)	0.36 (430 nm)	1.20 (430 nm)	1108±69	3556±54	6.09±0.14	0.238
BDP-mTR	8.30 (510 nm)	2.23 (360 nm)	1.06 (430 nm)	6.29 (430 nm)	929±52	5398±131	11.7±0.1	0.147
BDP	8.80 (514 nm)	1.26 (360 nm)	0.58 (420 nm)	–	5030±0	–	–	–

Table 5.4 Time constants (τ) and quantum yields (ϕ) for excited state photophysical pathways of BODIPY-TEMPO radicals.

entry	τ_S (ps)	τ_{ISC} (ps)	τ_T (μs)	ϕ_{ISC}	ϕ_F	ϕ_{IC}
BDP	5030±0	–	–	–	0.990	–
BDP-2AR	434±26	1417±61	31.7±4.3	0.234	0.146	0.620
BDP-2TR	1108±69	3556±54	6.09±0.14	0.238	0.194	0.568
BDP-mTR	929±52	5398±131	11.7±0.1	0.147	0.145	0.708

For **BDP**, IC and triplet are negligible as a result of near-unity ϕ_F. ϕ_{ISC} and ϕ_{IC} are the quantum yields of EISC and non-radiative internal conversion from the singlet state. The lifetime τ is the reciprocal of the corresponding rate constant k. $\phi_{IC} + \phi_F + \phi_{ISC} = 1$.

According to the global kinetics fit, the rate constant of ISC (τ_{ISC}) of all BODIPY-TEMPO radicals are in the order of several nanosecond, and the intersystem crossing efficiency is much enhanced compared to bare **BDP** (Table 5.4). The rate constant of **BDP-TEMPO** singlet excited state decay to the ground state ($1/\tau_S$) is also around 5~10 times faster than **BDP** singlet. Both enhanced intersystem crossing and internal conversion contribute to the rapid depletion of ^{1}BODIPY* in the radicals. The ISC quantum yield (ϕ_{ISC}), calculated according to $\phi_{ISC} = k_{ISC} / (k_{ISC} + k_S)$, are 0.234, 0.238 and 0.147 for **BDP-2AR**, **BDP-2TR** and **BDP-mTR**, respectively. The fluorescence quantum yields (ϕ_F) of BODIPY-TEMPO dyads are obtained from steady-state fluorescence measurements. From ϕ_{ISC} and $\phi_{F,}$ the yield of nonradiative internal conversion from the singlet excited (ϕ_{IC}) for **BDP-2AR**, **BDP-2TR**, and **BDP-mTR** can be calculated to be 0.620, 0.568, and 0.708, respectively (Table 5.4). Comparing between **BDP** and **BODIPY-TEMPO** dyads shows that in addition to ISC, the non-radiative internal conversion process is also enhanced by the radial attachment and become the major channel of the ^{1}BODIPY* decay. These findings are consistent with a previous report of perylenediimide-nitroxide radicals and similar **BODIPY-TEMPO** dyads which also show enhanced internal conversion and intersystem crossing with covalently attached radicals.[9-10, 31] However, the ϕ_{ISC} values measured in our study using ultrafast TA differ significantly from previously reported values of 0.55 for BDP-2AR[10] and 0.80 for BDP-mTR,[9] and the origin of this discrepancy is unclear.

Varying the distance and topology of the TEMPO free radical relative to the BODIPY should presumably influence the electron exchange interactions between ^{1}BODIPY* and the radical and

thus affect the kinetics of the BODIPY-TEMPO dyads. Indeed, the femtosecond TA spectra and kinetics show the ^{1}BODIPY* in **BDP-2AR** (τ = 434 ps) decays by 2.5-fold faster than in the **BDP-2TR** (τ = 1108 ps), and 2-folds faster than in **BDP-mTR** (τ = 929 ps) (Table 5.4). This fast decay of the singlet is accompanied by ultrafast EISC. For example, the non-radiative ISC lifetimes (τ_{ISC}, Table 5.4) of 1417±61, 3556±54, 5398±131 ps for **BDP-2AR**, **BDP-2TR**, and **BDP-mTR** respectively, show an increase by 5-folds as a result of an increase in the distance and change in topology of TEMPO relative to BODIPY core. Interestingly and contrary to previous reports,[9, 53] the distance here does not seem to play a significant role on the ISC and singlet decay when comparing the time constants for **BDP-2AR** and **BDP-2TR** where the TEMPO is connected through the 2-position despite the long linker in **BDP-2TR**. However, comparing ISC and singlet decay time constants of **BDP-2AR** to that of **BDP-2TR** suggest while the combination of distance and topology variation results in a decrease in the ISC rate, the topology seems to play more of a critical role. This is clearly obvious, if we compare the ISC and singlet decay time constants of **BDP-2TR** and **BDP-mTR**, which both have the same linker but connected either through the 2-position or *meso*-position of the BODIPY core. In general, the connection of TEMPO to the *meso*-position of BODIPY in **BDP-mTR** leads to slower ISC by 1.5-fold and a decrease in triplet lifetime by 2-folds compared to **BDP-2TR** (τ_{ISC}, τ_T, Table 5.4).

Although the BODIPY-TEMPO distance (both through bond and through space) in **BDP-2TR** and **BDP-mTR** is expected to be similar, the geometrical orientation of the radical N-O bond relative to the BODIPY core is likely very different, particularly in the folded conformation. The perpendicular-oriented **BDP-2TR** exhibited faster ISC (τ_{ISC} = 3556±54 vs 5398±131 ps), faster triplet decay (τ_T = 6.09±0.14 vs 11.7±0.1 μs), and higher ISC quantum yield (ϕ_{ISC} = 0.238 vs 0.147) compared to the antiparallel-oriented **BDP-mTR** (Table 5.4). The role of dipole orientation has

been invoked in BODIPY-Anthracene photosensitizers to rationalize the ISC efficiency.[60-61] While this system is slightly different, it is possible that the dipole of the TEMPO in both the folded and bond-through-space configurations whether in orthogonal or anti-parallel to the dipole of BODIPY plays a significant role in the excited-state dynamics of **BDP-2TR** and **BDP-mTR**.

The longest triplet lifetimes were observed in the BODIPY-TEMPO with the shortest through-bond-distance, **BDP-2AR** with τ_T = 31.7 μs compared to **BDP-2TR** with τ_T =6.09 μs and **BDP-mTR** τ_T = 11.7 μs. Interestingly, while **BDP-2AR** exhibited faster ISC than **BDP-2TR** (τ_{ISC} = 1417 vs 3556 ps), triplet decay became 5-fold slower than in **BDP-2TR** (τ_T =31.7 vs 6.09 μs). This is contrary to the typical direct correlation between τ_{ISC} and τ_T observed in other chromophore-radical systems,[9, 31] because both processes are spin-forbidden and are facilitated by the radical assisted spin-flip. Presumably, in the folded conformation of all BODIPY-TEMPO radicals, the TEMPO folds such that it reaches the BODIPY core with a short through-space distance that enhances the ISC and triplet decay processes. In the case of **BDP-2AR**, the molecular structure combines two factors that result in that observations both a short distance of through-bond distance and the flexibility of the TEMPO to fold-back to slow the radical induced triplet decay. These results suggest that through-bond distance effect EISC, while the triplet to ground state transition may be related to the spatial interaction, which explains the longer ^{3}BODIPY* lifetime in **BDP-2AR**. Nevertheless, **BDP-2AR** demonstrates a possible structure in which the k_{ISC} and ^{3}BODIPY* lifetime can be enhanced simultaneously, which is a desirable feature for EISC in organic chromophores.

5.2.6 DFT Simulation

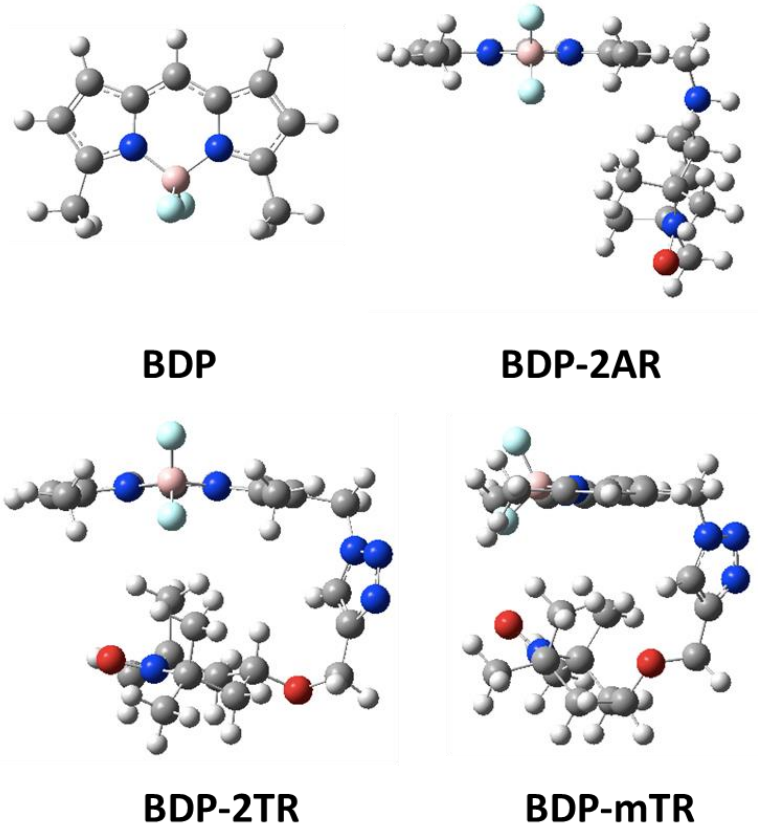

Figure 5.11 Ground state geometries obtained from the electronic structure calculations. The long alkyl chain in m position was substituted with hydrogen to simplify the calculations.

Electronic structure calculations of the ground and all relevant excited electronic states, followed by a detailed analysis of the frontier molecular orbitals (MO) provided a mechanistic insight for TEMPO radical's role in intersystem crossing enhancement. In brief, density functional theory (DFT) calculations were done at the wB97XD level of theory[62] with the 6-31++G(d,p) basis[63] to determine the optimal geometry of all the ground state species. The extended linker in **BDP-2TR** and **BDP-mTR** introduced extra flexibility to the molecule, thus we simulated the ground state geometry in the gas phase as shown in Figure 5.11. It is clear that the BODIPY ring is more rigid in these three molecules, while the TEMPO radical group tends to fold back to form

a "sandwich" structure with the BODIPY ring. With the increasing linker length, the plane of TEMPO folded from perpendicular to the BODIPY ring in **BDP-2AR** to almost parallel in **BDP-mTR**. Through this folded geometry, the TEMPO radical through space distance with BODIPY was not changed drastically. This would explain the similar ISC rate in these three molecules based on the ISC rate dependence on spin-orbital coupling strength in previous studies.[9] However, further investigation of the frontier molecular orbitals and excited state energies and optimized geometries provided new insights for the mechanism of TEMPO radical enhancement of ISC. The excited state calculations were done using the time-dependent (TD)-DFT[64] with the same functional and basis set.

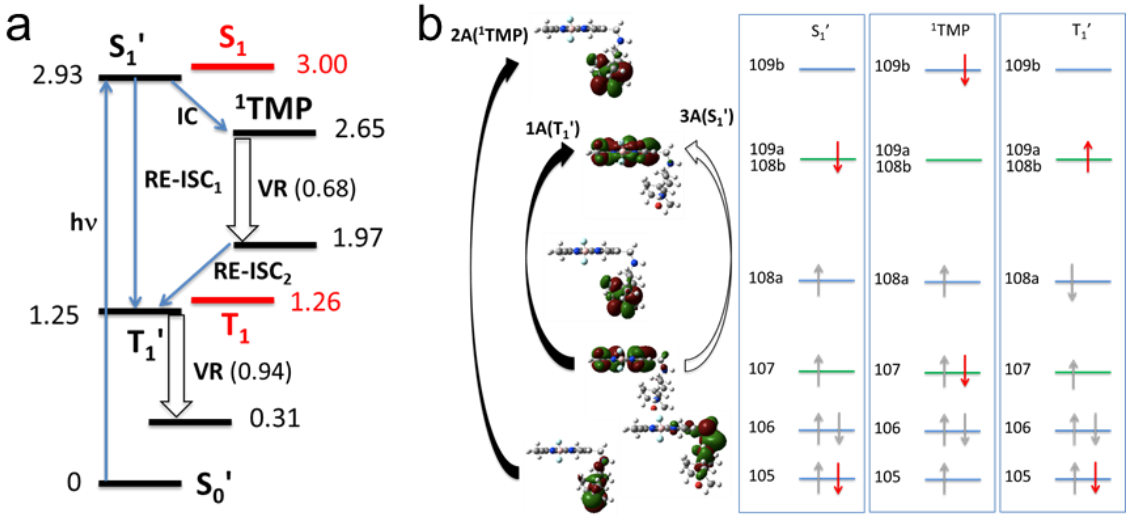

Figure 5.12 (a) The BDP-2AR radical states S_0', S_1', T_1' and the dark ^{1}TMP (in black), and the BDP molecular states S_1 and T_1 (in red). The numbers represent state energy levels in eV, and those in parentheses represent energy change upon vibrational relaxation (VR), also in eV. (b) Frontier molecular orbital of S_0', S_1', T_1' and ^{1}TMP state and corresponding electron configuration, the 107 and 108b/109a are π and π* localized on BDP ring (in green), the rest MOs are mainly contributed by TEMPO radical (in blue). Electron occupying different orbitals in different excited states are marked in red.

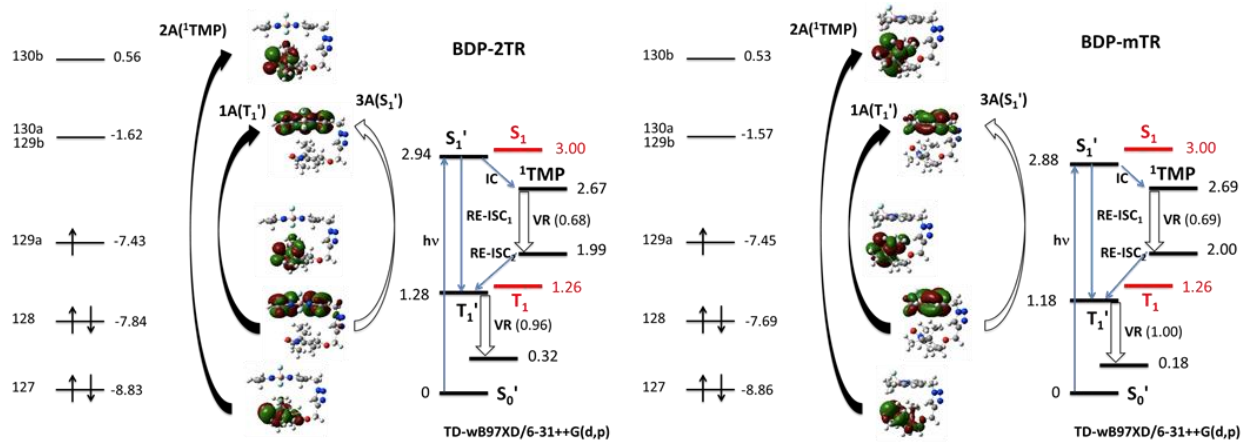

Figure 5.13 The frontier molecular orbital and states energetics for **BDP-2TR** and **BDP-mTR**.

Comparing to the non-radical **BDP**, the TEMPO radical only changed the energetics of singlet and triplet excited states by less than 70 meV in **BDP-2AR**. For **BDP-2TR** and **BDP-mTR**, the two molecules were thought to have weaker spin-orbital coupling due to the longer linker. However, the coupling was actually slightly stronger (~120 meV), likely due to the sandwich conformation. In both Figure 5.12a and Figure 5.13 the DFT calculations indicate that the singlet and triplet excited state energies do not change drastically, proving that the coupling between the radical and BODIPY is relatively weak. There are two possible pathways to generate triplet excited state once the radical is excited to S_1' as shown in Figure 5.12a, either directly through a radical enhanced ISC (denoted RE-ISC_1) via a spin allowed and vibrationally facilitated, off-resonant transition, or a stepwise resonant internal conversion (IC) to a vibrationally excited intermediate (^{1}TMP) followed by vibrational relaxation (VR) and enhanced ISC (RE-ISC_2) via spin allowed and vibrationally facilitated, resonant transition. The RE-ISC_1 pathway could be considered as going from the S_1' electron configuration directly to T_1' shown in Figure 5.12b, during which both the TEMPO radical electron (108a MO) and the BODIPY π^* electron (108b/109a) changes spin simultaneously. RE-ISC_1 is spin allowed since total spin wasn't changed ($\Delta S=0$), however, the

energy difference that needs to be mediated by VR between S_1' and T_1' (~1.7 eV) is too big for this pathway to be favorable. The second pathway, RE-ISC_2, facilitates the ISC process with an additional intermediate state, ^{1}TMP. Via the ^{1}TMP state, the 1.7eV energy gap is broken down into three smaller energy gaps, S_1' to ^{1}TMP (0.3 eV), ^{1}TMP vibrational relaxation (0.7 eV) and ^{1}TMP to T_1' (0.7 eV). During these three steps, the ^{1}TMP state was activated then deactivated acting as an intermediate. The corresponding electron (red on 105 MO) was excited (to 109b MO) then relaxed as shown in Figure 5.12b. This pathway is consisted of three steps each with significantly lower energy difference (<0.7 eV) comparing to RE-ISC_1 (1.7 eV), therefore, RE-ISC_2 is more easily facilitated by VR. Thus, we consider RE-ISC_2 is the more favorable pathway.

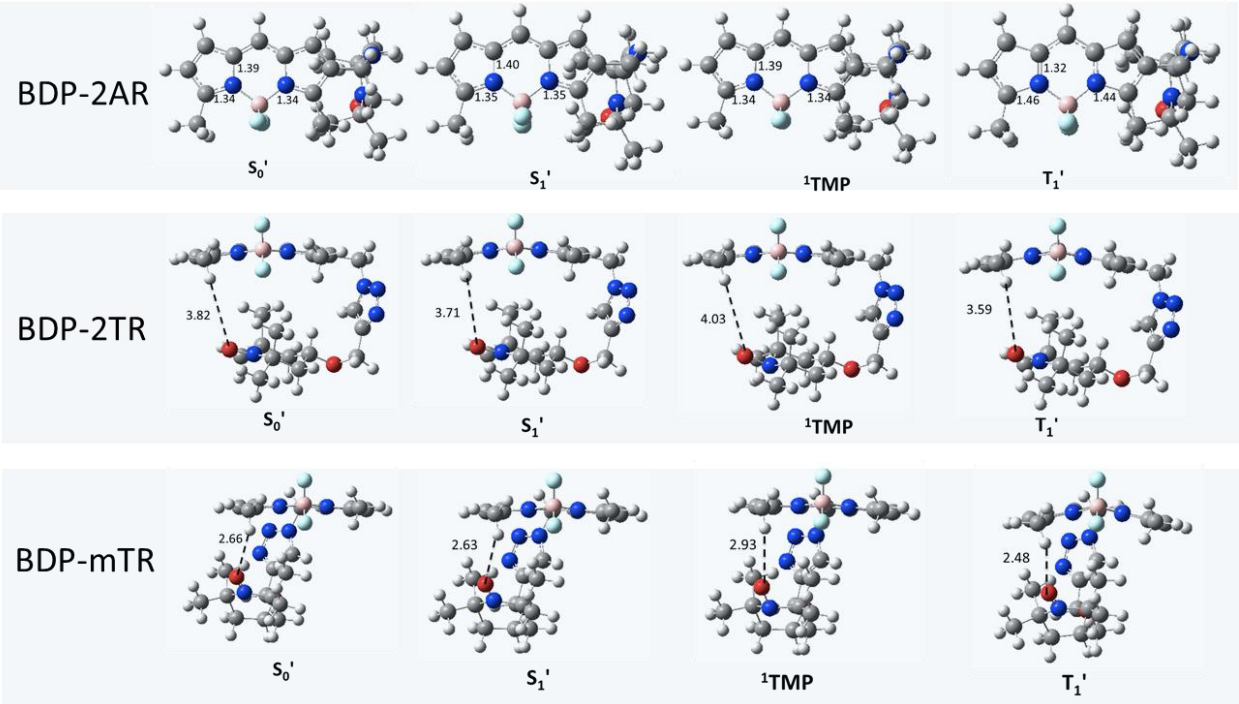

Figure 5.14 The optimized radical geometries in the S_0, S_1, ^{1}TMP and T_1 states for **BDP-2AR**, **BDP-2TR** and **BDP-mTR**. In **BDP-2TR** and **BDP-mTR** the distances between the terminal oxygen atom of TEMPO and a hydrogen atom from 5-methyl of BODIPY are shown.

The lifetime of the T_1' excited state in these three radical species could also be explained by the energy transfer pathway. This pathway is expected to proceed by vibrational relaxation, as discussed previously. Thus, we find it useful to analyze the excited state relaxed geometries to identify the vibrational modes that participate in the triplet decay. It is clear from Figure 5.14 that the extended linker (**BDP-2TR** and **BDP-mTR**) activates a vibrational "hinge" mode between the BODIPY and TEMPO, which provided an additional pathway besides the BODIPY ring in-plane vibrations. The hinge mode mediates the relatively large triplet excited state energy (~0.9 eV) that facilitates a faster decay of the triplet excited state, whereas in **BDP-2AR** the lack of a hinge mode significantly extends the triplet lifetime.

5.3 Conclusion

In conclusion, we observed intramolecular EISC introduced by the TEMPO radical in all of our synthesized BODIPY-TEMPO derivatives, compared to the **BDP** with negligible triplet quantum yield. The EISC effect depended on both BODIPY-TEMPO through-bond distance and the topology of the TEMPO radical with respect to BODIPY core. At a similar BODIPY-TEMPO distance, attaching TEMPO radical to the 2-position of BODIPY led to higher EISC and EIC rates than the *meso*-position. These rates were further increased simultaneously in **BDP-2AR** by the shorter through-bond distance between BODIPY and TEMPO. This is the first time that the distance dependence of radical EISC exhibits a reversed relationship between the EISC rate and the triplet lifetime of chromophore, features that may be due to the less flexible structure of **BDP-2AR**. Since a high ISC rate and a long triplet lifetime are both desirable features of radical EISC, we believe that our findings in these chromophore-radical systems with both properties will contribute to the development of organic radical photosensitizers.

5.4 Reference

1. Prier, C. K.; Rankic, D. A.; MacMillan, D. W. C., *Chem. Rev.* **2013,** *113* (7), 5322--5363.
2. Cakmak, Y.; Kolemen, S.; Duman, S.; Dede, Y.; Dolen, Y.; Kilic, B., . . . Akkaya, E. U., *Angew. Chem. Int. Ed.* **2011,** *50* (50), 11937--11941.
3. Kamkaew, A.; Lim, S. H.; Lee, H. B.; Kiew, L. V.; Chung, L. Y.; Burgess, K., *Chem. Soc. Rev.* **2013,** *42* (1), 77--88.
4. Lim, S. H.; Thivierge, C.; Nowak-Sliwinska, P.; Han, J.; van den Bergh, H.; Wagnières, G., . . . Lee, H. B., *J. Med. Chem.* **2010,** *53* (7), 2865--2874.
5. Zhao, J.; Xu, K.; Yang, W.; Wang, Z.; Zhong, F., *Chem. Soc. Rev.* **2015,** *44* (24), 8904--8939.
6. Rao, A.; Chow, P. C. Y.; Glinas, S.; Schlenker, C. W.; Li, C.-Z.; Yip, H.-L., . . . Friend, R. H., *Nature* **2013,** *500* (7463), 435--9.
7. Wu, W.; Guo, H.; Wu, W.; Ji, S.; Zhao, J., *J. Org. Chem.* **2011,** *76* (17), 7056--64.
8. Zhao, J.; Ji, S.; Guo, H., *RSC Adv.* **2011,** *1* (6), 937--950.
9. Wang, Z.; Zhao, J.; Barbon, A.; Toffoletti, A.; Liu, Y.; An, Y., . . . Hayvali, M., *J. Am. Chem. Soc.* **2017,** *139* (23), 7831--7842.
10. Wen, X.; Xu, W.; Zhao, W.; Khurgin, J. B.; Xiong, Q., *Nano letters* **2018,** *18* (3), 1686-1692.
11. Singh-Rachford, T. N.; Castellano, F. N., *Coord. Chem. Rev.* **2010,** *254* (21-22), 2560--2573.
12. Zhou, J.; Liu, Q.; Feng, W.; Sun, Y.; Li, F., *Chem. Rev.* **2015,** *115* (1), 395--465.
13. Yersin, H.; Rausch, A. F.; Czerwieniec, R.; Hofbeck, T.; Fischer, T., *Coord. Chem. Rev.* **2011,** *255* (21-22), 2622--2652.
14. Romero, N. A.; Nicewicz, D. A., *Chem. Rev.* **2016,** *116* (17), 10075--10166.
15. Bardeen, C. J., *Annu. Rev. Phys. Chem.* **2014,** *65* (1), 127--148.
16. Schmidt, T. W.; Castellano, F. N., *J. Phys. Chem. Lett.* **2014,** *5* (22), 4062--4072.
17. Shockley, W.; Queisser, H. J., *J. Appl. Phys.* **1961,** *32* (3), 510--519.
18. de Wild, J.; Meijerink, A.; Rath, J. K.; van Sark, W. G. J. H. M.; Schropp, R. E. I.; Nelles, G., . . . Wu, Y., *Energy Environ. Sci.* **2011,** *4* (12), 4835--4848.
19. Singh-Rachford, T. N.; Haefele, A.; Ziessel, R.; Castellano, F. N., *J. Am. Chem. Soc.* **2008,** *130* (48), 16164--16165.
20. Zhao, J.; Wu, W.; Sun, J.; Guo, S., *Chem. Soc. Rev.* **2013,** *42* (12), 5323--5351.
21. Turro, N. J.; Kavarnos, G. J.; Cole, T.; Scribe, P.; Dalton, J. C., *J. Am. Chem. Soc.* **1971,** *93* (4), 1032--1034.
22. Koziar, J. C.; Cowan, D. O., *Acc. Chem. Res.* **1978,** *11* (9), 334--341.
23. Carrera, E. I.; Seferos, D. S., *Macromolecules* **2015,** *48* (2), 297--308.
24. Gutierrez, G. D.; Sazama, G. T.; Wu, T.; Baldo, M. A.; Swager, T. M., *J. Org. Chem.* **2016,** *81* (11), 4789--4796.
25. Rey, Y. P.; Abradelo, D. G.; Santschi, N.; Strassert, C. A.; Gilmour, R., *Eur. J. Org. Chem.* **2017,** *2017* (15), 2170--2178.
26. Smith, M. B.; Michl, J., *Chem. Rev.* **2010,** *110* (11), 6891--6936.
27. Franco, L.; Mazzoni, M.; Corvaja, C.; Gubskaya, V. P.; Berezhnaya, L. S.; Nuretdinov, I. A., *Chem. Commun.* **2005,** *33* (16), 2128--2130.
28. Ishii, K.; Hirose, Y.; Kobayashi, N., *J. Am. Chem. Soc.* **1998,** *120* (40), 10551--10552.

29. Ishii, K.; Fujisawa, J.-i.; Adachi, A.; Yamauchi, S.; Kobayashi, N., *J. Am. Chem. Soc.* **1998,** *120* (13), 3152--3158.
30. Takeuchi, S.; Ishii, K.; Kobayashi, N., *J. Phys. Chem. A* **2004,** *108* (16), 3276--3280.
31. Giacobbe, E. M.; Mi, Q.; Colvin, M. T.; Cohen, B.; Ramanan, C.; Scott, A. M., . . . Wasielewski, M. R., *J. Am. Chem. Soc.* **2009,** *131* (10), 3700--3712.
32. Colvin, M. T.; Giacobbe, E. M.; Cohen, B.; Miura, T.; Scott, A. M.; Wasielewski, M. R., *J. Phys. Chem. A* **2010,** *114* (4), 1741--1748.
33. Ito, A.; Shimizu, A.; Kishida, N.; Kawanaka, Y.; Kosumi, D.; Hashimoto, H.; Teki, Y., *Angew. Chem. Int. Ed.* **2014,** *53* (26), 6715--6719.
34. Likhtenstein, G. I.; Ishii, K.; Nakatsuji, S. i., *Photochem. Photobiol.* **2007,** *83* (4), 871--881.
35. Huang, Y.; Egap, E., *Polym. J.* **2018,** *50*, 603--614.
36. Loudet, A.; Burgess, K., *Chem. Rev.* **2007,** *107* (11), 4891--932.
37. Ulrich, G.; Ziessel, R.; Harriman, A., *Angew. Chem. Int. Ed.* **2008,** *47* (7), 1184--1201.
38. Lu, H.; Mack, J.; Yang, Y.; Shen, Z., *Chem. Soc. Rev.* **2014,** *43* (13), 4778--4823.
39. Ahmed, E.; Morton, S. W.; Hammond, P. T.; Swager, T. M., *Adv. Mater.* **2013,** *25* (32), 4504--10.
40. Zhang, J.; Huang, Y.; Wang, D.; Pollard, A. C.; Chen, G.; Egap, E., *J. Mater. Chem. C* **2017,** *5* (23), 5685--5692.
41. Gabe, Y.; Urano, Y.; Kikuchi, K.; Kojima, H.; Nagano, T., *J. Am. Chem. Soc.* **2004,** *126* (10), 3357--3367.
42. Cheng, T.; Zhao, J.; Wang, Z.; An, J.; Xu, Y.; Qian, X.; Liu, G., *Dye. Pigment.* **2016,** *126*, 218--223.
43. Allen, J. P.; Pfrunder, M. C.; McMurtrie, J. C.; Bottle, S. E.; Blinco, J. P.; Fairfull-Smith, K. E., *Eur. J. Org. Chem.* **2017,** *2017* (3), 476--483.
44. Yapici, N. B.; Jockusch, S.; Moscatelli, A.; Mandalapu, S. R.; Itagaki, Y.; Bates, D. K., . . . Bi, L., *Org. Lett.* **2012,** *14* (1), 50--53.
45. Sagar, D.; Bain, C. D.; Verlet, J. R., *Journal of the American Chemical Society* **2010,** *132* (20), 6917-6919.
46. Morris, J. C.; McMurtrie, J. C.; Bottle, S. E.; Fairfull-Smith, K. E., *J. Org. Chem.* **2011,** *76* (12), 4964--4972.
47. Green, S. A.; Simpson, D. J.; Zhou, G.; Ho, P. S.; Blough, N. V., *J. Am. Chem. Soc.* **1990,** *112* (20), 7337--7346.
48. Herbelin, S. E.; Blough, N. V., *J. Phys. Chem. B* **1998,** *102* (42), 8170--8176.
49. Teki, Y.; Miyamoto, S.; Nakatsuji, M.; Miura, Y., *J. Am. Chem. Soc.* **2001,** *123* (2), 294--305.
50. Corvaja, C.; Maggini, M.; Prato, M.; Scorrano, G.; Venzin, M., *J. Am. Chem. Soc.* **1995,** *117* (34), 8857--8858.
51. Miura, Y.; Ushitani, Y.; Inui, K.; Teki, Y.; Takui, T.; Itoh, K., *Macromolecules* **1993,** *26* (14), 3698--3701.
52. Nishide, H.; Kaneko, T.; Nii, T.; Katoh, K.; Tsuchida, E.; Yamaguchi, K., *J. Am. Chem. Soc.* **1995,** *117* (1), 548--549.
53. Chernick, E. T.; Casillas, R.; Zirzlmeier, J.; Gardner, D. M.; Gruber, M.; Kropp, H., . . . Tykwinski, R. R., *J. Am. Chem. Soc.* **2015,** *137* (2), 857--863.
54. Kang, J.; Huo, F.; Yue, Y.; Wen, Y.; Chao, J.; Zhang, Y.; Yin, C., *Dye. Pigment.* **2017,** *136*, 852--858.

55. Boyer, J. H.; Haag, A. M.; Sathyamoorthi, G.; Soong, M.-L.; Thangaraj, K.; Pavlopoulos, T. G., *Heteroat. Chem.* **1993,** *4* (1), 39--49.
56. Green, J. A.; Singer, L. A.; Parks, J. H., *J. Chem. Phys.* **1973,** *58* (7), 2690--2695.
57. Chattopadhyay, S. K.; Das, P. K.; Hug, G. L., *J. Am. Chem. Soc.* **1983,** *105* (20), 6205--6210.
58. Weller, A., *Zeitschrift f \ u r Phys. Chemie* **1982,** *133* (1), 93--98.
59. Adarsh, N.; Avirah, R. R.; Ramaiah, D., *Org. Lett.* **2010,** *12* (24), 5720--5723.
60. Filatov, M. A.; Karuthedath, S.; Polestshuk, P. M.; Savoie, H.; Flanagan, K. J.; Sy, C., . . . Senge, M. O., *J. Am. Chem. Soc.* **2017,** *139* (18), 6282--6285.
61. Wang, Z.; Zhao, J., *Org. Lett.* **2017,** *19* (17), 4492--4495.
62. Chai, J.-D.; Head-Gordon, M., *Phys Chem Chem Phys* **2008,** *10* (44), 6615-6620.
63. Francl, M. M.; Pietro, W. J.; Hehre, W. J.; Binkley, J. S.; Gordon, M. S.; DeFrees, D. J.; Pople, J. A., *The Journal of Chemical Physics* **1982,** *77* (7), 3654-3665.
64. Furche, F.; Ahlrichs, R., *The Journal of Chemical Physics* **2002,** *117* (16), 7433-7447.

6. Chapter 6. Triplet Energy Transfer to Oligothiophene Molecule Sensitized by Quantum Dots

Reproduced in part with permission from Z. Xu, T. Jin, Y. Huang, K. Mulla, F. A. Evangelista, E. Egap and T. Lian, *Chem. Sci.*, 2019, **10**, 6120 **DOI:** 10.1039/C9SC01648A - Published by The Royal Society of Chemistry.

6.1 Introduction

Triplet excitons in organic materials exhibit long lifetime, extended diffusion length and low-lying energy levels,[1-3] and have found promising applications in photon upconversion.[4] For example, an optical upconversion layer on a solar cell can capture sub-bandgap photons and emit above bandgap photons,[5] increasing the efficiency of the conventional single-junction devices beyond the Shockley-Queisser limit.[6] Various strategies for improving the overall efficiency of upconversion systems have been developed. [7-10] In recent years, quantum dot (QD) sensitized upconversion systems [11-14] have attracted intense interest as a versatile and promising approach because of their large absorption coefficient,[15] small singlet-to-triplet energy gap and fast intersystem crossing (ISC) rate,[16] and tunable band gap and band alignment.[17]

In a typical photon-upconversion system, triplet excitons are generated through a sensitizer that undergoes intersystem crossing from an excited singlet state to a triplet state. This process is followed by a sequential triplet energy transfer first to the transmitter then to the emitter. The latter, can undergo triplet-triplet-annihilation (TTA) and emit a higher energy photon. [4, 11, 13, 18-22] Thus, the efficiency of a typical sensitizer-emitter-based upconversion system can be represented by the following equation:[4]

$\Phi_{UC} = \Phi_{ISC}\Phi_{TET}\Phi_{TTA}\Phi_{FL}$ (Eq. 6.1)

The overall upconversion efficiency (Φ_{UC}) is the product of efficiencies in each step involved, namely the ISC of the sensitizer (Φ_{ISC}), the triplet energy transfer (TET)[23] from the sensitizer to transmitter to emitter (Φ_{TET}), TTA of the emitter (Φ_{TTA}), and the emitter's fluorescence (Φ_{FL}). For a specific sensitizer and emitter, $\Phi_{ISC,}$ Φ_{TTA} and Φ_{FL} are determined by the material's properties. A promising area for performance improvement is the design of QD/transmitter complexes to enable efficient TET.[24]

In most reported QD sensitized upconversion systems, the transmitter/emitter molecules are solely limited to acenes and their derivatives, which have limited structural and energetic tunability and poor stability. [11, 13, 18-22, 25] Oligothiophenes have wide range of tunability in energetics and molecular structure,[26] making them a very desirable class of triplet acceptors/transmitters in QD-organic hybrid TTA upconversion systems. Although an example of oligothiophene phosphonic acid grafted to cadmium selenide (CdSe) QDs was previously reported,[27] the photoluminescence quenching was attributed to charge transfer and TET was not observed. We hypothesize that with appropriate design of the energetics of QDs and oligothiophene acceptors, efficient TET transfer can be facilitated while competing single energy and charge transfer pathways may be suppressed (Figure 6.1).

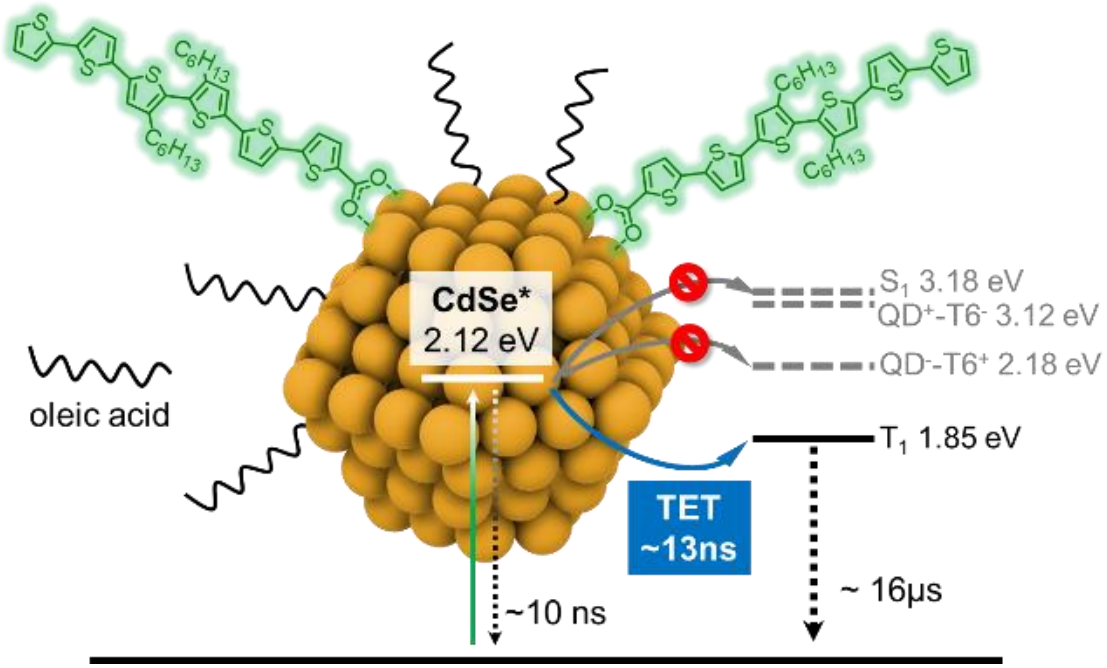

Figure 6.1 Cartoon of QD-T6 complexes showing the energetics of the relevant states and associated excited state decay processes.

In this work, we demonstrate for the first time a successful Dexter-type TET from CdSe QDs to carboxylic acid functionalized oligothiophene (3''',4''-dihexyl-[2,2':5',2'':5'',2''':5''',2'''':5'''',2'''''-sexithiophene]-5-carboxylic acid or **T6,** Figure 6.1). In this system, only the triplet energy transfer from the CdSe QD to T6 is energetically favored while the charge and singlet transfer are energetically uphill. We used transient absorption (TA) spectroscopy to first identify the lowest energy singlet (S_1) and triplet (T_1) state spectral features of free T6 molecules in solution. Then TA study of QD-T6 complexes provide direct evidence for triplet sensitization of T6 by CdSe QD. We also employed Density Function Theory (DFT) computations to characterize the low-lying excited states involved in the triplet-triplet transfer mechanism.

6.2 Results and Discussion

6.2.1 Synthesis, Design and Photophysical Property of T6

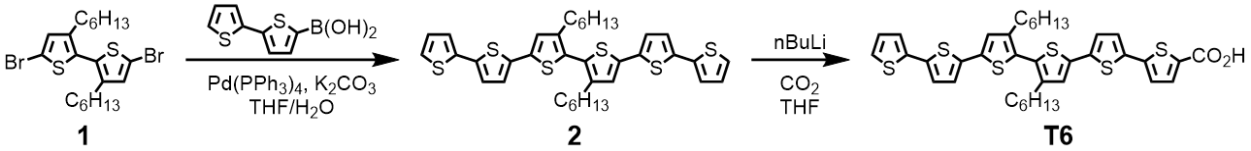

Figure 6.2 Synthesis Steps of T6

A mixture of compound **1** (428 mg, 0.870 mmol), [2,2'-bithiophen]-5-ylboronic acid[28] (0.402 mg, 1.91 mmol) and $Pd(PPh_3)_4$ (101 mg, 0.0870 mmol) was degassed and backfilled with argon three times before 13 mL THF and 3 mL 2M K_2CO_3 aqueous solution were added by syringe. The reaction mixture was stirred at 70 °C overnight before washed with saturated aqueous NH_4Cl solution and extracted with DCM. The organic layer was dried over anhydrous Na_2SO_4 and purified by column chromatography (SiO_2, 1:20 EtOAc-hexanes) to give the compound **2** as a yellow solid (300 mg, 52%). ^{1}H-NMR (400 MHz, $CDCl_3$): δ = 7.20 (dd, J = 5.1, 1.1 Hz, 2H), 7.16 (dd, J = 3.6, 1.2 Hz, 2H), 7.07 (d, J = 3.8 Hz, 2H), 7.06 (d, J = 3.8 Hz, 2H), 7.04 (s, 1H), 7.02 (dd, J = 5.1, 3.6 Hz, 2H), 2.51 (t, J = 7.9 Hz, 4H), 1.57 (quint, J = 7.0 Hz, 4H), 1.25 (m, 12H), 0.85 (t, J = 7.0 Hz, 6H).

To a solution of compound **2** (320 mg, 0.483 mmol) in 12 mL THF at –78 °C was added *n*-BuLi (0.19 mL, 2.5 M in hexanes) and the mixture was stirred for 3 h. Dry CO_2 was bubbled into the mixture at –78 °C for 1.5 h and at –20 °C for another 1 h during which the reaction turned cloudy. The reaction mixture was stirred overnight at room temperature, poured into 1 M HCl, and extracted with EtOAc. The crude product was purified by column chromatography (SiO_2, 99:1 EtOAc-AcOH) to give the T6 as orange red solid (95.0 mg, 29%). ^{1}H NMR (500 MHz, d_6-DMSO): δ = 13.2 (bs, 1H), 7.65 (d, J = 3.9 Hz, 1H), 7.51 (dd, J = 5.1, 1.1 Hz,1H), 7.43 (d, J = 3.8 Hz, 1H),

7.35 (d, J = 3.8 Hz,1H), 7.31-7.24 (m, 6H), 7.09-7.07 (m, 1H), 2.46 (t, J = 7.3 Hz, 4H), 1.51 (quin, J = 6.2 Hz, 4H), 1.20-1.17 (m, 12H), 0.77 (t, J = 6.6 Hz, 6H); ^{13}C NMR (125 MHz, d_6-DMSO): δ = 163.0, 143.93, 143.89, 142.6, 136.9, 136.5, 136.4, 136.1, 136.0, 135.1, 134.77, 134.74, 133.2, 128.9, 127.4, 127.3, 126.8, 126.7, 126.2, 125.7, 125.5, 125.3, 125.2, 124.7, 31.4, 30.3, 28.9, 22.4, 14.3; ESI-HRMS 706.1195 $[M]^+$; calculated for $[M]^+$ 706.1196. The NMR spectra are shown in Figure 6.3, Figure 6.4 and Figure 6.5.

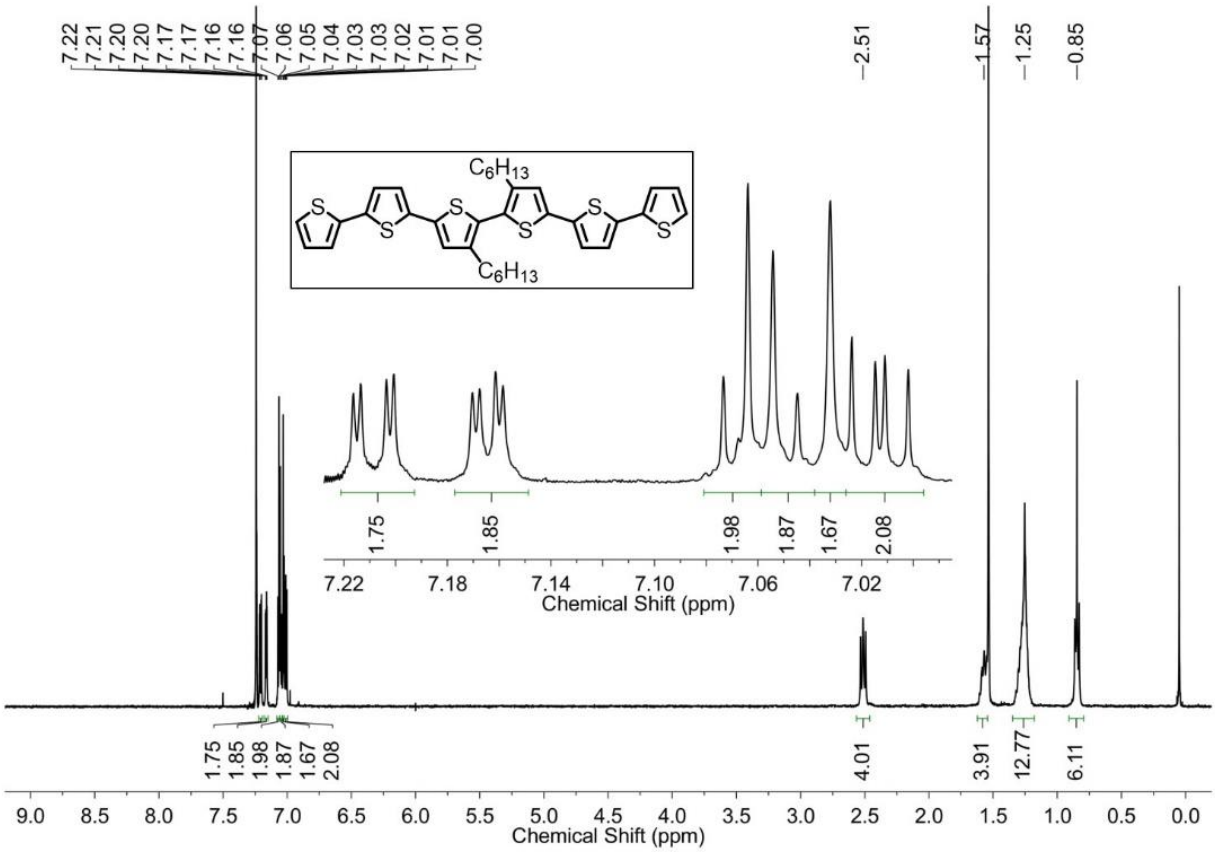

Figure 6.3 ^{1}H-NMR (400 MHz, $CDCl_3$) spectrum of compound **2**.

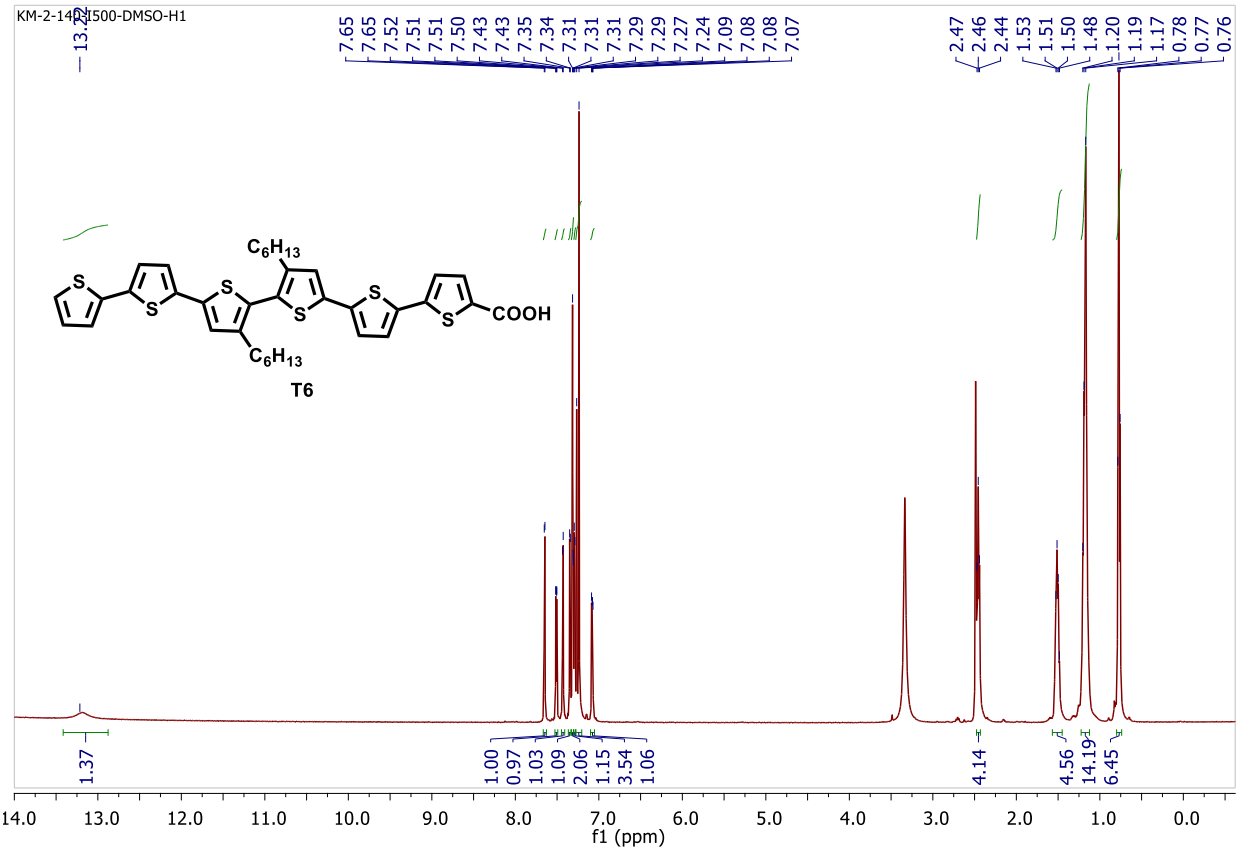

Figure 6.4 ^{1}H-NMR (500 MHz, $CDCl_3$) of compound T6.

5

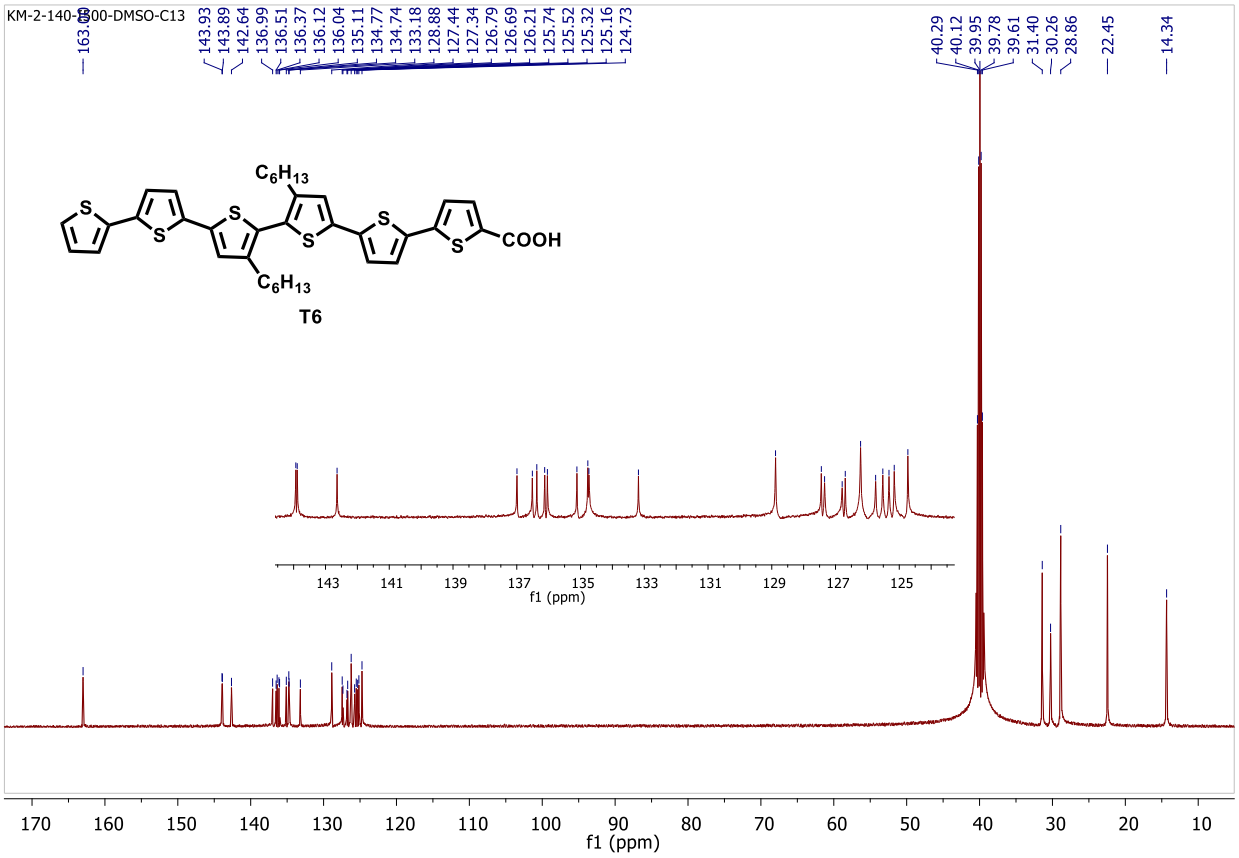

Figure 6.5 ^{13}C-NMR (500 MHz, $CDCl_3$) of compound T6.

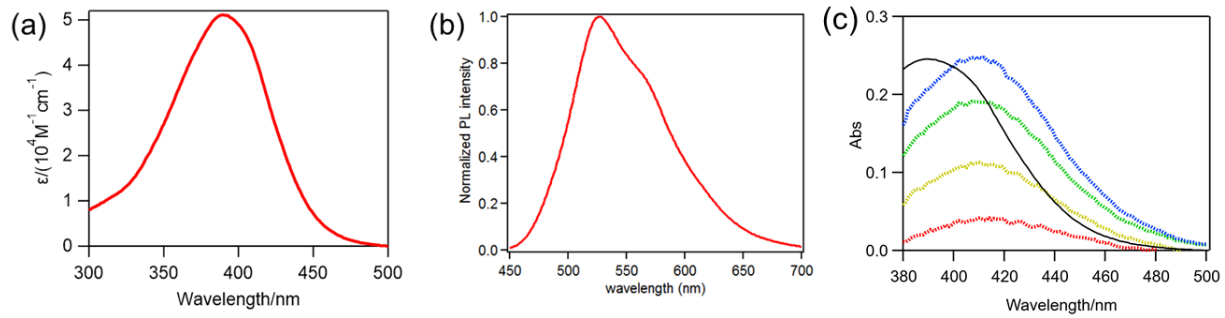

Figure 6.6 (a) Absorption spectra and (b) steady-state fluorescence of T6 in toluene. (c) Comparison of pristine T6 (black solid line) and QD bounded T6 (dashed line) with increasing T6 concentration (red to blue).

QD bounded T6 peak maximum shifted from 390 nm to 415 nm, however, based on the concentration of bounded T6, we calculated the peak maximum extinction coefficient at 415 nm to be 4.9×10^5 $M^{-1}cm^{-1}$, very close to the peak maximum extinction coefficient of pristine T6 at 390 nm (5.0×10^5 $M^{-1}cm^{-1}$). This indicates that the dielectric environment didn't change the transition oscillator strength much. In the later text, we used 4.9×10^5 $M^{-1}cm^{-1}$ for GSB extinction coefficient at 415 nm.

The T6 HOMO level was predicted both from theoretical and experimental method to be at -5.49eV.[29] The LUMO was determined to be at -2.31eV by adding the HOMO level and the optical bandgap measured by UV-Vis.

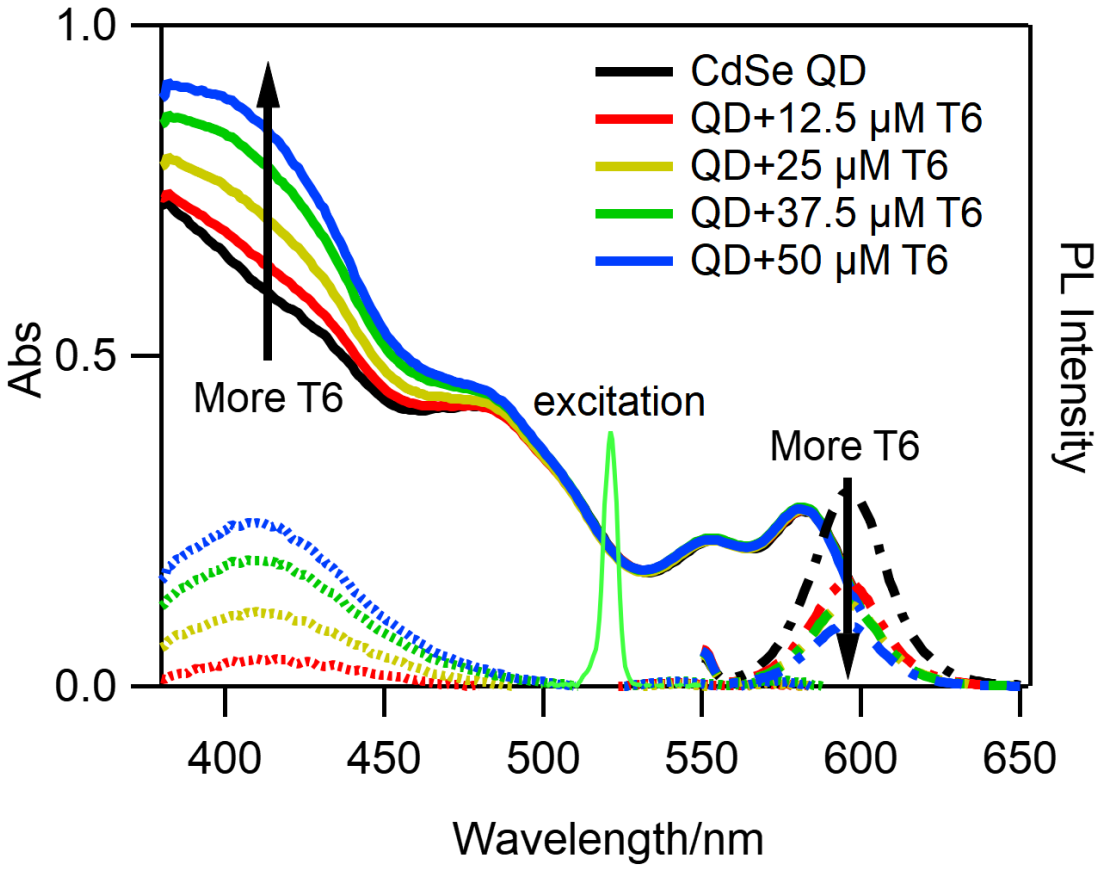

Figure 6.7 UV-Vis absorption (solid lines) and emission (dash-dot lines) spectra of QD-T6 samples with increasing T6 concentrations (0 to 50 microM) in toluene. The emission spectra were

measured with 520 nm excitation of the QDs. Black lines are QD samples without T6. The adsorbed T6 UV-Vis absorption spectra are shown in dashed lines. The excitation pulse used in the transient spectroscopy study is also shown here. The 520 nm pulse has no overlap with T6 absorbance.

T6 (shown in Figure 6.1) was synthesized following a literature procedure[28, 30] and characterized by ^{1}H-NMR, ^{13}C-NMR and high resolution mass spectrometry (Figure 6.3, Figure 6.4 and Figure 6.5). We characterize the QD-T6 complex steady state visible absorption spectra and emission spectra first. The absorption spectra of four QD-T6 complex samples with increasing T6 concentrations ranging from 12.5 to 50 μM are shown in Figure 6.7. These plots show a T6 band at 415 nm and the first excitonic peak of CdSe QDs at 584 nm. In contrast to the absorption spectrum of T6 in toluene (Figure 6.6, Figure 6.7), the QD-bound T6 shows a red-shift of ~20 nm, which is attributed to a change in the dielectric environment and has been observed in a similar system.[31] Subtracting QD contribution from QD-T6 complex allows the determination of total T6 concentration as shown in the legends. However, due to the competitive adsorption of the oleic acid ligand and T6, the QD bounded T6 could not be determined from UV-Vis. This value is later determined by kinetics modeling and fitting. QD photoluminescence (PL) intensity decreased with increasing T6 concentration (Figure 6.7), suggesting possible energy or charge transfer from the QD to T6.

6.2.2 Singlet, Triplet and Intersystem Crossing of T6

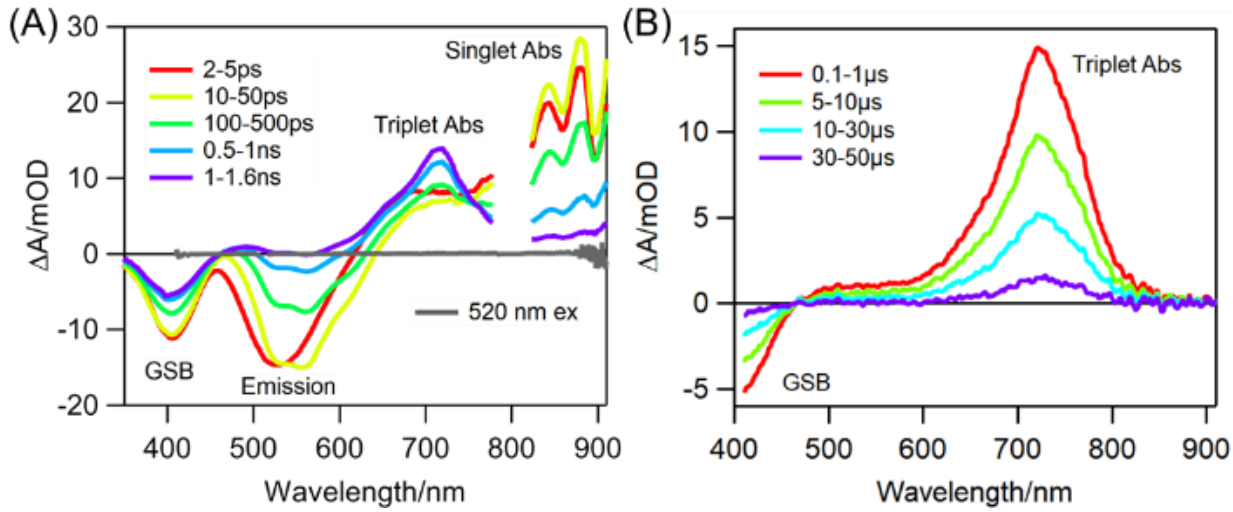

Figure 6.8 TA spectra and kinetics of T6 in toluene. TA spectra of T6 at indicated delay times after 500 microJ/cm^2 400 nm excitation: (A) 0-1.6 ns and (B) 0.1 - 50 microsecond. Data between 780-820 nm in (A) are cut out due to saturated probe light. 520 nm at 1 mJ/cm^2 could not directly excite free T6 as shown in panel A (grey lines, averaged from 2 ps to 1 ns).

To understand the fluorescence quenching mechanism in QD-T6 complexes, we studied pristine T6 first to characterize its excited states spectral signature via TA spectroscopy. The TA spectra of T6 measured with 400 nm excitation (Figure 6.8A, B) show clear evolution from a singlet to triplet excited state on the sub-nanosecond time scale. The TA spectra at < 0.5 ns (Figure 3A) show : (i) a ground (S_0) state bleach (GSB) centered at 400 nm caused by the decrease of ground state T6 molecules; (ii) a stimulated emission from the T6 singlet excited state appearing as a negative signal at 500-600 nm; and (iii) a broad singlet (S_1) excited state absorption (ESA) from 600 nm to 900 nm. The assignment of GSB and stimulated emission of T6 is based on comparison with the steady state absorption and emission spectra shown in Figure 6.6. The (S_1) ESA peak is formed at an early delay time (2-5 ps) and its amplitude grows from 2-5 ps (red) to 10-50 ps (yellow) as the stimulated emission band shifts to longer wavelength (by 20 nm) at the

same time, which is attributed to a fast relaxation from the initial excited state to the *v*=0 vibrational level of the S_1 excited state. Similar fast relaxation processes have also been observed in other oligothiophene molecules.[26, 32-35] Both the S_1 ESA and stimulated emission decay on the sub-nanosecond time scale to form the first triplet excited state (T_1) with an absorption peak (T_1 to T_n transition) centered at 715 nm (Figure 6.8B). The lifetime of this species is longer than 10 μs and can be shortened by more than 1000 times in the presence of oxygen (Figure S7), consistent with the assignment to a T_1 state.[36]

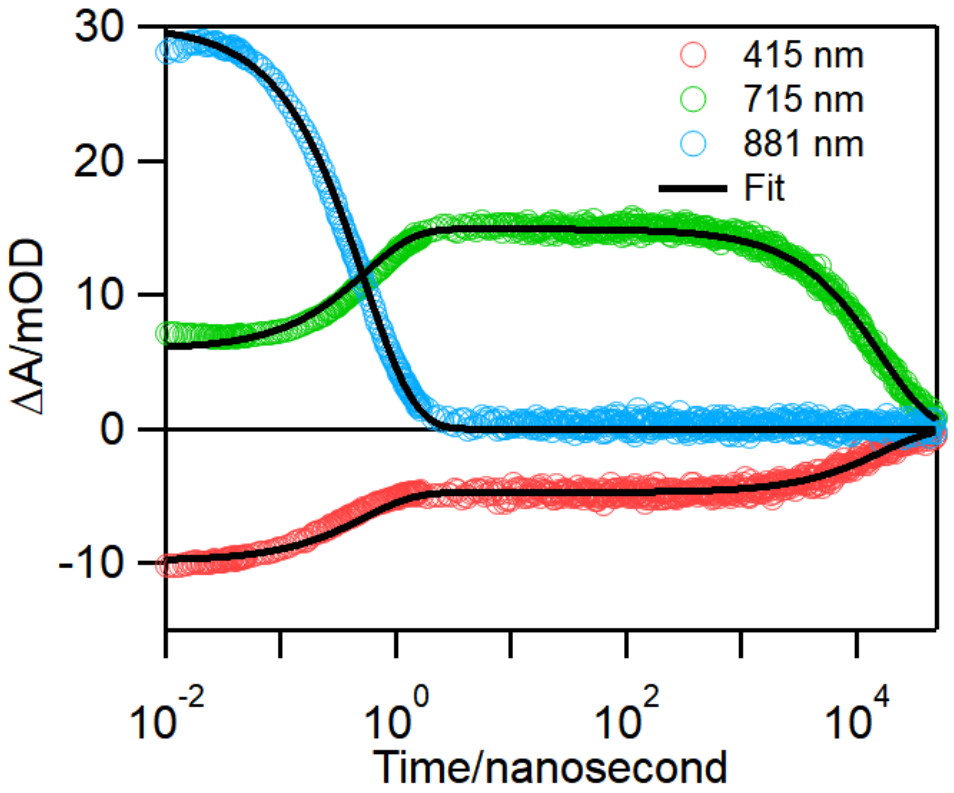

Figure 6.9 T6 kinetics of ground state at 415 nm, singlet at 881 nm and triplet excited state at 715 nm

To determine the rate of excited state decay processes (singlet and triplet decay and the intersystem crossing rate), kinetics at 415 nm (GSB), 715 nm (singlet+triplet ESA) and 881 nm (singlet ESA) were plotted in Figure 6.9 and fitted globally with the model described below. From

the fitting, the intersystem crossing rate k_{isc} is 0.914±0.008 ns^{-1}, the singlet excited state decay rate k_{SD} is 0.963±0.008 ns^{-1}, and the triplet excited state decay rate k_{TD} is 6.12±0.36×10 ms^{-1}. The similar intersystem crossing rate and singlet decay rate resulted in very high triplet yield at 48.7%. Fitting parameters including extinction coefficients of singlet and triplet excited-states are listed in Table 6.1. Related rate constants could be obtained from fitting of the kinetics at several wavelengths. The singlet excited state ($T6_S^*$) could decay by either intersystem crossing (k_{isc}) or return to the ground state (k_{SD}). The intersystem crossing product, triplet excited state ($T6_T^*$), has only one decay pathway that is another intersystem crossing process to the ground state (k_{TD}). Following this model, it is easy to write the expression for the singlet and triplet excited state kinetics.

$$[T6]_S^*(t) = [T6]_S^*(0)e^{-(k_{SD}+k_{isc})t} \qquad \text{Eq 6.1}$$

$$[T6]_T^*(t) = \frac{[T6]_S^*(0)k_{isc}}{k_{SD}+k_{isc}-k_{TD}}[e^{-k_{TD}t} - e^{-(k_{SD}+k_{isc})t}] \qquad \text{Eq 6.2}$$

Eq. 6.2 is a solution to Eq. 6.3 which describes the triplet excited state population growth and decay:

$$\frac{d[T6]_T^*(t)}{dt} = k_{isc}[T6]_S^*(t) - k_{TD}[T6]_T^*(t) \qquad \text{Eq 6.3}$$

Here, two wavelengths are picked to extract the singlet and triplet excited states. Since there is no available wavelength to represent singlet and triplet population individually, a global fitting is needed. One wavelength is the ground state bleach peak at 415 nm, which the signal kinetics could be written as:

$$\Delta A(415nm) = -\varepsilon_{T6}(415nm)\,[[T6]_S^*(t) + [T6]_T^*(t)] \qquad \text{Eq 6.4}$$

$\varepsilon_{T6}(415nm)$ is the extinction coefficient of ground state at 415 nm obtained from steady state UV-Vis absorbance data. Notice that both singlet and triplet excited state will have a contribution to the ground state bleach. Very importantly, we assumed that the singlet and triplet

ESA has very little contribution at 415 nm. The second wavelength is at 715 nm, which is the peak maximum for triplet excited state absorption. This will also serve a purpose to extract the triplet excited state absorption extinction coefficient. However, this wavelength also has a contribution from singlet excited state absorption at early time. Therefore, the expression is written as:

$$\Delta A(715nm) = \varepsilon_S(715nm)[T6]_S^*(t) + \varepsilon_T(715nm)[T6]_T^*(t) \qquad \text{Eq 6.5}$$

$\varepsilon_S(715nm)$ and $\varepsilon_T(715nm)$ is the extinction coefficient of singlet and triplet excited state absorption at 715 nm, respectively. The singlet ESA could be expressed at 881 nm as well by:

$$\Delta A(881nm) = \varepsilon_S(881nm)[T6]_S^*(t) \qquad \text{Eq 6.6}$$

Here Eq. 6.1 and Eq. 6.2 is plugged into Eq. 6.4 to 6.6, the kinetics could be fitted using these two equations globally. The global fitting curve is shown in Figure 6.9. The fitting result is in Table 6.1. In the fitting, the instrument response is also considered and is treated as a convolution with the Eq. 6.4 and 6.5. Here, the $\varepsilon_T(715nm)$ is pre-determined by the ratio of the signal amplitude of 715 nm and 415 nm at later time (>10ns) due to complete depletion of singlet excited state at this time range. The fast relaxation from 1ps to 10ps is ignored to simplify the fitting process. The fitting result gave out several critical parameters listed in Table 6.1 below.

Table 6.1 Global Fitting parameters of T6

PARAMETERS	**VALUE**
$\varepsilon_{T6}(415nm)$	$4.9\times10^{4}M^{-1}cm^{-1}$
$\varepsilon_{S}(881nm)$	$1.14\pm0.006\times10^{5}M^{-1}cm^{-1}$
$\varepsilon_{S}(715nm)$	$2.36\pm0.02\times10^{4}M^{-1}cm^{-1}$
$\varepsilon_{T}(715nm)$	$1.19\pm0.04\times10^{5}M^{-1}cm^{-1}$
k_{SD}	$0.963\pm0.008ns^{-1}$
k_{isc}	$0.914\pm0.008ns^{-1}$
k_{TD}	$6.12\pm0.36\times10^{1}ms^{-1}$
Triplet Yield	$48.7\pm0.8\%$

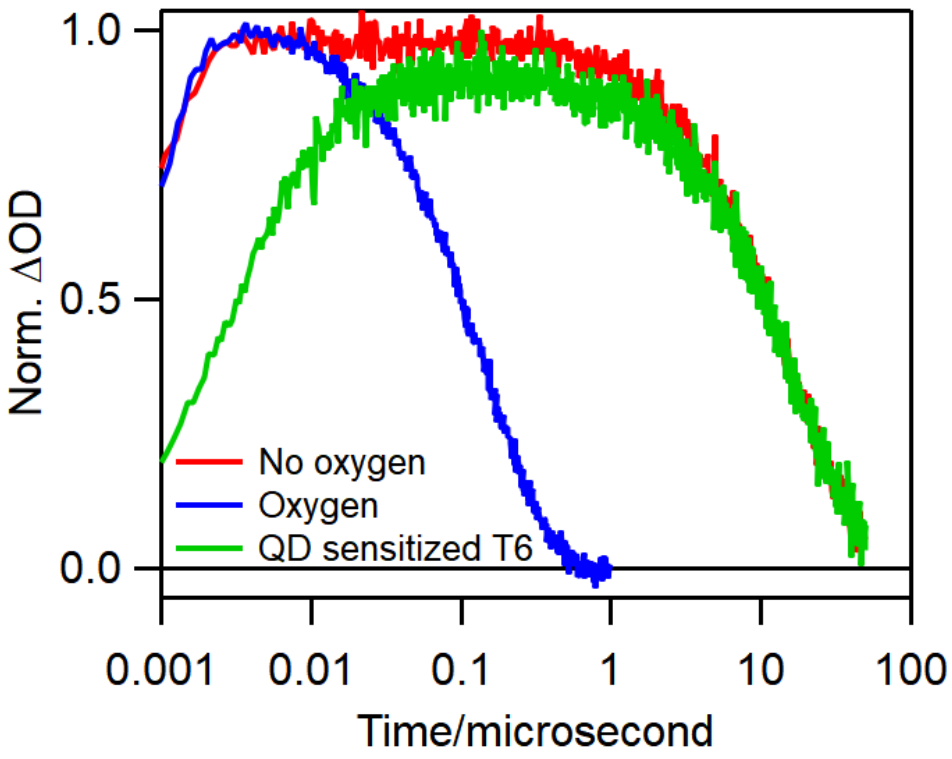

Figure 6.10 Kinetics of T6 triplet ESA signal at 715 nm: T6 without oxygen (Red), T6 with oxygen (Blue) and CdSe-T6 complex without oxygen (Green) are shown.

The triplet lifetime of pristine T6 is shown in Figure 6.10 pristine. Here T6 was excited at 400nm. QD-T6 was excited at 520 nm to avoid exciting T6 directly. An exponential fit is used to fit the decay of the T6 triplet excited state decay. The fitting determined the triplet decay rate is $6.12 \pm 0.36 \times 10^{1}$ ms^{-1} without oxygen, over 1000 times slower than the energy transfer rate constant, therefore, it is acceptable to fit the growth of triplet excited state population without considering the decay. Comparing the T6 triplet lifetime with and without the presence of oxygen, it is very obvious that the T6 triplet is heavily quenched by ground state triplet oxygen.

6.2.3 DFT Calculation of Energetics of T6

To compute oscillator strengths for the $T_1 \rightarrow T_N$ transitions, we performed a TD-DFT calculation at the optimized geometry of the T_1 state using the triplet state as a reference. The

vertical excitation spectrum of T_1 is dominated by a transition at 1.88 eV (659 nm, f_{osc} = 3.70) with a less intense peak at 2.18 eV (568 nm, f_{osc} = 0.24). These results are in good agreement with the experimental observation of a transient peak at 715 nm in the transient absorption spectra for t > 100 ns.

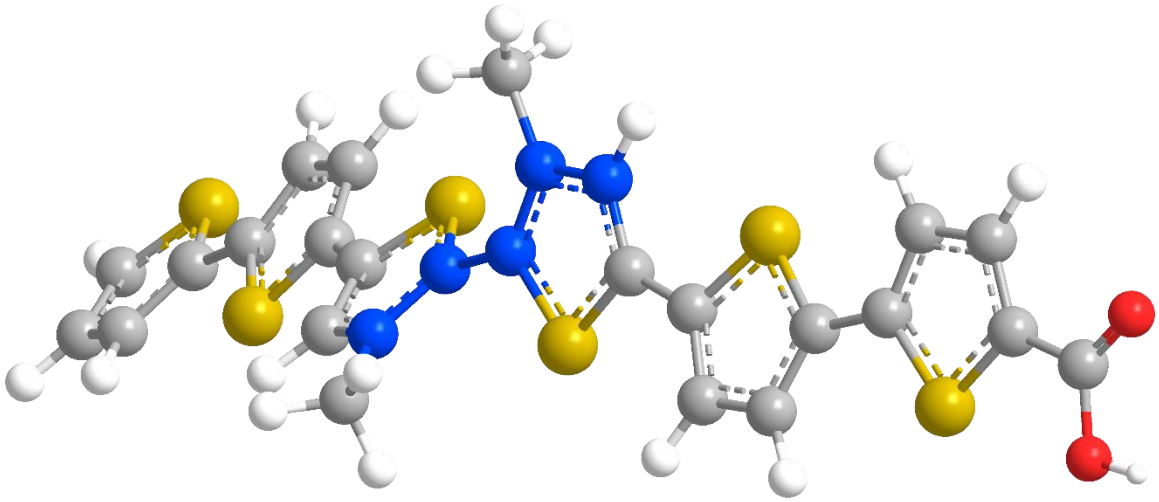

Figure 6.11 Restricted B3LYP/def2-SVP Equilibrium Geometry of the S_0 state. The twist angle ϕ is defined as the di-hedral angle of the third and fourth thiophene ring as shown in the blue carbon atoms.

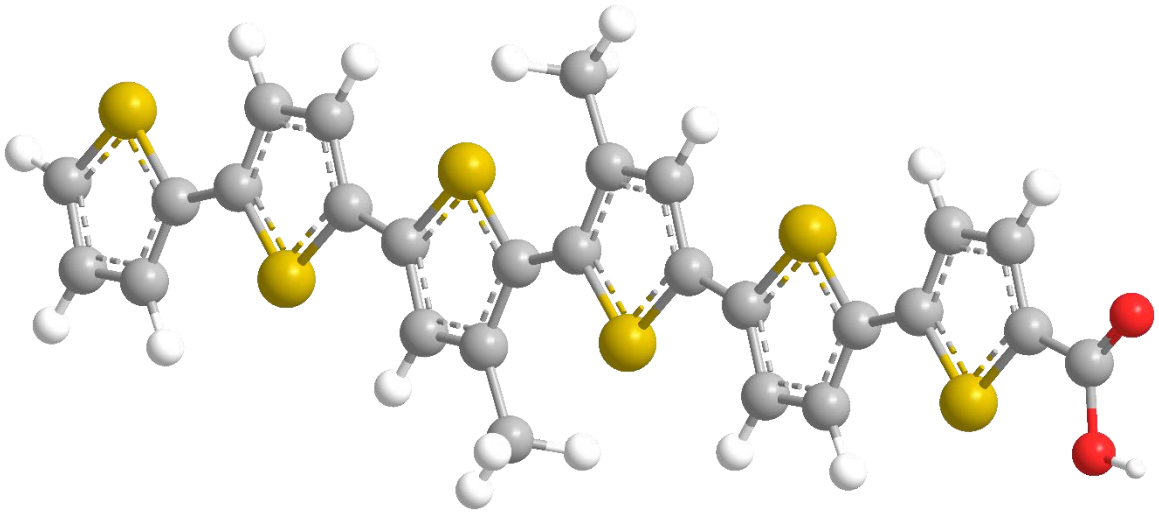

Figure 6.12 Unrestricted B3LYP/def2-SVP Equilibrium Geometry of the T_1 state.

The DFT equilibrium structure of S_0 deviates from planarity due to a twisting of the C-C bond between the third and fourth thiophene rings by an angle ϕ = 44° (see Figure 6.11 for the definition of ϕ). Upon excitation to the T_1 state, T6 undergoes a significant rearrangement from a twisted to a planar structure (ϕ = 0°) as shown in Figure 6.12. The reason for this change in geometry can be traced to the character of the HOMO and LUMO orbitals. While the HOMO is antibonding (π*) with respect to the middle C-C bond and favors a twisted (ϕ = 90°) configuration, the LUMO is a bonding orbital (π) and favors a planar geometry (ϕ = 0°). Therefore, upon excitation of one electron from the HOMO to the LUMO, it is energetically advantageous for the T_1 state to adopt a planar geometry.

Table 6.2 TD-B3LYP and CIS excitation energies (in eV) for T6 computed at the S0 state equilibrium geometry. The geometry was optimized at the restricted B3LYP/def2-SVP level of theory.

	TD-B3LYP	**CIS**
S_0	**0.000**	**0.000**
S_1	**2.562**	**3.459**
S_2	**2.965**	**3.992**
S_3	**3.359**	**4.837**
T_1	**1.848**	**1.747**
T_2	**2.089**	**1.904**
T_3	**2.640**	**2.480**
T_4	**2.824**	**2.774**

Table 6.3 TD-B3LYP and CIS excitation energies (in eV) for T6 computed at the T_1 state equilibrium geometry. The geometry was optimized at the unrestricted B3LYP/def2-SVP level of theory. Note that the B3LYP/def2-SVP T_1 state equilibrium geometry, the S_0 state lies 0.349 eV above the ground state equilibrium energy.

	TD-B3LYP	**CIS**
S_0	**0.000**	**0.000**
S_1	**2.114**	**2.337**
S_2	**2.420**	**3.545**
S_3	**2.994**	**4.360**
T_1	**1.030**	**0.719**
T_2	**1.734**	**1.520**
T_3	**2.266**	**2.061**
T_4	**2.326**	**2.638**

To identify low-lying electronic excited states involved in the triplet-triplet transfer mechanism we performed time-dependent density functional theory (TD-DFT) computations starting from DFT singlet ground state. Vertical excitation energies were performed both at the S_0 and T_1 equilibrium geometries. At the S_0 geometry, T_1 lies 1.85 eV above the ground state and is characterized by a spin-flip HOMO → LUMO excitation. Geometric relaxation of the T_1 state stabilizes it by 0.47 eV, giving an adiabatic S_0 to T_1 transition energy of 1.38 eV. The second triplet state corresponds to a HOMO → LUMO + 1 excitation, with vertical transition energy of 2.10 eV. Interestingly, the energy of the second triplet state does not change significantly upon planarization of the molecule. Inspection of the LUMO + 1 orbital reveals that this orbital does not involve the middle C-C bond, which is likely to reduce the energy dependence with respect to the twisting

angle ϕ. The third and fourth triplet states are predicted to lie at higher energies (2.64 and 2.82 eV) and therefore should not be operative in the observed triplet-triplet energy transfer. Configuration interaction singles (CIS) excitation energies for all triplet states are found to be in good agreement (deviation less than 0.2 eV) with those from TD-B3LYP.

6.2.4 Synthesis and Transient response of CdSe QD.

Cadmium oxide (CdO, 99.5%), selenium powder (Se, 100 mesh, 99.99%), trioctylphosphine oxide (TOPO, 99%), n-octadecylphosphonic acid (ODPA), trioctylphosphine (TOP, 97%) and all other solvents mentioned in synthesis procedures were purchased from Sigma-Aldrich. All chemicals were used without further purification.

CdSe quantum dots were synthesized through a procedure of previous literature[12]. For a typical CdSe synthesis procedure, 120 mg CdO, 560 mg ODPA and 3 g TOPO were mixed in a 50 mL three-neck flask. Upon removing O_2 with Ar, the mixture was heated to 350 °C until the mixture became clear solution. 1 mL TOP was then added into the flask and the system was heated further to 360 °C. After which the solution of 120 mg Se in 1mL TOP was injected quickly into the system. Needle tip aliquots were taken for UV-vis measurement to monitor the reactions until the desired size was achieved. The reaction mixture was then cooled to room temperature, and CdSe was separated by centrifuge and washed twice with toluene and ethanol. The CdSe precipitation was dissolved in toluene. Finally, ligand exchange from TOP to oleic acid was conducted following procedures of previous literature[12]. The CdSe was finally dissolved in toluene and the concentration of CdSe was determined from UV-vis spectrum[15].

The QD VB band edge was determined to be at -5.43eV by the equation[17] $E_{VB} = -5.23 - 0.74D^{-0.95}eV$, the VB band edge is determined to be at -3.31eV by the sum of VB and the band gap obtained from optical transition.

The synthesized T6 powder was dissolved into a toluene solution. 1mL CdSe solution was mixed with certain amount of T6 solution to obtain solutions in which ratios of concentration of CdSe and T6 were 1:1, 2:1, 3:1 and 4:1, respectively. The samples were ultrasonicated for 2 hours at 25 °C and underwent freeze-pump-thaw degassing procedures to remove oxygen in solution. The processed solution was finally stored in a glove box with Argon inert atmosphere and then transferred to a 1 mm path length quartz cell (Starna) for transient absorption experiment.

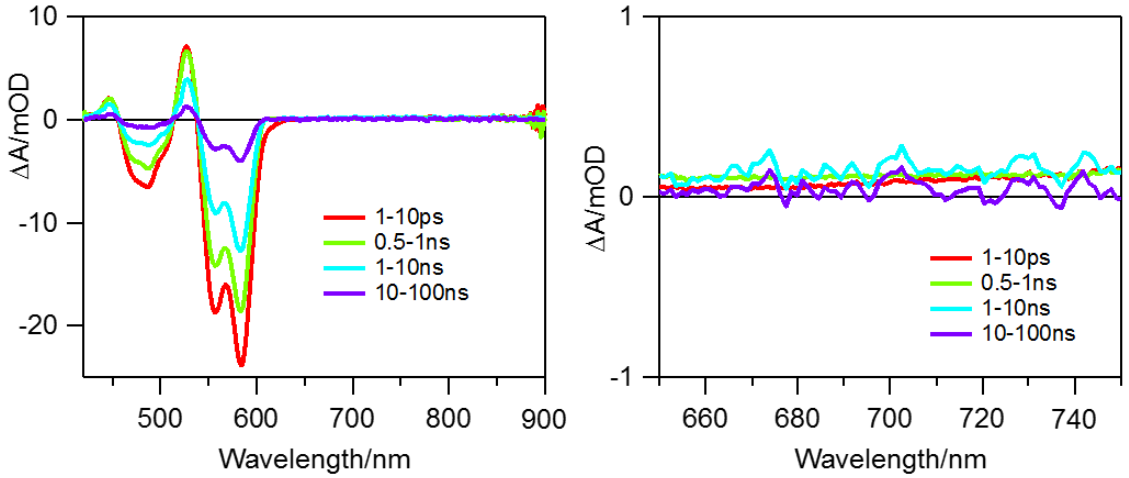

Figure 6.13 Left: Transient absorption spectrum of 584nm CdSe QD under 520nm excitation. Right: Zoom in region of 650-750nm.

The Transient absorption spectra of CdSe QD is shown in Figure 6.13.

6.2.5 CdSe Quantum Dot Sensitized Direct Energy Transfer

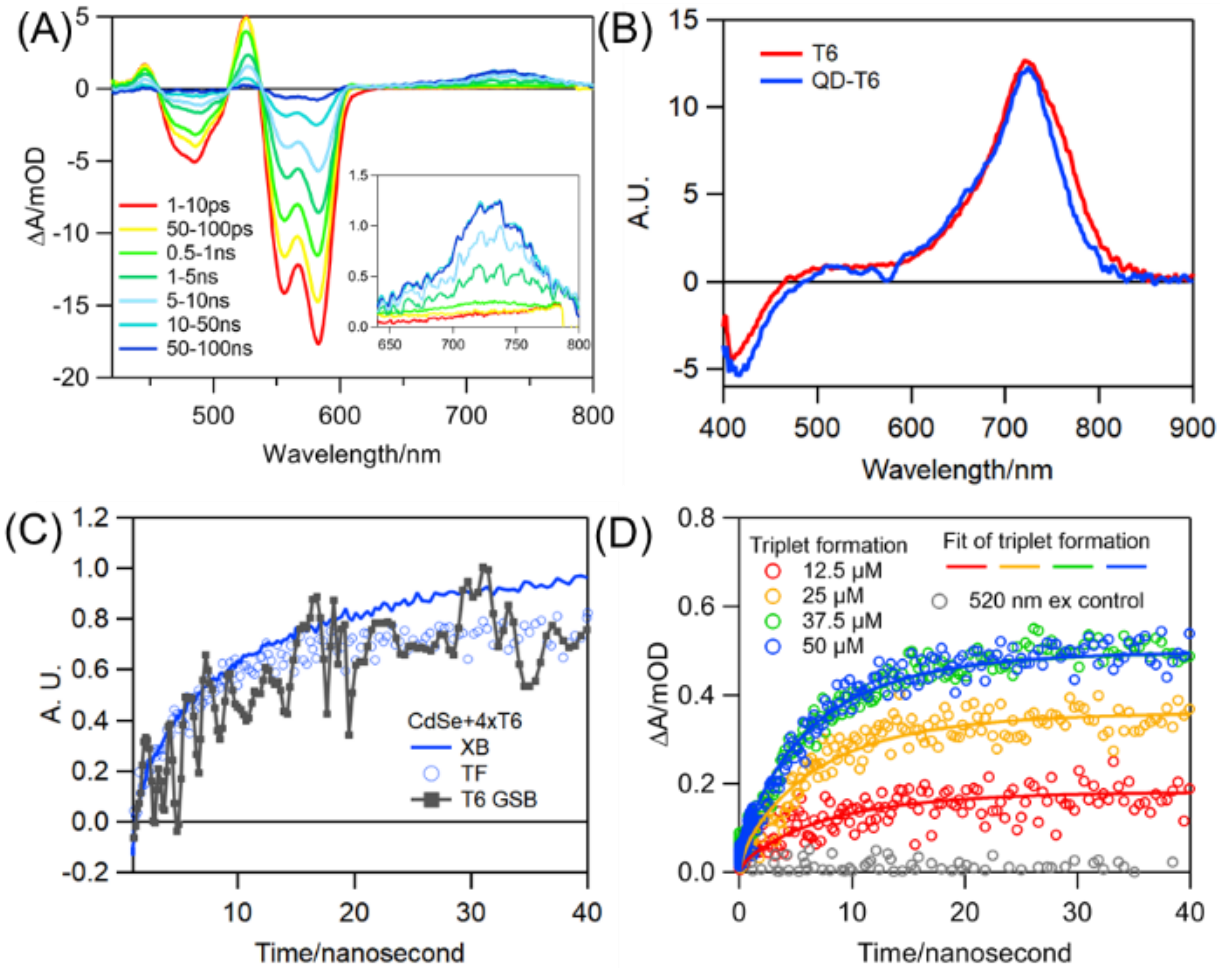

Figure 6.14 Transient spectra and kinetics of QD/T6 complexes measured at 520 nm excitation. (A) TA spectra of QD-T6 excited at indicated delay times. Inset: expanded view of the triplet spectra at 540 -800 nm. (B) Comparison of the averaged TA spectra (from 100 ns to 5 μs) of QD-T6 complexes (excited at 520 nm) and pristine T6 (excited at 400 nm). (C) Comparison of the kinetics of triplet formation of T6 (715 nm, blue circle), T6 GSB (415 nm, grey square, inverted and scaled) and QD exciton bleach (584 nm, blue line, inverted and scaled) in QD-T6 complexes. (D) Kinetics of T6 triplet formation (TF) with increasing T6 concentration (red, yellow, green, blue) in QD-T6 complexes. Solid lines: fits according to a model described in the main text. Grey dots: T6 signal of a control sample with 50 microM T6 and no QD measured

under same condition at 520 nm excitation, showing no triplet signal. Excitation pulse energy density is 35 $\mu J/cm^2$ for panel A, C and D, 500 $\mu J/cm^2$ for panel B.

The mechanism of exciton quenching in CdSe QD/T6 complexes were then studied by transient absorption spectroscopy, which probes directly not only the quenching kinetics, but also the identity of intermediates and products. The TA spectra of the QD-T6 complexes at early delay times (1-10 ps) show that the selective excitation of CdSe QDs at 520 nm (where T6 does not absorb) leads to a QD ground state bleach and excited state absorption[37-40] at 420-620 nm (Figure 6.14A), similar to those observed in QD only samples (Figure 6.13) and indicative of excitons in the QD. The TA spectra at later delay times (Figure 6.14A) show the decay of the QD exciton and the formation of a new absorption peak at 640-800 nm and a S_0 ground state bleach (Figure 6.14B). These features are absent in QD only samples and can be assigned to T6 triplet formation by comparing to the T6 triplet TA spectrum (Figure 6.14B). Control experiment of T6 only samples at 520 nm excitation (grey lines in Figure 6.8A) shows negligible T6 triplet signal in the absence of QDs. Here the TA spectra data directly proved a successful triplet sensitization of T6 by QD.

To determine the mechanism of triplet formation, we compare the kinetics of T6 triplet state growth and exciton decay in QDs. The kinetics of triplet formation (Figure 6.14C) can be monitored by both the triplet ESA (TF, blue circle) and S_0 ground state bleach (GSB, black square). Here, triplet ESA kinetics was obtained by averaging TA signals from 650 nm to 780 nm to increase the signal/noise ratio. The T6 GSB is obtained by subtracting the overlapping QD contribution at 415 nm from the total signal. As reported previously, the CdSe XB signal is dominated by state filling of electrons in the conduction band edge.[37-41] As shown in Figure 6.14C, the triplet formation kinetics agree well with the exciton bleach (XB, blue line) up to ~20 ns, consistent with a direct Dexter type TET from the QD to T6. These kinetics deviate after ~ 20 ns,

which suggests the presence of other exciton decay pathways. As discussed below, we attribute this to the presence of QDs without adsorbed T6, in which excitons decay by radiative and nonradiative pathways within the QD. It has been previously reported that QD sensitized triplet formation can also occur via sequential charge transfer pathways: electron (hole) transfer followed by hole (electron) transfer.[42-44] These pathways would produce $T6^+$ or $T6^-$ intermediates, which are not observed in our study. This observation is also supported by the energetics alignment that prohibits charge transfer or singlet energy transfer shown below in Figure 6.15. Therefore, we attribute this sensitization process to be a direct Dexter-type triplet energy transfer from a triplet exciton state in the QD.

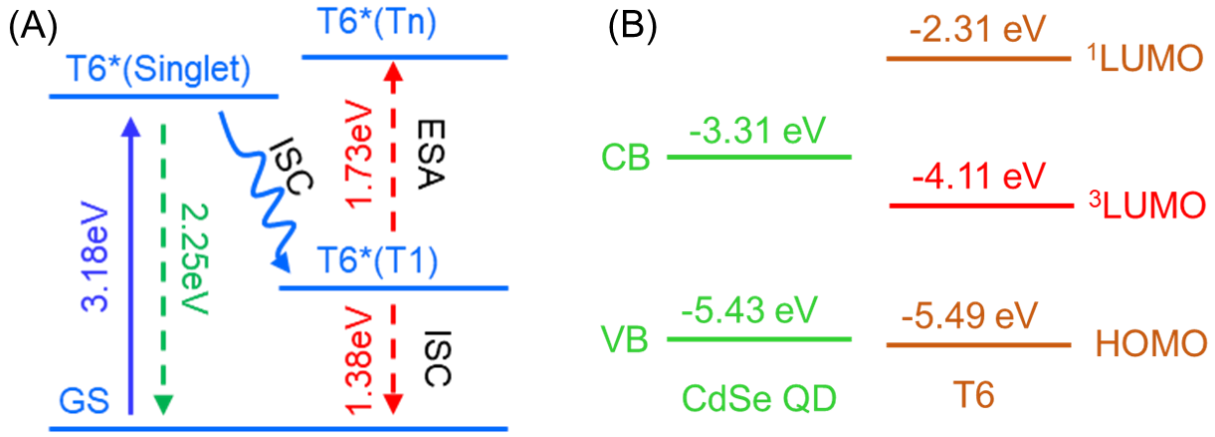

Figure 6.15 (A) T6 energetics obtained by combination of optical absorbance measurements and DFT calculation. The S0 to S1 transition (3.18eV, purple) is measured by UV-Vis absorption. The S1 to S0 emission (2.25 eV, green) is measured by fluorescence spectrum. The T1 excited state energy (1.38eV, red) is obtained by DFT calculation as described above. The T1 to Tn transition (1.73eV, red) is observed by transient absorption measurement. (B) The band alignment between CdSe QD and T6 molecule.

6.2.6 Determine Intrinsic Triplet Energy Transfer Rate

To examine whether TET occurs via static or dynamic quenching mechanisms, we measure TET kinetics as a function of total T6 concentration in the sample. As shown in Figure 6.14D, the final amplitude and apparent formation rate of the T6 triplet state increase with the total T6 concentration, until it reaches saturation. Similar acceptor concentration dependent kinetics has been observed in previous studies of QD/electron acceptor complexes.[40, 45-48] This kinetics can be well described by a model that assumes that the number of adsorbed acceptor molecules in QD/acceptor complexes follows a Poisson distribution and the rate of transfer is proportional to the number of adsorbed acceptors. Assuming the same model for TET in QD/acceptor complexes, we can derive an expression of the kinetics of triplet formation and QD exciton bleach recovery.

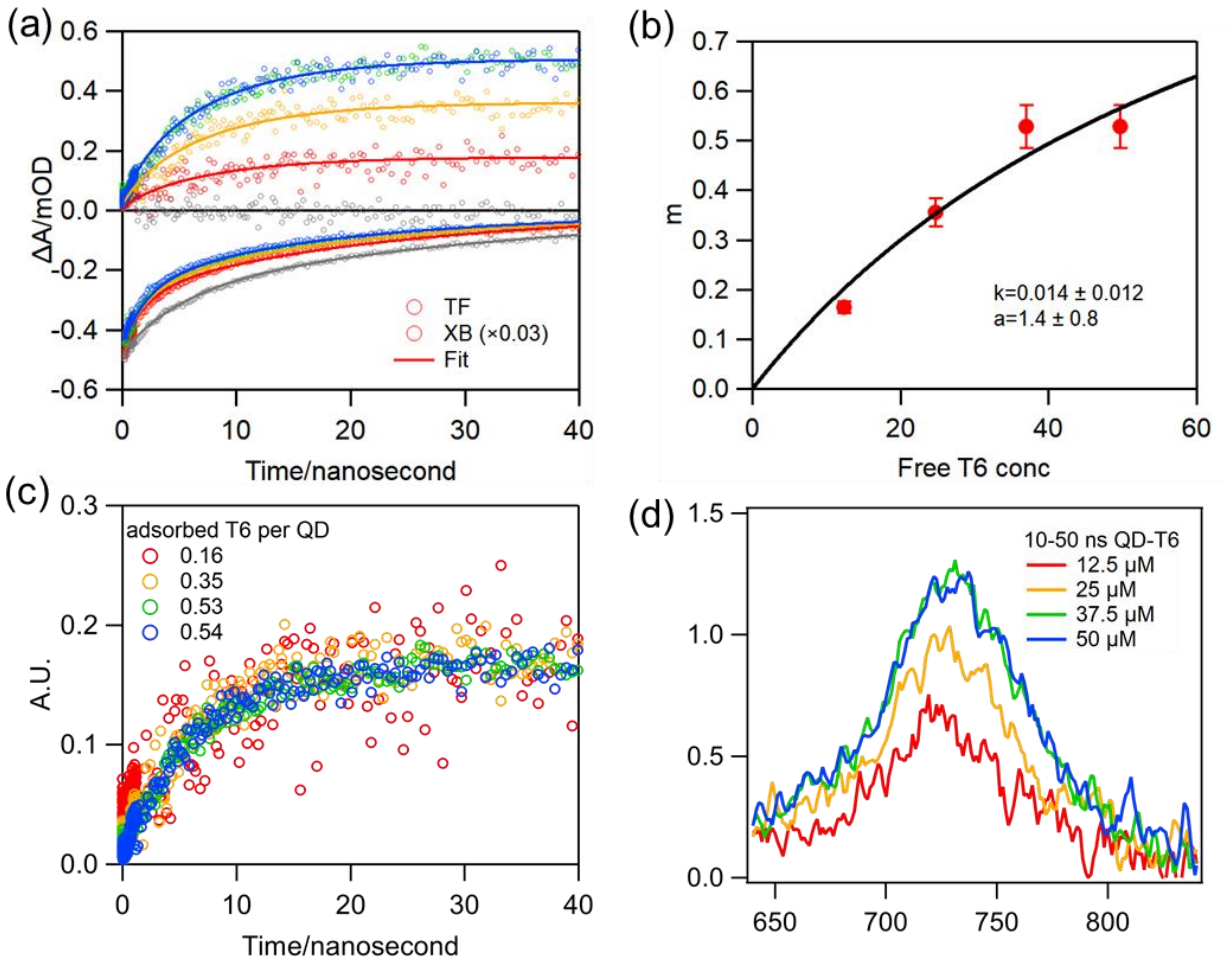

Figure 6.16 (a) Triplet formation kinetics and QD exciton bleach kinetics (circles, grey: QD only; red, yellow, green, blue: QD+1-4xT6 with increasing loading), global fitting (corresponding color solid line). (b) Average adsorption number of T6 (noted as m) dependence on unbounded T6 concentration (red circle), the black solid line showed the Langmuir isotherm fitting results. Here k is the binding constant, a is the maximum adsorption number. (c) Triplet formation kinetics normalized by the averaged bounded T6 number per QD (m) obtained from the fitting in panel b. As the similar growth kinetics shown, the efficiency is still limited by the adsorbed T6 amount. (d) T6 triplet signal at maximum amplitude (10-50 ns averaged) TA spectra with increasing T6 concentration.

QD exciton population can be described as:

$$[QD(t)]^* = [QD(0)]^* e^{-(k_1 + ik_{TET})t} \qquad \text{Eq. 6.7}$$

During the fitting shown in Figure 6.16a using Eq. 6.7, we found that more than one recombination rate k_1 is needed to achieve a reasonable fit. Thus, a coefficient term a_j is added to represent the weight of QD population with different k_{1j}. The apparent triplet energy transfer rate (k_{app}) is obtained from:

$k_{app} = ik_{TET}$ (Eq. 6.8)

i is the number of T6 attached to each QD surface, k_{ET} is the intrinsic energy transfer rate. The T6 triplet growth kinetics the for QD with i T6 can be written as:

$$\frac{d[T6]_T^*(t)}{dt} = [QD(t)]^* ik_{TET} \qquad \text{Eq. 6.9}$$

Previous studies have shown that adsorption of molecules on QD surface follows a Poisson distribution[40, 45-48]. Considering the probability of finding i T6 on QD where the average number of T6 adsorbed per QD is m, T6 triplet excited state growth is written as below with the consideration of Poisson distribution:

$$[T6]_T^*(t) = [QD(0)]^* \sum_i P(m,i) \sum_j a_j \, ik_{ET} \left(\frac{1 - e^{-(k_{1j} + ik_{TET})t}}{k_{1j} + ik_{TET}} \right) \qquad \text{Eq. 6.10}$$

Table 6.4 Poisson Distribution of P(m, i)

i	0	1	2	3	4	5
P(0.5,i)	0.6065	0.3033	0.0758	0.0126	0.0016	0.0002
P(0.16,i)	0.8521	0.1363	<0.01	-	-	-
P(0.35,i)	0.7047	0.2466	0.0432	<0.01	-	-
P(0.53,i)	0.5886	0.3120	0.0827	<0.01	-	-
P(0.54,i)	0.5828	0.3147	0.0849	<0.01	-	-

To simplify the fitting function, only i=1-4 is considered because all terms where i is larger than 5 are negligible according to Table 6.4. Global fitting is used to fit the XB and TF curves in Figure 6.16a with Eq. 6.7 and 6.10 simultaneously. The resulting fitting curves are in solid lines with each curve generating different m value, and the intrinsic TET rate constant being a global parameter is also obtained to be 0.077±0.002ns^{-1}. (m_1=0.16±0.01, m_2=0.35±0.03, m_3=0.53±0.04, m_4=0.54±0.04). Then the triplet formation kinetics in Figure 6.16a is scaled based on the m number obtained from the fitting and plotted in Figure 6.16c. It is easy to notice the similar growth kinetics between different amount of adsorbed T6. This could be explained by realizing the m number obtained is less than 1. This means that, according to Poisson distribution, the QD has mainly two population. One has no T6 bounded, other has only one T6 bounded. This is also calculated in Table 6.4. For all T6 concentration these two population (0 and 1 T6 per QD) takes more than 90% of total QD. In conclusion, the efficiency of TET is limited by the adsorbed amount of T6 in this system.

Langmuir isotherm equation is used to obtain the binding constant and maximum adsorption site for QD-T6 complex due to the competitive adsorption[49]:

$$\frac{m}{\theta} = \frac{K[T6]}{1+K[T6]} \quad \text{Eq. 6.11}$$

Here θ is the maximum binding sites for T6 per QD, K is the binding constant and [T6] is the concentration of unbound T6. From the UV-Vis spectrum and extinction coefficient, the QD concentration and T6 total concentration (including adsorbed on QD and dissolved in the solvent) can be calculated; the unbound T6 concentration can be calculated as [T6_free] = $[T6]_{total}$-m[QD]. By fitting the data shown in Figure 6.16b with Eq. 6.11, the maximum sites and binding constant are obtained. (θ=1.4±0.8, K=0.014±0.012μM^{-1})

The TET efficiency could be estimated by the following equation:

$$\eta = \frac{\Delta A[T6]_T^*}{\varepsilon_T(715nm)} \Big/ \frac{\Delta A[QD]^*}{\varepsilon_{QD}(584nm)}$$

The extinction coefficient of T6 triplet ESA at 715 nm was decided earlier in the pristine T6 fitting, the extinction coefficient of QD is calculated to be $2.238\times10^5 M^{-1}cm^{-1}$ based on previous studies.[3] Notice that the maximum signal amplitude for T6 at 715 nm is 1.6 mOD instead of 0.5 mOD due to the averaging for better signal to noise in the kinetics fitting shown in Figure 4. Therefore,

$$\eta = \frac{\frac{\Delta A[T6]_T^*}{\varepsilon_T(715nm)}}{\frac{\Delta A[QD]^*}{\varepsilon_{QD}(584nm)}} = \frac{\frac{1.6\text{mOD}}{1.19 \pm 0.04 * 10^{-5} M^{-1}cm^{-1}}}{\frac{19.4\text{mOD}}{2.24 * 10^{-5} M^{-1}cm^{-1}}} = 15.4 \pm 0.6\%$$

If the non-radiative channel is not heavily overwhelming, the PL quenching should increase as the TET transfer efficiency increases. The TET efficiency is 4.6%, 9.1%, 15.1%, 15.4% for the QD-T6 complex with T6 concentration at 12.5, 25, 37.5, 50 μM. However, the PL quenching is 46.9%, 57.9%, 57.9% and 67.9% correspondingly as shown in Fig 2. Although the quenching indeed increased with more T6, however, the correlation between these two are not good. This result means that the TET is only one of the pathways that induced the PL quenching. One explanation is that, during the preparation of the QD-T6 complex, the sample undergoes vigorous sonication to force the ligand exchange between the stabilizing oleic acid and T6. This process might have changed the surface ligand coverage for the QD to introduce trap states that quenches PL intensity. This results in the increase of non-radiative decay channel in the QD, which makes the PL intensity only indicative of TET, but not quantitively determination of TET efficiency.

Poisson distribution usually is applied with mean value of adsorbate (m) well above 1. However, in the analysis here the m ranges only from 0.16 to 0.54. This suggests that over 90% of QD population is either free QD or QD with one T6 bounded (Table 6.4). Therefore, the triplet formation kinetics appear similar after normalized by the m (Figure 6.16c) since the triplet formation is mostly contributed by QD with one bounded T6. The increased T6 signal amplitude in Figure 6.14D is mostly contributed by the increased percentage of T6 bounded QD.

From the relative amplitude of the triplet state absorption and QD exciton bleach and their extinction coefficients, we can estimate a TET efficiency of 15.4±0.6% in the sample with 50 μM T6 concentration. The low efficiency can be attributed to both the lower number of adsorbed T6 molecules and slow intrinsic TET rate. The average number of adsorbed T6 per QD is only around 0.5 at the highest coverage level, presumably limited by the competitive adsorption between T6 and the stabilization oleic acid ligand on the QD surface. In comparison, the Castellano group reported CdSe QD to 9-anthracene carboxylic acid (ACA) Dexter TET with an overall rate of 2×10^{9} s^{-1} with an average number of ACA per QD of 12.[12] This yields a similar intrinsic TET rate constant of 0.17 ns^{-1}. To verify this point, we vigorously sonicated the sample with excess amount of T6 (375 μM) and measured the TA spectrum within an hour. This temporarily created a high loading which leads to more efficient TET at 31.8±1.2% as shown in Figure S9. Thus, a promising approach to increase the overall TET rate and efficiency in the T6/QD complex is to improve the binding strength of T6, through perhaps a different anchoring group.

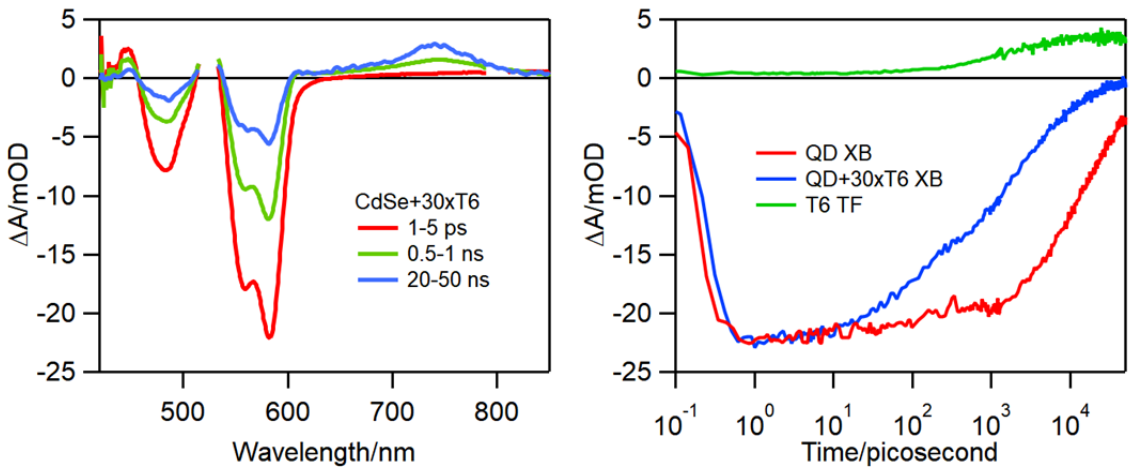

Figure 6.17 TA spectrum and kinetics at QD XB and T6 triplet ESA of 584 nm CdSe with 30 times concentration (375 μM T6) under 520 nm excitation.

CdSe QD with 375 μM T6 after vigorous sonication could temporarily improve the loading amount of T6 on QD surface, thus improve the overall efficiency. Here it is clearly shown in Fig S9 that the triplet signal of T6 is increased at 20-50 ns TA spectrum. At the same time the QD XB recovery rate is also increased. We could calculate the transfer efficiency as below.

$$\eta = \frac{\frac{\Delta A[T6]_T^*}{\varepsilon_T(715nm)}}{\frac{\Delta A[QD]^*}{\varepsilon_{QD}(584nm)}} = \frac{\frac{3.8\text{mOD}}{1.19 \pm 0.04 * 10^{-5} M^{-1} cm^{-1}}}{\frac{22.5\text{mOD}}{2.24 * 10^{-5} M^{-1} cm^{-1}}} = 31.8 \pm 1.2\%$$

6.3 Conclusion

We have demonstrated the first example of triplet energy sensitization of an oligothiophene (T6) by CdSe QDs. By TA spectroscopy we confirmed this process occur via direct Dexter-type triplet energy transfer. The efficiency of TET increases with the concentration of T6 in solution, reaching a value of 15.4±0.6% in the sample with 50 μM T6 and 31.8±1.2% in the sample with 375 μM of T6, although the latter exhibits poor long-term stability. The T6 concentration-

dependent TET kinetics can be understood by a model that assumes a Poisson distribution of adsorbed T6 molecule on the QD. This analysis suggests that TET rates are similar in the 1:1 QD-T6 and previously reported QD-anthracene complexes, but T6 acceptors have relatively weaker binding constant on the surface, which leads to a smaller average number of acceptors and slower apparent TET rate. Our finding suggests that TET efficiency QD-T6 complexes can likely be further improved by increasing the acceptor binding strength (through modification of the acceptor and QD surface ligands) and fine-tuning energetic levels. Finally, this work identifies a new class of stable and highly tunable/functionalizable organic TET acceptors.

6.4 References

1. Bardeen, C. J., *Annual Review of Physical Chemistry* **2014,** *65*, 127-148.
2. Köhler, A.; Bässler, H., *J. Mater. Chem.* **2011,** *21*, 4003-4011.
3. Köhler, A.; Bässler, H., *Materials Science and Engineering: R: Reports* **2009,** *66*, 71-109.
4. Singh-Rachford, T. N.; Castellano, F. N., *Coordination Chemistry Reviews* **2010,** *254*, 2560-2573.
5. de Wild, J.; Meijerink, A.; Rath, J. K.; van Sark, W. G. J. H. M.; Schropp, R. E. I., *Energy & Environmental Science* **2011,** *4* (12), 4835-4848.
6. Shockley, W.; Queisser, H. J., *Journal of Applied Physics* **1961,** *32* (3), 510-519.
7. Peng, J.; Guo, X.; Jiang, X.; Zhao, D.; Ma, Y., *Chemical Science* **2016,** *7* (2), 1233-1237.
8. Wu, T. C.; Congreve, D. N.; Baldo, M. A., *Applied Physics Letters* **2015,** *107* (3).
9. Yanai, N.; Kozue, M.; Amemori, S.; Kabe, R.; Adachi, C.; Kimizuka, N., *Journal of Materials Chemistry C* **2016,** *4* (27), 6447-6451.
10. Yanai, N.; Kimizuka, N., *Accounts of Chemical Research* **2017,** *50* (10), 2487-2495.
11. Huang, Z.; Li, X.; Mahboub, M.; Hanson, K. M.; Nichols, V. M.; Le, H., . . . Bardeen, C. J., *Nano Letters* **2015,** *15* (8), 5552-5557.
12. Mongin, C.; Garakyaraghi, S.; Razgoniaeva, N.; Zamkov, M.; Castellano, F. N., *Science* **2016,** *351* (6271), 369-372.
13. Gutierrez, G. D.; Sazama, G. T.; Wu, T.; Baldo, M. A.; Swager, T. M., *J. Org. Chem.* **2016,** *81* (11), 4789--4796.
14. Okumura, K.; Mase, K.; Yanai, N.; Kimizuka, N., *Chem-Eur J* **2016,** *22* (23), 7721-7726.
15. Yu, W. W.; Qu, L.; Guo, W.; Peng, X., *Chemistry of Materials* **2003,** *15* (14), 2854-2860.
16. Scholes, G. D.; Rumbles, G., *Nat Mater* **2006,** *5* (9), 683-696.
17. Jasieniak, J.; Califano, M.; Watkins, S. E., *ACS Nano* **2011,** *5* (7), 5888-5902.
18. Huang, Z.; Li, X.; Yip, B. D.; Rubalcava, J. M.; Bardeen, C. J.; Tang, M. L., *Chemistry of Materials* **2015,** *27* (21), 7503-7507.
19. Mahboub, M.; Huang, Z.; Tang, M. L., *Nano Letters* **2016,** *16* (11), 7169-7175.

20. Gray, V.; Xia, P.; Huang, Z.; Moses, E.; Fast, A.; Fishman, D. A., . . . Lee Tang, M., *Chem Sci* **2017,** *8* (8), 5488-5496.
21. Mahboub, M.; Maghsoudiganjeh, H.; Pham, A. M.; Huang, Z.; Tang, M. L., *Advanced Functional Materials* **2016,** *26* (33), 6091-6097.
22. Huang, Z.; Simpson, D. E.; Mahboub, M.; Li, X.; Tang, M. L., *Chemical Science* **2016,** *7* (7), 4101-4104.
23. L. J. Dexter, D., 1953; Vol. 21, p 836-850.
24. Huang, Z.; Tang, M. L., *Journal of the American Chemical Society* **2017,** *139* (28), 9412-9418.
25. Reddy, A. R.; Bendikov, M., *Chemical Communications* **2006,** (11), 1179-1181.
26. Becker, R. S.; deMelo, J. S.; Macanita, A. L.; Elisei, F., *J Phys Chem-Us* **1996,** *100* (48), 18683-18695.
27. Stalder, R.; Xie, D.; Zhou, R.; Xue, J.; Reynolds, J. R.; Schanze, K. S., *Chemistry of Materials* **2012,** *24* (16), 3143-3152.
28. Dufresne, S.; Hanan, G. S.; Skene, W. G., *The Journal of Physical Chemistry B* **2007,** *111* (39), 11407-11418.
29. Camarada, M. B.; Jaque, P.; Diaz, F. R.; del Valle, M. A., *J Polym Sci Pol Phys* **2011,** *49* (24), 1723-1733.
30. Huang, Y.; Xu, Z.; Jin, S.; Li, C.; Warncke, K.; Evangelista, F. A., . . . Egap, E., *Chemistry of Materials* **2018,** *30* (21), 7840-7851.
31. Huang, Z.; Xu, Z.; Mahboub, M.; Li, X.; Taylor, J. W.; Harman, W. H., . . . Tang, M. L., *Angewandte Chemie* **2017,** *129* (52), 16810-16814.
32. Becker, R. S.; Demelo, J. S.; Macanita, A. L.; Elisei, F., *Pure Appl Chem* **1995,** *67* (1), 9-16.
33. Yang, J. P.; Paa, W.; Rentsch, S., *Chemical Physics Letters* **2000,** *320* (5-6), 665-672.
34. Yang, J. P.; Paa, W.; Rentsch, S., *Synthetic Met* **1999,** *101* (1-3), 624-625.
35. Lap, D. V.; Grebner, D.; Rentsch, S., *J Phys Chem A* **1997,** *101* (2), 107-112.
36. Grewer, C.; Brauer, H.-D., *The Journal of Physical Chemistry* **1994,** *98* (16), 4230-4235.
37. Chen, J. Q.; Wu, K. F.; Rudshteyn, B.; Jia, Y. Y.; Ding, W. D.; Xie, Z. X., . . . Lian, T. Q., *Journal of the American Chemical Society* **2016,** *138* (3), 884-892.
38. Zhu, H.; Song, N.; Lian, T., *Journal of the American Chemical Society* **2010,** *132* (42), 15038-15045.
39. Huang, J.; Huang, Z.; Yang, Y.; Zhu, H.; Lian, T., *J Am Chem Soc* **2010,** *132* (13), 4858-64.
40. Huang, J.; Stockwell, D.; Huang, Z.; Mohler, D. L.; Lian, T., *J Am Chem Soc* **2008,** *130* (17), 5632-3.
41. Klimov, V. I., *Annu Rev Phys Chem* **2007,** *58*, 635-673.
42. Garakyaraghi, S.; Mongin, C.; Granger, D. B.; Anthony, J. E.; Castellano, F. N., *The Journal of Physical Chemistry Letters* **2017,** *8* (7), 1458-1463.
43. Skourtis, S. S.; Liu, C.; Antoniou, P.; Virshup, A. M.; Beratan, D. N., *Proceedings of the National Academy of Sciences* **2016,** *113* (29), 8115-8120.
44. Weinberg, D. J.; Dyar, S. M.; Khademi, Z.; Malicki, M.; Marder, S. R.; Wasielewski, M. R.; Weiss, E. A., *Journal of the American Chemical Society* **2014,** *136* (41), 14513-14518.
45. Boulesbaa, A.; Issac, A.; Stockwell, D.; Huang, Z.; Huang, J.; Guo, J.; Lian, T., *J Am Chem Soc* **2007,** *129* (49), 15132-3.

46. Tagliazucchi, M.; Tice, D. B.; Sweeney, C. M.; Morris-Cohen, A. J.; Weiss, E. A., *ACS Nano* **2011,** *5* (12), 9907-17.
47. Issac, A.; Jin, S.; Lian, T., *J Am Chem Soc* **2008,** *130* (34), 11280-1.
48. Jin, S.; Hsiang, J. C.; Zhu, H.; Song, N.; Dickson, R. M.; Lian, T., *Chem Sci* **2010,** *1* (4), 519-526.
49. Morris-Cohen, A. J.; Vasilenko, V.; Amin, V. A.; Reuter, M. G.; Weiss, E. A., *ACS Nano* **2012,** *6* (1), 557-65.

7. Chapter 7. Photophysics of a Quantum Dot based Photon Upconversion

Reproduced in part with permission from Huang, Z., Xu, Z., Mahboub, M., Li, X., Taylor, J. W., Harman, W. H., ... & Tang, M. L. (2017). *Angewandte Chemie International Edition*, *56*(52), 16583-16587.

7.1 Introduction

It remains challenging to control light-matter interactions at the nanoscale. Compared to bulk materials, quantum confined semiconductor nanocrystals, or quantum dots (QDs), have tunable band gaps; strong, stable emission; and low thresholds for multiple exciton generation.[1-5] These properties make QDs potentially useful for solid-state lighting,[6] bioimaging[7] and next-generation photovoltaic applications.[8] More recently, QDs have been shown to be excellent triplet sensitizers for photon upconversion[9-11] because of the small energy difference between their singlet and triplet exciton states.[12-13] Efficient triplet energy transfer (TET) from CdSe QDs to molecular acceptors has been demonstrated.[14-15] However, efforts to achieve efficient triplet sensitization in the infrared have been hampered in part by competition with other exciton decay pathways (such as electron or hole transfer and nonradiative recombination within the QD). Previous studies have shown that core/shell structures with type I or type II band alignments between the core and shell materials can be used to control the spatial distribution of the electron and hole.[16-17] This offers additional control of the rate of electron and hole transfer. In principle, such core/shell heterostructures can also be used to selectively suppress charge transfer and enhance TET.

Here, by introducing a sub-monolayer thick layer of cadmium sulfide on lead sulfide NCs, we demonstrate that the linear photon upconversion quantum yield (QY) is enhanced by a factor

of 1.4, from 3.5% to 5.0%. This photon upconversion system consists of QD sensitizers (PbS or PbS/CdS), surface-bound transmitter ligands (5-carboxylic acid tetracene, or **5-CT**), and triplet annihilators (rubrene). Transient absorption (TA) spectroscopy on the exciton decay pathway in QD//**5-CT** complexes shows that in the PbS/CdS core/shell heterostructure, the sub-monolayer CdS shell suppresses the hole transfer processes and prolongs the lifetime of the **5-CT** triplet excited state, thus enhancing the efficiency of TET, Φ_{TET}, from the QD donor to the transmitter ligand. Our data shows that hole transfer from the PbS QD to **5-CT** is detrimental to TET and does not contribute to triplet formation, in contrast to a related system composed of PbS QDs and surface bound pentacene.[18]

7.2 Results and Discussion

7.2.1 Synthesis of PbS QD, PbSCdS QD and 5-CT

2.7 nm diameter PbS QD were synthesized following the method of Hines and Scholes.[19-20]

3.2 nm diameter PbS/CdS core-shell QD was synthesized with cation exchange.[11, 21] First, a cadmium-oleate stock solution was made by dissolving 30 mg of $Cd(OAc)_2 \cdot H_2O$ in 88.7 μL of oleic acid and 347.9 μL of 1-octadecene at 120 °C until a clear solution forms. 176 μL of this Cd-oleate stock solution was transferred into 4 mL vials. Then 277 μL of 30 mg/mL of 3.2 nm diameter PbS core solution was injected to the Cd-oleate solution while stirring at 90 °C. Right after injection, the temperature was set to 80 °C. After 19 min, 0.416 μL of hexane was injected to quench the reaction. The QD were precipitated with acetone and centrifuging at 7800 rpm for 5 min. The black pellet was then redispersed in hexane. The precipitation/ redispersion procedure

was repeated three more times with a combination of methanol/ hexane. After the final precipitation, the QD were dissolved in 1 mL toluene and stored in the glovebox in the dark. The thickness of the CdS shell on the QD was determined by the difference of the QD sizes before and after cation exchange reaction based on the absorption λ_{max} of the PbS core. The concentration of QD were determined by the absorption at 400 nm.[22]

5-CT was synthesized following published work.[23]

PbS//**5-CT** complex: Ligand exchange reaction was performed by mixing 10 µM QD with 500 µM **5-CT** in toluene and stirring for 40 min. Acetone was added as a bad solvent to crash out the QD//**5-CT** complex by centrifuging for 5 min at 7830 rpm. The clear supernatant was discarded. For the upconversion sample, the pellet was redispersed in 20 mM rubrene/toluene solution and then transferred to 1 cm by 1 cm path length Starna cuvettes containing 100 µm thick borosilicate capillary tubes adhered to the wall. The solution will diffuse up through the space inside the capillary tube. The final concentration of QD is 10 µM. The upconversion sample is loaded in a 100 µm path length capillary tube to minimize the reabsorption of upconverted photon by QDs. For transient absorption measurements, the pellet was redispersed in toluene and transferred in a 1 mm path length cuvette sealed with greased Teflon cap and electrical tape. The final concentration of QD is 50 µM. All samples were prepared in an argon glovebox.

PbS/CdS//**5-CT** complex: methods and conditions are the same as those for PbS//**5-CT** except that the concentration of **5-CT** in ligand exchange solution is 300 µM, and methanol is used as the bad solvent to crash out the complex instead of acetone.

As controls in the transient absorption measurements, PbS and PbS/CdS QD capped with oleic acid are prepared by dissolving as-synthesized QD in toluene with the same QD concentrations as those for QD//**5-CT** complexes.

The photon upconversion QY, Φ_{UC} is defined as:

$$\Phi_{UC} = 2 \times \Phi_{ref} \times \frac{(photons\ absorbed\ by\ reference)}{(photons\ absorbed\ by\ UC\ sample)} \times \frac{PL\ signal(UC\ sample)}{PL\ signal(reference)} \quad \text{Eq 7.1}$$

where Φ_{ref} is the photoluminescence QY of the rubrene reference, which is 98% in toluene.

7.2.2 PbS QD Sensitized Photon Upconversion

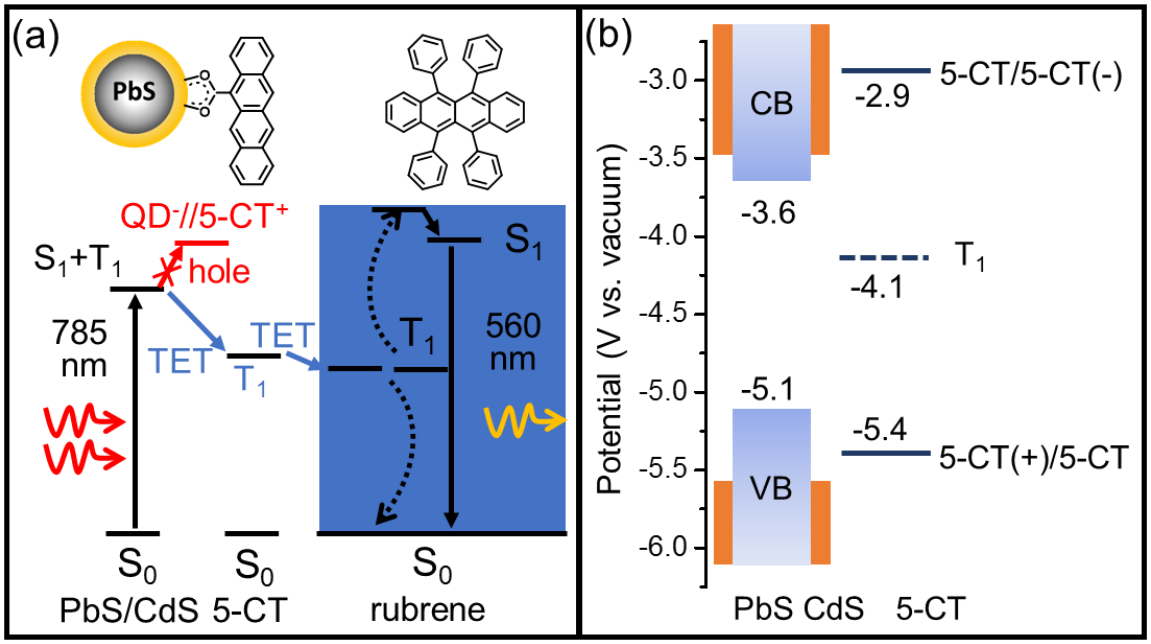

Figure 7.1 (a) Schematic of the energy transfer processes during photon upconversion using a hybrid PbS QD-tetracene-rubrene platform. (b) Redox potentials of PbS/CdS QD and **5-CT** measured by cyclic voltammetry in dichloromethane at -50°C for the QD and RT for free **5-CT**. The T_1 state of **5-CT** (1.25 eV[10] relative to the HOMO) is presented as a dashed line.

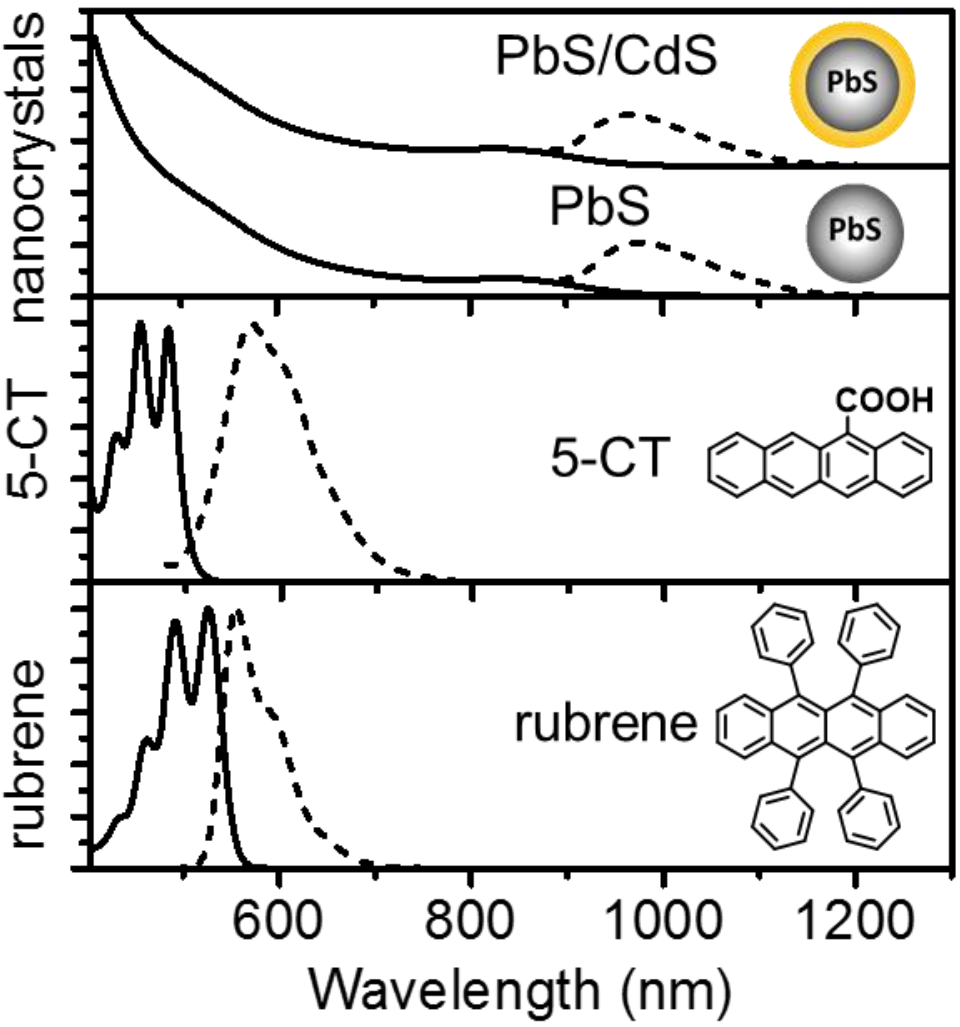

Figure 7.2 Absorption (solid line) and photoluminescence (dashed line) spectra of 3.2 nm diameter PbS/CdS core-shell QD with 0.25 nm shell thickness, 2.7 nm diameter PbS QD (top), **5-CT** (middle) and rubrene (bottom) in toluene measured at room temperature.

The hybrid inorganic/organic platform for photon upconversion is shown in Figure 7.1a. Photoexcitation of the QD with a 785 nm CW laser results in energy transfer to the triplet state of the bound **5-CT**, then to rubrene. Two rubrene triplets then annihilate to form a singlet-excited state that emits at 560 nm. Two QD light absorbers, 2.7 nm diameter PbS QD and 3.2 nm diameter

PbS/CdS core-shell QDs[11, 19-21] with similar absorption and emission maxima are used here (λ_{abs} and λ_{ems} respectively, Table 1 and spectra in Figure 7.2). This indicates that they have approximately the same PbS core size, which is important because photon upconversion is enhanced with smaller QDs due to the larger driving force for TET from QD donor to molecular acceptor.[19, 24] The PbS/CdS core-shell QD is synthesized via cation exchange from a 3.2 nm diameter PbS QD and the size is assumed to be unchanged. As a transmitter, the long-lived triplet state of **5-CT** mediates TET from the QD to rubrene by forming an energy cascade (Figure 7.1a), and increases the photon upconversion QY by a factor of 80.[25] When individually mixed with 20 mM rubrene emitter in toluene, the two **5-CT** functionalized light absorbers, i.e. the PbS core only QDs and PbS/CdS core/shell QDs, give photon upconversion QYs of 3.5% and 5.0% respectively. Photon upconversion is optimized by varying the concentration of **5-CT** during ligand exchange as can be seen in Figure 7.3. Considering the surface density of the original oleic acid ligands (3 nm^{-1})[26] and **5-CT** before and after ligand exchange, 28% and 35% of the original oleic acid are exchanged with **5-CT** for PbS core and PbS/CdS core-shell QDs respectively. The upconversion QYs and other parameters relating to TET are summarized in Table 1.

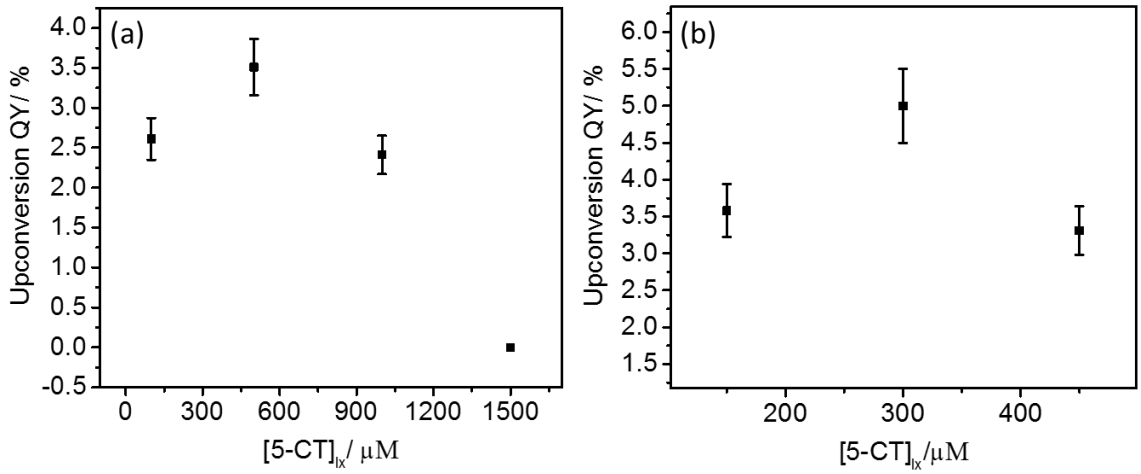

Figure 7.3 The relationship between upconversion QY and the concentration of **5-CT** in ligand exchange, [**5-CT**]$_{LX}$, for (a) PbS QD and (b) PbS/CdS core-shell QD. The optimal average number of bound 5-carboxylic acid tetracene (**5-CT**) per QD is 22 for PbS QDs and 34 for PbS/CdS QDs

Table 7.1 Key parameters for the hybrid photon upconversion system: absorption maxima, λ_{abs}; emission maxima, λ_{ems}; photon upconversion quantum yield (UCQY); efficiency of triplet energy transfer (TET) from QD to 5-CT, Φ_{TET}; and the rate of TET, k_{ET}

QD	λ_{abs} / λ_{ems} (nm)[a]	UCQY (%)[b]	Φ_{TET} (%) [c]	k_{ET} (10^9 s^{-1})[d]
PbS	837 / 978	3.5± 0.3	60.3 ± 6.1	5.91± 0.60
PbS/CdS	826 / 967	5.0± 0.5	71.8 ± 6.2	1.03± 0.09

[a] Toluene at RT; [b]10 μM QD in 20 mM rubrene in toluene at RT, CW 785 nm laser at 26.4 W/cm^2; [c]Φ_{TET} and [d] k_{ET} from transient absorption.

7.2.3 Determine QD, 5-CT redox potential by Cyclic Voltammetry

The sensitivity of the overall photon upconversion efficiency on the composition of the QD suggests that the TET between QD and **5-CT** is one of the key limiting steps. In addition to this desired process, excitons in the QD can also decay by radiative recombination within the QD and charge (electron or hole) transfer to **5-CT**. Shown in Figure 7.1b is the reduction and oxidation potential of PbS/CdS and **5-CT** measured by cyclic voltammetry.

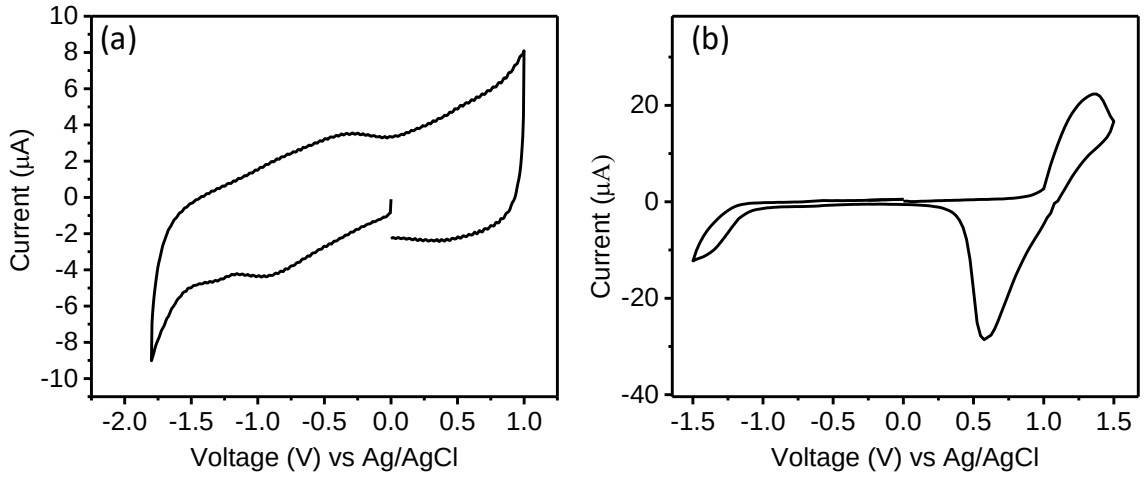

Figure 7.4 Cyclic voltammogram (CV) of (a) PbS/CdS core-shell QD measured at -50°C and (b) 5-carboxylic acid tetracene measured RT. Both CVs were performed in dichloromethane at a scan speed of 100 mV s^{-1}.

Cyclic voltammetry measurements were conducted on a Gamry interface 1000 electrochemical analyzer with a three-electrode system in an argon glove box in an anhydrous dichloromethane (DCM) solution containing tetra-*n*-butylammonium hexafluorophosphate (0.1 M) as electrolyte (Acros Organics). A glassy carbon electrode was used as a working electrode, a platinum-wire was used as the counter electrode, and an Ag/AgCl electrode was used as the reference electrode. For the QD, in a bath of ethanol/ H_2O (1:1 v/v)/ dry ice was used maintain the

temperature at -50°C. The CV curves were calibrated with the ferrocene/ferrocenium (Fc/Fc^+) redox couple as a standard measured under the same conditions. The energy level of Fc/Fc^+ was assumed at to be – 4.8 eV with respect to vacuum.[27] These CV curves show that the oxidation and reduction potential of **5-CT** are at -5.4V and -3.6 V vs vacuum, respectively.

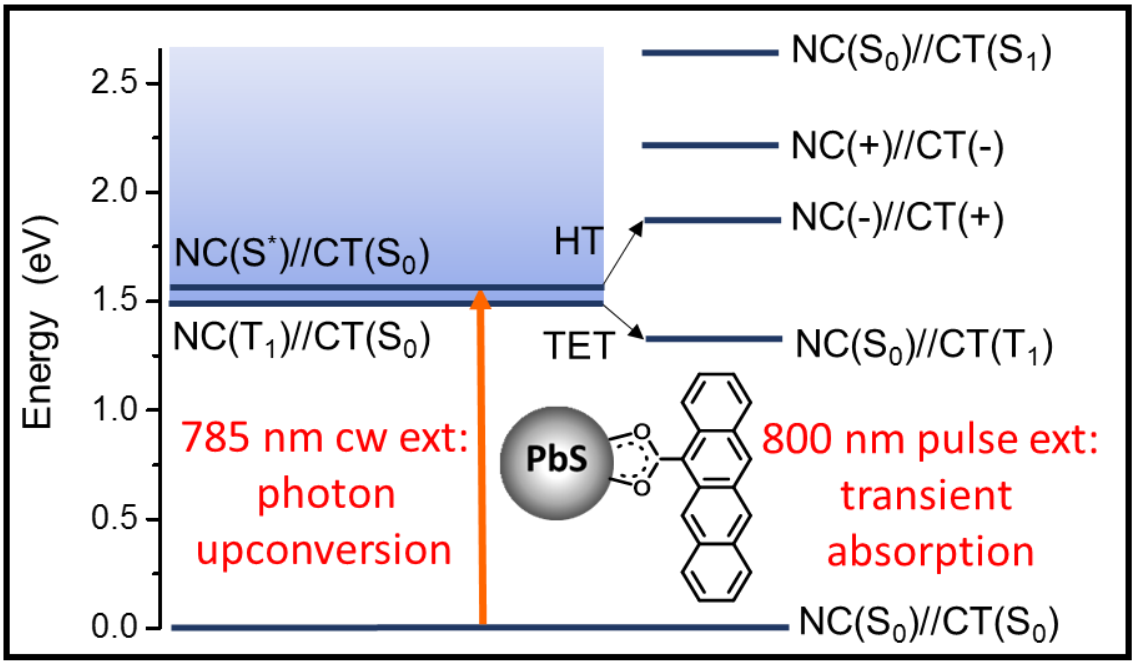

Figure 7.5 Energy level of various energy and charge transfer states involved in the decay of QD excitons. Also shown is the initial excitation (orange arrow), hole transfer (HT), and triplet energy transfer (TET). The energy level of each state is determined by the QD optical bandgap (1.48 eV), excitation energy (800 nm, 1.55 eV), the energy of S_1 (2.58 eV) and T_1 (1.25 eV) states of **5-CT**, and the energy barrier for electron (0.7 eV) and hole (0.3 eV) transfer from QD to **5-CT** based on the energies of conduction and valance band edges of QD, and HOMO, LUMO of **5-CT** from CV measurements.

These values, in combination with the optical gaps (Figure 7.2) give the reduction and oxidation potentials of **5-CT** and PbS/CdS QDs (-2.9 V and -5.1 V respectively). Figure 7.5 shows

the energy levels of various states generated by energy, electron or hole transfer from QDs. It is clear that starting from the band edge excitonic state in the QD, i.e. QD(T_1)/**5-CT**(S_0), electron (hole) transfer from the conduction (valence) band edge of the QD to **5-CT** is uphill with the change of free energy of +0.7 (+0.3) eV. Only TET from QD(T_1) to **5-CT**(S_0), forming QD(S_0)//**5-CT**(T_1), is energetically downhill by 0.23 eV.

7.2.4 Transient Absorption Spectroscopy of 5-CT, PbS, PbSCdS and PbS-CT, PbSCdS-CT

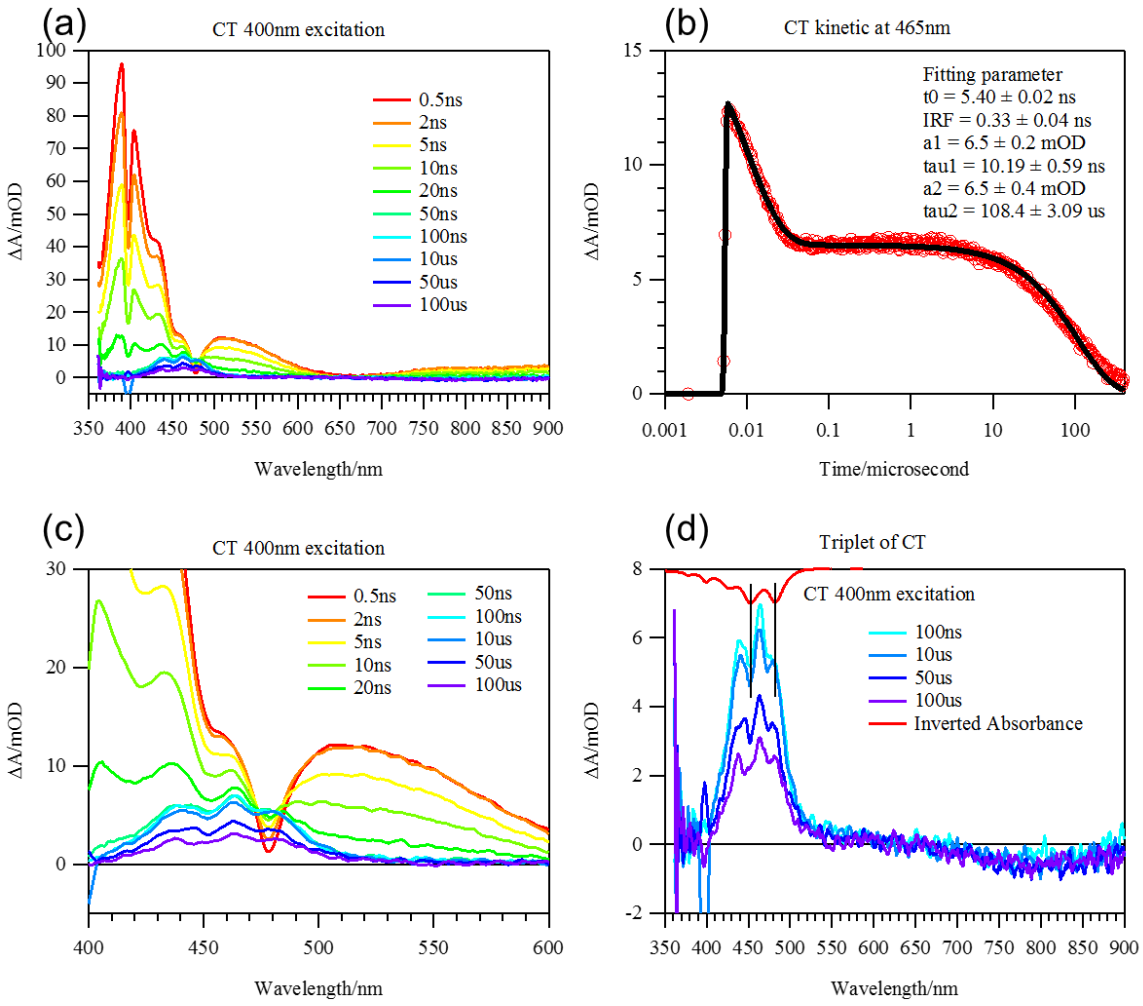

Figure 7.6 TA spectra and kinetics of 5-carboxylic acid tetracene (**5-CT**) in solution.

The 5-CT dissolved in toluene was first studied by transient absorption spectroscopy. The sample was excited at 400 nm, populating the singlet state which is dominating the spectra up to tens of nanosecond as can be seen in Figure 7.6(a) Nanosecond transient absorption spectra of **5-CT** in tetrahydrofuran at room temperature measured with 400 nm excitation. After certain delay time the intersystem crossing described in detail in Chapter 5 occurs as shown in time delay above 100 ns in panel a. Transient kinetics of **5-CT** probed at 465 nm (open symbols) and biexponential fit (solid line) shown in panel b reveals the singlet and triplet lifetime, yielding a singlet lifetime of 10.19 ns and triplet lifetime of 108.4 μs (c) and (d) provide an expanded view of triplet excited state absorption of **5-CT**. The triplet spectra consist of positive triplet absorption bands (T_1 to T_n) and negative dips corresponding depletion of the ground state. Both the ground state and triplet state absorption spectra of **5-CT** adsorbed on oleic-acid capped QDs are red-shifted from the free molecule in THF, likely caused by the different solvation environments.

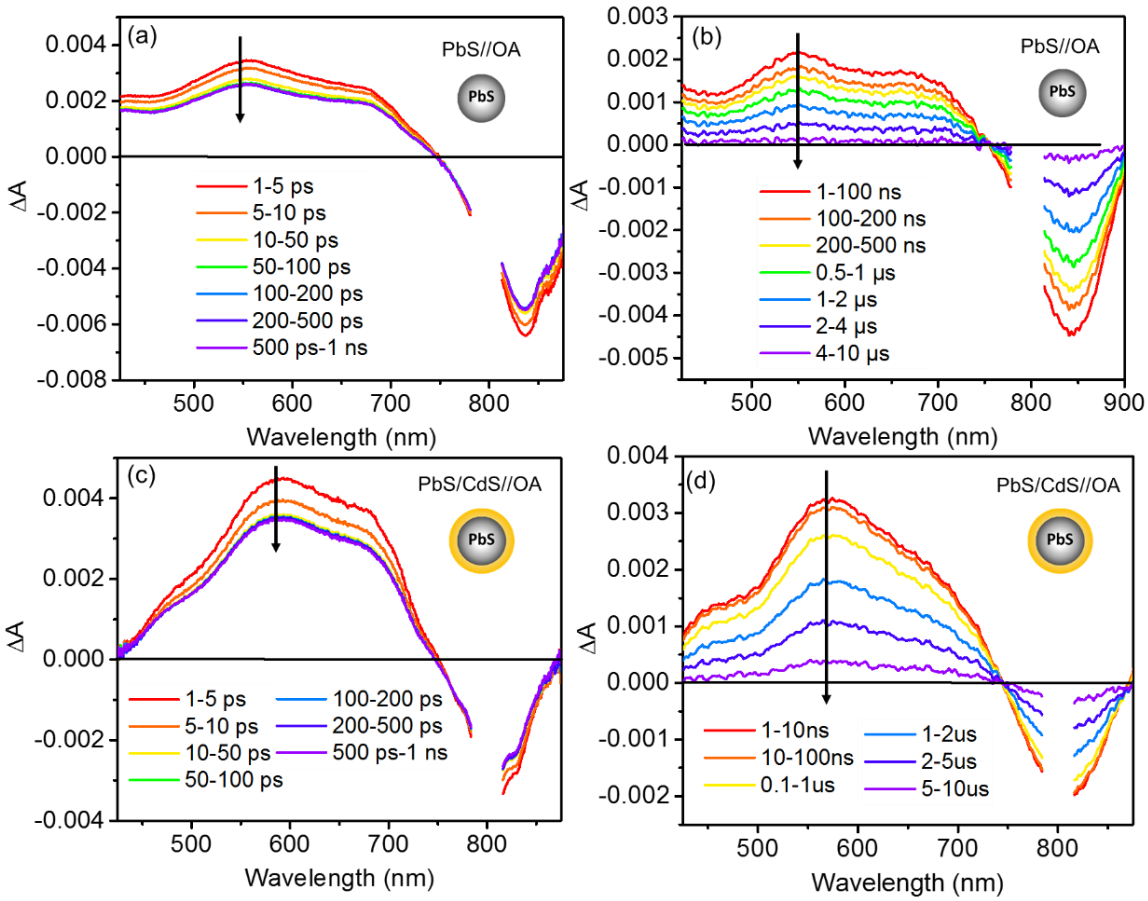

Figure 7.7 Femtosecond and nanosecond TA spectra of (a), (b) PbS//**OA** and (c), (d) PbS/CdS//**OA**. Samples are dissolved in toluene and excited at 800nm. Each curve in (a) and (b) is the average of the spectra within the indicated delay time window.

In order to explain the ~40% enhancement in the photon upconversion QY in the presence of the CdS shell, TA measurements were performed to study the kinetics of charge and energy transfer from QDs to **5-CT**. Here, four samples consisting of as-synthesized PbS core and PbS/CdS core/shell QDs and the **5-CT** functionalized QDs that gave the highest photon upconversion QYs in toluene were studied. The QDs in all four samples were selectively excited at 800 nm. TA spectra of PbS//**OA** and PbS/CdS//**OA** are shown in Figure 7.7.

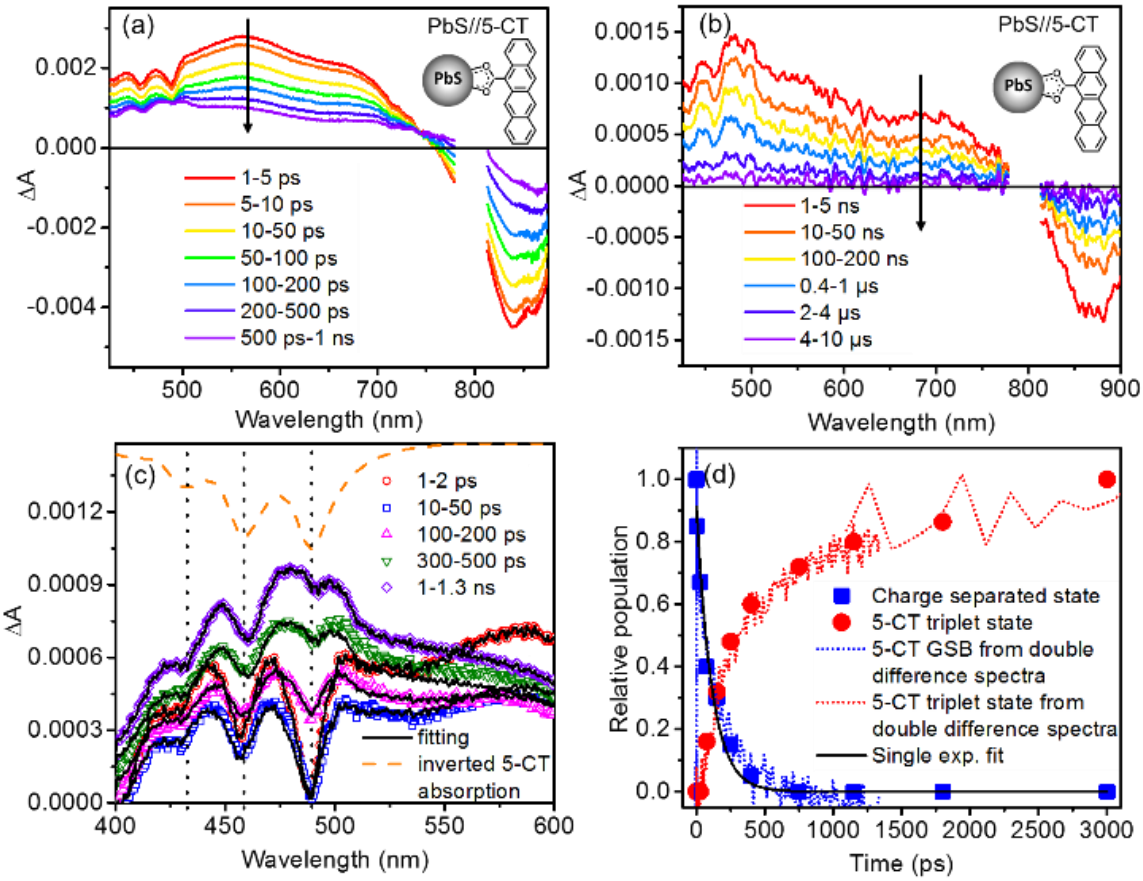

Figure 7.8 (a) Femtosecond and (b) nanosecond TA spectra of PbS QD capped with **5-CT**, PbS//**5-CT**, in toluene, excited at 800nm. Each trace is the average of the spectra within the indicated time window. Spectra from 785 to 815 nm are truncated due to saturation of the probe. (c) Double difference spectra of PbS//**5-CT** obtained by subtracting the PbS//**OA** TA signal from PbS//**5-CT**. The black solid curve shows the fit of this spectra to the sum of the basis spectra consisting of the charge separated state (CS state, 1-2 ps, red circle) and **5-CT** triplet state (1-1.3 ns, purple diamond). Also shown is the linear absorption spectra of **5-CT** on PbS QDs (orange dashed curve, inverted). Vertical lines indicate the ground state bleach. (d) Relative population of the CS state (blue square) and **5-CT** triplet excited state (red dot) in PbS//**5-CT** from the fits in (c), normalized to a maximum of 1. The red dashed line is the kinetics at 489 nm in (c), the T_1-T_n transition of **5-CT**. The dashed blue line is the difference of the ODs at 475 nm (peak) and 489 nm (valley) in (c)

and corresponds to the ground state bleach of **5-CT**. The black solid line is a single exponential fit of the CS state.

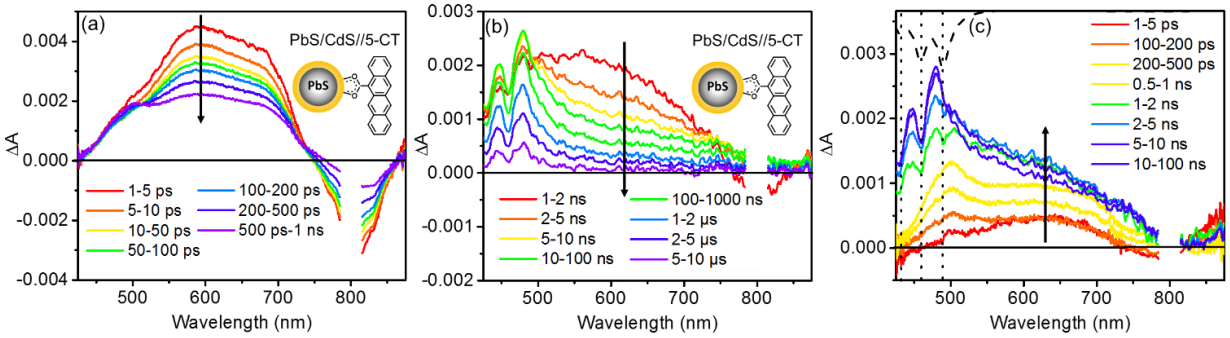

Figure 7.9 (a) Femtosecond and (b) nanosecond TA spectra of PbS/CdS QD capped 5-CT, PbS/CdS//5-CT. (c) Double difference TA spectrum of PbS/CdS //5-CT. The black dashed curve shows the inverted linear absorption spectrum of bound 5-CT. The sample was excited at 800 nm.

5-CT capped PbS QDs (PbS//**5-CT**) and PbS/CdS QDs (PbS/CdS//**5-CT**) are shown in Figure 7.8(a, b) and Figure 7.9(a, b) respectively. For QD only samples, the broad positive feature from 400 to 750 nm is the excited state absorption (ESA), and the negative peak from 750 to 900 nm is the ground state bleach (GSB). Both features decay with the same kinetics (see below), reflecting the electron and hole dynamics within the QD.[28] The presence of **5-CT** leads to faster decay of QD ESA and recovery of the GSB, indicating that **5-CT** depletes the QD exciton. In the 420-500 nm spectral region, the ESA of the QDs overlaps with features from **5-CT**. To better observe the spectral evolution of the **5-CT** features, we constructed a double difference TA spectra, in which the contributions of the QD were removed by subtracting the QD//**OA** spectra scaled

such that the GSB of the QD around 750-900nm, where the **5-CT** contribution is negligible, matched the GSB of the QD//**5-CT** at the same time delays.

For PbS QDs functionalized with **5-CT**, charge transfer is observed at early times at sub-ps timescales, while triplet transfer is seen at long delay times. As shown in Figure 7.8c, the double difference spectrum at the delay time of 1-1.3 ns resembles that of the triplet state of free **5-CT** in tetrahydrofuran (THF, Figure 7.6). This confirms triplet sensitization by these QDs.

The double difference spectrum at 1-2 ps delay times in Figure 7.8c also shows a bleach of the **5-CT** ground state, but no absorption corresponding to the **5-CT** triplet state. A comparison of the kinetics for the recovery of the QD GSB for PbS//**OA** and PbS//**5-CT** (Figure 7.10a) shows that the initial exciton bleach amplitude is smaller when **5-CT** is present despite excitation of the same proportion of QDs in both samples. Taken together, this suggests an ultrafast transfer of electrons or holes from QD to **5-CT** occurring prior to their relaxation to the band-edge (< 0.3ps). This process is likely due to hole transfer from PbS to **5-CT.** From the reported spectra of **5-CT** anion (-) and cation (+) radicals, only **5-CT** (+) is consistent with the observed TA spectra at early times.[29-31] Formation of reduced **5-CT** should exhibit an absorption peak at 360 and 400 nm.[30] This is not observed. Furthermore, as shown in Figure 7.1b, hole transfer from the QD to **5-CT** to form the QD(-)//CT(+) charge separated (CS) state is more energetically favorable than electron transfer. Considering the fact that CV measurements are generally accurate to 0.1 eV, the energy barrier for hole transfer could be smaller than 0.3 eV.

7.2.5 Kinetics of PbS triplet energy transfer to 5-CT

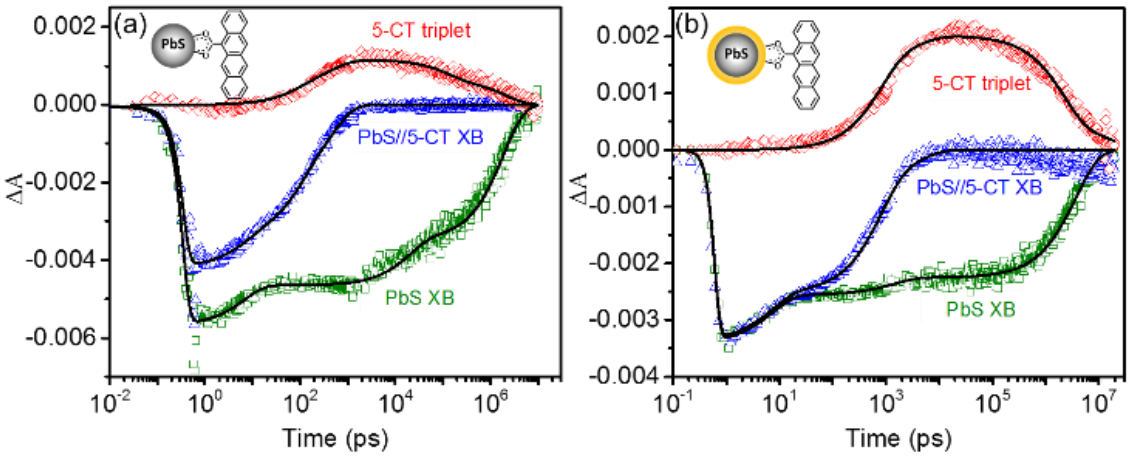

Figure 7.10 Kinetics of QD exciton bleach (XB, blue triangles) at 820 nm and 5-CT triplet (red diamonds) at 489 nm for (a) PbS//5-CT and (b) PbS/CdS//5-CT. Also shown are the XB kinetics of QDs without 5-CT (green squares). Solid lines are a global fit according to the model described in the text.

This ultrafast hole transfer from PbS to **5-CT** is effectively suppressed by the growth of CdS shell. Figure 7.9 presents the TA spectra of PbS/CdS//**5-CT**. As shown in Figure 7.9c, no molecular GSB is observed at ps timescales, and only the **5-CT** triplet excited state grows in at later times. Furthermore, in the presence of the CdS shell, in contrast to the core-only PbS system (Figure 7.10a), the ultrafast recovery of the QD exciton bleach is not observed (Figure 7.10b), indicating suppression of charge transfer by the removal of trap states. The efficiency of TET, Φ_{TET}, from PbS QD to **5-CT** is enhanced by the CdS shell. Shown in Figure 7.10a and b are the kinetics of the **5-CT** triplet state and QD exciton bleach recovery in **PbS//5-CT** and **PbS/CdS//5-CT**, respectively. These kinetics can be fit to a model that accounts for the intrinsic decays in the QDs, TET between QDs and **5-CT**, and ultrafast hole transfer between PbS QDs and **5-CT** (in **PbS//5-CT** only).

The intrinsic decay of free quantum dots can be well fit by three decays, with amplitudes and time constants of a_i and k_i (i=1-3), respectively.

$$[QD^*](t) = [QD^*](0)\sum_{i=1}^{3} a_i e^{-k_i t} \qquad \text{Eq. 7.2}$$

In QD//**5-CT** complexes, due to triplet energy transfer (with rate constant k_{ET}) to **5-CT**, the decay kinetics of the QD becomes:

$$[QD^*//CT](t) = [QD^*//CT](0)\sum_{i=1}^{3} Aa_i e^{-(k_i+k_{ET})t} \qquad \text{Eq. 7.3}$$

In Eq. 7.3, the coefficient A represents the percentage of QDs excitons that undergo triplet energy transfer to **5-CT**. The remaining portion (1-*A*) accounts for the initial fast charge transfer pathway observed in PbS//**5-CT**.

The kinetics of the formation and decay of the **5-CT** triplet excited state is given by:

$$[QD//CT^*](t) = \sum_{i=1}^{3} \frac{\varepsilon A a_i [QD^*//CT](0) k_{ET}}{k_{ET}+k_i-k_T}[e^{-k_T t} - e^{-(k_{ET}+k_i)t}] \qquad \text{Eq. 7.4}$$

In Eq. 7.4, k_T is the decay of rate constant of triplet excited state.

During the global fitting process, a_i, $k_i$and [QD](0) are independently determined by the decay of free quantum dot and are fixed for the decay of GSB and growth of triplet for QD//**5-CT** complex. The instrument response function (IRF) and time zero are determined by fitting the solvent response. Therefore, there are only four variables including k_{ET}, k_T, ε and A to be determined for the global fitting process.

In Figure 7.10, the exciton bleach kinetics represent the QD excited state, and the **5-CT** triplet excited state is represented by the amplitude of triplet ESA peak at 489 nm of the double difference spectra. ε accounts for the ratio of extinction coefficients between these wavelengths. The fitting results are shown as black lines in Figure 7.10 and the fitting parameters are listed in Table 7.2. Here the k_{ET} and k_T are the weighted average value since there are two k_{ET} and k_T used in the fitting to achieve best results.

Table 7.2 Parameters obtained from fitting kinetics traces

	PbS//5-CT	**PbS/CdS//5-CT**
[QD] (0)	-5.63±0.03mOD	-3.35±0.03mOD
a_1	17.5±0.5%	23.9±0.9%
a_2	20.8±0.4%	9.1±0.3%
a_3	61.6±3.9%	67.2±0.1%
k_1	0.149±0.009ps^{-1}	0.137±0.010ps^{-1}
k_2	51.1±2.9μs^{-1}	0.70±0.13ns^{-1}
k_3	0.528±0.016μs^{-1}	0.26±0.01μs^{-1}
A	0.733±0.050	0.987±0.006
k_{ET}	5.91±0.60ns^{-1}	1.03±0.09ns^{-1}
k_{CS}	8.94±0.98ns^{-1}	-
k_T	3.67±0.52μs^{-1}	0.37±0.02μs^{-1}
ε	-0.339±0.004	-0.844±0.008
IRF	0.293±0.009ps^{-1}	0.293±0.009ps^{-1}
t_0	0.301±0.003ps^{-1}	0.301±0.003ps^{-1}
Total TET%	60.3±6.1%	71.8±6.2%

The TET efficiency is given by:

$$\sum_{i=1}^{3} \frac{Aa_i k_{ET}}{k_{ET}+k_i} \qquad \text{Eq. 7.5}$$

The calculated efficiencies are shown in Table 7.3.

Table 7.3 Component corresponded TET efficiency

PbSCT			**PbSCdS CT**		
Component	Percent	TET	Component	Percent	TET
a_1	17.5±0.5%	3.8±0.4%	a_1	23.9±0.9%	0.75±0.06%
a_2	20.8±0.4%	99.1±10.1%	a_2	9.1±0.3%	59.5±5.2%
a_3	61.6±3.9%	100±10.2%	a_3	67.2±0.1%	100±8.7%

From the fitting parameters one can calculate that the TET efficiency is 60.3 ±6.1% for PbS//**5-CT** and 71.8 ±6.2% for PbS-CdS//**5-CT**. A detailed comparison of exciton decay dynamics in PbS/CdS//**5-CT** and PbS//**5-CT** shows that the presence of the CdS shell suppresses the initial hot hole transfer pathway, enhancing the efficiency of TET. However, in PbS/CdS//**5-CT**, the TET efficiency is only 71.8 ±6.2%, suggesting additional loss pathways. As shown in Figure 7.10 the kinetics of free QD exciton bleach can be well described with three exponential decays and the TET efficiency for these components can be calculated (see Table 7.3). For the fastest decay component (~24% of total amplitude), the intrinsic decay within the PbS/CdS QD (with a rate constant of 0.137±0.010 ps^{-1}) outcompetes the TET process in PbS/CdS//**5-CT**. For the intermediate component (~9% of total amplitude), the intrinsic decay rate (0.70±0.13ns^{-1}) within the QD is similar to the rate of TET, leading to 59.5±5.2% TET efficiency. The rate of TET is

much faster than the slowest decay component (~67% of the amplitude). These results suggest that defect-induced fast nonradiative e-h recombination within the QD is the major competing loss pathway for PbS/CdS//**5-CT**. Further improvements that can eliminate these fast exciton pathways of PbS/CdS QDs would further enhance the TET efficiency.

In Figure 7.10, the pristine QD exciton bleach kinetics represented by the green dots showed an extended exciton lifetime of PbS/CdS QD compared to PbS QD. The presence of the thin shell does reduce the surface trap states, which is reflected on the increase of the exciton lifetime. However, both PbS and PbS/CdS QD experienced a fast exciton decay at early time (30% decay from time zero to 2 ps). We could assign such decay to the fast trapping of exciton which is a major limitation on the TET efficiency in this work. Such decay was not suppressed by the introduction of a sub-monolayer CdS shell, possibly because the shell didn't cover the entire surface.

The trajectory of the **5-CT** triplet can be monitored by the TA signal at 489 nm where the CS state has no features. The fits show that the formation of **5-CT** triplet occurs in tandem with the recovery of the QD GSB. This suggests that energy transfer occurs from the band edge in both QDs to **5-CT.** The TET efficiency is 60.3± 6.1% for PbS//**5-CT** and 71.8± 6.2% for PbS/CdS//**5-CT**. This enhancement is due to the suppression of hole transfer from PbS QD to **5-CT** by growth of CdS shell. However, the CdS shell slows down TET from 5.91± 0.60 ns^{-1} in PbS//**5-CT** to 1.03± 0.09 ns^{-1} in PbS/CdS//**5-CT**, consistent with the shell being a barrier for TET.[32-33] Interestingly, the decay of the **5-CT** triplet state also slows down from 3.67± 0.52μs^{-1} in PbS//**5-CT** to 0.37± 0.02μs^{-1} in PbS/CdS//**5-CT**. Both decay rates are faster than triplet decay of free **5-CT** (0.0090±0.0003 μs^{-1} in THF), which suggests that the presence of QDs speeds up intersystem crossing (from T_1 to S_0) in **5-CT**. Thus, the prolonged **5-CT** triplet excited state lifetime in

PbS/CdS/**5-CT** compared to that in PbS/**5-CT** may enhance TET from **5-CT** to the rubrene emitter. This, in combination with the higher Φ_{TET} from QD to **5-CT**, enhances the upconversion QYs.

7.3 Conclusion

Hole transfer from PbS QDs to surface anchored **5-CT** is detrimental to TET efficiency and photon upconversion. Thus far, this work and a previous report[34] show no direct relationship between triplet and charge transfer from QDs to molecule. Although both processes deplete the QD exciton, they occur on very different timescales (ns for triplet vs ps for charge transfer). For **PbS//5-CT**, the **5-CT** triplet population peaks at ~ 1 ns (Figure 7.10a), whereas the ground state bleach of **5-CT** is formed within 1-2 ps (Figure 7.8c). At 1-2 ps, the absence of triplets allows the GSB of **5-CT** to be assigned to the formation of the CS state. At intermediate times between 2 ps and 1 ns, the double difference spectra can be well fit to a sum of only two species: the CS state and **5-CT** triplet state. Fits of the relative populations of these two species are plotted in Figure 7.8d, together with the recovery of the **5-CT** GSB and growth of **5-CT** triplet. As expected, the fit for the growth of the **5-CT** triplet (red dot) tracks the kinetics of **5-CT** triplets (red dashed curve). Additionally, the fit of the decay of the CS state (blue square) tracks the GSB of **5-CT** (blue dashed curve). This suggests that the product of CS decay is the regeneration of the **5-CT** ground state, through charge recombination. The relative population of the CS state is described well by a single decay constant of 8.94± 0.98 ns^{-1}, while the growth of the triplet excited state, k_{ET}=5.91± 0.60 ns^{-1}. This discrepancy further supports the assignment that the decay of charge separated state does not lead to the formation of the triplet state. Furthermore, the recovery of the GSB of the QD is correlated with the growth of the triplet exciton on **5-CT** (Figure 7.10) in both the core only PbS and core/shell PbS/CdS donors, suggesting that **5-CT** triplet is formed by energy transfer from

band edge excitons in both QDs. Our result indicates that the initial hole transfer in the absence of a Cd shell is a loss process that should be minimized in order to enhance the formation of **5-CT** triplet for increased photon upconversion QYs. A similar system composed of 3.5 nm diameter PbS QD and surface-anchored TIPS pentacene also observed the ultrafast formation of this CS state but a disparity in the recovery of the GSB of PbS QDs (<100ps) and the growth of the triplet on pentacene (~6 ns).[34] The lack of correlation between the kinetics of the exciton bleach recovery of the QD donor and pentacene acceptor was explained by an electron transfer event at intermediate times that was not experimentally observed.

In conclusion, this work demonstrates that compared to PbS QDs, PbS/CdS QDs enhance the photon unconversion QY by suppressing the hole transfer pathway. Detailed TA studies of QD/**5-CT** complexes clearly show formation of the **5-CT** triplet and corresponding recovery of the QD band edge exciton on the same time scale, confirming TET from QDs to **5-CT** for both QDs. In PbS//**5-CT**, there also exists a competitive ultrafast hole transfer process that reduces the efficiency of triplet transfer, Φ_{TET}. In core/shell PbS/CdS//**5-CT**, although the CdS shell slows down the rate of TET from 5.91± 0.60 ns^{-1} to 1.03± 0.09 ns^{-1}, Φ_{TET} is higher in the presence of the CdS shell. TET rates are still faster than the intrinsic exciton lifetime of the QD. Furthermore, the decay of the **5-CT** triplet is slower on PbS/CdS compared to PbS, which likely further enhances Φ_{TET}. This work shows that core/shell structures can be used to tune the rates of competing energy and charge transfer processes, and to prolong the lifetime of triplets. It provides insight into the rational design of semiconductor QDs for triplet sensitization and photon upconversion applications.

7.4 Reference

1. Semonin, O. E.; Luther, J. M.; Choi, S.; Chen, H.-Y.; Gao, J.; Nozik, A. J.; Beard, M. C., *Science* **2011,** *334* (6062), 1530-1533.
2. Klimov, V. I., *Annu. Rev. Phys. Chem.* **2007,** *58*, 635-673.
3. Rabani, E.; Baer, R., *Nano letters* **2008,** *8* (12), 4488-4492.
4. Talapin, D. V.; Lee, J.-S.; Kovalenko, M. V.; Shevchenko, E. V., *Chemical Reviews* **2010,** *110* (1), 389-458.
5. Cozzoli, P. D.; Pellegrino, T.; Manna, L., *Chemical Society Reviews* **2006,** *35* (11), 1195-1208.
6. Colvin, V. L.; Schlamp, M. C.; Alivisatos, A. P., *Nature* **1994,** *370* (6488), 354-357.
7. Kairdolf, B. A.; Smith, A. M.; Stokes, T. H.; Wang, M. D.; Young, A. N.; Nie, S. M., *Annu Rev Anal Chem* **2013,** *6*, 143-162.
8. Carey, G. H.; Abdelhady, A. L.; Ning, Z. J.; Thon, S. M.; Bakr, O. M.; Sargent, E. H., *Chemical Reviews* **2015,** *115* (23), 12732-12763.
9. Huang, Z. Y.; Li, X.; Mahboub, M.; Hanson, K. M.; Nichols, V. M.; Le, H., . . . Bardeen, C. J., *Nano Letters* **2015,** *15* (8), 5552-5557.
10. Wu, M. F.; Congreve, D. N.; Wilson, M. W. B.; Jean, J.; Geva, N.; Welborn, M., . . . Baldo, M. A., *Nat Photonics* **2016,** *10* (1), 31-34.
11. Mahboub, M.; Huang, Z. Y.; Tang, M. L., *Nano Letters* **2016,** *16* (11), 7169-7175.
12. Nirmal, M.; Norris, D. J.; Kuno, M.; Bawendi, M. G.; Efros, A. L.; Rosen, M., *Phys Rev Lett* **1995,** *75* (20), 3728-3731.
13. Efros, A. L.; Rosen, M.; Kuno, M.; Nirmal, M.; Norris, D. J.; Bawendi, M., *Physical Review B* **1996,** *54* (7), 4843.
14. Mongin, C.; Garakyaraghi, S.; Razgoniaeva, N.; Zamkov, M.; Castellano, F. N., *Science* **2016,** *351* (6271), 369-372.
15. Li, X.; Fast, A.; Huang, Z. Y.; Fishman, D. A.; Tang, M. L., *Angew Chem Int Edit* **2017,** *56* (20), 5598-5602.
16. Zhu, H. M.; Lian, T. Q., *Energy & Environmental Science* **2012,** *5* (11), 9406-9418.
17. Ding, T. N. X.; Olshansky, J. H.; Leone, S. R.; Alivisatos, A. P., *Journal of the American Chemical Society* **2015,** *137* (5), 2021-2029.
18. Garakyaraghi, S.; Mongin, C.; Granger, D. B.; Anthony, J. E.; Castellano, F. N., *The Journal of Physical Chemistry Letters* **2017,** *8* (7), 1458-1463.
19. Mahboub, M.; Maghsoudiganjeh, H.; Pham, A. M.; Huang, Z. Y.; Tang, M. L., *Advanced Functional Materials* **2016,** *26* (33), 6091-6097.
20. Hines, M. A.; Scholes, G. D., *Adv Mater* **2003,** *15* (21), 1844-1849.
21. Neo, D. C. J.; Cheng, C.; Stranks, S. D.; Fairclough, S. M.; Kim, J. S.; Kirkland, A. I., . . . Watt, A. A. R., *Chemistry of Materials* **2014,** *26* (13), 4004-4013.
22. Moreels, I.; Lambert, K.; Smeets, D.; De Muynck, D.; Nollet, T.; Martins, J. C., . . . Hens, Z., *Acs Nano* **2009,** *3* (10), 3023-3030.
23. Okamoto, T.; Suzuki, T.; Tanaka, H.; Hashizume, D.; Matsuo, Y., *Chem-Asian J* **2012,** *7* (1), 105-111.

24. Huang, Z. Y.; Li, X.; Yip, B. D.; Rubalcava, J. M.; Bardeen, C. J.; Tang, M. L., *Chemistry of Materials* **2015,** *27* (21), 7503-7507.
25. Huang, Z. Y.; Simpson, D. E.; Mahboub, M.; Li, X.; Tang, M. L., *Chemical Science* **2016,** *7* (7), 4101-4104.
26. Moreels, I.; Justo, Y.; De Geyter, B.; Haustraete, K.; Martins, J. C.; Hens, Z., *Acs Nano* **2011,** *5* (3), 2004-2012.
27. Liu, Y.; Liu, M. S.; Jen, A. K. Y., *Acta Polym* **1999,** *50* (2-3), 105-108.
28. Yang, Y.; Rodriguez-Cordoba, W.; Lian, T. Q., *Journal of the American Chemical Society* **2011,** *133* (24), 9246-9249.
29. Kimura, K.; Yamazaki, T.; Katsumat.S, *J Phys Chem-Us* **1971,** *75* (12), 1768-&.
30. Shida, T.; Iwata, S., *Journal of the American Chemical Society* **1973,** *95* (11), 3473-3483.
31. Brodard, P.; Sarbach, A.; Gumy, J. C.; Bally, T.; Vauthey, E., *J Phys Chem A* **2001,** *105* (27), 6594-6601.
32. Mahboub, M.; Huang, Z. Y.; Tang, M. L., *Nano Letters* **2016,** *16* (12), 8037-8037.
33. Gray, V.; Xia, P.; Huang, Z. Y.; Moses, E.; Fast, A.; Fishman, D. A., . . . Tang, M. L., *Chemical Science* **2017,** *8* (8), 5488-5496.
34. Garakyaraghi, S.; Mongin, C.; Granger, D. B.; Anthony, J. E.; Castellano, F. N., *J Phys Chem Lett* **2017,** *8* (7), 1458-1463.

8. Chapter 8. Surface Chemistry as a Key Factor in Photon Upconversion System

8.1 Introduction

Colloidal semiconductor nanocrystals (NCs) have quantum confined states that make them interesting for many optoelectronic applications.[1-4] However, these quantized states are subject to the vagaries of the surface, i.e. differences at the atomic scale that are difficult to quantify, especially when compounded with the intrinsic disorder both at the nanoscale and in the ensemble. Thus, nominally identical nanomaterial may give rise to dramatically different rates and yields of energy and charge transfer. A case in point are two recent reports that are in direct conflict with each other, regarding singlet fission (or lack thereof) from the same tetracene molecule covalently bound to PbS NCs. One found no evidence of singlet fission from TIPS-tetracene bound to three different sizes of PbS NCs[5] while the other reported quantitative yields of singlet fission and subsequent energy transfer on nominally the same material combination.[6] Both used the same carboxylic acid functionalized TIPS-tetracene with oleic acid capped PbS NCs. In this case, the dissimilar ligand exchange protocol and solvent during photoexcitation may explain the discrepancy between the electronic communication in surface bound tetracene in both reports.

This extreme sensitivity to quenching mechanisms on the surface is not surprising for short-range Dexter-type processes describing charge and energy transfer. In comparison, long-range Förster type transfers are relatively forgiving.[7-10] In this work, we show that surface states resulting

from different synthetic procedures significantly impact triplet energy transfer (TET), specifically in the context of semiconductor NCs as triplet sensitizers for photon upconversion[11-12]. Here, transient absorption measurements explain the reasons why PbS NC triplet photosensitizers made with different precursors result in photon upconversion quantum yields (QYs) that routinely differ by a factor of 2–3. This work shows that detailed control of surface chemistry through advanced synthesis represents an attractive alternative strategy that eliminates the need for shell layers by increasing the surface bound-tetracene triplet lifetime without sacrificing energy transfer rate.[13-14] This approach is particularly important for applications in photon upconversion, because efficient Dexter-like TET[15-1615-1615-1615-1615-1615-1615-1615-16] from NCs to molecules is often one of the key steps that limit the overall efficiency.

8.2 Results and Discussion

8.2.1 Synthesis of PbS QD and Sample Preparation

2.7 nm diameter PbS-S NCs were synthesized following the modified method of Scholes et al:[17]

450 mg PbO, 2 mL oleic acid and 18 mL 1-octadecene were added into a 50 mL 3-necked round bottom flask and heated at 110 ^{o}C for 1 hour under vacuum. The flask was then filled with argon. Once the solution turned clear, the temperature was set to 90 ^{o}C and 0.21 mL bis(trimethylsilyl)sulfide in 10 mL 1-octadecene injected and allowed to react for 3 min. Then the reaction was cooled down to room temperature with a water bath. Nanocrystals were washed in a

nitrogen glovebox by three precipitation/redispersion cycles with ethanol/hexane and stored in hexane in the glovebox in dark.

2.7 nm diameter PbS-T NCs were synthesized following the modified method of Owen et al:[18]

Pb and S precursor solutions were prepared by dissolving 0.88g $Pb(OA)_2$ in 14.75 mL 1-octene, and 0.17 g N-(3,5-bis(trifluoromethylphenyl))-N'-phenylthiourea in 0.5 mL diglyme in glovebox. Both solutions were heated to 95 ^{o}C and equilibrated for 15 min. The *N*-(3,5-bis(trifluoromethylphenyl))-*N'*-phenylthiourea solution was injected into the $Pb(OA)_2$ solution and reacted for 1 min. The reaction was then cooled down to room temperature and PbS NCs were washed by three cycles of precipitation from hexane with ethanol and stored in hexane in the glovebox in dark. 5-CT was synthesized following published work.[19]

PbS NCs were synthesized under air-free conditions based on two different methods pioneered by Scholes[17] and Owen.[18] In this paper, these PbS NCs are denoted by PbS-S and PbS-T because of their bis(trimethylsilyl)sulfide and thiourea sulfur precursors respectively. Both PbS NCs are 2.8 nm in diameter, with the lowest energy exciton peak around 840 nm (Figure 8.1/

Table 8.1). The size distribution obtained from transmission electron microscopy shows that PbS-T has better size homogeneity (Figure 8.3). The absorption spectra of three pairs of similarly sized

NCs (Figure 8.4) reveal that PbS-T has a sharper absorption peak compared to PbS-S. As shown in

Table 8.1, the emission properties of these QDs are similar, with PbS-T and PbS-S NCs showing photoluminescence QYs of (34.1±1.3)% and (29.5±1.2)%, respectively. Note that PbS-T was synthesized from highly purified precursors, lead oleate and *N*-(3,5-bis(trifluoromethylphenyl))-*N'*-phenylthiourea at 95 °C in diglyme and 1-octene, while PbS-S was prepared with commercially available PbO, oleic acid and bis(trimethylsilyl)sulfide as received at 90 °C in 1-octadecene. The highly purified precursors may allow a more uniform nucleation process in the synthesis of PbS-T NCs. Both PbS-S and PbS-T were purified in the same way with three cycles of precipitation from hexanes with ethanol.

8.2.2 Photon Upconversion Quantum Yield

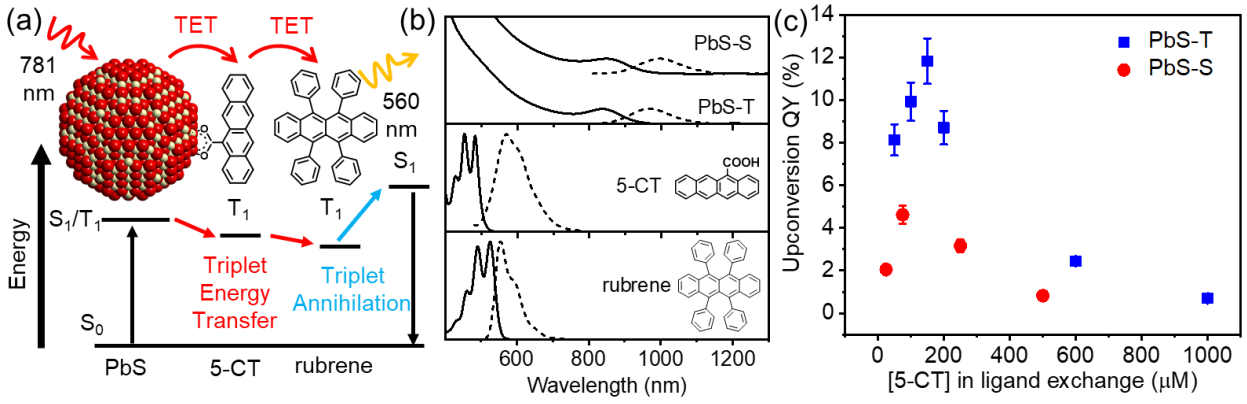

Figure 8.1 (a) Illustration of energy transfer during near-infrared photon upconversion. (b) Absorption and emission (solid and dashed lines respectively) of PbS NCs synthesized with different sulfur precursors, PbS-S and PbS-T, **5-CT** and rubrene. (c) Upconversion quantum yields with different **5-CT** concentrations in ligand exchange for PbS-T (blue squares) and PbS-S (red dots) NCs.

Ligand exchange reaction was performed by mixing 10 μM PbS NCs with 5-CT in different concentrations (Figure 8.1c) in toluene and stirring for 40 min. The total volume during ligand exchange solution is 0.3 mL. 1.2 mL acetone was added and the PbS/5-CT complex was crashed out by centrifuging for 10 min at 7830 rpm. The clear supernatant was discarded.

For upconversion measurements, the pellet was redispersed in 0.3 mL 20 mM rubrene/toluene solution and then transferred to 1 cm by 1 cm path length Starna cuvettes containing 200 μm thick borosilicate capillary tubes (Friedrich & Dimmock) adhered to the wall. The solution will diffuse up through the space inside the capillary tube. The final concentration of QD is 10 μM. All samples were prepared in a nitrogen glovebox.

Table 8.1 Key Parameters of PbS NCs

NCs	PbS-T	PbS-S
λ_{abs}/ λ_{ems} (nm)	836/ 966	845/ 998
D (nm)[a]	2.7	2.7
n[b]	14.8	13.9
Φ_{PL} (%)[c]	34.1±1.3	29.5±1.2
Φ_{UC} (%)[d]	11.8 ± 1.1	4.6 ± 0.4
k_{TET} (ns^{-1})[e]	2.56±0.13	3.77±0.13
Φ_{TET} (%)[e]	69.5±1.4	57.6±2.2
τ_T (μs) [e]	2.86±0.08	0.27±0.02

[a]Diameter, determined by the first exciton absorption maxima of PbS nanocrystals[20] [b]5-CT per PbS, determined by O.D. and molar extinction coefficients of **5-CT** and PbS NCs in PbS/**5-CT** complexes.[21] [c]PbS PL QY, indocyanine green in DMSO as standard.[22] [d]In 20 mM rubrene. [e]Obtained from TAS. All measurements are at RT in toluene.

We first compared the performances of these NCs in a photon-upconversion system consisting of PbS NCs (light absorber), surface anchored 5-carboxylic acid tetracene (**5-CT)** molecules (transmitter) and rubrene molecules (emitter) in toluene. As shown in Figure 8.1a, to initiate the photon upconversion process, PbS NCs are photoexcited by 781 nm continuous-wave laser, which does not excite **5-CT** or rubrene (Figure 8.1b). The excited PbS NCs undergo TET to surface anchored **5-CT**, which further transmits triplet energy to the rubrene down an energy cascade. Two rubrene triplets then annihilate to form a singlet, followed by the emission of 560 nm visible light, thus, converting two near IR 781 nm photons into a visible photon. Figure 8.1c shows the highest UC QYs for PbS-T and PbS-S NCs at optimal loading are 11.8±1.1% and 4.6±0.4%, respectively. Our previous work showed that the use of the **5-CT** transmitter is crucial as it can increase the QY by up to 80 times.[23]

The photon upconversion QY, Φ_{UC} is defined as:

$$\Phi_{UC} = 2 \times \Phi_{ref} \times \frac{(photons\ absorbed\ by\ reference)}{(photons\ absorbed\ by\ UC\ sample)} \times \frac{PL\ signal(UC\ sample)}{PL\ signal(reference)} \quad \text{Eq 8.1}$$

where Φ_{ref} is the photoluminescence QY of the rubrene reference, which is 98% in toluene.

Photon upconversion is performed with a 781 nm cw OBIS laser. The total number of absorbed photons per second, <*photon*>, equals to:

$$< photon >= \frac{Energy\ absorbed}{time*photon\ energy} = \frac{power*(1-10^{-OD_{781nm}})}{hc/\lambda} \qquad \text{Eq. 8.2}$$

Upconversion is detected in front face geometry at 45 degrees to the laser beam. Assuming an oblique cylindrical volume, the number of NC within the excitation volume is:

$$N_{PbS} = [PbS] * excitation\ volume * N_A = \frac{OD_{781nm}}{\varepsilon_{781nm}*d} * \sqrt{2} * \pi r^2 * d * N_A \qquad \text{Eq. 8.3}$$

where ε_{781nm} is the extinction coefficient of PbS NCs at 781 nm,[24] d is the optical path length or 200 μm, r is laser beam radius, 96.3 μm. N_A is Avogadro's number. Therefore,

$$< N_{exc} >= \frac{<photon>}{N_{PbS}} \qquad \text{Eq. 8.4}$$

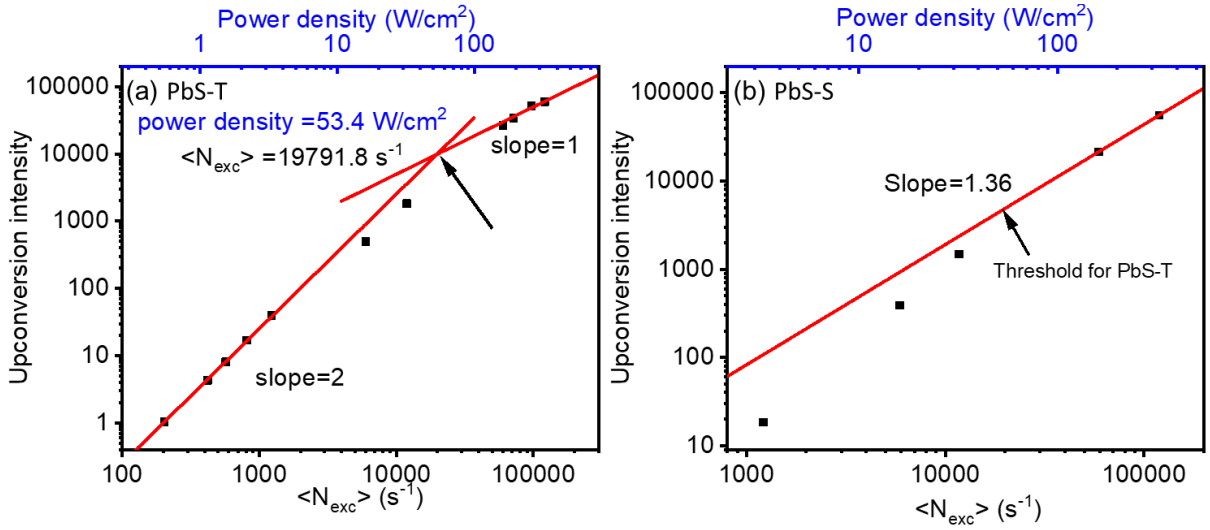

Figure 8.2 The plot of upconverted photons (rubrene emission) versus the average photoexcitations per NC per second <N_{exc}> (bottom axis), and the excitation power density (top axis) for (a) PbS-T and (b) PbS-S. Samples are with optimal 5-CT ligand loadings.

Table 8.2 Absorption maxima $\boldsymbol{\lambda_{abs}}$, diameter ***d***, and upconversion quantum yield Φ_{UC} with optimal surface loading of 5-CT for PbS-T and PbS-S NCs.

Nanocrystals	$\boldsymbol{\lambda_{abs}}$ **(nm)**	***d*** **(nm)**	$\boldsymbol{\Phi_{UC}}$ **(%)**
PbS-T	830	2.6	11.2
	836	2.7	11.8
PbS-S	845	2.7	4.60
	865	2.8	2.19
	942	3.1	0.330

With the optimal **5-CT** surface coverage, the PbS-T NCs routinely outperform PbS-S by a factor of 2–3 as the light absorber/sensitizer during photon upconversion (see Table S1 for multiple batches of PbS NCs result), even though the emission energies and quantum yields of these NCs are similar (Table 8.1, Figure 8.4c).[11, 25] The highest QY of photon upconversion with PbS-T NC sensitizers is 11.8±1.1 % (Table 8.1), which, to our knowledge, is the record for the NIR-to-visible upconversion with semiconductor NC sensitizers. As a comparison, the highest upconversion QY of PbS-S is only 4.6±0.4%, 2.6 times lower than that for PbS-T. Both PbS NCs have on average 14–15 **5-CT** transmitter ligands on PbS (see **n** in Table 8.1).

8.2.3 Comparison of PbS-S and PbS-T QD

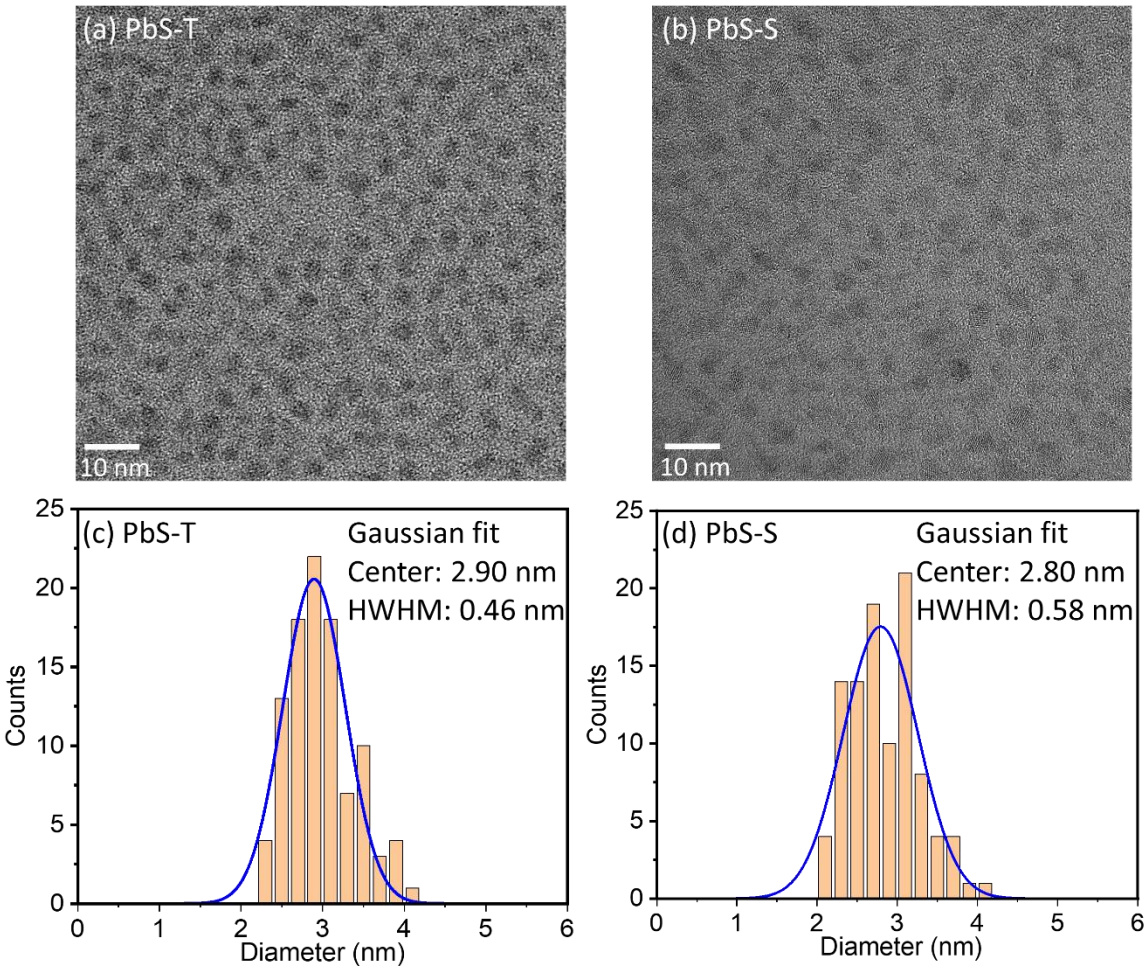

Figure 8.3 TEM images of 2.8 nm PbS-T (a) and PbS-S (b) nanocrystals with their corresponding size distribution histograms (c), (d) and Gaussian fit (blue curve).

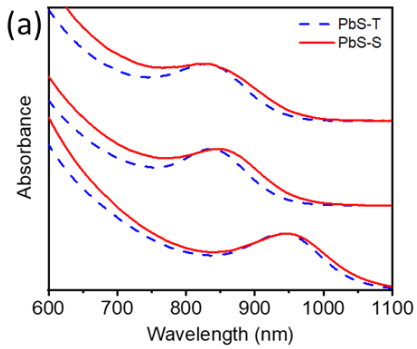

(b)	1st excitonic peak (nm)	HWHM (nm)
PbS-T	830	63
PbS-S	830	79
PbS-T	836	59
PbS-S	845	70
PbS-T	942	63
PbS-S	947	68

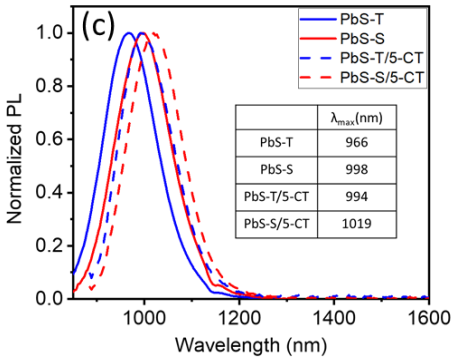

Figure 8.4 (a) Absorption spectra of three pairs of PbS-S (blue dashed line) and PbS-T (red solid line) nanocrystals similar in size. The half width at half maximum (HWHM) of the 1st excitonic peak is listed in the (b). (c) Normalized photoluminescence spectra of PbS nanocrystals in PbS-S/5-CT (red, 1st excitonic peak=845 nm) and PbS-T/5-CT (blue, 1st excitonic peak=830 nm) with/without optimal 5-CT surface coverage. Samples are dissolved in toluene and excited by 781 nm cw laser.

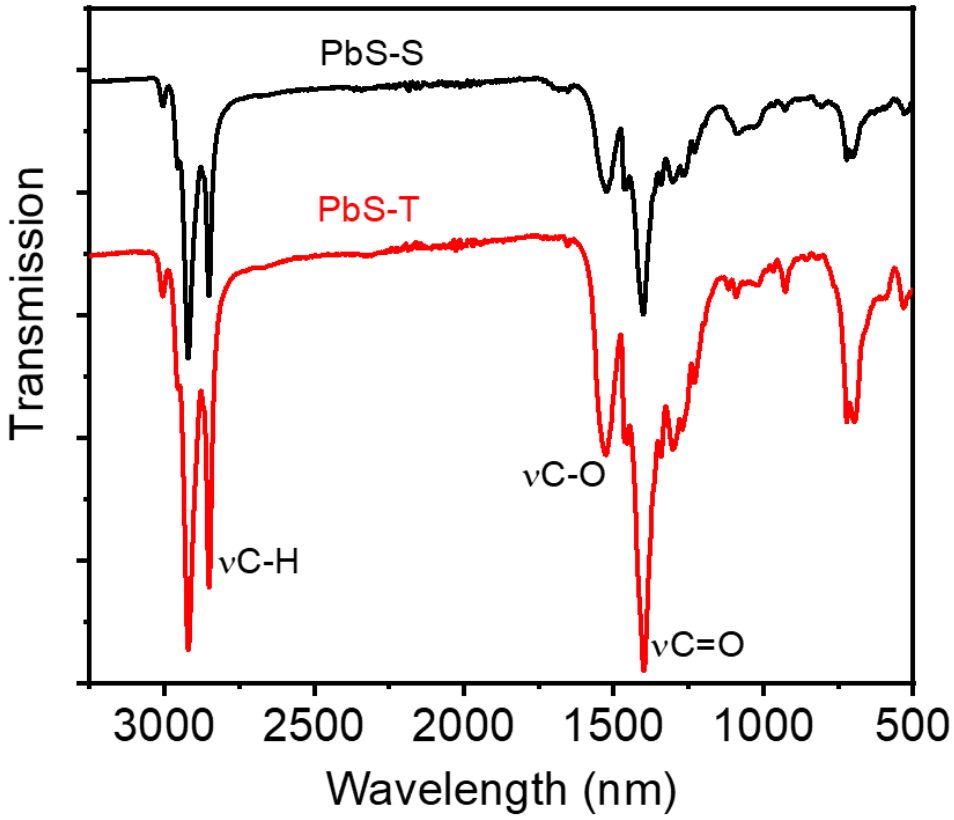

Figure 8.5 Infrared spectra of PbS-S (black) and PbS-T (red) capped with oleic acid. C-H, C-O and C=O vibrational modes in oleic acid are labeled.

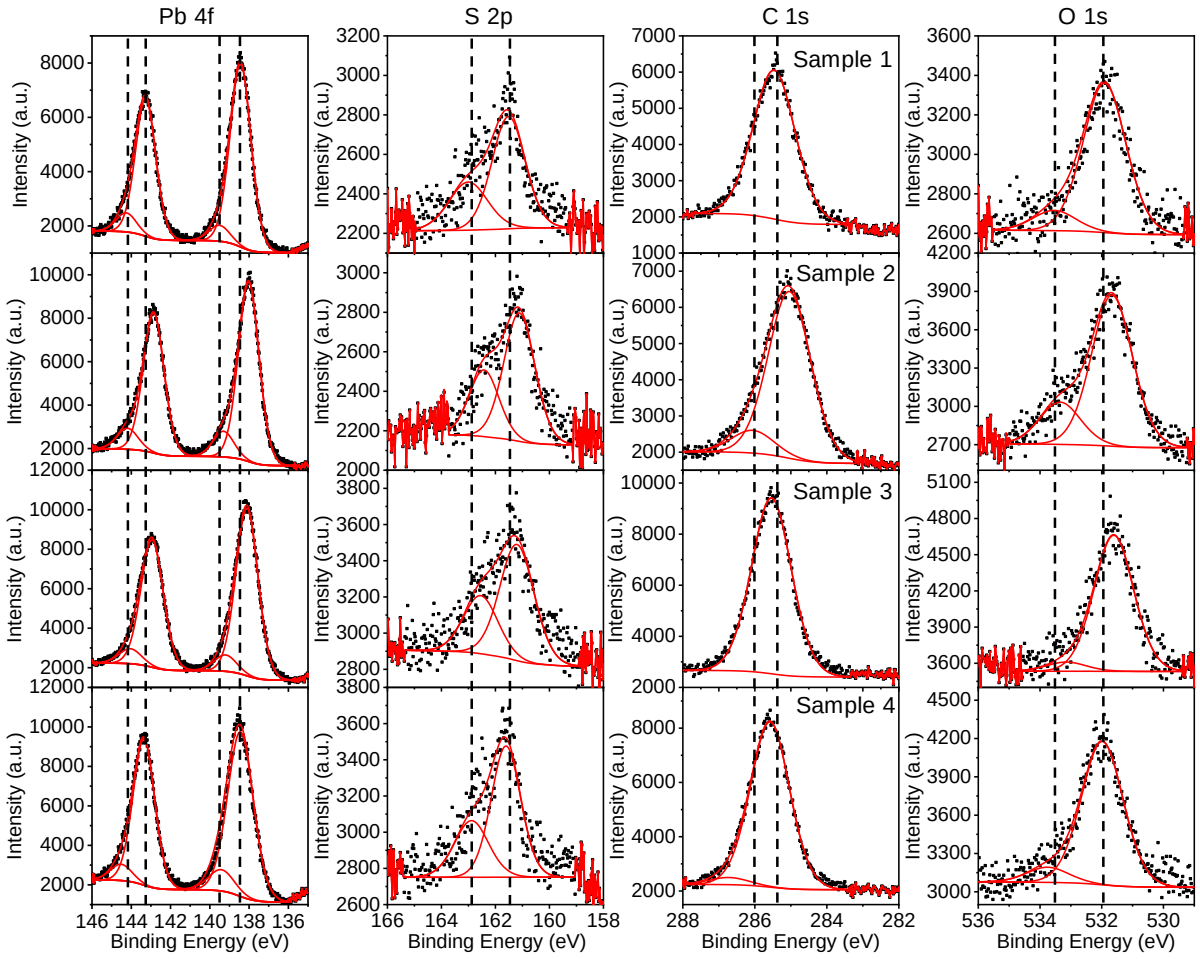

Figure 8.6 The XPS spectra of (from top to bottom) PbS-T, PbS-T/5-CT, PbS-S, PbS-S/5-CT for (from left to right) Pb 4f, S 2p, C 1s and O 1s. Black dots are raw data and red solid curves are the fittings. Vertical dashed lines are used for peak alignment.

Table 8.3 Elemental composition and binding energy from the XPS spectra in Figure 8.6 for PbS-T (absorption maxima at 830 nm) and PbS-S (absorption maxima at 865 nm) with and without surface anchored 5-CT. Error estimates are based on the noise in the data and the uncertainty in the background assignment. Systematic errors are not accounted for.

		Element composition (%)					**Binding energy/ eV**					
	Nanocrystal	Pb	S	C	O	Pb/S	Pb 4f7/2	Pb 4f5/2	S 2p3/2	S 2p1/2	C 1s	O 1s
Sample 1	PbS-T (830)	7.8 ± 0.2	7.9 ± 0.1	77.1 ± 0.4	7.4 ± 0.6	0.98 ± 0.02	138.4 139.5	143.3 144.3	161.5	163.0	285.5	531.9 533.5
Sample 2	PbS-T +5-CT	7.3 ± 0.1	6.5 ± 0.2	75.8 ± 0.2	10.5 ± 0.2	1.14 ± 0.04	138.0 139.3	142.9 144.2	161.1	162.4	285.1 286.1	531.7 533.4
Sample 3	PbS-S (865)	6.6 ± 0.1	6.1 ± 0.2	81.1 ± 0.5	6.2 ± 0.3	1.08 ± 0.03	138.1 139.2	142.9 144.1	161.2	162.5	285.5	531.6
Sample 4	PbS-S +5-CT	7.7 ± 0.2	6.1 ± 0.1	76.7 ± 0.7	9.0 ± 0.7	1.25 ± 0.02	138.4 139.4	143.4 144.5	161.6	162.9	285.6 286.7	532.0 533.8

X-ray photoelectron spectra (XPS) and Fourier-transform infrared (FT-IR) spectra show that both PbS NCs are bound with carboxylates, likely from the native oleic acid (Figure 8.5) and there is no thiourea precursor remaining in PbS-T. No prominent difference is observed between two PbS NCs in terms of the binding energy for Pb, S, C, and O (Figure 8.6, Table 8.3). Zherebetskyy et al.[26] have reported that the use of PbO and oleic acid (OA) in the synthesis of PbS-S generates water molecules that bind to $Pb(OA)_2$ that further dissociates to form hydroxyl

groups that stabilize PbS(111) facets. Unfortunately, the presence of the carboxylate ligands or Pb-O bonds precludes firm assignment of Pb-OH species because these binding energies overlap.

8.2.4 Transient absorption spectroscopy results

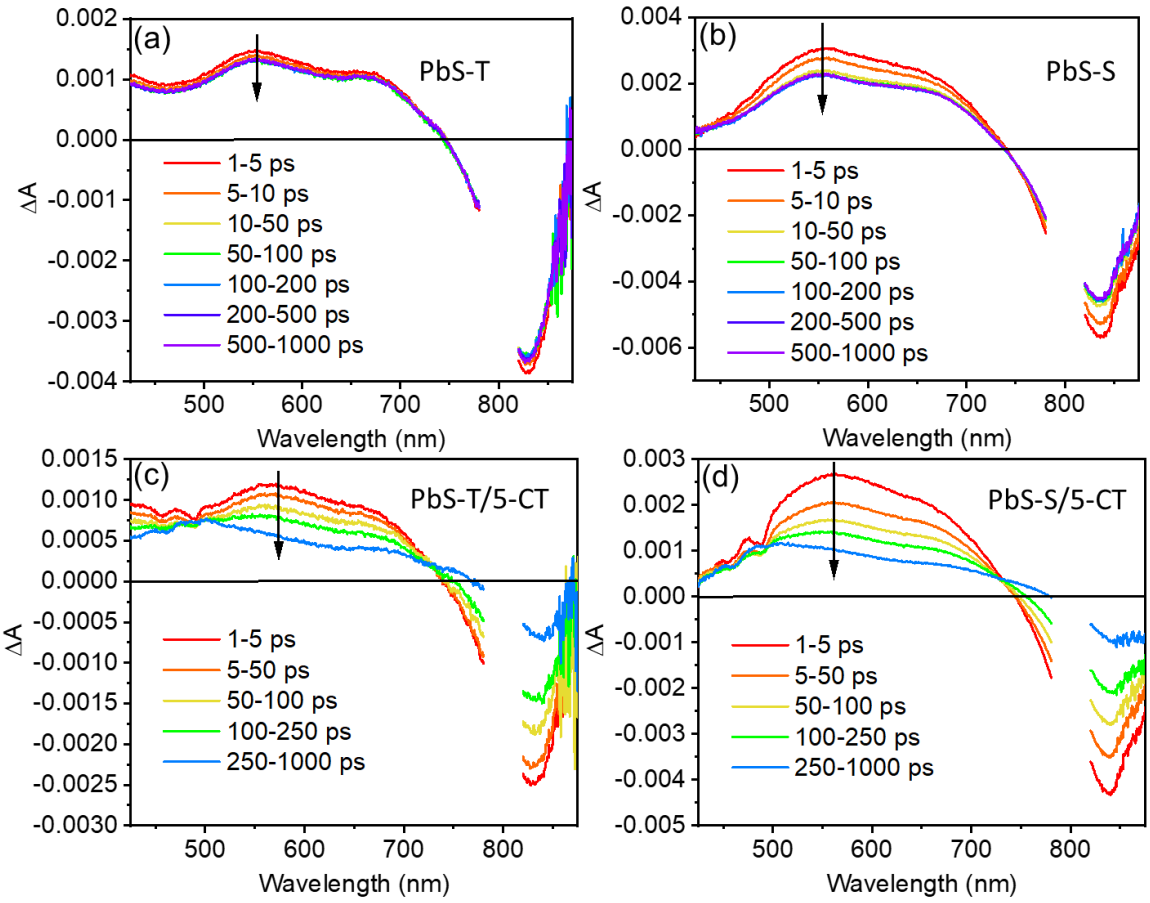

Figure 8.7 Femtosecond transient absorption spectra of (a) PbS-T, (b) PbS-S nanocrystals, (c) PbS-T/**5-CT**, and (d) PbS-S/**5-CT** complexes in toluene. Samples are excited at 800 nm.

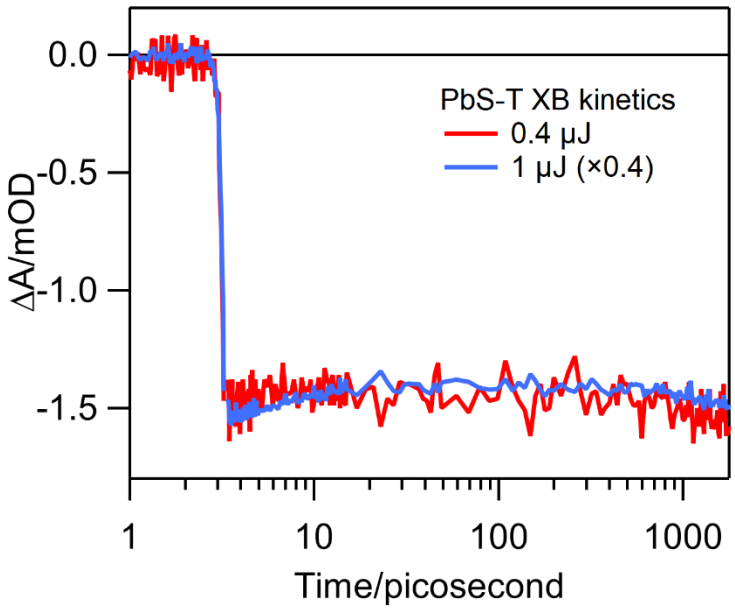

Figure 8.8 Exciton bleach kinetics monitored at 830 nm of PbS-T under low and high pump energy. The blue curve shows scaled (by a factor of 0.4) XB kinetics under 1 microJ 800 nm pulse energy (TAS experimental condition). The similar kinetics between 0.4 and 1 microJ excitation indicate Auger process is negligible and TAS measurements are conducted in the single exciton regime.

Transient absorption (TA) spectroscopy reveals major differences in the excited state dynamics of PbS-T and PbS-S as well as their complexes with **5-CT**. The TA spectra of PbS-T and PbS-S NCs from 1 ps to 1 ns are compared in Figure 8.7a and b. The TA spectra consists of PbS excited state absorption (ESA) and exciton bleach (XB) signals. Within the same time window from 1 ps to 1 ns, the exciton of PbS-T and PbS-S NCs decays by 11.5% and 29.3%, respectively, suggesting longer lived excitons in PbS-T. The exciton kinetics is measured under single exciton condition (Figure 8.8). In PbS/**5-CT** complexes (Figure 8.7c and d), over 50% of the exciton decays within 1 ns, much faster than the decay of PbS NCs, indicating energy and charge transfer from PbS NCs to **5-CT**. This is also supported by the observation of a 5-CT ground state bleach (GSB) (dips from 425 to 500 nm), and the presence of the 5-CT triplet (absorption band at 500

nm). Furthermore, the TA spectra of PbS/**5-CT** at longer delay times (1 ns to 10 microseconds, Figure 8.9c and d) are dominated by the PbS ESA and the **5-CT** triplet state.

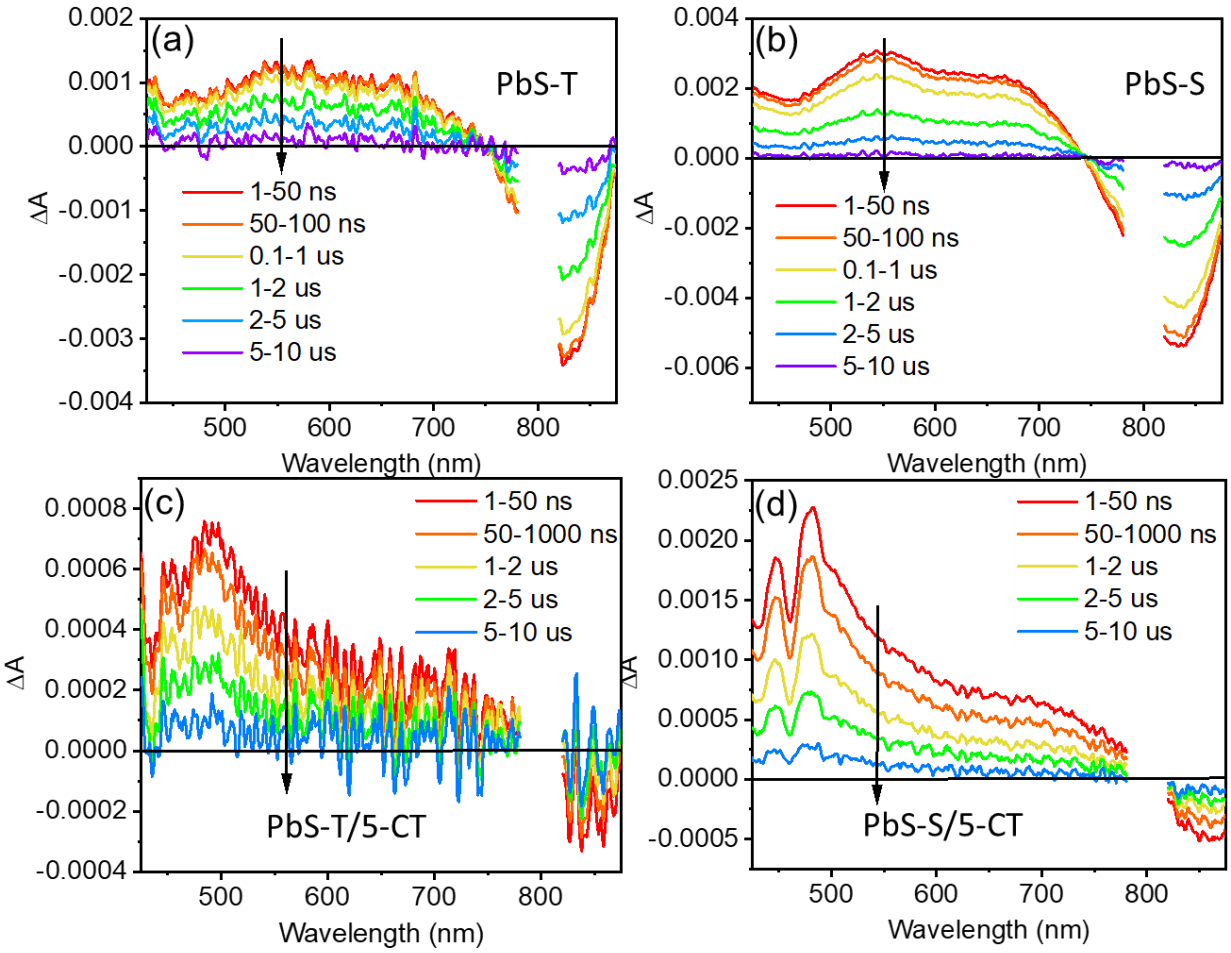

Figure 8.9 Nanosecond transient absorption spectra of (a) PbS-T, (b) PbS-S nanocrystals, (c) PbS-T/5-CT, and (d) PbS-S/5-CT complexes in toluene. Samples are excited at 800 nm. Each curve is the average over all the spectra within the corresponding time window. Spectra from 780 to 820 nm are truncated due to the saturation of the detector by excitation.

8.2.5 Double Difference Spectra to separate CS and Triplet State

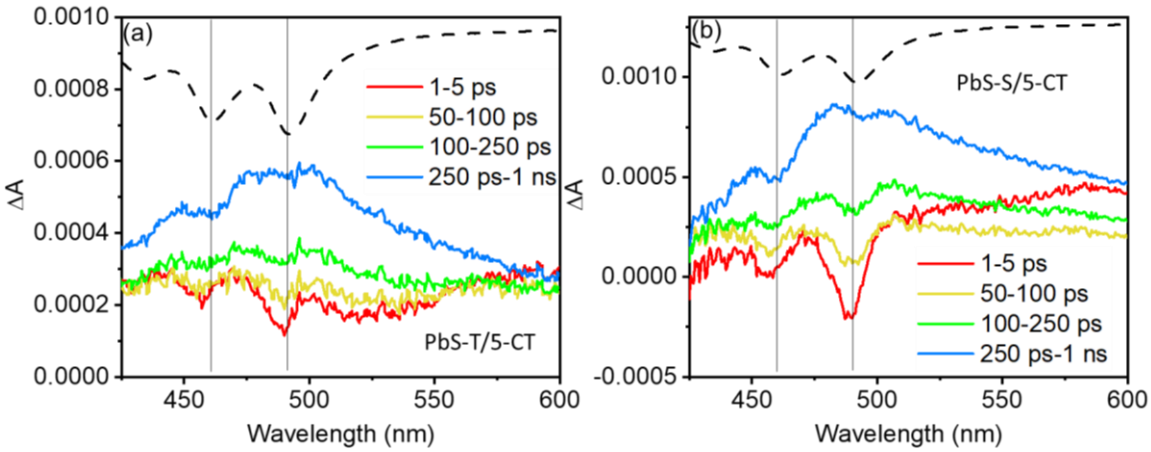

Figure 8.10 Double difference spectra of (a) PbS-T/**5-CT** and (b) PbS-S/**5-CT** after normalized to those of PbS/**5-CT** at the exciton peak at 830 nm. The dashed curve is the linear absorption spectrum of PbS bounded **5-CT** (inverted). The vertical gray lines indicate **5-CT** linear absorption maxima, which match the negative features of double difference spectra at 460 and 489 nm.

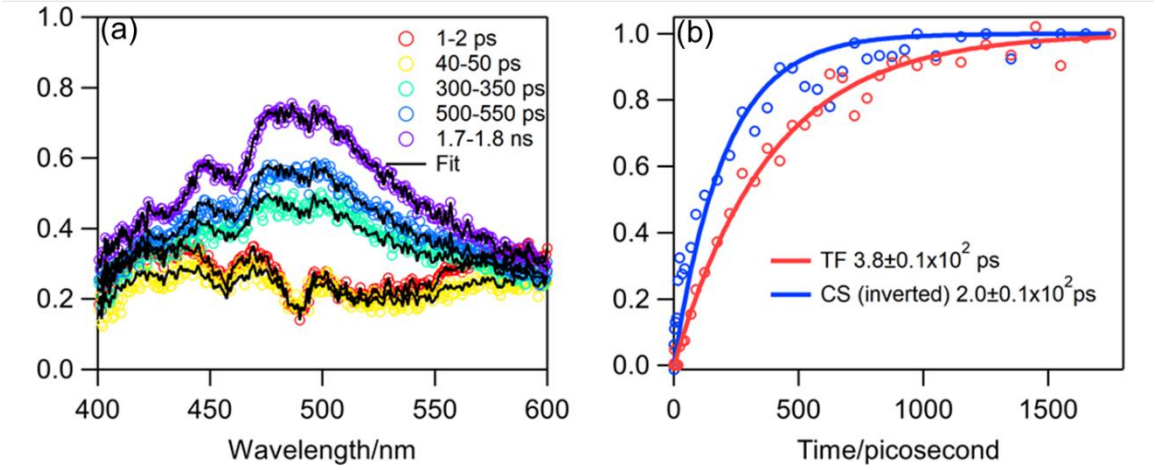

Figure 8.11 (a) The double difference spectra of PbS-T/5-CT. The double difference spectra at 1-2 ps and 1.7-1.8 ns are regarded as the spectra of the pure charge separation state and 5-CT triplet state, and the spectra between 1 ps and 2 ns can be fitted as the sum of the two states with a specific relative population (black solid curve). (b) Relative populations of charge separation (CS) state

(blue circles) and 5-CT triplet formation (TF, red circles) on PbS-T NCs. Solid curves are the monoexponential fittings. This graph shows that the CS state does not decay to 5-CT triplet state because the two processes have different time constants (labeled in panel b).

To differentiate possible exciton quenching pathways, we further analyze the spectral features associated with **5-CT** by constructing the double difference spectra in which the overlapping broad PbS ESA band is removed. This is obtained by subtracting the TA spectra of PbS (containing only PbS contributions) from that of PbS/**5-CT** (with the former spectra normalized to the amplitude of the latter at 830 nm). As shown in Figure 8.10a and b, the double difference spectra for both PbS NCs have two clear ground state bleach features at 460 and 489 nm that match the absorption maxima of **5-CT** in its linear absorption spectra. The double difference spectra at 250 ps – 1 ns can be attributed to the formation of **5-CT** triplet, showing both the broad triplet absorption from 400-600 nm (with a peak at ~500nm) and the narrow ground state bleach at 460 and 489 nm.[27] The spectra also show pronounced **5-CT** GSB at 1-5 ps without the formation of triplet, suggesting additional exciton quenching pathways at early delay times. This initial bleach of surface bound **5-CT** has been attributed to the formation of **5-CT** cation radicals by ultrafast hole transfer.[27] Because of the overlap between the TA spectra of charge separated (CS) and the triplet (TF) state, the double difference spectra were fit to the sum of these species with the assumption that the spectra at early delay time (first few ps) is purely CS and spectra at 1 ns or longer is purely TF, as shown in Figure 8.11a. From the fit, we obtained the kinetics of CS decay and TF formation (Figure 8.11b). Comparison of these kinetics shows that the decay of the charge separated state (with a time constant of $2.0\pm0.1\times10^2$ ps) is significantly faster than the growth of **5-CT** triplet state ($3.8\pm0.1\times10^2$ ps), indicating that the hole transfer step or charge separated state is not an intermediate to the formation of the triplet state.

8.2.6 Competition of Charge separation state and triplet state

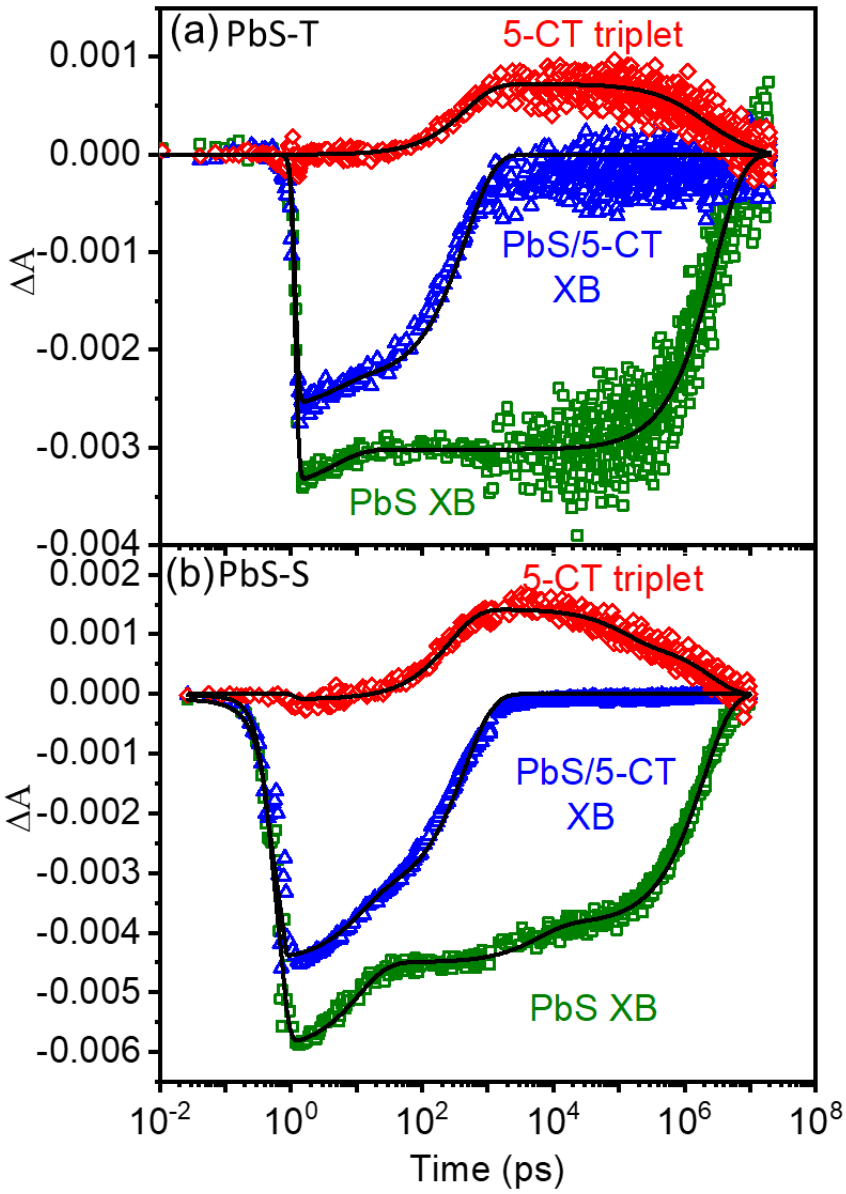

Figure 8.12 Comparison of the kinetics of the exciton bleach of PbS NCs (green squares) and PbS/**5-CT** (blue triangles) at 830 nm, the **5-CT** triplet (red diamonds) at 489 nm for (a) PbS-T and (b) PbS-S. Black solid curves are fits according to a model described in main text.

The competition between charge and energy transfer from NCs to **5-CT** within ~1 ns has been observed in our previous study.[27] By constructing the double difference spectra (Figure 8.10)

and fitting the spectra with charge separation state spectrum and triplet state spectrum (Figure 8.11), we concluded that there exist two subpopulations of PbS/**5-CT** complexes with two exciton decay pathways: one by TET to form the desired **5-CT** triplet state and the other by hole transfer to **5-CT** cation radical, which presumably decays back to ground state through charge recombination. The distribution of these subpopulations determines the overall TET efficiency. Competition between the hole and triplet energy transfer pathways can be more clearly seen by comparing the exciton bleach decay kinetics in PbS and PbS/**5-CT** as well as the **5-CT** triplet formation for both PbS-T (Figure 8.12a) and PbS-S (Figure 8.12b).

Exciton bleach kinetics is monitored at 830 nm and the bleach amplitudes in PbS and PbS/**5-CT** have been normalized to correspond to the same number of absorbed photons. **5-CT** triplet kinetics (red diamonds, Figure 8.12) was obtained by subtracting the charge separated state kinetics (see Figure 8.10 and Figure 8.11) from total the kinetics at the peak of triplet ESA (489 nm) in the double difference spectra. The **5-CT** triplet kinetics can be fitted with a single exponential growth and decay component to obtain the TET rate constant and triplet lifetime, respectively. The single exponential growth time constant (390 ps) is consistent with the triplet state formation time obtained through the spectral fitting procedure (380 ps, Figure 8.11b) described above. Using the TET rate, the decay of the exciton bleach of PbS NCs (green squares) and PbS /**5-CT** (blue triangles) were globally fit to obtain the intrinsic decay amplitude and time constants of QD excitons and the amplitude of fast hole transfer component. Some of the key fitting parameters are listed in Table 8.1.

The intrinsic decay of PbS NCs can be well fit by triexponential decays, with amplitudes and time constants of a_i and k_i (i=1-3), respectively.

$$[QD^*](t) = [QD^*](0)\sum_{i=1}^{3} a_i e^{-k_i t} \qquad \text{Eq. 8.5}$$

In PbS/5-CT complexes, due to triplet energy transfer (with rate constant k_{ET}) to 5-CT, the decay kinetics of the QD becomes:

$$[QD^*//CT](t) = [QD^*//CT](0)\sum_{i=1}^{3} Aa_i e^{-(k_i+k_{ET})t} \qquad \text{Eq. 8.6}$$

where A is the percentage of PbS NC excitons that undergo triplet energy transfer to 5-CT. The remaining portion (1-A) accounts for the initial instrument response limited fast charge transfer pathway.

5-CT triplet state is fitted by a growth component (triplet energy transfer rate constant k_{ET}), and a decay component (5-CT triplet decay rate constant k_T):

$$[CT^*](t) = a_{ET} * e^{-k_{ET}*t} + a_T * e^{-k_T*t} \qquad \text{Eq. 8.7}$$

where a_{ET}, a_T are the amplitudes.

The kinetics of excitons in PbS and PbS/5-CT and 5-CT triplet state as well as their fits according to the model above are shown in Figure 8.12a and b. In the fitting process, the kinetics of triplet 5-CT triplet was first fitted by Eq. 8.7 to obtain k_{ET} and k_T. These values were used to fit globally the exciton decay of PbS and PbS/5-CT by Eq. S5 and S6 to obtain the intrinsic decay rate (k_i) and amplitude (a_i) as well as A.

The TET efficiency is given by:

$$\sum_{i=1}^{3} \frac{Aa_i k_{ET}}{k_{ET}+k_i} \qquad \text{Eq. 8.8}$$

Table 8.4 Parameters obtained from fitting kinetics traces

	PbS-T	PbS-S
[QD](0)	-3.36±0.05 mOD	5.90±0.04 mOD
a_1	9.64±1.20%	23.8 ±0.4%

a_2	91.0±0.3%	10.9±0.2%
a_3[a]		65.3±0.1%
k_1	0.208±0.059ps^{-1}	0.0918±0.0038 ps^{-1}
k_2	0.345±0.011μs^{-1}	0.164±0.012 ns^{-1}
k_3		0.514±0.004 μs^{-1}
A	0.763±0.007	0.751±0.002
k_{ET}	2.56±0.13ns^{-1}	3.77±0.13 ns^{-1}
k_T	0.35±0.01μs^{-1}	3.69±0.20 μs^{-1}
TET%	69.5±1.4	57.6±2.2

[a]biexponential is used to fit the exciton bleach of PbS-T.

Table 8.5 Component contribution to TET efficiency

PbS-T			**PbS-S**		
Component	Percent	TET%	Component	Percent	TET%
a_1	9.64±1.20%	0.9±0.0%	a_1	23.8 ±0.4%	3.0±0.1%
a_2	91.0±0.3%	76.2±1.6%	a_2	10.9±0.2%	72.0±3.2%
			a_3	65.3±0.1%	75.1%

The fitting result reveals that in both PbS/**5-CT** complexes, fast hole transfer to **5-CT** accounts for ~ 25% of the exciton decay. This occurs within the instrument response time (<< 150 fs) (Figure 3a and b). The TET rate constant for PbS-T/**5-CT** is 2.56 ns^{-1}, slightly smaller than 3.37

ns^{-1} for PbS-S/**5-CT**. However, the calculated TET efficiency for PbS-T/**5-CT** (69.5%) is higher than PbS-S/**5-CT** (57.6 %). This difference can be attributed to a smaller contribution of the fast intrinsic exciton decay component (Figure 8.12a and b) in PbS-T (with amplitude and time constant of 9.6%, ~ 5 ps) than that in PbS-S (~ 23.8%, ~10 ps) (see Table 8.4 and Table 8.5). This is consistent with the power dependence during photon upconversion- a lower quadratic-to-linear threshold intensity is obtained for PbS-T (Figure 8.2). However, this 20% enhancement in TET efficiency does not explain the 2.6 times enhancement of the photon upconversion QY, suggesting important differences in the latter steps of overall process (Figure 8.1).

8.3 Conclusion

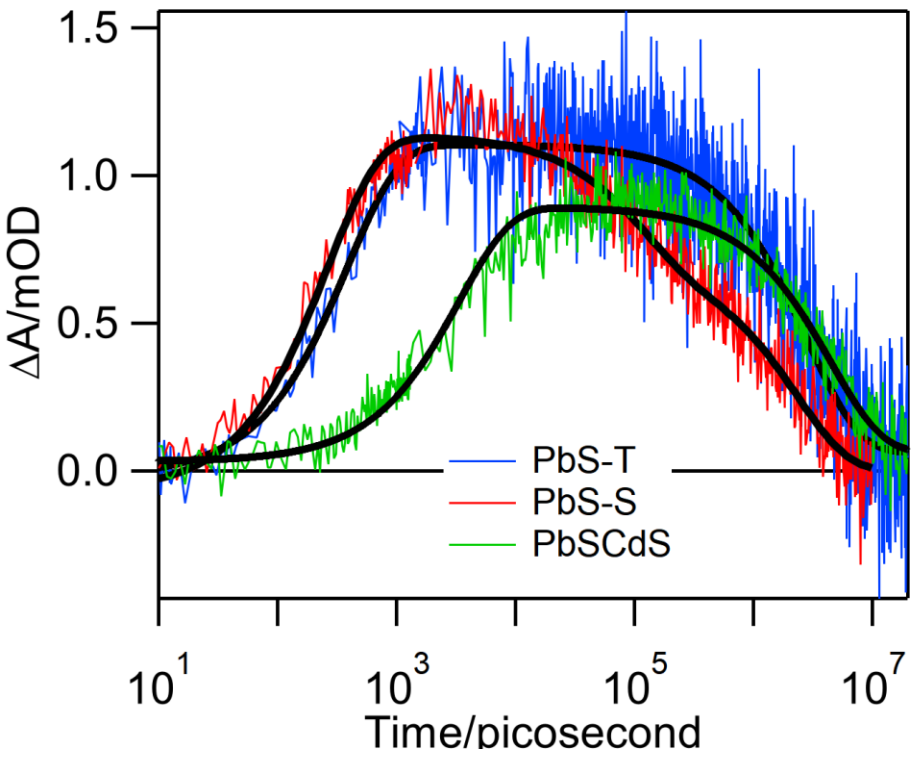

Figure 8.13 Kinetics of the surface bound 5-CT triplet created from energy transfer after photoexcitation of various PbS NCs: PbS-T (blue), PbS-S (red) and PbS-S/CdS core-shell NCs (green, with the same PbS core diameter).6 Curves are plotted after scaling. Black curves are the fitting with the method discussed above

Kinetic models show that TET efficiency from the light absorber/transmitter to emitter is unity if the donor's triplet lifetime exceeds 10 μs and the acceptor concentration > 10 mM, and becomes lower than unity at lower triplet lifetime and/or emitter concentration.[28] Since **5-CT** lifetime is less than 3 μs (Table 8.1), TET efficiency from PbS/**5-CT** photosensitizer to rubrene annihilator is likely a limiting factor here. The triplet lifetime of **5-CT** anchored on the surface of PbS-T is 2.86 μs, about ten times longer than that of 0.27 μs for PbS-S NCs (Figure 8.13). The longer triplet lifetime on PbS-T enhances TET from **5-CT** to rubrene, thus bolstering the upconversion QY. The triplet lifetime of free 5-CT in solution is more than 100 μs[27], which is

shortened by ~50 and ~500 times when adsorbed on PbS-T and PbS-S, respectively. The result suggests that the triplet lifetime of 5-CT is significantly reduced by interaction with PbS QDs through the heavy atom effect and this interaction is sensitive to the surface chemistry of the QDs. We have also shown in our previous work[27] that a submonolayer CdS shell on PbS-S also stabilizes the triplet of adsorbed **5-CT**. Here, **5-CT** on PbS-T has a comparable triplet lifetime to that for PbS-S/CdS core-shell NCs (2.70 μs, Figure 8.13), but PbS-T NCs can achieve 2.5 times faster TET rate by eliminating the insulating shell, suggesting that controlling the surface chemistry is a more effective way to improve the upconversion efficiency. Although the exact chemical origin for the observed surface effect of these QDs are unclear, our result demonstrates their significance and motivates further investigations along this direction.

In summary, we have demonstrated an efficient photon upconversion system that achieved a maximum QY of 11.8% for converting 780 nm into 560 nm when using PbS-T NCs, which were synthesized using highly purified precursors. Detailed TA spectroscopy studies reveal that the better performing PbS-T NCs have a smaller fast (a few ps) nonradiative decay component, giving rise to a 20% higher TET efficiency from the NC to **5-CT**. More importantly, the lifetime of **5-CT** triplet excited state is about ten times longer on PbS-T than on PbS-S, due to yet-to-be understood subtle differences in the surface chemistry of these QDs. These factors combine to result in higher upconversion efficiency in the PbS-T NCs. Our result demonstrates that synthetic control of NC surface chemistry and excited state dynamics is an important approach for enhancing the efficiency of NC sensitizer based photon upconversion systems.

8.4 References

1. Alivisatos, A. P., *Science* **1996,** *271* (5251), 933-937.
2. Colvin, V. L.; Schlamp, M. C.; Alivisatos, A. P., *Nature* **1994,** *370* (6488), 354-357.
3. Pietryga, J. M.; Park, Y.-S.; Lim, J.; Fidler, A. F.; Bae, W. K.; Brovelli, S.; Klimov, V. I., *Chemical Reviews* **2016,** *116* (18), 10513-10622.
4. Carey, G. H.; Abdelhady, A. L.; Ning, Z.; Thon, S. M.; Bakr, O. M.; Sargent, E. H., *Chemical Reviews* **2015,** *115* (23), 12732-12763.
5. Kroupa, D. M.; Arias, D. H.; Blackburn, J. L.; Carroll, G. M.; Granger, D. B.; Anthony, J. E., . . . Johnson, J. C., *Nano Letters* **2018,** *18* (2), 865-873.
6. Davis, N. J. L. K.; Allardice, J. R.; Xiao, J.; Petty, A. J.; Greenham, N. C.; Anthony, J. E.; Rao, A., *The Journal of Physical Chemistry Letters* **2018,** *9* (6), 1454-1460.
7. Főrster, T., *Discussions of the Faraday Society* **1959,** *27* (0), 7-17.
8. Dexter, D. L., *The Journal of Chemical Physics* **1953,** *21* (5), 836-850.
9. Wenger, O. S., *Chemical Society Reviews* **2011,** *40* (7), 3538-3550.
10. Adams, D. M.; Brus, L.; Chidsey, C. E. D.; Creager, S.; Creutz, C.; Kagan, C. R., . . . Zhu, X., *The Journal of Physical Chemistry B* **2003,** *107* (28), 6668-6697.
11. Huang, Z.; Li, X.; Mahboub, M.; Hanson, K. M.; Nichols, V. M.; Le, H., . . . Bardeen, C. J., *Nano letters* **2015,** *15* (8), 5552-5557.
12. Wu, M.; Congreve, D. N.; Wilson, M. W.; Jean, J.; Geva, N.; Welborn, M., . . . Baldo, M. A., *Nat Photonics* **2016,** *10* (1), 31-34.
13. Chen, Y.; Vela, J.; Htoon, H.; Casson, J. L.; Werder, D. J.; Bussian, D. A., . . . Hollingsworth, J. A., *Journal of the American Chemical Society* **2008,** *130* (15), 5026-5027.
14. Chen, O.; Zhao, J.; Chauhan, V. P.; Cui, J.; Wong, C.; Harris, D. K., . . . Bawendi, M. G., *Nat Mater* **2013,** *12* (5), 445-451.
15. Li, X.; Huang, Z.; Zavala, R.; Tang, M. L., *The Journal of Physical Chemistry Letters* **2016,** *7* (11), 1955-1959.
16. Nienhaus, L.; Wu, M.; Geva, N.; Shepherd, J. J.; Wilson, M. W. B.; Bulović, V., . . . Bawendi, M. G., *ACS Nano* **2017,** *11* (8), 7848-7857.
17. Hines, M. A.; Scholes, G. D., *Adv Mater* **2003,** *15* (21), 1844-1849.
18. Hendricks, M. P.; Campos, M. P.; Cleveland, G. T.; Jen-La Plante, I.; Owen, J. S., *Science* **2015,** *348* (6240), 1226-1230.
19. Okamoto, T.; Suzuki, T.; Tanaka, H.; Hashizume, D.; Matsuo, Y., *Chemistry – An Asian Journal* **2012,** *7* (1), 105-111.
20. Yu, W. W.; Qu, L.; Guo, W.; Peng, X., *Chem. Mater.* **2003,** *15* (14), 2854-2860.
21. Mahboub, M.; Huang, Z.; Tang, M. L., *Nano Letters* **2016,** *16* (11), 7169-7175.
22. Shao, W.; Chen, G.; Kuzmin, A.; Kutscher, H. L.; Pliss, A.; Ohulchanskyy, T. Y.; Prasad, P. N., *Journal of the American Chemical Society* **2016,** *138* (50), 16192-16195.
23. Huang, Z.; Simpson, D. E.; Mahboub, M.; Li, X.; Tang, M. L., *Chemical Science* **2016,** *7* (7), 4101-4104.
24. Moreels, I.; Lambert, K.; Smeets, D.; De Muynck, D.; Nollet, T.; Martins, J. C., . . . Allan, G., *ACS nano* **2009,** *3* (10), 3023-3030.
25. Mahboub, M.; Maghsoudiganjeh, H.; Pham, A. M.; Huang, Z.; Tang, M. L., *Advanced Functional Materials* **2016,** *26* (33), 6091-6097.

26. Zherebetskyy, D.; Scheele, M.; Zhang, Y.; Bronstein, N.; Thompson, C.; Britt, D., . . . Wang, L.-W., *Science* **2014,** *344* (6190), 1380-1384.
27. Huang, Z.; Xu, Z.; Mahboub, M.; Li, X.; Taylor, J. W.; Harman, W. H., . . . Tang, M. L., *Angewandte Chemie International Edition* **2017,** *56* (52), 16583-16587.
28. Schmidt, T. W.; Castellano, F. N., *The journal of physical chemistry letters* **2014,** *5* (22), 4062-4072.

9. Conclusion and Outlook

In Chapter 3, we demonstrated an *in situ* measurement of transient reflectance (TR) modulation signal and IPCE simultaneously. Through modelling and fitting, we have demonstrated that both measurements are fundamentally based on the charge separation efficiency. Under high intensity pulsed laser excitation, the power dependent charge separation efficiency is attributed to the effect of band flattening. We have also observed that the *p-n* junction photoelectrode has a stronger built-in field that enhances charge separation even at very high photon flux and is, thus, superior to single junction photoelectrodes for efficient charge separation. This high charge separation efficiency has enabled us to measure meaningful IPCEs even under femtosecond laser excitation. We have then established a strong correlation between the initial charge carrier separation efficiency obtained by TR spectroscopy and the IPCE in this TiO_2/GaP system. This discovery provides an insight that the overall photoelectrochemical efficiency is largely determined by the initial charge carrier separation efficiency. This method also provides a powerful tool to study similar PEC systems to evaluate the charge separation efficiency. In Chapter 4, we demonstrated time resolved electrical field induced second harmonic generation (TR-EFISH) in typical pump-probe setup provides direct observation over accumulated charge carriers' kinetics. The EFISH signal is largely induced by the electrical field at the depletion region of the semiconductor, which is universal to these semiconductor photoelectrodes. TR-EFISH technique, unlike the Franz Keldysh Oscillation employed in Chapter 3, does not rely on the optical transition of the semiconductor itself.

We propose to further employ TR and TR-EFISH for application on photoelectrochemical (PEC) system where we could extract the charge carrier dynamics from excitation to separation to migration and eventually, to chemical reaction. We have demonstrated some success on III-V

semiconductor GaP, we believe a similar study could be conducted on other single crystal electrode such as GaAs and Si which have shown promising PEC performance. The PEC performance could be highly improved after grafting catalyst on the surface, however, the catalyzing mechanisms are often unclear. We hope observation on the charge carrier dynamics at the catalyst reaction time scale could provide mechanistic insights. Such study is highly valuable in understanding the mechanism and yet no other technique offers similar feasibility in application to multiple systems.

In Chapter 5 we demonstrated an enhanced intersystem crossing by a TEMPO radical on a BODIPY molecule and showed that the geometry of the molecule could decouple the enhancement in triplet yield and decrease in triplet lifetime. Moreover, DFT calculations revealed an internal conversion coupled decay pathway for triplet excited state in this BODIPY system. In Chapter 6, we developed a representative molecule from oligothiophene family that showed promising potential as a triplet energy acceptor which is successfully sensitized by CdSe quantum dots. Then we carefully studied such triplet energy transfer pathways and determined it to be a Dexter type direct energy transfer and the intrinsic energy transfer rate is measured. In Chapter 7, we studied the competition between triplet energy transfer and charge transfer in a PbS quantum dot sensitized photon up conversion system. In this system, the triplet energy mediator, carboxylic acid modified tetracene, shows that the charge transfer is a loss pathway for triplet energy transfer efficiency. After shutting down such pathway with a sub monolayer CdS shell, the triplet energy transfer efficiency is enhanced. Combined with the study of similar system in Chapter 8, where we carefully examined two PbS QD synthesized by different methods that have different surface chemistry, we realized the limiting factor in heavy atom contained QD photon up conversion system is actually the mediator's triplet lifetime. This can be explained by the long mediator lifetime needed for the diffusion limited triplet-triplet annihilation process of the final emitter. The

mediator's triplet lifetime is mainly quenched by the heavy atom (Pb) in the QD. The Pb has been studied to facilitate the spin-orbital coupling that weakens the spin selection rule, therefore, the spin-forbidden process of triplet decay becomes more allowed. Therefore, we concluded that in the heavy atom containing QD the main loss pathway is the inefficient triplet energy transfer from the mediator to the emitter due to the shortened mediator triplet lifetime.

With this we proposed to further enhance the upconversion efficiency by utilizing the less or no heavy atom containing QD as a sensitizer. We have preliminary results showing the cadmium (atomic mass=112) QD comparing to Pb (atomic mass=207) has significantly less quenched mediator lifetime. We believe with the right sensitizer the triplet upconversion quantum yield could be further improved. We are also interested in validating the fundamental theory of triplet energy transfer. Dexter theory has predicted how the triplet energy transfer rate will be affected by the distance and energy difference between the donor and acceptor. Previously Dexter theory has been examined by molecular systems where both the donor and acceptor are molecules. However, the disadvantage with these studies is that the energy level in a molecular system is hard to tune. With QD's highly tunable band gap, we should be able to carefully examine the transfer rate dependence on the energy difference and thus, validating Dexter theory. A smaller band gap allows absorbance of low energy photon, but the triplet energy transfer rate might go down when moving away from the resonance with the mediator molecule. This study should provide a design principle that improves the overall upconversion quantum yield by selecting appropriate band gap QD.